Theoretical Spectroscopy of Ga$_2$O$_3$

Dissertation

zur Erlangung des akademischen Grades

doctor rerum naturalium

(Dr. rer. nat.)

im Fach Physik

Spezialisierung: Theoretische Physik

eingereicht an der

Mathematisch-Naturwissenschaftlichen Fakultät

der Humboldt-Universität zu Berlin

von

M.Sc. Christian Wolfgang Vorwerk

Präsidentin der Humboldt-Universität zu Berlin

Prof. Dr. Sabine Kunst

Dekan der Mathematisch-Naturwissenschaftlichen Fakultät

Prof. Dr. Elmar Kulke

GutachterInnen: 1. Prof. Dr. Dr. hc Claudia Draxl

2. Prof. Dr. Giulia Galli

3. Dr. Francesco Sottile

Tag der mündlichen Prüfung: 01.10.2020

Ich erkläre, dass ich die Dissertation selbständig und nur unter Verwendung der von mir gemäß §7 Abs. 3 der Promotionsordnung der Mathematisch-Naturwissenschaftlichen Fakultät, veröffentlicht im Amtlichen Mitteilungsblatt der Humboldt-Universität zu Berlin Nr. 42/2018 am 11.07.2018 angegebenen Hilfsmittel angefertigt habe.

Weiterhin erkläre ich, dass ich mich nicht bereits anderwärts um einen Doktorgrad im Promotionsfach Physik beworben habe beziehungsweise einen entsprechenden Doktorgrad besitze.

Ich habe Kenntnis der dem Promotionsverfahren zugrunde liegenden Promotionsordnung der Mathematisch-Naturwissenschaftlichen Fakultät, veröffentlicht im Amtlichen Mitteilungsblatt der Humboldt-Universität zu Berlin Nr. 42/2018 am 11.07.2018.

Berlin, den 10. Dezember 2020

Mathematisch-Naturwissenschaftliche Fakultät
Institut für Physik

Theoretical Spectroscopy of Ga$_2$O$_3$

Electronic Excitations from the UV to the Hard X-ray Regime

Ph.D. Thesis
by Christian Wolfgang Vorwerk

Supervisor: Prof. Dr. Claudia Draxl

To Mariella.

Zusammenfassung

Um neue Halbleiter-Bauelemente zu entwickeln und die Effizienz bereits existierender zu verbessern, müssen neue Materialien erkundet und untersucht werden. Für Anwendungen in Hochleistungselektronik und UV-Optoelektronik werden momentan Halbleiter mit ultraweiter Bandlücke erforscht. Mit seiner Bandlücke von 4.8 eV ist Ga_2O_3 ein vielversprechender Kandidat in dieser Gruppe von Materialien. Seine Anwendung in „sonnenblinden" UV-Detektoren und Hochleistungselektronik haben zu wachsendem Interesse an seinen fundamentalen elektronischen und optischen Eigenschaften geführt. Diese Dissertation stellt eine umfassende *ab initio*-Untersuchung der elektronischen Anregungen in Ga_2O_3 dar, um zu dem Verständnis dieser fundamentalen Eigenschaften beizutragen. Die Dissertation besteht aus zwei Teilen:

Im ersten Teil präsentieren wir eine Methode zur konsistenten Berechnung der neutralen Anregungen von Valenz- und Kernelektronen in kristallinen Halbleitern. Diese beschreibt die Vielteilchen-Wechselwirkungen innerhalb des Rahmens der Vielteilchen-Störungstheorie, und ermöglicht so die präzise Berechnung von Absorptions- und inelastischen Streuungsspektren im optischen, UV- und Röntgenbereich. Während diese spektroskopischen Methoden entweder die Valenz- oder die Kernanregungen untersuchen, deckt resonante inelastische Röntgenstreuung (RIXS) die Wechselwirkungen zwischen den beiden Anregungen auf. Wir präsentieren einen neuartigen Ausdruck für den RIXS-Wirkungsquerschnitts innerhalb unseres Vielteilchen-Formalismus, der eine detaillierte Analyse dieser Wechselwirkungen erlaubt. Mit ausgewählten Beispielen demonstrieren wir das Potential unserer Implementation, die Spektren dieser verschiedenen spektroskopischen Methoden zu berechnen, zu analysieren und zu interpretieren.

Im zweiten Teil der Dissertation verwenden wir unsere Methode, um die Anregungen der Valenzelektronen, sowie der Ga 1*s*-, Ga 2*p*- und Sauerstoff 1*s*-Elektronen in Ga_2O_3 zu berechnen. Wir finden ausgeprägte Unterschiede in den diversen Röntgenabsorptionsspektren von Ga_2O_3-Polymorphen, die von der unterschiedlichen lokalen elektronischen Struktur stammen. Wir bestimmen die Zusammensetzung der Valenz- und Kernanregungen, analysieren ihre Signatur in den verschiedenen Absorptions- und Streuungsspektren und untersuchen wie ihr Charakter mit der elektronischen Struktur zusammenhängt. Abschließend demonstrieren wir wie RIXS einen zusätzlichen Blickwinkel auf die Valenz- und Kernanregungen und deren Wechselwirkungen ermöglicht.

Summary

To develop new semiconductor devices and improve the performance of existing ones, the exploration and understanding of novel materials is required. The group of ultra-wide band-gap semiconductors are currently being investigated for application in power electronics and UV optoelectronics. With a band gap of around 4.8 eV, Ga_2O_3 is a promising candidate in this group of materials. Its applications in solar-blind UV detectors and power electronics have led to an increasing interest in its fundamental electronic and optical properties. In this thesis, we present a comprehensive first-principles study of the electronic excitations of Ga_2O_3 to contribute to the understanding of these fundamental properties. The thesis consists of two parts:

In the first part, we present an all-electron approach for consistent calculations of neutral core and valence excitations. It yields an accurate description of the electronic interactions within the framework of many-body perturbation theory (MBPT) and thus enables accurate calculation of absorption and inelastic scattering spectra in the optical, UV, and x-ray region. While these spectroscopic techniques probe either the valence or core excitations, resonant inelastic x-ray scattering (RIXS) reveals the interplay between the two. We present a novel expression for the RIXS cross section within our all-electron many-body formalism that allows for a detailed analysis of this interplay. We demonstrate the capability of our implementation to compute, analyze, and interpret the different spectroscopic techniques with selected examples of prototypical insulators.

In the second part, we apply our approach to study valence excitations, as well as excitations of various core states, *i.e.* the gallium 1s, gallium 2p, and oxygen 1s states in Ga_2O_3. Comparing the core spectra of Ga_2O_3 polymorphs, we find distinct differences that originate from their local environments. We determine the composition of valence and core excitons, and analyze their signatures in the various absorption and scattering spectra. We investigate how the character of various valence excitons depends on the electronic structure. Finally, we demonstrate how RIXS can be employed to provide a different viewpoint on the core and valence excitations and unravel the interplay between them.

Preface

Modern semiconductor technologies have transformed human society with an unprecedented speed since the invention of the transistor in 1947 [1]. The fields of electronics and optoelectronics as we know them today were initially based on Ge-, Si-, and GaAs-devices. All of these materials are characterized by their relatively small band gaps below approximately 2.3 eV [2]. As such, devices produced with these materials have severe limitations, most notably the fact that green and blue lasers could not be manufactured. Yet, the development of devices based on novel semiconducting compounds with larger band gaps has proved challenging. In the 1980s and 1990s, crucial material breakthroughs [3, 4] opened the field of wide band-gap semiconductor technologies based on GaN- and InGaN-devices and led to the first development of a blue light emitting diode (LED). For these breakthroughs, Akasaki, Amano, and Nakamura were rewarded with the Nobel prize in 2014 [5]. Since then, the development of ultra-wide band-gap semiconductors has become the new frontier, promising another substantial step in device performance and opening the path towards UV optoelectronics [2]. Several materials, such as AlN, diamond, Ga_2O_3, and cubic BN, all with band gaps beyond 3.4 eV, are actively being investigated for their potential application in a new generation of devices, with a wide range of applications [2, 6], such as UV lasers, UV photodetectors [6], and high-power electronics.

Ga_2O_3 is a promising candidate in the group of ultra-wide band-gap materials [7–9] due to its large band gap of around 4.8 eV. It has been employed in solar-blind UV detectors [10–13] both in bulk [14–16] and nanostructure [17–19] geometries. It also emerged as a favorable material in power electronics due to the large breakdown field [8, 20], beyond those of SiC and GaN. Another benefit of Ga_2O_3 is that excellent growth in large sample sizes has been achieved [2, 7, 9], an important advantage for industrial device production. These advantages have led to an increasing interest in its fundamental electronic and optical properties [7, 21]. To get insight into these from a theoretical point of view, a number of *ab initio* studies have shed light on the electronic structure [22–29], effects of doping [25, 30–32], and surface states [33, 34] and its optical properties [28, 35]. Nevertheless, essential open questions remain to be addressed from first principles. In this thesis, we focus on two groups of questions:

The first one concerns the influence of the local structure on valence and core excitations. Bulk Ga_2O_3 consists of networks of either distorted octahedra or tetrahedra, with their centers being gallium atoms and their corners being oxygen ones. Combining these distorted polyhedra in various ratios lead to different structural phases, resulting in a pro-

nounced polymorphism of this material, similar to that of other oxides such as Al_2O_3 [36, 37], In_2O_3 [38, 39], and Sb_2O_3 [40]. Due to the low symmetry of the Ga_2O_3 polymorphs, the local electronic structure in the vicinity of different oxygen atoms differs depending on the number of bonds they share with either tetrahedral or octahedral gallium atoms. Even more distinct is the local bonding environment of the gallium atoms. Previous *ab initio* studies have focussed either on the electronic structure [23, 24, 28, 41, 42], the optical excitations [28, 43, 44], or the core excitations [45] of selected polymorphs. Experimental x-ray absorption near-edge spectra (XANES) have shown pronounced signatures of the local electronic structure in the excitations of both gallium [46–51] and oxygen core states [45, 358], yet a systematic *ab initio* study of the core excitations in Ga_2O_3 polymorphs is still missing. The open questions are therefore:

What are the signatures of the local geometry in the absorption and scattering spectra? Do they allow us to distinguish the spectra of different structural phases?

The second group of questions is related to the formation of bound excitons in the core and valence excitations. Considering the large band gap, the formation of bound excitons with considerable binding energies has been postulated within the Wannier-Mott model [52]. Experimentally, such binding energies of several hundred meV have been derived from reflectance studies [53, 54]. In optical absorption measurements [43, 44], however, the pronounced peaks originating from bound excitons, which have been predicted by *ab initio* calculations [35], have not been observed. Overall, little is known about bound excitons in the optical spectra, and, for core excitations, only binding energies for the oxygen $1s$ spectra have been reported [45]. In this thesis, we aim to answer the questions:

What is the nature of the valence and core excitations in Ga_2O_3? How strongly are excitons bound in this material? How are they formed and what is their signature in excitation spectra?

First-principles theoretical spectroscopy can yield valuable insight to answer these questions. In the last decades, many-body perturbation theory (MBPT) [55–61] has become the state of-the-art approach to determine neutral excitations and has been applied to solids with considerable success to determine optical and x-ray absorption spectra. However, theoretical studies so far have focussed on a specific energy region, studying either core or valence excitations. This has hindered comprehensive studies of excitations over a large energy range. In this thesis, we present an all-electron MBPT approach that overcomes this limitations and thus enables consistent calculations of neutral electronic excitations. We show how it can be used to calculate absorption and inelastic scattering spectra, from the optical to the x-ray region. While these spectroscopic techniques probe either the valence or core excitations, the interplay of the two can be revealed by resonant inelastic x-ray scattering (RIXS). We present a novel many-body approach to determine RIXS spectra in solids, which makes use of the valence and core excitations determined within our all-electron approach.

In this thesis, we apply our first-principles framework to answer the above raised questions on the neutral electronic excitations of Ga_2O_3. To this end, we present results for the valence excitations, as well as for various core edges, *i.e.* the gallium $1s$, gallium $2p$, and oxygen $1s$. We explore the influence of the local and global structure by analyzing and contrasting the excitation spectra of polymorphs, and by identifying signatures of the local structure in the core excitation spectra. We present a comprehensive analysis of the binding and structure of excitons in the core and valence excitations and discuss the signatures of bound excitons in the various absorption and scattering spectra in detail. Moreover, we propose resonant inelastic x-ray scattering (RIXS) as a complementary tool to unravel the nature of the elementary excitations in this material. It yields not only a different viewpoint on the core and valence excitations, but furthermore gains insight into the interaction between the two.

Combining all these puzzle pieces, this thesis contributes to a deeper understanding of Ga_2O_3 and, in particular, its excitations.

Contents

Part I

Contemporary Theoretical Spectroscopy

CHAPTER 1

Electronic Structure Theory

1.1 The Many-body Problem

Theoretical spectroscopy aims at determining the interaction of a system of electrons with a probe particle, typically a photon or an electron, as a function of its energy and momentum. In any spectroscopic experiment, the probe particle transfers energy and momentum to the electronic system, driving it out of its ground state. In this way, information on the excited states of the electronic system can be inferred. Formally, the ground state and excited states of any system of N electrons and M ions are the eigenstates Ψ of the time-independent Schrödinger equation $\hat{H}\Psi = E\Psi$, where the many-body Hamiltonian is given by

$$\hat{H} = -\frac{1}{2}\sum_i^N \nabla_i^2 - \sum_i^N\sum_I^M \frac{Z_I}{|\mathbf{r}_i - \mathbf{R}_I|} + \frac{1}{2}\sum_{i\neq j}^N \frac{1}{|\mathbf{r}_i - \mathbf{r}_j|} - \sum_I^M \frac{1}{2M_I}\nabla_I^2 + \frac{1}{2}\sum_{I\neq J}^M \frac{Z_I Z_J}{|\mathbf{R}_I - \mathbf{R}_J|}. \quad (1.1)$$

Here, the sums over i and j include all electrons in the system, the sums over I and J all atomic nuclei. The many-body wavefunction $\Psi(\{\mathbf{r}\}, \{\mathbf{R}\})$ is a function of all electronic positions $\{\mathbf{r}\} = \{\mathbf{r}_1, \cdots, \mathbf{r}_i, \cdots, \mathbf{r}_j, \cdots, \mathbf{r}_N\}$, as well as all nuclear positions $\{\mathbf{R}\} = \{\mathbf{R}_1, \cdots, \mathbf{R}_I, \cdots, \mathbf{R}_J, \cdots, \mathbf{R}_M\}$. The first term of Eq. 1.1 yields the kinetic energy of the electrons, the second one the Coulomb interaction of the electrons with the ions of charge Z_I. The third term describes the Coulomb interaction between the electrons. Finally, the fourth and fifth term describe the kinetic energy of the ions with mass M_I and the Coulomb repulsion between the ions, respectively.

Although the Hamiltonian in Eq. 1.1 appears compact, a straight-forward solution is impossible for any system containing more than a few electrons. Due to the Coulomb interaction between all particles, the Hamiltonian does not factorize and leads to a coupled system of differential equations of enormous dimensionality [62, 63]. Therefore, established alternative approaches exist that yield spectroscopic properties without knowledge of the full many-body wavefunctions. The derivation of these approaches and their application to real crystalline materials requires a number of approximations, which we will motivate and discuss in the following.

The first approximation that is typically introduced in theoretical spectroscopy concerns

the dynamics of the electrons and the nuclei. Since the nuclei are at least three orders of magnitude heavier than the electrons, their dynamics is much slower. As such, the electrons follow the atomic motion almost instantaneously, while the nuclei cannot follow the electron motion and rather encounter a time-averaged electronic potential [62]. This mismatch in the dynamics can be formalized by expanding the Hamiltonian in Eq. 1.1 in terms of $\left(m_e/M_I\right)^{1/4}$ [64]. An expansion up to first order yields a Hamiltonian for the electronic system at a fixed set of nuclear positions $\{\mathbf{R}\}$. This approximation is known as the *Born-Oppenheimer approximation* [64], and results in a Schrödinger equation $\hat{H}^{\mathrm{BO}}\Psi_e = E_e\Psi_e$ for the electronic wavefunction $\Psi_e(\mathbf{r}_1, \mathbf{r}_2, ..., \mathbf{r}_N)$, where the electronic Hamiltonian is given by

$$\hat{H}^{\mathrm{BO}} = -\frac{1}{2}\sum_i^N \nabla_i^2 + \frac{1}{2}\sum_{i\neq j}^N \frac{1}{|\mathbf{r}_i - \mathbf{r}_j|} + \sum_i^N V_{e-n}(\mathbf{r}_i, \{\mathbf{R}\}) + V_{n-n}(\{\mathbf{R}\}) \tag{1.2}$$

with the electron-nucleus potential $V_{e-n}(\mathbf{r}) = \sum_I \frac{Z_I}{|\mathbf{r}_i - \mathbf{R}_I|}$ and the nucleus-nucleus potential $V_{n-n} = \frac{1}{2}\sum_{I\neq J}\frac{Z_I Z_J}{|\mathbf{R}_I - \mathbf{R}_J|}$. The Hamiltonian in Eq. 1.2 is a function of the electronic positions $\{\mathbf{r}\}$ and only depends parametrically on the nuclear configuration $\{\mathbf{R}\}$ through the electron-nucleus potential V_{e-n}. For a given nuclear configuration, the potential V_{n-n} adds only a constant to the total energy, without affecting the electronic wavefunctions. The Hamiltonian in Eq. 1.2 thus yields the wavefunctions and energies of interacting electrons in the external potential of the ions. We note that Eq. 1.2 is not the most general Hamiltonian for the electronic system in spectroscopic experiments. Generally, the Hamiltonian should include the probe particle and its interaction with the electrons as well. In Chapter 3, we will show the generalized form of the Hamiltonian (Eqs. 3.4 and 3.28) including the quantized electromagnetic field and a fast-moving probe electron, respectively. A solution of the full coupled system is not necessary within linear-response theory, and we only have to consider the excited states of the Hamiltonian in Eq. 1.2.

While the Born-Oppenheimer approximation simplifies the Hamiltonian, the electronic-structure problem, *i.e.* the solution of Eq. 1.2 for a system of N electrons, is still highly non-trivial. In the remaining chapter, we will discuss two successful approaches to obtain the electronic structure in solids: *density functional theory* (DFT) and *many-body perturbation theory* (MBPT). We will then see how spectroscopic quantities for a wide range of photon energies from the hard x-ray to the optical region, can be obtained from the solutions of the electronic structure problem.

1.2 Density Function Theory

Solving the Schrödinger equation 1.2 for a system of N interacting is a daunting task, since it requires the determination of the many-electron wavefunction $\Psi_e(\mathbf{r}_1, \mathbf{r}_2, ..., \mathbf{r}_N)$, which

depends on the $3N$ electronic coordinates. The problem thus becomes extremely complex, especially in solids, where the number of electrons is of the order of Avogadro's constant, *i.e.* N $\propto 10^{23}$. A way to reduce the complexity of the problem is offered by *density functional theory* (DFT), which allows one to reformulate the problem in terms of the ground-state density $n_0(\mathbf{r})$ instead of the wavefunction. In DFT, the special role of the ground-state density is employed: Any property of a system of interacting particles can be expressed as a unique functional of the ground-state density. Thus, the ground-state density can be employed as the basic variable of any property. In recent decades, DFT has become the workhorse in materials science, computational solid-state physics and quantum chemistry [65–68], as it allows for efficient and accurate calculations of ground-state properties, such as total energies, crystal structures, phonon dispersions, and many more [69, 70]. In this chapter, we will shortly introduce the basics of DFT as it is relevant for this work. More detailed introductions into DFT and its application can be found *e.g.* in Refs. [69, 70].

1.2.1 Hohenberg-Kohn Theorems

A mathematically rigorous foundation of DFT is provided by the two Hohenberg-Kohn theorems [71]. The first one states that for any system of interacting particles in an external potential V_{ext}, the potential is uniquely determined by the ground-state density $n_0(\mathbf{r})$ and vice-versa. This theorem guarantees that any property of the system is determined by the density alone. The second theorem states that one can define a universal functional $E[n(\mathbf{r})]$ of the electron density $n(\mathbf{r})$ for the total energy (for which the variational principle can be used), and that for any external potential, the ground-state total energy E_0 is given by $E_0 = \min_{n(\mathbf{r})} E[n(\mathbf{r})]$. The density which minimizes the total energy is the exact ground-state density $n_0(\mathbf{r})$. The most general expression for the energy functional is given by

$$E[n] = T[n] + E_{\text{inter}}[n] + \int d^3r \; V_{ext}(\mathbf{r})n(\mathbf{r}) + V_{n-n}, \qquad (1.3)$$

where $T[n]$ is the kinetic energy, $E_{\text{inter}}[n]$ is the interaction energy of the electrons, and V_{n-n} is the nuclei-nuclei interaction of Eq. 1.1. Proofs of the Hohenberg-Kohn theorems are not provided here, they can be found in numerous reviews of DFT, *e.g.* Refs. [69, 70].

1.2.2 Kohn-Sham Equations

While the Hohenberg-Kohn theorems prove that it is sufficient to determine the ground-state density to obtain all properties of the many-electron system, they do not determine any approach to determine this density. Such an approach is provided by the *Kohn-Sham ansatz* [72]. The actual interacting many-body system is replaced by an auxiliary system

of non-interacting electrons that yield the same ground-state density and thus the ground-state total energy. The energy functional E_{KS} for these fictitious non-interacting particles is given by

$$E_{KS}[n] = T_s[n] + \int d^3r V_{ext}(\mathbf{r})n(\mathbf{r}) + E_H[n] + E_{xc}[n] + V_{n-n},\tag{1.4}$$

where T_s is the kinetic energy of the non-interacting system, and E_H the Hartree energy, which describes the classical electrostatic energy term for the charge density $n(\mathbf{r})$:

$$E_H[n] = \frac{1}{2}\int\int d^3r d^3r' \frac{n(\mathbf{r})n(\mathbf{r}')}{|\mathbf{r} - \mathbf{r}'|}.\tag{1.5}$$

In Eq. 1.4, the exchange-correlation energy E_{xc} ensures that the energies in Eqs. 1.4 and 1.3 are identical. It can thus be expressed as

$$E_{xc}[n] = \big(T[n] - T_s[n]\big) + \big(E_{\text{inter}}[n] - E_H[n]\big),\tag{1.6}$$

which shows that the exchange-correlation energy is given by two contributions, the difference of the kinetic energy between the interacting and non-interacting system on the one hand, and the electron-electron interactions beyond the Hartree energy on the other hand. A set of N non-interacting electronic orbitals ψ_i^{KS} can now be defined as the solutions of the Kohn-Sham Hamiltonian $\hat{H}^{KS}$

$$\hat{H}^{KS}\psi_i^{KS} = \epsilon_i^{KS}\psi_i^{KS},\tag{1.7}$$

such that the ground-state density $n_0(\mathbf{r})$ of the interacting electrons is obtained as

$$n_0(\mathbf{r}) = \sum_i^N |\psi_i^{KS}(\mathbf{r})|^2.\tag{1.8}$$

The Kohn-Sham Hamiltonian $\hat{H}^{KS}$ is obtained from Eq. 1.4 by minimizing the functional under the constraint that the particle number is constant. We obtain it as

$$\hat{H}^{KS} = -\frac{1}{2}\nabla^2 + v_{ext}(\mathbf{r}) + v_H(\mathbf{r}) + v_{xc}(\mathbf{r}),\tag{1.9}$$

where the Hartree potential $v_H(\mathbf{r})$ is given by

$$v_H(\mathbf{r}) = \frac{\delta E_H}{\delta n(\mathbf{r})} = \int d^3r' \frac{n(\mathbf{r}')}{|\mathbf{r} - \mathbf{r}'|},\tag{1.10}$$

and the exchange-correlation potential $v_{xc}(\mathbf{r})$ by

$$v_{xc}(\mathbf{r}) = \frac{\delta E_{xc}}{\delta n(\mathbf{r})}. \tag{1.11}$$

In the Kohn-Sham approach, a set of fictitious non-interacting orbitals $\{\psi_i^{KS}\}$ is determined to yield the exact ground-state density of the interacting system. The complexity of the many-body problem is contained in the exchange-correlation functional in Eq. 1.6. While the expression may appear simple, neither the difference in kinetic energy nor the interaction beyond the Hartree energy are known. Nevertheless, successful approximations to this universal functional have been developed in the last decades.

A simple approximation for the exchange-correlation functional $E_{xc}[n(\mathbf{r})]$ was already suggested in the seminal work of Hohenberg and Kohn [71]. Here, the exchange-correlation energy per particle is given, for each point $\mathbf{r}$ in space, by the corresponding exchange-correlation energy per particle $e_{xc}(n(\mathbf{r}))$ of the homogeneous electron gas (HEG), *i.e.*

$$E_{xc}^{LDA}[n(\mathbf{r})] = \int d^3 r n(\mathbf{r}) e_{xc}^{HEG}(n(\mathbf{r})). \tag{1.12}$$

This approximation is known as the *local density approximation* (LDA), since the exchange-correlation energy only depends locally on the electronic density. Several analytical parameterizations of $e_{xc}^{HEG}(n)$ are obtained from Monte Carlo calculations of the homogeneous electron gas, combined with exact limits and scaling laws of e_{xc} [73–75]. Even though the LDA appears as a crude approximation, as it neglects any non-local dependence of the functional on the density, it has been applied to a wide range of materials with remarkable success.

The exchange-correlation functional can be improved beyond the LDA, if effects of the non-homogeneous electronic density are included in the exchange-correlation functional. This is done in the *generalized gradient approximation* (GGA), where the exchange-correlation functional E_{xc}^{GGA} is expressed as

$$E_{xc}^{GGA}[n(\mathbf{r})] = \int d^3 r f(n(\mathbf{r}), \nabla n(\mathbf{r})), \tag{1.13}$$

where $f(\cdot)$ is a local function of the density and the density gradient. Therefore GGA functionals are denoted as *semilocal functionals*. Numerous expressions for GGA functionals have been developed, the most popular choices for crystalline materials are the Perdew-Burke-Ernzerhof (PBE) functional [76] and the optimized PBE functional for solids (PBEsol) [77]. While these GGA functionals yield quantitatively improved results for a number of properties compared to LDA, formal deficiencies of both LDA and GGA functionals can lead to quantitatively and qualitatively incorrect results for specific observ-

ables [78], most notably the band gap [79, 80]. These shortcomings occur since any semilocal functional disobeys two important restraints, the derivative discontinuity [81–85] and the cancellation of the self-interaction [78, 86].

By reducing the self-interaction [86, 87], *hybrid functionals* yield improved results for the electronic and structural properties [78, 88, 89], especially the band gap [90–92]. These approximations to the exchange-correlation functional combine semilocal approximations with the Hartree-Fock exchange energy E_x^{HF}. Formally, they are derived either from the adiabatic connection [93, 94] between the non-interacting and the fully interacting system, or from generalized Kohn-Sham theory [95, 96], where the system of non-interacting electrons is described by a single Slater determinant. The hybrid functional PBE0 [93, 94], for example, approximates the exchange-correlation energy as

$$E_{xc}^{PBE0} = E_{xc}^{PBE} + \frac{1}{4}\left(E_x^{HF} - E_x^{PBE} \right).$$ (1.14)

The mixing parameter of $\frac{1}{4}$ is fixed *a priori* [93]. Many other hybrid functionals exist, with various combinations of GGA functionals and different mixing parameters. Splitting the exchange-correlation functional into long- and short-range interactions and employing different levels of approximations for the different ranges, yields further improvement of the hybrid functionals. These functionals are known as *range-separated hybrid functionals* [97, 98].

1.2.3 Time-dependent Density Functional Theory

While the Kohn-Sham approach formally yields the exact ground-state energy and ground-state density, theoretical spectroscopy aims at determining the electronic system under a time-dependent external potential. DFT provides access to spectroscopic observables via its time-dependent extension, *time-dependent density functional theory* (TDDFT) [99]. Analogously to the Hohenberg-Kohn theorem, the Runge-Gross theorem [100] ensures the one-to-one correspondence between a given time-dependent external potential, $v_{ext}(\mathbf{r}, t)$, and the time-dependent density, $n(\mathbf{r}, t)$, for any many-body system which evolves from a given initial state. In close correspondence to the Kohn-Sham scheme, a set of non-interacting electrons can be constructed that yield the correct time-dependent density of the system. The electronic wavefunctions $\psi_i^{KS}(\mathbf{r}, t)$ obey

$$\mathrm{i}\frac{\partial}{\partial t}\psi_i^{KS}(\mathbf{r}, t) = \hat{H}^{KS}\psi_i^{KS}(\mathbf{r}, t) = \left[-\frac{\nabla^2}{2} + v_{KS}[n](\mathbf{r}, t) \right] \psi_i^{KS}(\mathbf{r}, t).$$ (1.15)

The effective potential v_{KS} includes, as in the Kohn-Sham scheme, the exchange-correlation potential, for which approximations have to be found. More information are provided in

several reviews of TDDFT [101–103].

The description of spectroscopic techniques, such as optical absorption, has originally been approached from TDDFT, employing widely used approximations such as the adiabatic local density approximation (ALDA) [104, 105], with unsatisfactory results, in particular for insulating solids [106, 107]. To overcome the problem, several approximations beyond ALDA have been proposed [108–113], with important improvements over ALDA. An important class of functionals, particularly successful for the description of absorption in solids, was derived from the Bethe-Salpeter equation (BSE) (see Section 1.3.3) [114–119], but at a comparable computational cost. While long-range corrected approximations to the exchange-correlation functional [101, 120, 121] work well for continuum excitons and require modest computational efforts, they fail in reproducing strongly bound excitons. Range separated hybrid functionals [112, 122–124] behave similarly to the long-range corrected ones, yet with additional computational effort and reliance on adjustable parameters. A comparative review of TDDFT and many-body perturbation theory can be found in Ref. [103].

1.3 Many-body Perturbation Theory

In the previous sections, we have shown how the complexity of the many-body problem can be reduced by expressing the energy as a functional of the electronic density $n(\mathbf{r})$ instead of as an eigenvalue of the many-body Hamiltonian. This reformulation is powerful as it allows us to calculate properties of the electronic structure from the density, an object with much reduced dimensionality compared to the many-body wavefunction. On the other hand, we have also seen the limitations of this approach when it comes to the calculation of spectroscopic observables, limiting the applicability of DFT in theoretical spectroscopy considerably. In this chapter, we therefore consider the Green's function theory, an approach that employs the one-particle Green's function $G(\mathbf{r}_1, t_1, \mathbf{r}_2, t_2)$, and the corresponding two-particle one, $G_2(\mathbf{r}_1, t_1, \mathbf{r}_2, t_2; \mathbf{r}_1', t_1', \mathbf{r}_2', t_2')$, as fundamental ingredients. We will show how these Green's functions yield spectroscopic observables. Our derivation follows that in Refs. [63] and [57].

1.3.1 One- and Two-particle Green's Function

The time-ordered one-particle Green's function $G(\mathbf{r}_1, t_1, \mathbf{r}_2, t_2) = G(1, 2)$ is defined as

$$G(1, 2) = (-\mathrm{i})\langle 0|\hat{T}[\hat{\psi}(1)\hat{\psi}^\dagger(2)]|0\rangle, \tag{1.16}$$

where $\hat{\psi}(1)$ is the field operator and $\hat{T}$ the fermionic time-ordering operator. Here, we have introduced a shorthand notation that contracts space- and time-variables as $(\mathbf{r}_1, t_1) = (1)$. The expectation value in the definition is taken with respect to the many-body groundstate $|0\rangle$. The one-particle Green's function $G(1, 2)$ describes the propagation of an electron or hole (depending on the sign of the time difference $t_1 - t_2$) from $1 = (\mathbf{r}_1, t_1)$ to $2 = (\mathbf{r}_2, t_2)$.[1] The corresponding time-ordered two-particle Green's function $G_2(1, 2; 1', 2')$ is defined as

$$G_2(1, 2; 1', 2') = (-\mathrm{i})^2 \langle 0|\hat{T}[\hat{\psi}(1)\hat{\psi}(2)\hat{\psi}^\dagger(2')\hat{\psi}^\dagger(1')]|0\rangle, \tag{1.17}$$

and describes the correlated propagation of two particles. Generally, the n-particle Green's function G_n is defined as

$$G_n(1, \ldots, n; 1', \ldots, n') = (-\mathrm{i})^n \langle 0|\hat{T}\left[\hat{\psi}(1)\ldots\hat{\psi}(n)\hat{\psi}^\dagger(1')\ldots\hat{\psi}^\dagger(n')\right]|0\rangle \tag{1.18}$$

The equation of motion for these Green's functions is derived from the equation of motion for the field operators in the Heisenberg picture [125, 126]. For the one-particle Green's function, the equation of motion is given by [2]

$$\left[\mathrm{i}\frac{\partial}{\partial t_1} - \hat{h}(\mathbf{r}_1)\right] G(1, 1') + \mathrm{i} \int d^3r_2 \, v_C(\mathbf{r}_1, \mathbf{r}_2)G_2(1, 2; 1', 2^+)\Bigg|_{t_2=t_1^+} = \delta(1, 1'), \tag{1.19}$$

where we define the single-particle Hamiltonian as $\hat{h}(\mathbf{r}) = \frac{1}{2}\nabla^2 + V_{e-n}(\mathbf{r})$, and v_C is the Coulomb potential. The corresponding equation of motion for G_2 is given by [126]

$$\left[\mathrm{i}\frac{\partial}{\partial t_1} - \hat{h}(\mathbf{r}_1)\right] G_2(1, 2; 1', 2') + \mathrm{i} \int d^3r_3 \, v_C(\mathbf{r}_1, \mathbf{r}_3)G_3(1, 2, 3; 1', 2', 3)\Bigg|_{t_3=t_1^+}$$
$$= \delta(1, 1') - \delta(1, 2')G(2, 1'). \tag{1.20}$$

It can be seen in Eqs. 1.19 and 1.20 that the determination of the Green's functions G and G_2 require knowledge of higher order Green's functions, G_2 and G_3, respectively, due to the two-body nature of the Coulomb interaction. Generally, the determination of the n-particle Green's function G_n requires knowledge of both G_{n-1} and G_{n+1}. The set of equations connecting the Green's functions is called the *Martin-Schwinger hierarchy* [63, 125, 126]. It is apparent that, at this point, the determination of the one-particle Green's function is as complex as the solution of the many-body Hamiltonian in Eq. 1.2 as it requires knowledge of all higher-order Green's functions.

The correlation between the propagation of the two particles in the Green's function G_2 of

---

[1]In addition to this, a simplification consists in neglecting the spin degree of freedom.

[2]In the treatment of time-ordered quantities, it is often necessary to introduce positive infinitesimal time differences δt, and we define $t^+ = t + \delta t$.

Eq. 1.19 can be made explicit by introducing the two-particle correlation function L as

$$L(1, 2; 1', 2') = -G_2(1, 2; 1', 2') + G(1, 1')G(2, 2'), \qquad (1.21)$$

such that the independent propagation of the electron hole, given by $G(1, 1')G(2, 2')$ is removed from the two-particle Green's function. Inserting Eq. 1.21 into Eq. 1.19 yields

$$G(1, 1') = G_0(1, 1') + G_0(1, \bar{2})v_H(\bar{2})G(\bar{2}, 1') + iG_0(1, \bar{2})v_C(\bar{2}, \bar{3})L(\bar{2}, \bar{3}^+; 1', \bar{3}^{++}). \qquad (1.22)$$

Here, we have introduced the Green's function G_0 for a system of independent electrons in an external potential. G_0 is determined by the equation of motion

$$\left[i\frac{\partial}{\partial t_1} - \hat{h}(\mathbf{r}_1) \right] G_0(1, 1') = \delta(1, 1'), \qquad (1.23)$$

which is obtained from Eq. 1.19 when the Coulomb is removed.

1.3.2 Dyson Equation

While the one-particle Green's function is fully determined by the equation of motion 1.19, we have seen that the calculation of the Green's function requires knowledge of the two-particle Green's function. Thus, in principle, the Green's functions G_n to all orders have to be determined, and the task of calculating G_1 has the same complexity as the task to solve the many-body Schrödinger equation in Eq. 1.2. A way to eliminate the undesired dependence of higher-order Green's function is to express L in Eq. 1.21 as the variation of the one-particle Green's function with respect to a fictitious perturbation $u(1, 2)$, which vanishes at the end of the calculation [62, 63]:

$$L(1, 2, 1', 2') = \left[\frac{\delta G(1, 1')[u]}{\delta u(2', 2)} \right]_{u=0}. \qquad (1.24)$$

In general, Eq. 1.24 does not require the potential u to vanish. Calculations with a non-vanishing external potential yield the non-equilibrium dynamics of a system in an external potential. We will not consider this case here, and refer the interested reader to Ref. [63]. To determine the one-particle Green's function, only knowledge of selected components of L, namely $L(2, 3, 1', 3^+)$, is required. In this case, the fictitious potential is local, *i.e.* $u(3, 3^+) \equiv u(3)$, while for the calculation of the full correlation function L, a non-local fictitious potential $u(1, 2)$ has to be employed. Using Eq. 1.24 above, we can now express

Eq. 1.22 for the Green's function G_u in the presence of the fictitious potential as

$$G_u(1,1') = G^0(1,1') + G^0(1,\bar{2})] \times \left[[u(\bar{2},\bar{2}^+) + v_H(\bar{2})]G_u(\bar{2},1') + iv_C(\bar{2},\bar{3})\frac{\delta G_u(\bar{2},1')}{\delta u(\bar{3}^+,\bar{3}^{++})} \right].$$

(1.25)

The inverse Green's function G_u^{-1} is then given by

$$
\begin{aligned}
G_u^{-1}(1,1') =& G_0^{-1}(1,1') - \left[u(1^+,1) + v_H(1)\right]\delta(1,1') - iv_C(1,\bar{3})\frac{\delta G_u^{-1}(1,\bar{2})}{\delta u(\bar{3}^{++},\bar{3}^+)}G_u^{-1}(\bar{2},1') \\
=& G_0^{-1}(1,1') - \left[u(1) + v_H(1)\right]\delta(1,1') - \Sigma_{xc}(1,1') \\
=& G_0^{-1}(1,1') - \Sigma_u(1,1'),
\end{aligned}
$$

(1.26)

where we have introduced the self-energy $\Sigma_u = u + v_H + \Sigma_{xc}$ with the so-called exchange-correlation self-energy Σ_{xc} defined as

$$\Sigma_{xc} = iv_C(1,\bar{3})\frac{\delta G_u^{-1}(1,\bar{2})}{\delta u(\bar{3}^{++},\bar{3}^+)}G_u^{-1}(\bar{2},1').$$

(1.27)

G_u^{-1} in Eq. 1.26 describes the propagation of the particle that deviates from the free propagation, given by G_0^{-1}, due to the influence of the many-body surrounding. The deviation from the free propagation originates from the external fictitious potential u, the Hartree potential v_H, and an additional term Σ_{xc}, which includes both the effects of exchange and correlation beyond the interaction of electrons due to the Hartree potential. Equation 1.25 is well-behaved for the limit $u \to 0$, and we arrive at the *Dyson Equation* [127] for the one-particle Green's function:

$$G(1,1') = G^0(1,1') + G^0(1,\bar{2})\Sigma(\bar{2},\bar{2}')G(\bar{2}',1'),$$

(1.28)

with the self-energy $\Sigma(1,2) = v_H(1)\delta(1,2) + \Sigma_{xc}(1,2)$.

At this point, we have found a closed equation to determine the one-particle Green's function (Eq. 1.28) without requiring explicit information on higher-order Green's functions. The complexity of the problem has been transferred to the problem of finding the self-energy Σ (Eq. 1.27). A main benefit of this reformulation is that even low-order approximations to the self-energy yields contributions to all orders in the Green's function. These contributions are conveniently contained in an infinite sum in the Dyson equation. In the following, we will show how to apply a similar treatment to the two-particle Green's function G_2. We will then present how these Dyson equations can be combined in a closed set of integro-differential equations, known as Hedin's equations.

1.3.3 The Bethe-Salpeter Equation

As for the one-particle Green's function G in the previous section, the two-particle correlation function is also determined by a Dyson equation. Inserting the identity $G(1,1') = G(1,\bar{3})G^{-1}(\bar{3},\bar{3}')G(\bar{3}',1')$ in Eq. 1.22 and using the product rule, we obtain

$$L(1,2,1',2') = G(1,\bar{3})\frac{\delta G^{-1}(\bar{3},\bar{3}')}{\delta u(2,2')}G(\bar{3},1') + 2L(1,2,1',2')$$

$$\Rightarrow L(1,2,1',2') = -G(1,\bar{3})\frac{\delta G^{-1}(\bar{3},\bar{3}')}{\delta u(2,2')}G(\bar{3},1'). \tag{1.29}$$

The functional derivative $\delta G^{-1}/\delta u$ can be evaluated using Eq. 1.26, which yields

$$L(1,2,1',2') = G(1,2')G(2,1') + G(1,\bar{3})\frac{\delta\Sigma(\bar{3},\bar{3}')}{\delta u(2',2)}G(\bar{3}',1'). \tag{1.30}$$

Since the self-energy is a functional of the Green's function, we can employ the chain rule and obtain

$$\frac{\delta\Sigma(\bar{3},\bar{3}')}{\delta u(\bar{2},\bar{2}')} = \frac{\delta\Sigma(\bar{3},\bar{3}')}{\delta G(\bar{5},\bar{5}')}\frac{\delta G(\bar{5},\bar{5}')}{\delta u(\bar{2},\bar{2}')} = \frac{\delta\Sigma(\bar{3},\bar{3}')}{\delta G(\bar{5},\bar{5}')}L(\bar{5},2,\bar{5}',2'), \tag{1.31}$$

where in the last step, the definition of L in Eq. 1.21 is used. We now express the Hartree potential v_H of Eq. 1.10 in terms of the Green's function by using $n(1) = -iG(1,1^+)$, such that $v_H(\bar{3}) = -iG(\bar{5},\bar{5}^+)v(\bar{5},\bar{3})$. Combining the expression for the Hartree potential with the self-energy in Eq. 1.26, we define the *interaction kernel* Ξ as

$$\Xi(\bar{3},\bar{4},\bar{3}',\bar{4}') \equiv \frac{\delta\Sigma(\bar{3},\bar{3}')}{\delta G(\bar{4}',\bar{4})} = -i\delta(\bar{3},\bar{3}')\delta(\bar{4}'^+,\bar{4})v_C(\bar{4},\bar{3}^+) + \frac{\delta\Sigma_{xc}(\bar{3},\bar{3}')}{\delta G(\bar{4}',\bar{4})}. \tag{1.32}$$

Finally, inserting the definition of the interaction kernel of Eq. 1.32 into Eq. 1.30 yields the Dyson equation for the two-particle correlation function, known as the *Bethe-Salpeter equation* [128, 129] as

$$L(1,2,1',2') = L_0(1,2,1',2') + L_0(1,\bar{3}',1',\bar{3})\Xi(\bar{3},\bar{4},\bar{3}',\bar{4}')L(\bar{4}',2,\bar{4},2'), \tag{1.33}$$

where we define

$$L_0(1,2,1',2') = G(1,2')G(2,1'). \tag{1.34}$$

1.3.4 Hedin's Equation

The Dyson equations 1.28 and 1.33 for the one- and two-particle Green's functions can be combined to obtain a closed set of integro-differential equations. In the previous sec-

tions, the Green's functions were expressed using the fictitious non-local potential $u(1) = u(1, 1^+)$. As we anticipate the effects of the electronic screening to be strong, we now want to find expression in terms of a potential that already contains some contributions from the screening. Consequently, we will find expressions in terms of the *total classical potential* [63] $v_{cl}(1) = u(1)+v_H(1)$, where we add the Hartree potential $v_H(1) = v_C(1, \bar{2})n(\bar{2})$. The total classical potential thus includes the classical electrostatic screening. We first employ the chain rule to re-write the exchange-correlation self energy as

$$
\begin{aligned}
\Sigma_{xc}(1, 2) &= -iv_C(1^+, \bar{3}')G(1, \bar{2})\frac{\delta G^{-1}(\bar{2}, 1')}{\delta u(\bar{3})} \\
&= -iv_C(1^+, \bar{3}')G(1, \bar{2})\frac{\delta G^{-1}(\bar{2}, 1')}{\delta v_{cl}(\bar{4})}\frac{\delta v_{cl}(\bar{4})}{\delta u(\bar{3})}.
\end{aligned}
\tag{1.35}
$$

The variation of the classical potential with respect to the external potential is given by the inverse dielectric function $\varepsilon^{-1}(1, 2) = \frac{\delta v_{cl}(1)}{\delta u(2)}$. We furthermore define the *screened Coulomb interaction* W as

$$
W(1, 2) = \varepsilon^{-1}(1, \bar{3})v_C(\bar{3}, 2).
\tag{1.36}
$$

Lastly, we define the *vertex function* as

$$
\Gamma(1, 2; 3) = -\frac{\delta G^{-1}(1, 2)}{\delta v_{cl}(3)}.
\tag{1.37}
$$

These definitions yield the exchange-correlation self energy as

$$
\Sigma_{xc}(1, 2) = iG(1, \bar{2})W(\bar{4}, 1^+)\Gamma(\bar{2}, 1'; \bar{4}).
\tag{1.38}
$$

Equation 1.26 is used to determine the vertex function, starting from Eq. 1.37:

$$
\Gamma(1, 2; 3) = \delta(3, 2)\delta(1, 3) + G(\bar{4}, \bar{6})G(\bar{7}, \bar{5})\frac{\delta\Sigma(1, 2)}{\delta G(\bar{4}, \bar{5})}\Gamma(\bar{6}, \bar{7}; \bar{3}).
\tag{1.39}
$$

So far, the vertex function Γ, the self-energy Σ, and the Green's function G are connected by Eqs. 1.38, 1.28, and 1.39. In order to close the equations, an expression for the screened Coulomb potential W is needed. To find this expression, we introduce the retarded reducible polarizability χ and its irreducible counterpart $\tilde{\chi}$.[3] These are defined as

$$
\chi(1, 2) = \frac{\delta n(1)}{\delta u(2)}
\tag{1.40}
$$

---

[3]We have defined here the *time-ordered polarizability*, as we are working in the framework of time-ordered Green's functions. More details on the time-ordered polarizability and the *retarded polarizability* are provided in Section 2.2.1 and Appendix B

and

$$\tilde{\chi}(1,2) = \frac{\delta n(1)}{\delta v_{cl}(2)}. \tag{1.41}$$

As such, the reducible correlation function χ describes the variation of the density with respect to the external potential u, while the irreducible correlation function $\tilde{\chi}$ yields the variation with respect to the total classical one, v_{cl}. The inverse dielectric function $\varepsilon^{-1}(1,2)$ is then given as

$$\varepsilon^{-1}(1,2) = \frac{\delta v_{cl}(1)}{\delta u(2)} = \frac{u(1) + v_H(1)}{\delta u(2)} = \delta(1,2) + v_C(1,\bar{3})\chi(\bar{3},2), \tag{1.42}$$

where we use the explicit form $v_H(1) = v_C(1,\bar{3})n(\bar{3})$ of the Hartree potential. Equivalently, the dielectric function $\varepsilon(1,2)$ is obtained as

$$\varepsilon(1,2) = \frac{\delta u(1)}{\delta v_{cl}(2)} = \frac{v_{cl}(1) - v_H(1)}{\delta v_{cl}(2)} = \delta(1,2) - v_C(1,\bar{3})\tilde{\chi}(\bar{3},2), \tag{1.43}$$

where we use that the total classical potential is given by $v_{cl} = u + v_H$. The reducible and irreducible correlation functions are connected by a Dyson equation as

$$\chi(1,2) = \frac{\delta n(1)}{\delta u(2)} = \frac{\delta n(1)}{\delta v_{cl}(\bar{3})}\frac{\delta v_{cl}(\bar{3})}{\delta u(2)} = \chi(1,\bar{3})\varepsilon^{-1}(\bar{3},2)$$
$$= \tilde{\chi}(1,2) + \tilde{\chi}(1,\bar{3})v_C(\bar{3},\bar{4})\chi(\bar{4},2). \tag{1.44}$$

Equations 1.43, 1.42, and 1.40 yield a Dyson equation for the screened Coulomb potential as

$$W(1,2) = \varepsilon^{-1}(1,\bar{3})v_C(\bar{3},2) = \left[\delta(1,\bar{3}) + v_C(1,\bar{5})\chi(\bar{5},\bar{3})\right]v_C(\bar{3},2)$$
$$= v_C(1,2) + v_C(1,\bar{5})\left[\tilde{\chi}(\bar{5},\bar{3}) + \tilde{\chi}(\bar{5},\bar{6})v_C(\bar{6},\bar{6}')\chi(\bar{6}',\bar{3})\right]v_C(\bar{3},2)$$
$$= v_C(1,2) + v_C(1,\bar{5})\tilde{\chi}(\bar{5},\bar{6})\varepsilon^{-1}(\bar{6},\bar{3})v_C(\bar{3},2)$$
$$= v_C(1,2) + v_C(1,\bar{5})\tilde{\chi}(\bar{5},\bar{6})W(\bar{6},2). \tag{1.45}$$

Finally, the irreducible polarizability $\tilde{\chi}$ is expressed in terms of the Green's function and the vertex function using $n(1) = -iG(1,1^+)$:

$$\tilde{\chi}(1,2) = \frac{\delta n(1)}{\delta v_{cl}(2)} = -i\frac{\delta G(1,1^+)}{\delta v_{cl}(2)} = iG(1,\bar{3})G(\bar{4},1)\Gamma(\bar{3},\bar{4};2). \tag{1.46}$$

Equations 1.28, 1.35, 1.46, 1.39, and 1.45 form a closed set of equation, commonly referred
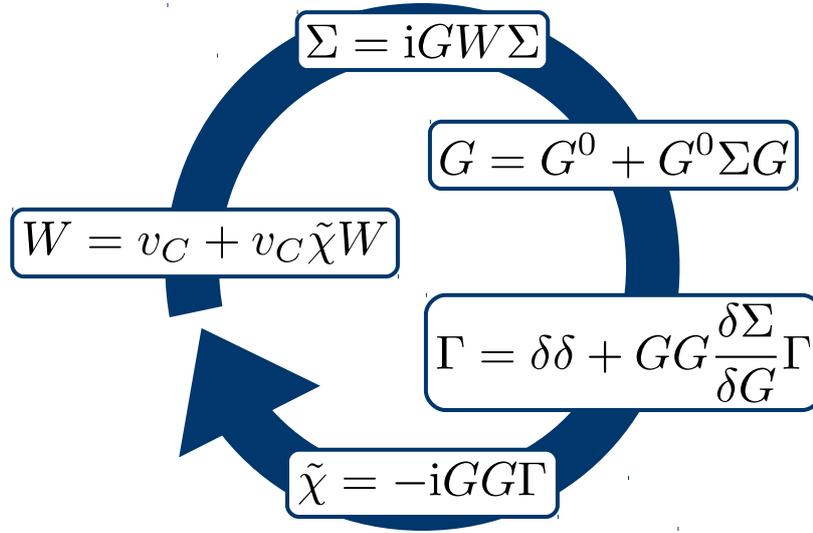
Figure 1.1: Schematical representation of the Hedin's equations 1.47-1.49. The arrows indicate in which order one quantity can be obtained from the previous one. The quantities are arranged on a circle to indicate that a full solution has to be obtained self-consistently.

to as *Hedin's equations* [130]:

Hedin's equations

$$\Sigma_{xc}(1, 2) = iG(1, \bar{2})W(\bar{4}, 1^+)\Sigma(\bar{2}, 1'; \bar{4}) \tag{1.47}$$

$$G(1, 1') = G^0(1, 1') + G^0(1, \bar{2})\Sigma(\bar{2}, \bar{2}')G(\bar{2}', 1') \tag{1.48}$$

$$\Gamma(1, 2; 3) = \delta(3, 2)\delta(1, 3)$$
$$+ G(\bar{4}, \bar{6})G(\bar{7}, \bar{5})\frac{\delta\Sigma_{xc}(1, 2)}{\delta G(\bar{4}, \bar{5})}\Gamma(\bar{6}, \bar{7}; 3) \tag{1.49}$$

$$\tilde{\chi}(1, 2) = -iG(1, \bar{3})G(\bar{4}, 1)\Gamma(\bar{3}, \bar{4}; 2) \tag{1.50}$$

$$W(1, 2) = v_C(1, 2) + v_C(1, \bar{5})\tilde{\chi}(\bar{5}, \bar{6})W(\bar{6}, 2) \tag{1.51}$$

1.3.5 The GW Approximation

While Hedin's equations are formally exact, finding a full solution is a challenging task even for model systems. Therefore, a vast variety of iterative approaches are employed, starting with $\Sigma_{xc} = 0$ or $\Gamma = \delta$, with different initial guesses for G_0, such as Kohn-Sham or Hartree-Fock Green's functions, and with different levels of self-consistency. In the following, we only introduce the approximations that we will employ to determine spectroscopic

observables. More detailed reviews can be found in Refs. [63, 131]. A common approximation is obtained by neglecting vertex corrections, *i.e.* setting $\Gamma(1, 2; 3) = \delta(1, 2)\delta(1, 3)$. Inserting this approximation into Eq. 1.50 for the irreducible polarizability, one obtains the *random-phase approximation* [132–134] (RPA) as

$$\tilde{\chi}(1, 2) \approx \tilde{\chi}_0(1, 2) \equiv -iG(1, 2)G(2, 1). \tag{1.52}$$

In this approximation, the polarizability is due to the formation of a non-interacting electron-hole pair, which can be seen in the opposite time-ordering of the Green's functions in Eq. 1.52. The vertex correction, which are neglected in RPA, introduce the effect of electron-hole correlation in the polarizability. The RPA polarizability can be employed to calculate the screened Coulomb potential as

$$W(1, 2) = \varepsilon_{RPA}^{-1}(1, \bar{5})v_C(\bar{5}, 3) = \left[1 - v_C\tilde{\chi}_0\right]^{-1}(1, \bar{5})v_C(\bar{5}, 3). \tag{1.53}$$

Successively, the approximation to both the vertex and the screened Coulomb potential yield the exchange-correlation self energy as

$$\Sigma_{xc}^{GW}(1, 2) \approx iG(1, 2)W(2, 1^+). \tag{1.54}$$

Due to schematic expression for the self-energy as $\Sigma_{xc} = iGW$, this approximation is known as the GW approximation (GW) . In this approximation, the self energy is given by the interaction of the particle with the screened potential W. The screening of the Coulomb potential, in turn, is determined by the polarizability of the system. Finally, the interaction kernel in Eq. 1.32 is expressed in the GWA as

$$\Xi(1, 2, 1', 2') \approx -i\delta(1, 1')\delta(2, 2'^+)v_C(2, 1^+) + i\delta(1, 2')\delta(2', 1)W(1', 1^+) + iG(1, 1')\frac{\delta W(1', 1^+)}{\delta G(2', 2)}. \tag{1.55}$$

The interaction kernel describes the interaction of electrons and holes, and the terms in Eq. 1.55 allow for a physical interpretation of their interaction: The first term introduces the exchange interaction of two fermionic particles, while the second term introduces the attractive Coulomb interaction of these oppositely charged particles. The interaction is given by the screened Coulomb potential W due to the presence of all the other electrons in the system. Finally, the last term describes how the screened Coulomb interaction changes due to the propagation of these particles, and it thus describes the feedback of the propagating particles on the many-electron system.

1.3.6 Quasiparticle Approximation

The approach presented in the previous section allows for the determination of the one- and two-particle Green's functions, including a full treatment of many-body effects. In many systems, however, it has been observed that the structure of the charged excitations around the band gap, *i.e.* the energy addition and removal energies, resemble [4] those of a system of non-interacting particles, even though the Coulomb interaction between the electrons is comparable to the kinetic energies of the electrons. The concept was first introduced by Landau to analyze the excitation in liquid He^{II} [135]. The elementary excitations of these systems behave as *quasiparticles*: The propagation of an electron or hole induces a perturbation in the charge density. Thus, a charge cloud forms around the particle, and what is observed is not the propagation of the bare electrons or holes, but rather the dressed quasiparticles. The interaction of these quasiparticles is screened by the charge cloud, therefore they often behave as weakly interacting particles, even in systems where the propagation of the bare electrons is strongly correlated. More rigorously, it can be shown that the Dyson equation 1.48 can be approximately solved within the *quasiparticle approximation* as

$$G(\mathbf{r}_1, \mathbf{r}_2; \omega) = \sum_{v\mathbf{k}} \frac{\psi_{v\mathbf{k}}^{QP}(\mathbf{r}_1) \left[\psi_{v\mathbf{k}}^{QP}(\mathbf{r}_2)\right]^*}{\omega - \epsilon_{v\mathbf{k}}^{QP} - i\eta} + \sum_{c\mathbf{k}} \frac{\psi_{c\mathbf{k}}^{QP}(\mathbf{r}_1) \left[\psi_{c\mathbf{k}}^{QP}(\mathbf{r}_2)\right]^*}{\omega - \epsilon_{c\mathbf{k}}^{QP} + i\eta}, \qquad (1.56)$$

where $\psi_{i\mathbf{k}}^{QP}$ and $\epsilon_{i\mathbf{k}}^{QP}$ are the quasiparticle wavefunctions and energies, respectively. These quasiparticles are obtained from the quasiparticle Schrödinger equation

$$\hat{h}_0 \psi_{i\mathbf{k}}^{QP}(\mathbf{r}) + \int d^3r' \Sigma(\mathbf{r}, \mathbf{r}', \epsilon_{i\mathbf{k}}^{QP}) \psi_{i\mathbf{k}}^{QP}(\mathbf{r}') = \epsilon_{i\mathbf{k}}^{QP} \psi_{i\mathbf{k}}^{QP}(\mathbf{r}). \qquad (1.57)$$

We then describe the N-particle many-body groundstate $|0\rangle$ as a single Slater determinant of the quasiparticles. The $(N + 1)$- and $(N - 1)$-particle excited states are then given as independent-particle excitations and de-excitations of the groundstate, *i.e.* $\sum_n |N + 1, n\rangle \approx \sum_{c\mathbf{k}} \hat{c}_{c\mathbf{k}}^\dagger |0\rangle$ and $\sum_n |N-1, n\rangle \approx \sum_{v\mathbf{k}} \hat{c}_{v\mathbf{k}} |0\rangle$, where $\hat{c}$ and $\hat{c}^\dagger$ are the quasiparticle annihilation and creation operators, respectively. In the following, the quasiparticle approximation will mostly be employed in the form

$$\sum_{i\mathbf{k}} \sum_{j\mathbf{k}'} \hat{c}_{i\mathbf{k}}^\dagger \hat{c}_{j\mathbf{k}} |0\rangle \approx \sum_{i\mathbf{k}} \sum_{j\mathbf{k}'} \Theta(\epsilon_{i\mathbf{k}}^{QP} > \epsilon_F) \Theta(\epsilon_{j\mathbf{k}'}^{QP} \langle \epsilon_F) \hat{c}_{i\mathbf{k}}^\dagger \hat{c}_{j\mathbf{k}} |0\rangle = \sum_{c\mathbf{k}} \sum_{v\mathbf{k}'} \hat{c}_{c\mathbf{k}}^\dagger \hat{c}_{v\mathbf{k}'} |0\rangle, \qquad (1.58)$$

such that we treat the groundstate as the Slater determinant of a system of quasiparticles, where excitations require that a hole is created in a valence state $(v\mathbf{k}')$ and an electron in a conduction state $(c\mathbf{k})$. While this statement may sound trivial, it can only be formulated

---

[4]More accurately, the shape of the *spectral function* $A(\omega) = \frac{1}{\pi}|\text{Im } G(\omega)|$ is similar to the independent-particle one. For a more in-depth discussion, see Ref. [63]

in the quasiparticle approximation, where the strong many-body interactions are already included in the formation of the quasiparticle, such that the resulting particles can be approximated as non-interacting.

1.3.7 Tamm-Dancoff Approximation

In general, the Bethe-Salpeter Eq. 1.33 contains the information on all charge-neutral excited states. Generally, any charge-neutral excited state $|f\rangle$ can be expanded as

$$|f\rangle = \sum_{c\mathbf{k}} \sum_{v\mathbf{k}'} A^f_{c\mathbf{k},v\mathbf{k}'} \hat{c}^\dagger_{c\mathbf{k}} \hat{c}_{v\mathbf{k}'} |0\rangle + \sum_{i\mathbf{k}'''} \sum_{j\mathbf{k}''} \sum_{c\mathbf{k}} \sum_{v\mathbf{k}'} B^f_{i\mathbf{k}'',j\mathbf{k}''',c\mathbf{k},v\mathbf{k}'} \hat{c}^\dagger_{i\mathbf{k}''} \hat{c}_{j\mathbf{k}'''} \hat{c}^\dagger_{c\mathbf{k}} \hat{c}_{v\mathbf{k}'} |0\rangle + \dots \quad (1.59)$$

where $A^f_{c\mathbf{k},v\mathbf{k}'}$ and $B^f_{i\mathbf{k}'',j\mathbf{k}''',c\mathbf{k},v\mathbf{k}'}$ are the expansion coefficients of $|f\rangle$ in singlet excitations, containing one valence hole and one excited electron, and doublet excitations, containing two valence holes and two excited electrons, respectively. Generally, we employ an infinite summation over all possible neutral excitations of the groundstate to obtain the excited state $|f\rangle$. Often, the possible excited states in MBPT calculations are restricted to singlet excitations, *i.e.* it is assumed that the excited states contain one hole and one excited electron at a given time [125]. In this approximation, known as Tamm-Dancoff approximation [136, 137], the excited state is now approximated as[5] [60, 125, 138, 139]

$$|f\rangle \approx \sum_{c\mathbf{k}} \sum_{v\mathbf{k}'} \tilde{A}^f_{c\mathbf{k},v\mathbf{k}'} \hat{c}^\dagger_{c\mathbf{k}} \hat{c}_{v\mathbf{k}'} |0\rangle, \quad (1.60)$$

where the excited state is given as a linear combination in terms of excitations from a valence state $v\mathbf{k}'$ to a conduction state $c\mathbf{k}$ with expansion coefficient $\tilde{A}^f_{c\mathbf{k},v\mathbf{k}'}$. The main advantage of the Tamm-Dancoff approximation is that it allows to express the Bethe-Salpeter Eq. 1.33 as a Hermetian eigenvalue problem, which can be approached with general linear algebra algorithms [140, 359]. The Tamm-Dancoff approximation is valid for excited states that dominantly have the form of singlet excitations, such as excitons and band transitions in solid semiconductors [141, 142] and molecules [143–145]. Nevertheless, it has been shown that the TDA systematically underestimates excitation energies [146] and exciton binding energies [147]. For collective excitations, such as plasmons, the TDA introduces a larger error, as these excitations can not be represented as singlet excitations [148–151]. Nevertheless, in many nanostructured materials, such as nanotubes, the separation of excitations into collective excitations and excitons becomes invalid and the TDA fails [149].

---

[5]In Eqs. 1.59 and 1.60, we employ the quasiparticle approximation (Eq. 1.58).

CHAPTER 2

X-Ray and Optical Absorption Spectroscopy

The optical absorption spectrum can be obtained by directing light of known wavelength on a sample and recording the transmitted light. This allows one to determine the absorbance of the sample, defined as the logarithm of the ratio of incoming and transmitted radiant flux. However, the direct measurement of the transmission is only possible for thin films or transparent materials, since otherwise the intensity of the transmitted beam is too low compared to the noise level of the measurement. To obtain optical properties of bulk materials, the reflectance on the sample surface is measured under normal light incidence. Through a Kramers-Kronig analysis of the reflectance data, the complex dielectric tensor of the material can be recovered. Since the Kramers-Kronig analysis requires knowledge of the reflectance over a wide frequency range, one has to extrapolate the recorded absorption spectra, which introduces uncertainties for the dielectric function [152]. Another experimental approach to the dielectric function is offered by ellipsometry [153], where the change of polarization of the reflected light beam is observed at non-normal incidence. From the parallel and perpendicular polarized reflectance, the complex dielectric tensor can be recovered without the need of Kramers-Kronig analysis. Nevertheless, the determination of the dielectric function requires to interpolate the reflectance using analytical models [154, 155].

For spectroscopy in the x-ray region, different modes to record absorption spectra are available: In transmission mode, the intensity of the transmitted x-ray beam is measured directly. In the fluorescence mode, the fluorescent light, emitted by in the decay process of the excited states, is gathered. In the total-electron-yield mode, the number of electrons emitted from the sample due to the absorption of the x-ray photon is measured. All modes yield consistent results for the x-ray absorption spectra, if the data is corrected for the mode-specific deviations [156, 157].

In this chapter, we will introduce how the dielectric response that is measured by absorption spectroscopies in the optical and the x-ray region is calculated on a microscopic level within the many-body perturbation theory introduced in the previous chapter.

2.1 Microscopic Dielectric Theory

In general, the absorption of light by a system of interacting electrons is obtained from the solutions of the Hamiltonian that contains both the electronic and photonic degrees of freedom, as well as the interactions between the two. We will introduce this Hamiltonian in Eq. 3.4 to describe the scattering of photons. The full solution of this Hamiltonian is provided within quantum electrodynamics [158–160], which has been employed to determine the response of systems in optical cavities, where the interactions between the electrons and the electrodynamic fields are strong [158, 161]. In the absorption spectroscopy that we want to describe here, however, the intensity of the electrodynamic fields are weak. Therefore, a semi-classical approach is applicable, where the radiation field is described classically by the Maxwell equations, while the electronic system is treated quantum-mechanically [162].

2.1.1 Maxwell Equation

The microscopic Maxwell equations[1] in atomic units are given as [163, 164]

Maxwell equations

$$\nabla \cdot \mathbf{E} = 4\pi n \tag{2.1}$$

$$\nabla \times \mathbf{E} = -\partial_t \mathbf{B} \tag{2.2}$$

$$\nabla \cdot \mathbf{B} = 0 \tag{2.3}$$

$$\nabla \times \mathbf{B} = 4\pi \mathbf{j} + \partial_t \mathbf{E} \tag{2.4}$$

These connect the electric field $\mathbf{E}$, the magnetic field $\mathbf{B}$, the charge density n, and the charge current $\mathbf{j}$. The electric field originates from the total charge density n, which can be separated into the *external charge density* n^{ext} and the *induced charge density* n^{ind}, *i.e.* $n = n^{ext} + n^{ind}$. We then define the *electric displacement* $\mathbf{D}$, which is generated by the external charge density n^{ext} by $\nabla \cdot \mathbf{D} = 4\pi n^{ext}$. The electric displacement is then connected to the electric field by

$$\mathbf{D} = \mathbf{E} + \mathbf{P}, \tag{2.5}$$

where the polarization $\mathbf{P}$ is connected to the induced charge density by $\nabla \cdot \mathbf{P} = -n^{ind}$. We can expand the electric displacement in orders of the electric field. To first order, the polarization depends linearly on the electric field, and the *microscopic dielectric function* $\varepsilon_{ij}(\mathbf{r}, \mathbf{r}', t - t')$ is the expansion coefficient, such that Eq. 2.5 becomes

$$D_i(\mathbf{r}, t) = \int d^3 r' \int dt' \varepsilon_{ij}(\mathbf{r}, \mathbf{r}', t - t') E_i(\mathbf{r}', t'). \tag{2.6}$$

---

[1]In the following, we assume that the systems are non-magnetics, such that the magnetic permeability $\mu = 1$.

2.1.2 Transversal and Longitudinal Fields

Any electric field $\mathbf{E}$ propagating along a wave vector $\mathbf{q}$ can be separated into a longitudinal part $\mathbf{E}_L$ ($\mathbf{q} \times \mathbf{E}_L = 0$) and a transversal part $\mathbf{E}_T$ ($\mathbf{q} \cdot \mathbf{E}_T = 0$), such that $\mathbf{E} = \mathbf{E}_T + \mathbf{E}_L$. Physically, the longitudinal electric field oscillates along the direction of motion, while the transversal field oscillates in the plane normal to the wave vector. Formally, we define longitudinal and transversal projectors $\hat{T}_L$ and $\hat{T}_T$ as

$$\hat{T}_L = \frac{\mathbf{q} \cdot \mathbf{q}^T}{|q|^2} \quad \hat{T}_T = \delta_{ij} - \frac{\mathbf{q} \cdot \mathbf{q}T}{|q|^2} \tag{2.7}$$

These projectors are applied to the electric field and the electric displacement in Eq. 2.6, and Eq. 2.5 becomes

$$\begin{pmatrix} \mathbf{D}_L \\ \mathbf{D}_T \end{pmatrix} = \begin{pmatrix} \varepsilon_{LL} & \varepsilon_{LT} \\ \varepsilon_{TL} & \varepsilon_{TT} \end{pmatrix} \begin{pmatrix} \mathbf{E}_L \\ \mathbf{E}_T \end{pmatrix}, \tag{2.8}$$

where the matrix elements of the dielectric tensor are defined as $\varepsilon_{XY} = \hat{T}_X \varepsilon \hat{T}_Y$, *e.g.* the longitudinal-longitudinal dielectric tensor is given by $\varepsilon_{LL} = \hat{T}_L \varepsilon \hat{T}_L = \sum_{ij} \frac{q_i \varepsilon_{ij} q_j}{|q|^2}$. We note that while the dielectric function is fundamentally a 3×3 tensor, the longitudinal-longitudinal dielectric function is a scalar function, since it describes the response to an electric field polarized along the wave vector $\mathbf{q}$. The transversal-transversal dielectric function ε_{TT} is then a 2×2 tensor, as it describes the response to an electric field polarized in the plane orthogonal to the wave vector $\mathbf{q}$. The longitudinal-transversal and transversal-longitudinal components describe the mixing of transversal and longitudinal response.

In homogeneous media, *e.g.* the homogeneous electron gas, the response to a longitudinal (transversal) external field is purely longitudinal (transversal), and thus $\varepsilon_{LT} = \varepsilon_{TL} = 0$. In inhomogeneous media, such as crystalline solids, however, a longitudinal (transversal) field induces both transversal and longitudinal currents. As we are interested in the response to light, which is described by a transversal electro-magnetic field, we are interested to the response to an external transversal field $\mathbf{D}_T$. Due to the coupling of transversal and longitudinal response, the full dielectric tensor has to be determined in general. In the long-wavelength limit, *i.e.* for $\mathbf{q} \to 0$, it has been shown that the transversal response to a transversal external field is identical to the response to a longitudinal perturbation[165, 166]. Therefore, we will limit our discussion to the longitudinal-longitudinal dielectric function ε_{LL} and we drop the index LL in the following.

The Maxwell equations are formally solved by introducing the scalar potential V and the vector potential $\mathbf{A}$, which yield the electric field $\mathbf{E} = -\nabla V - \partial_t \mathbf{A}$ and the magnetic field $\mathbf{B} = \nabla \times \mathbf{A}$. Within the Coulomb gauge ($\nabla \cdot \mathbf{A} = 0$), we obtain the longitudinal electric field $D_L = \hat{P}_L(-\nabla V^{ext})$ and the electric displacement $E_L = \hat{P}_L(-\nabla V)$, with the external potential V^{ext} and the total Coulomb potential V. The total potential $V = V^{ext} + V^{ind}$ is defined as the sum of the external potential V^{ext} and the induced potential V^{ind}. This finally allows us

to rewrite Eq. 2.6 in terms of potentials instead of fields:

$$V^{ext}(\mathbf{r}, t) = \int d^3 r' \int dt \; \varepsilon(\mathbf{r}, \mathbf{r}', t - t') V(\mathbf{r}', t'). \tag{2.9}$$

The inverse dielectric function is then given by

$$V(\mathbf{r}, t) = \int d^3 r' \int dt \; \varepsilon^{-1}(\mathbf{r}, \mathbf{r}', t - t') V^{ext}(\mathbf{r}', t'). \tag{2.10}$$

In Eqs. 1.42, 1.43, and 1.40 in Chapter 1, the dielectric function and the polarizability are introduced in the context of many-body perturbation theory. There, the reducible and irreducible polarizability describe the change in density due to external and total potential, respectively. We now see that the definition in Eq. 2.9 is identical to the one in Eq. 1.43, where we identify the external potential $u(1^+, 1) = V^{ext}(1)$ and the total potential $v_{cl}(1) = V(1)$. Since the electrons interact through the Coulomb potential, the external perturbation, which is introduced in Chapter 1 to derive Hedin's equations 1.47-1.48, is identical to the external potential in the Maxwell equations. Thus, we can write the dielectric function and its inverse as

$$\varepsilon(\mathbf{r}, \mathbf{r}', t, t') = \delta(\mathbf{r} - \mathbf{r}')\delta(t - t') - \int d^3 r'' v_C(|\mathbf{r} - \mathbf{r}''|)\tilde{\chi}(\mathbf{r}'', \mathbf{r}', t'', t')\delta(t - t''), \tag{2.11}$$

and

$$\varepsilon^{-1}(\mathbf{r}, \mathbf{r}', t, t') = \delta(\mathbf{r} - \mathbf{r}')\delta(t - t') + \int d^3 r'' dt'' v_C(|\mathbf{r} - \mathbf{r}''|)\chi(\mathbf{r}'', \mathbf{r}', t'', t')\delta(t - t''). \tag{2.12}$$

This way, we have found a way to calculate the response of a system of interacting electrons to an external electric field from many-body perturbation theory.

2.1.3 Macroscopic Dielectric Function

The dielectric function, defined in the previous sections, relates the total and external potentials, where the total potential may oscillate on a microscopic scale due to the quantum-mechanical response of the electrons to the external potential. In absorption experiments, however, only the macroscopic response of the material to an external macroscopic potential is accessible. To determine the *macroscopic dielectric function*, we first have to define what macroscopic quantities are. We define a macroscopic counterpart $f_M(\mathbf{R})$ to a microscopic function $f(\mathbf{r})$ as the average for each lattice position $\mathbf{R}$ over the surrounding unit

cell volume V_0:

$$
\begin{aligned}
f_M(\mathbf{R}) &= \frac{1}{V_0} \int_{V_0} d^3 r f(\mathbf{R} + \mathbf{r}) = \sum_{\mathbf{G},\mathbf{q}} e^{i\mathbf{q}\mathbf{R}} f_{\mathbf{G}}(\mathbf{q}) \frac{1}{V_0} \int_{V_0} d^3 r e^{i\mathbf{G}\mathbf{r}} e^{i\mathbf{q}\mathbf{r}} \\
&\approx \sum_{\mathbf{G},\mathbf{q}} e^{i\mathbf{q}\mathbf{R}} f_{\mathbf{G}}(\mathbf{q}) \frac{1}{V_0} \int_{V_0} d^3 r e^{i\mathbf{G}\mathbf{r}} \delta_{\mathbf{q},0} = \sum_{\mathbf{G},\mathbf{q}} e^{i\mathbf{q}\mathbf{R}} f_{\mathbf{G}}(\mathbf{q}) \delta_{\mathbf{G},0} \delta_{\mathbf{q},0}.
\end{aligned}
\tag{2.13}
$$

Here, we have used the definitions of the Fourier transformation in Eq. A.7. The approximation in Eq. 2.13 is obtained by assuming $e^{i\mathbf{q}\mathbf{r}} \approx \delta_{\mathbf{q},0}$, *i.e.* $\mathbf{q}$ being small compared to the dimensions of the unit cell. Furthermore, we employ Eq. A.10 to evaluate the integral over the unit cell volume V_0. Comparing Eq. 2.13 with the definition of the Fourier transform in Eq. A.7 shows that Fourier components of the macroscopic function $[f_M]_{\mathbf{G}}(\mathbf{q}) = f_{\mathbf{G}=0}(\mathbf{q} = 0)$ are given by the $\mathbf{q} = 0, \mathbf{G} = 0$ element of the Fourier transform of the corresponding microscopic function.

To obtain the macroscopic dielectric function ε_M, we first consider which potentials vary on a macroscopic scale, and which of them additionally have microscopic components. We assume that the external potential is macroscopic, *i.e.* $V_{\mathbf{G}}^{ext} = V_{\mathbf{G}}^{ext} \delta_{\mathbf{G},0}$, as the incoming light is a plane wave with a long wavelength. The total potential, on the other hand, has both macroscopic and microscopic components, *i.e.* $V_{\mathbf{G}} \neq V_{\mathbf{G}} \delta_{\mathbf{G},0}$ since the induced potential V^{ind} varies on the microscopic scale. Nevertheless, we can define the macroscopic component of the total potential $V_M = V_{\mathbf{G}=0}(\mathbf{q} = 0)$ from Eq. 2.13. The macroscopic total potential can now be expressed in terms of the external potential through Eq. 2.10 as

$$
V_M(\omega) = V_{\mathbf{G}=0}(\mathbf{q} = 0, \omega) = \sum_{\mathbf{G}'} \varepsilon_{0\mathbf{G}'}^{-1}(\mathbf{q} = 0, \omega) V_{\mathbf{G}'}^{ext}(\mathbf{q} = 0, \omega) = \sum_{\mathbf{G}'} \varepsilon_{0\mathbf{G}'}^{-1}(\mathbf{q} = 0, \omega) V_M^{ext} \delta_{\mathbf{G}',0}
\tag{2.14}
$$

As such, the macroscopic inverse dielectric function ε_M^{-1} is defined as

$$
V_M = \varepsilon_{00}^{-1}(\mathbf{q} = 0, \omega) V_M^{ext} \equiv \varepsilon_M^{-1} V_M^{ext}.
\tag{2.15}
$$

Thus, the macroscopic inverse dielectric function $\varepsilon_M^{-1}(\omega) = \varepsilon_{00}^{-1}(\omega)$ is given by the $\mathbf{G} = 0, \mathbf{G}' = 0$ element of the microscopic dielectric function. The macroscopic dielectric function $\varepsilon_M(\omega)$ is then given by inverting of Eq. 2.14 as

$$
\varepsilon_M(\omega) = \frac{1}{\varepsilon_{00}^{-1}(\mathbf{q} = 0, \omega)} = \frac{1}{1 + v_0(\mathbf{q} = 0)\chi_{00}(\mathbf{q} = 0, \omega)} \neq \varepsilon_{00}(\mathbf{q} = 0, \omega).
\tag{2.16}
$$

The macroscopic dielectric function is identical to the head ε_{00}, only if the microscopic variations of the induced potential are neglected. This approximation is known as the *neglecting local field effects* (NLFE). For the response at finite momentum transfer, where the external potential oscillates with a wavevector $\mathbf{Q} = \mathbf{G} + \mathbf{q}$, Eq. 2.14 can be generalized,

such that the macroscopic dielectric function at finite momentum transfer is defined as

$$\varepsilon_M(\mathbf{Q}, \omega) = \frac{1}{\varepsilon_{\mathrm{GG}}^{-1}(\mathbf{q}, \omega)}. \tag{2.17}$$

2.2 Bethe-Salpeter Equation Formalism

2.2.1 BSE for the Polarizability

The previous section shows that the absorption spectrum can be obtained from the longitudinal reducible polarizability χ defined in Eq. 1.40, which is connected to the inverse dielectric function through Eq. 2.12. Following linear response theory [167], the retarded polarizability χ^R can be expressed as [57, 63, 125]

$$\chi^R(\mathbf{r}_1, \mathbf{r}_2, t_1, t_2) = \frac{n(\mathbf{r}_1, t_1)}{\delta u(\mathbf{r}_2, t_2)} = -\mathrm{i}\Theta(t_1 - t_2)\langle 0| \left[\hat{n}(\mathbf{r}_1, t_1), \hat{n}(\mathbf{r}_2, t_2)\right] |0\rangle, \tag{2.18}$$

where we have defined the time-dependent density operator as
$\hat{n}(\mathbf{r}, t) = e^{-\mathrm{i}\hat{H}t} \left[\sum_j^N \delta(\mathbf{r} - \mathbf{r_j})\right] e^{\mathrm{i}\hat{H}t}$. The Heaviside step function $\Theta(t_1 - t_2)$ ensures causality, such that the response of the density at t_1 follows the perturbation at t_2. Within many-body perturbation theory, the reducible polarizability is given as

$$\chi(1, 2) = \frac{\delta n(1)}{\delta u(2)} = -\mathrm{i}\frac{\delta G(1, 1^+)}{\delta u(2^+, 2)} = -\mathrm{i}L(1, 2; 1^+, 2^+), \tag{2.19}$$

where $n(1) = -\mathrm{i}G(1, 1^+)$ and we use Eq. 1.24. While we have defined the *retarded polarizability* χ^R in Eq. 2.18, Eq. 2.19 defines the *time-ordered polarizability* χ. The relationship between the two is discussed in detail in appendix B. The polarizability can be obtained from the Bethe-Salpeter equation 1.33 for the correlation function $L(1, 2; 1', 2')$ by contracting the indices. The BSE then takes the form

$$L(1, 2; 1^+, 2^+) = L_0(1, 2; 1^+, 2^+) + L_0(1, \bar{3}'; 1^+, \bar{3})\Xi(\bar{3}, \bar{4}, \bar{3}', \bar{4}')L(\bar{4}', 2, \bar{4}, 2^+), \tag{2.20}$$

where the interaction kernel in the GWA is given in Eq. 1.55 as

$$\Xi^{GWA}(3, 4, 3', 4') = -\mathrm{i}\delta(3, 3')\delta(4'^+, 4)v_C(4, 3^+) + \mathrm{i}\delta(3, 4')\delta(3', 4)W(3', 3^+). \tag{2.21}$$

The last term in Eq. 1.55, $\delta W/deltaG$, describes the change in the screened Coulomb interaction due to the presence of an excitation, and is neglected in Eq. 2.21 since it is assumed to be small [168]. We note that there is no corresponding Dyson-like equation for the polariz-

ability, since Eq. 2.20 can not be written in a closed form in the contracted correlation function, but instead requires, at least, knowledge of the three-point function $L(\bar{4}', 2, \bar{4}, 2^+)$.

The full electron-hole correlation function $L(1, 2, 3, 4)$ depends on four points in space and time, which is reduced for time-independent potentials to three points in time due to translational symmetry in time. For the calculation of optical properties, only the contracted correlation function $L(1, 2; 1^+, 2^+)$ in Eq. 2.20 is required, which depends only on the time difference $t \equiv t_2 - t_1$ if translational symmetry in time holds, *i.e.* for the case of time-independent potentials. Yet, the interaction kernel Ξ depends on four points in space and time. For most *ab initio* Bethe-Salpeter equations in solid-state physics, as well as for the implementation presented here, the dependence of Ξ in Eq. 2.21 on four different time points is computationally too involved [63]. To simplify the expression further, the interaction is assumed to be static and instantaneous, *i.e.* $W(3', 3^+) = W(\mathbf{r}_{3'}, \mathbf{r}_3)\delta(t_{3'} - t_3^+)$. In that way, the interaction kernel does not depend on time anymore, and both the independent-particle correlation function L^0 and the full one, L, depend solely on the time difference $t_2 - t_1$. We can express the BSE for the Fourier-transformed correlation function $L(1, 2; \omega)^2$ as

$$L(1, 2; \omega) = L_0(1, 2; \omega) + L_0(1, \bar{3}', 1, \bar{3}; \omega)\Xi(\bar{3}, \bar{4}, \bar{3}', \bar{4}')L(\bar{4}', 2, \bar{4}, 2; \omega) \qquad (2.22)$$

To obtain the polarizability directly from Eq. 2.19 directly, a prefactor $-i$ should be multiplied to the Bethe-Salpeter equation, which leads to Dyson's equation for $-iL$ in terms of $-iL_0$

$$-iL(1, 2; \omega) = \left[-iL_0(1, 2; \omega)\right] + \left[-iL_0(1, \bar{3}', 1, \bar{3}; \omega)\right]\left[i\Xi(\bar{3}, \bar{4}, \bar{3}', \bar{4}')\right]\left[-iL(\bar{4}', 2, \bar{4}, 2; \omega)\right].$$
$$(2.23)$$

Inserting the explicit form of Ξ in Eq. 2.21, we obtain

$$-iL(1, 2; \omega) = \left[-iL_0(1, 2; \omega)\right] +$$
$$\left[-iL_0(1, \bar{3}', 1, \bar{3}; \omega)\right]\left[\delta(\bar{3}, \bar{3}')\delta(\bar{4}, \bar{4}')v_C(\bar{3}, 4) - \delta(\bar{3}, \bar{4}')\delta(\bar{3}', \bar{4})W(\bar{3}', \bar{3})\right] \times \qquad (2.24)$$
$$\times \left[-iL(\bar{4}', 2, \bar{4}, 2; \omega)\right].$$

This equation is the final result of this Chapter, the Bethe-Salpeter equation for the polarizability. The dielectric properties, especially the macroscopic dielectric tensor, are obtained from the solutions of Eq. 2.24.

2.2.2 Lehmann Representations

Equation 2.19 shows that the polarizability χ is obtained by a contraction of the electron-hole correlation function L. Lehmann representations of L_0 and χ similar to the ones known

---

[2]Here, we introduce an additional notation for non-local functions, where $(1, 2; \omega) = (\mathbf{r}_1, \mathbf{r}_2; \omega)$. This differs from the notation used before, but the chosen notation will be clear from context.

for the one- and two-particle Green's function [63, 125] can be derived. These Lehmann representations are employed in the next chapters to connect observables in absorption and scattering spectroscopy to quantities determined within many-body perturbation theory.

A fundamental ambiguity in the Lehmann representation exists for time-ordered quantities that only depend on time differences $t_1 - t_2$, since the Fourier transformations with respect to either time differences $\tau^{(1)} = t_1 - t_2$ or $\tau^{(2)} = t_2 - t_1$ yield distinctly different Lehmann representations. While physical observables are unaffected by the choice of Lehmann representation, the implementation of absorption and scattering spectroscopy differ depending on the choice of time direction in the Fourier transformation. For the polarizability $\chi(1, 2)$, we obtain the Lehmann representation $\chi_{\tau^{(1)}}(\mathbf{r}_1, \mathbf{r}_2, \omega)$ with respect to $\tau^{(1)}$ as

$$
\chi_{\tau^{(1)}}(\mathbf{r}_1, \mathbf{r}_2, \omega) = \sum_{N \neq 0} \frac{\langle 0|\hat{\psi}^\dagger(\mathbf{r}_1)\hat{\psi}(\mathbf{r}_1)|N\rangle\langle N|\hat{\psi}^\dagger(\mathbf{r}_2)\hat{\psi}(\mathbf{r}_2)|0\rangle}{\omega - E_N + i\eta}
$$
$$
- \frac{\langle 0|\hat{\psi}^\dagger(\mathbf{r}_2)\hat{\psi}(\mathbf{r}_2)|N\rangle\langle N|\hat{\psi}^\dagger(\mathbf{r}_1)\hat{\psi}(\mathbf{r}_1)|0\rangle}{\omega + E_N - i\eta},
$$

(2.25)

where the sum includes all excited many-body states $|N\rangle$ with total energy E_N. Without loss of generality, the total energy of the ground state is set to zero, *i.e.* $E_0 = 0$. The polarizability is given as the sum of two terms, where the first, called the resonant contribution, has poles at the excitation energies $\omega = E_N$, while the second, the anti-resonant contribution, has poles at negative excitation energies, $\omega = -E_N$. Matrix elements of the polarizability $\chi_{ij\mathbf{k},i'j'\mathbf{k}'}(\mathbf{q})$ in an arbitrary single-particle basis $\{\psi_{i\mathbf{k}}(\mathbf{r})\}$ are given as

$$
\chi_{ij\mathbf{k},i'j'\mathbf{k}'}(\mathbf{q}, \omega) = \sum_{N \neq 0} \frac{\langle 0|\hat{c}_{i\mathbf{k}}\hat{c}^\dagger_{j(\mathbf{k}+\mathbf{q})}|N\rangle\langle N|\hat{c}^\dagger_{i'(\mathbf{k}'+\mathbf{q})}\hat{c}_{j'\mathbf{k}'}|0\rangle}{\omega - E_N + i\eta} + \frac{\langle 0|\hat{c}_{i\mathbf{k}}\hat{c}^\dagger_{j(\mathbf{k}+\mathbf{q})}|N\rangle\langle N|\hat{c}^\dagger_{i'(\mathbf{k}'+\mathbf{q})}\hat{c}_{j'\mathbf{k}'}|0\rangle}{\omega + E_N - i\eta}.
$$

(2.26)

Equation 2.25 can be simplified by applying both the quasiparticle approximation (Eq. 1.58) and the Tamm-Dancoff approximation (Eq. 1.60). As such, the field operators $\hat{\psi}(\mathbf{r}) = \sum_{i\mathbf{k}} \phi_{i\mathbf{k}}(\mathbf{r})\hat{c}_{i\mathbf{k}}$ are expanded in quasiparticle wavefunctions $\phi_{i\mathbf{k}}$, and we obtain

$$
\chi_{\tau^{(1)}}(\mathbf{r}_1, \mathbf{r}_2, \omega) = \sum_{\mathbf{q}} \sum_{cv\mathbf{k}} \sum_{c'v'\mathbf{k}'} \phi^*_{v\mathbf{k}}(\mathbf{r}_1)\phi_{c(\mathbf{k}+\mathbf{q})}(\mathbf{r}_1)\chi^{R,1}_{cv\mathbf{k},c'v'\mathbf{k}'}(\mathbf{q}, \omega)\phi^*_{c'(\mathbf{k}'+\mathbf{q})}(\mathbf{r}_2)\phi_{v\mathbf{k}'}(\mathbf{r}_2)
$$
$$
+ \phi_{v\mathbf{k}}(\mathbf{r}_1)\phi^*_{c(\mathbf{k}+\mathbf{q})}(\mathbf{r}_1)\chi^{A,1}_{cv\mathbf{k},c'v'\mathbf{k}'}(\mathbf{q}, \omega)\phi_{c'(\mathbf{k}'+\mathbf{q})}(\mathbf{r}_2)\phi^*_{v'\mathbf{k}'}(\mathbf{r}_2).
$$

(2.27)

Here, we have used the translational symmetry of the non-local polarizability, *i.e.* $\chi(\mathbf{r} + \mathbf{R}, \mathbf{r}' + \mathbf{R}; \omega) = \chi(\mathbf{r}, \mathbf{r}'; \omega)$ for any lattice vector $\mathbf{R}$, such that we can write the polarizability as $\chi = \sum_{\mathbf{q}} \chi(\mathbf{q})$. As in Eq. 2.27, we find resonant and anti-resonant contributions, and the

corresponding matrix elements of the polarizability are given by

$$\chi^{R1}_{cv\mathbf{k},c'v'\mathbf{k}'}(\mathbf{q},\omega) = \sum_{N\neq0} \frac{\langle0|\hat{c}^\dagger_{v\mathbf{k}}\hat{c}_{c(\mathbf{k}+\mathbf{q})}|N\rangle\langle N|\hat{c}^\dagger_{c'(\mathbf{k}'+\mathbf{q})}\hat{c}_{v'\mathbf{k}'}|0\rangle}{\omega - E_N + \mathrm{i}\eta},\tag{2.28}$$

and

$$\chi^{A1}_{vc\mathbf{k},v'c'\mathbf{k}'}(\mathbf{q},\omega) = \sum_{N\neq0} \frac{\langle0|\hat{c}^\dagger_{v'\mathbf{k}'}\hat{c}_{c'(\mathbf{k}'+\mathbf{q})}|N\rangle\langle N|\hat{c}^\dagger_{c(\mathbf{k}+\mathbf{q})}\hat{c}_{v\mathbf{k}}|0\rangle}{\omega + E_N - \mathrm{i}\eta}.\tag{2.29}$$

Alternatively, a Lehmann representation $\chi_{\tau^{(2)}}(\mathbf{r}_1,\mathbf{r}_2,\omega)$ with respect to $\tau^{(2)} = t_2 - t_1$ is obtained as

$$\chi_{\tau^{(2)}}(\mathbf{r}_1,\mathbf{r}_2,\omega) = \sum_{N\neq0} \frac{\langle0|\hat{\psi}^\dagger(\mathbf{r}_2)\hat{\psi}(\mathbf{r}_2)|N\rangle\langle N|\hat{\psi}^\dagger(\mathbf{r}_1)\hat{\psi}(\mathbf{r}_1)|0\rangle}{\omega - E_N + \mathrm{i}\eta} - \frac{\langle0|\hat{\psi}^\dagger(\mathbf{r}_1)\hat{\psi}(\mathbf{r}_1)|N\rangle\langle N|\hat{\psi}^\dagger(\mathbf{r}_2)\hat{\psi}(\mathbf{r}_2)|0\rangle}{\omega + E_N - \mathrm{i}\eta},\tag{2.30}$$

which, in quasiparticle and Tamm-Dancoff approximation, becomes

$$\chi_{\tau^{(2)}}(\mathbf{r}_1,\mathbf{r}_2,\omega) = \sum_{\mathbf{q}}\sum_{cv\mathbf{k}}\sum_{c'v'\mathbf{k}'} \phi_{v\mathbf{k}}(\mathbf{r}_1)\phi^*_{c(\mathbf{k}+\mathbf{q})}(\mathbf{r}_1)\chi^{R,2}_{cv\mathbf{k},c'v'\mathbf{k}'}(\mathbf{q},\omega)\phi_{c'(\mathbf{k}'+\mathbf{q})}(\mathbf{r}_2)\phi^*_{v\mathbf{k}'}(\mathbf{r}_2)$$
$$+\phi^*_{v\mathbf{k}}(\mathbf{r}_1)\phi_{c(\mathbf{k}+\mathbf{q})}(\mathbf{r}_1)\chi^{A,2}_{cv\mathbf{k},c'v'\mathbf{k}'}(\mathbf{q},\omega)\phi^*_{c'(\mathbf{k}'+\mathbf{q})}(\mathbf{r}_2)\phi v'\mathbf{k}'(\mathbf{r}_2).\tag{2.31}$$

The matrix element in this representation are defined as

$$\chi^{R2}_{cv\mathbf{k},c'v'\mathbf{k}'}(\mathbf{q},\omega) = \sum_{N\neq0} \frac{\langle0|\hat{c}^\dagger_{v'\mathbf{k}'}\hat{c}_{c'(\mathbf{k}'+\mathbf{q})}|N\rangle\langle N|\hat{c}^\dagger_{c(\mathbf{k}+\mathbf{q})}\hat{c}_{v\mathbf{k}}|0\rangle}{\omega - E_N + \mathrm{i}\eta},\tag{2.32}$$

and

$$\chi^{A2}_{vc\mathbf{k},v'c'\mathbf{k}'}(\mathbf{q},\omega) = \sum_{N\neq0} \frac{\langle0|\hat{c}^\dagger_{v\mathbf{k}'}\hat{c}_{c(\mathbf{k}+\mathbf{q})}|N\rangle\langle N|\hat{c}^\dagger_{c'(\mathbf{k}'+\mathbf{q})}\hat{c}_{v'\mathbf{k}'}|0\rangle}{\omega + E_N - \mathrm{i}\eta}.\tag{2.33}$$

It is apparent, that the matrix elements χ^{R1} in Eq. 2.28 and χ^{R2} in Eq. 2.32, as well as their antiresonant counterparts in Eqs. 2.29 and 2.33, are closely related. The denominator is identical in the two representations, while the nominator in the second one is complex conjugated with respect to the first one. Although the difference appears miniscule, we will demonstrate that it leads to different expressions for the dielectric function and other spectroscopic observables in the two different representations. More details on the Lehmann representations, and their relationship to the retarded polarizability are provided in Appendix B.

CHAPTER 3

Inelastic X-ray and Electron Scattering Spectroscopy

In a general x-ray or electron scattering experiment, a collimated beam of monochromatic particles, either x-ray photons or electron, is focussed on a sample, and the scattered beam is recorded at a certain solid angle Ω_2. The scattered beam is then analyzed spectrally with an energy resolution $d\hbar\omega_2$. The probability of scattering into the solid angle element $\left[\Omega_2, \Omega_2 + d\Omega_2\right]$ within an energy range $\left[\hbar\omega_2, \hbar\omega_2 + d\hbar\omega_2\right]$ is given by the *double differential cross section* $d^2\sigma/d\Omega_2 d\omega_2$. Quantum-mechanically, the many-body systems is scattered from an initial many-body state $|i, \mathbf{K}_1\lambda_1\rangle$, which consists of the initial many-electron state $|i\rangle$ and the state $|\mathbf{K}_1\lambda_1\rangle$ of the incident particle, where $\mathbf{K}_1$ is the momentum of the incoming particle and λ_1 is a generic quantum number. The final state $|f, \mathbf{K}_2\lambda_2\rangle$ is a superposition of the final (excited) electronic many-body state $|f\rangle$ and the state $|\mathbf{K}_2\lambda_2\rangle$ of the scattered particle. For photons, λ_1 and λ_2 characterize the polarization states of the incoming and scattered photon, respectively, which can be either two linear polarization states or left- and right-hand circular polarization states. Generally, the scattering rate $d^2\sigma$ is given by [169, 170]

$$\mathrm{d}^2\sigma = \frac{j_2(\mathbf{r}, \mathbf{K}_2, \lambda_2)\hat{l}r^2\mathrm{d}\Omega_2\mathrm{d}E_1}{j_1}, \tag{3.1}$$

where j_1 is the incoming current, and the numerator describes the number of scattered particles, since $j_2(\mathbf{r}, \mathbf{K}_2, \lambda_2)$ is the current of scattered particles in state $|\mathbf{K}_2, \lambda_2\rangle$ in the direction of $\mathbf{r}$, and $\hat{l} = \mathbf{r}/r$ is the direction vector along $\mathbf{r}$. In the quantum-mechanical scattering theory, the numerator of Eq. 3.1 is given by the transition probability $w(i, \mathbf{K}_1, \lambda_1; f, \mathbf{K}_2, \lambda_2)$ as

$$j_2(\mathbf{r}, \mathbf{K}_2, \lambda_2)\hat{l}r^2\mathrm{d}\Omega_2\mathrm{d}E_1 = N_0 \sum_f \sum_{\mathbf{K}_2\lambda_2} w(i, \mathbf{K}_1, \lambda_1; f, \mathbf{K}_2, \lambda_2)D(\mathbf{K}_2)\mathrm{d}^3K_2, \tag{3.2}$$

where N_1 is the number of probing particles that impinge on the sample and $D(\mathbf{K}_2) = \left(\frac{V}{2\pi}\right)$ is the density of states of the scattered particle. We write $D(\mathbf{K}_2)d^3K_2 = \frac{V}{2\pi}\mathbf{K}_2\mathrm{d}\Omega_2$. The

double differential cross section is given as

$$\frac{\mathrm{d}^2\sigma}{\mathrm{d}\Omega_2\mathrm{d}K_2} = \frac{N_0 V}{2\pi j_1} \sum_{\mathbf{K}_2\lambda_2} w(i, \mathbf{K}_1, \lambda_1; f, \mathbf{K}_2, \lambda_2). \tag{3.3}$$

The initial current j_1 and the dispersion $E_2(\mathbf{K}_2)$ differ depending on the probing particle, and the transition probability w depends on the interaction of the probing particle with the sample.

In the following chapter, an expression for the double differential cross section, known as the generalized Kramers-Heisenberg formula, is derived from a perturbative treatment of the electron-photon interaction. We will then show that two distinctive scattering processes occur depending on the energy of the probing particle, known as the resonant and non-resonant scattering. For the non-resonant scattering, we will derive a simplified expression that connects the cross section to the dielectric tensor introduced in Chapter 2. Finally, we discuss the process of resonant inelastic scattering.

3.1 Generalized Kramers-Heisenberg Formula

In Eq. 1.2, the Hamiltonian of a system of interacting electrons in the electrostatic potential of the nuclei has been introduced. For a system of interacting electrons in a quantized electromagnetic field, a more general Hamiltonian is needed, which also includes the Hamiltonian of the photons and the interaction between electrons and photons. The most general form of this Hamiltonian is given by [170]

$$
\begin{aligned}
H = H_0 &+ \frac{\alpha^2}{2} \sum_j \mathbf{A}^2(\mathbf{r}_j) - \alpha \sum_j \mathbf{A}(\mathbf{r}_j) \cdot \mathbf{p}_j \\
&- \frac{\alpha}{2} \sum_j \boldsymbol{\sigma}_j \cdot \left[\nabla \times \mathbf{A}(\mathbf{r}_j)\right] - \frac{\alpha^2}{4} \sum_j \boldsymbol{\sigma}_j \cdot \left[\dot{\mathbf{A}}(\mathbf{r}_j) \times \mathbf{A}(\mathbf{r}_j)\right] \\
&- \frac{\alpha^3}{4} \sum_j \left[\nabla V(\mathbf{r}_j) \times \mathbf{A}(\mathbf{r}_j)\right] + \frac{\alpha^3}{4} \sum_j \dot{\mathbf{A}}(\mathbf{r}_j) \times \mathbf{p}_j + H_R \\
\Rightarrow H = H_0 &+ H_i + H_R,
\end{aligned}
\tag{3.4}
$$

where $\mathbf{A}$ is the electromagnetic vector potential, $\dot{\mathbf{A}} = \partial/\partial t \mathbf{A}$ its time-derivative, and V the scalar potential, as introduced in Section 2.1.2, and $\alpha = \frac{1}{c} \approx \frac{1}{137}$ is the fine-structure constant in atomic units. In the last line of Eq. 1.2, we have introduced the electronic Hamiltonian H_0, the radiation-field Hamiltonian H_R, and the Hamiltonian H_i of the electron-phonon

interaction. H_0 gathers all terms that describe solely the electronic system, *i.e.*

$$H_0 = \sum_j \frac{1}{2} \mathbf{p}_j^2 + \frac{1}{2} \sum_{j \neq j'} \frac{1}{|\mathbf{r}_j - \mathbf{r}_{j'}|} + \sum_j V_{e-n}(\mathbf{r}_j) + V_{n-n} + \frac{\alpha^2}{4} \sum_j \boldsymbol{\sigma}_j \cdot \left[\nabla \phi \times \mathbf{p}_j \right]. \tag{3.5}$$

The Hamiltonian H_0 differs from the one in Eq. 1.2 only by the last term, which introduces the spin-orbit coupling. This relativistic effect is not included in the non-relativistic Hamiltonian in Eq. 1.2. The radiation-field Hamiltonian H_R is given by

$$H_R = \sum_{\mathbf{K}\lambda} \omega_{\mathbf{K}} \left(\hat{a}_{\mathbf{K}\lambda}^\dagger \hat{a}_{\mathbf{K}\lambda} + \frac{1}{2} \right), \tag{3.6}$$

with the photon creation and annihilation operators $\hat{a}_{\mathbf{K}\lambda}^\dagger$ and $\hat{a}_{\mathbf{K}\lambda}$ of a phonon state $(\mathbf{K}, \lambda)$ with energy $\omega_{\mathbf{K}}$, respectively. Here, λ enumerates the two orthogonal polarization states of the photon field, $\mathbf{K}$ is the photon wavevector. The interaction between electrons and photons originates from terms proportional to the electromagnetic vector potential $\mathbf{A}$ and its time derivative $\dot{\mathbf{A}}$. We recall the expression of the vector potential $\mathbf{A}(\mathbf{r})$ in terms of creation and annihilation operators of the photon field, $\hat{a}_{\mathbf{K}\lambda}^\dagger$ and $\hat{a}_{\mathbf{K}\lambda}$:

$$\mathbf{A}(\mathbf{r}) = \sum_{\mathbf{K}\lambda} \left(\frac{2\pi c^2}{V \omega_{\mathbf{K}}} \right)^{\frac{1}{2}} \left[\mathbf{e}_{\mathbf{K}\lambda} \hat{a}_{\mathbf{K}\lambda} e^{i\mathbf{K}\mathbf{r} - i\omega_{\mathbf{K}} t} + \mathbf{e}_{\mathbf{K}\lambda}^* \hat{c}_{\mathbf{K}\lambda}^\dagger e^{-i\mathbf{K}\mathbf{r} + i\omega_{\mathbf{K}} t} \right] \tag{3.7}$$

where $\mathbf{e}_{\mathbf{K}\lambda}$ is the polarization vector of the photon in state $(\mathbf{K}\lambda)$. We express the interaction Hamiltonian as the sum of six terms, given by

$$H_{i1} = \frac{\alpha^2}{2} \sum_j \mathbf{A}^2(\mathbf{r}_j) \tag{3.8}$$

$$H_{i2} = -\alpha \sum_j \mathbf{A}(\mathbf{r}_j) \cdot \mathbf{p}_j \tag{3.9}$$

$$H_{i3} = -\frac{\alpha}{2} \sum_j \boldsymbol{\sigma}_j \cdot \left[\nabla \times \mathbf{A}(\mathbf{r}_j) \right] \tag{3.10}$$

$$H_{i4} = -\frac{\alpha^2}{4} \sum_j \boldsymbol{\sigma}_j \cdot \left[\dot{\mathbf{A}}(\mathbf{r}_j) \times \mathbf{A}(\mathbf{r}_j) \right] \tag{3.11}$$

$$H_{i5} = -\frac{\alpha^3}{4} \sum_j \left[\nabla \phi(\mathbf{r}_j) \times \mathbf{A}(\mathbf{r}_j) \right] \tag{3.12}$$

$$H_{i6} = \frac{\alpha^3}{4} \sum_j \dot{\mathbf{A}}(\mathbf{r}_j) \times \mathbf{p}_j. \tag{3.13}$$

According to Fermi's Golden Rule [171], the transition rate w is obtained from a perturbative treatment of the electron-photon interaction $\hat{H}_i$ up to second order as

$$w = 2\pi \sum_F \left| \langle F|\hat{H}_i|I\rangle + \sum_N \frac{\langle F|\hat{H}_i|N\rangle\langle N|\hat{H}_i|I\rangle}{E_I - E_N} \right|^2 \delta(E_I - E_F), \tag{3.14}$$

where $|I\rangle$, $|F\rangle$, and $|N\rangle$ are initial, final, and intermediate many-body state, respectively. We furthermore restrict our perturbation series to terms of order α^2 in Eqs. 3.8-3.13, *i.e.* to the non-relativistic case [170, 172]. The electron-photon interaction terms in Eq. 3.8-3.13 contain the vector potential $\mathbf{A}$, and thus the photonic annihilation and creation operators through Eq. 3.7, to different orders. Not all terms contribute to the scattering, since we have restricted the possible many-body states by imposing that the initial state $|i, \mathbf{K}_1\lambda_1\rangle$ and the final state $|f, \mathbf{K}_2\lambda_2\rangle$ contain only one photon each[1]. As such, in the first-order treatment of Eq. 3.14 only the terms H_{i1} and H_{i4} contribute, as these contain terms of the form $c(\mathbf{K}\lambda)c^\dagger(\mathbf{K}'\lambda')$ that conserve the number of photons. To second order, both terms in $O\left(\mathbf{A}\right)$ and $O\left(\mathbf{A}^2\right)$ contribute. Inserting the terms H_{i1} or H_{i4} for the second-order term in Eq. 3.14, the intermediate states $|N\rangle$ contain a photon, as these terms conserve the photon number. However, these terms are proportional to α^4 and are neglected in our non-relativistic treatment. Similarly, within first- and second-order perturbation theory the terms H_{i5} and H_{i6} only contribute for orders of $O\left(\alpha^4\right)$. Thus, only the interaction terms H_{i2} and H_{i3} remain. Since in this work we focus on non-magnetic systems, we neglect the spin-dependent interactions H_{i3} and H_{i4}. Thus, we express the transition rate as

$$w = 2\pi \sum_F \left| \langle F|H_{i1}|I\rangle + \sum_N \frac{\langle F|H_{i2}|N\rangle\langle N|H_{i2}|I\rangle}{E_I - E_N} \right|^2 \delta(E_I - E_F). \tag{3.15}$$

Combining Eqs. 3.8,3.9,3.15, and 3.7, the photonic states can be traced out, such that the expression only contains expectation values for the electronic states $|i\rangle$, $|n\rangle$, and $|f\rangle$. We obtain

$$
\begin{aligned}
w = 2\pi &\left(\frac{V^2\omega_2\alpha^3}{(2\pi)^2}\right)^2 \sum_f \left| \alpha^2\langle f|\mathbf{e}_1 \cdot \mathbf{e}_2^* \sum_j e^{i\mathbf{Q}\mathbf{r}_j}|0\rangle \right. \\
&\left. + \alpha^2 \sum_n \frac{\langle f|\sum_j e^{-i\mathbf{K}_2\mathbf{r}_j}\mathbf{e}_2^* \cdot \mathbf{p}_j|n\rangle\langle n|e^{i\mathbf{K}_2\mathbf{r}_j}\mathbf{e}_1 \cdot \mathbf{p}_j|0\rangle}{\omega_1 - E_n} \right|^2 \times \delta((\omega_1 - \omega_2) - E_f),
\end{aligned}
\tag{3.16}
$$

---

[1]With other boundary conditions, the transition rate of other spectroscopies can be calculated. For example, the absorption rate is obtained with $|F\rangle = |f, 0\rangle$

where we have used that the energies are given by $E_I = E_0 + \omega_1$ where E_0 is the energy of the initial electronic system, $E_N = E_n$, where E_n is the energy of the intermediate electronic system, and $E_F = E_f + \omega_2$, where E_f is the energy of the final electronic state. Furthermore, before the scattering process the electronic system is in the groundstate, such that $|i\rangle = |0\rangle$ and $E_i = 0$. We now employ Eqs. 3.3 to obtain the double differential cross section. For photons, the dispersion relation is $E_2(\mathbf{K}_2) = c\mathbf{K}_2$ and the initial current is $j_1 = \frac{N_0 c}{V}$. This yields the double differential cross section as

$$
\frac{\mathrm{d}^2\sigma}{\mathrm{d}\Omega_2 \mathrm{d}\omega_2} = \alpha^4 \left(\frac{\omega_2}{\omega_1}\right) \sum_f \left| \langle f | \mathbf{e}_1 \cdot \mathbf{e}_2^* \sum_j \mathrm{e}^{\mathrm{i}\mathbf{Q}\mathbf{r}_j} |0\rangle \right.
$$
$$
\left. + \sum_n \frac{\langle f | \sum_j \mathrm{e}^{-\mathrm{i}\mathbf{K}_2\mathbf{r}_j} \mathbf{e}_2^* \cdot \mathbf{p}_j |n\rangle \langle n | \mathrm{e}^{\mathrm{i}\mathbf{K}_2\mathbf{r}_j} \mathbf{e}_1 \cdot \mathbf{p}_j |0\rangle}{\omega_1 - E_n} \right|^2 \times \delta((\omega_1 - \omega_2) - E_f).
$$

(3.17)

This expression, known as the generalized Kramers-Heisenberg formula [171, 173], contains the two scattering processes that occur up to second order in non-magnetic materials: the first term represents the *Non-Resonant Inelastic Scattering* (NRIXS), the second term the *Resonant Inelastic Scattering* (RIXS).

3.2 Non-Resonant Inelastic X-ray Scattering Spectroscopy

For excitation energies ω_1 far from any excitation energies E_n of the system, the resonant term in Eq. 3.17 vanishes and the double differential cross section becomes

$$
\frac{\mathrm{d}^2\sigma}{\mathrm{d}\Omega_2 \mathrm{d}\omega_2} = \alpha^4 \left(\frac{\omega_2}{\omega_1}\right) |\mathbf{e}_1 \cdot \mathbf{e}_2^*|^2 \sum_f \sum_{jj'} \langle i | \mathrm{e}^{-\mathrm{i}\mathbf{Q}\mathbf{r}_j} |f\rangle \langle f | \mathrm{e}^{\mathrm{i}\mathbf{Q}\mathbf{r}_{j'}} |i\rangle \delta(\omega - E_f)
$$
$$
= \left(\frac{\mathrm{d}\sigma}{\mathrm{d}\Omega_2}\right)_{\mathrm{Th}} \sum_f \sum_{jj'} \langle i | \mathrm{e}^{-\mathrm{i}\mathbf{Q}\mathbf{r}_j} |f\rangle \langle f | \mathrm{e}^{\mathrm{i}\mathbf{Q}\mathbf{r}_{j'}} |i\rangle \delta(\omega - E_f),
$$

(3.18)

where the prefactors are gathered in the Thompson cross section $\left(\frac{\mathrm{d}\sigma}{\mathrm{d}\Omega_2}\right)_{\mathrm{Th}} = \alpha^4 \left(\frac{\omega_2}{\omega_1}\right) |\mathbf{e}_1 \cdot \mathbf{e}_2|$ and we have define the energy loss $\omega = \omega_1 - \omega_2$. The many-body operator $\hat{D} = \sum_j \exp\left(\mathrm{i}\mathbf{Q}\mathbf{r}_j\right)$ can be represented in the quasi-particle basis with the quasiparticle wavefunctions $\psi_{i\mathbf{k}}^{QP}(\mathbf{r})$ of Eq. 1.57. With $\hat{c}_{i\mathbf{k}}$ and $\hat{c}_{i\mathbf{k}}^{\dagger}$ as the annihilation and creation operator,

respectively, the operator is expressed as

$$
\begin{aligned}
\hat{D} &= \sum_{mn} \sum_{\mathbf{kk'}} \langle m\mathbf{k}|e^{i\mathbf{Qr}}|n\mathbf{k'}\rangle \hat{c}_{m\mathbf{k}}\hat{c}_{n\mathbf{k'}}^{\dagger} \\
&= \sum_{mn} \sum_{\mathbf{k}} M_{mn\mathbf{k}}(-\mathbf{G}-\mathbf{q})\hat{c}_{m\mathbf{k}}^{\dagger}\hat{c}_{n(\mathbf{k}-\mathbf{q})} \\
&= \sum_{mn} \sum_{\mathbf{k}} M_{nm(\mathbf{k}-\mathbf{q})}^{*}(\mathbf{G}+\mathbf{q})\hat{c}_{m\mathbf{k}}^{\dagger}\hat{c}_{n(\mathbf{k}-\mathbf{q})},
\end{aligned}
\tag{3.19}
$$

where we have used that any reciprocal vector can be expressed as $\mathbf{Q} = \mathbf{G} + \mathbf{q}$, with a reciprocal lattice vector $\mathbf{G}$ and a vector $\mathbf{q}$ from the 1st Brillouin zone. We furthermore introduce the plane-wave matrix elements $M_{fi\mathbf{k}_f}(\mathbf{G}+\mathbf{q})$ as

$$
M_{fi\mathbf{k}_f}(\mathbf{G}+\mathbf{q}) = \langle f\mathbf{k}|e^{-i(\mathbf{G}+\mathbf{q})\mathbf{r}}|i(\mathbf{k}_f+\mathbf{q})\rangle_{V_0}.
\tag{3.20}
$$

In this definition, $\langle ..|..|..\rangle_{V_0}$ indicates that the integral of the expectation value is only performed in the unit cell with volume V_0. Any plane-wave expectation value can then be expressed as $\langle m\mathbf{k}|\exp\left(-i(\mathbf{G}+\mathbf{q})\mathbf{r}\right)|n\mathbf{k'}\rangle = M_{mn\mathbf{k}}(\mathbf{G}+\mathbf{q})\delta_{\mathbf{k'}(\mathbf{k}+\mathbf{q})}$. We now insert the form of the operator of Eq. 3.19 into Eq. 3.18. The δ-function $\delta(\omega - E_f)$, which ensures the energy conservation of the total process, is expressed as

$$
\delta(\omega - E_f) = \lim_{\eta \to 0^+} -\frac{1}{\pi}\text{Im}\,\frac{1}{\omega - E_f + i\eta}
\tag{3.21}
$$

using the Sokhotski-Plemelj theorem. This yields

$$
\frac{d^2\sigma}{d\Omega_2 d\omega_2} = -\frac{1}{\pi}\left(\frac{d\sigma}{d\Omega_2}\right)_{Th}\text{Im}\sum_{ij\mathbf{k}}\sum_{i'j'\mathbf{k'}}
$$

$$
M_{ij\mathbf{k}}(\mathbf{G}+\mathbf{q})\left[\sum_f \frac{\langle 0|\hat{c}_{i\mathbf{k}}^{\dagger}\hat{c}_{j(\mathbf{k}+\mathbf{q})}|f\rangle\langle f|\hat{c}_{i'\mathbf{k'}}^{\dagger}\hat{c}_{j'(\mathbf{k'}-\mathbf{q'})}|0\rangle}{\omega - E_f + i\eta}\right]M_{j'i'(\mathbf{k'}-\mathbf{q'})}^{*}(\mathbf{G}+\mathbf{q}).
\tag{3.22}
$$

The central bracket in Eq. 3.22 is identical to the matrix elements $\chi_{ij\mathbf{k},i'j'\mathbf{k'}}(\mathbf{q},\omega)$ of the polarizability in Eq. 2.26. This allows us to express Eq. 3.22 as

$$
\begin{aligned}
\frac{d^2\sigma}{d\Omega_2 d\omega_2} &= -\frac{1}{\pi}\left(\frac{d\sigma}{d\Omega_2}\right)_{Th}\text{Im}\sum_{ij\mathbf{k}}\sum_{j'i'\mathbf{k'}}M_{ij\mathbf{k}}(\mathbf{G}+\mathbf{q})\chi_{ij\mathbf{k},j'i'\mathbf{k'}}(\mathbf{q},\omega)M_{j'i'\mathbf{k'}}^{*}(\mathbf{G}+\mathbf{q}) \\
&= -\frac{1}{\pi}\left(\frac{d\sigma}{d\Omega_2}\right)_{Th}\text{Im}\,\chi_{\mathbf{GG}}(\mathbf{q},\omega),
\end{aligned}
\tag{3.23}
$$

where we have introduced the Fourier components $\chi_{GG}(\mathbf{q}, \omega)$ of the polarizability following Eq. A.15. Additionally, we have shifted the summation over $\mathbf{k}'$, such that $\mathbf{k}' \to \mathbf{k}' + \mathbf{q}$ without loss of generality. Using the relation $\epsilon_{GG}^{-1} = 1 + v_G(\mathbf{q}) \chi_{GG}(\mathbf{q}, \omega)$ and the fact that the Fourier components $v_G(\mathbf{q})$ are real-valued, the double-differential cross section can be expressed in terms of the inverse dielectric function as

$$\frac{d^2\sigma}{d\Omega_2 d\omega_2} = -\frac{1}{\pi} \left(\frac{d\sigma}{d\Omega_2} \right)_{Th} v_G^{-1}(\mathbf{q}) \text{Im } \epsilon_{GG}^{-1}(\mathbf{q}, \omega). \tag{3.24}$$

Alternatively, the double-differential cross section is expressed in terms of the structure factor [169, 170] $S(\mathbf{G} + \mathbf{q}, \omega) = -\frac{1}{\pi} \text{Im } \chi_{GG}(\mathbf{q}, \omega)$ as

$$\frac{d^2\sigma}{d\Omega_2 d\omega_2} = \left(\frac{d\sigma}{d\Omega_2} \right)_{Th} S(\mathbf{G} + \mathbf{q}, \omega). \tag{3.25}$$

A more intuitive interpretation of Eq. 3.22 can be obtained by applying the quasiparticle approximation of Eq. 1.58, which restricts the sums over i and j' to valence, the sums over j and i' to conduction states. We thus obtain

$$\frac{d^2\sigma}{d\Omega_2 d\omega_2} = -\frac{1}{\pi} \left(\frac{d\sigma}{d\Omega_2} \right)_{Th} \text{Im} \sum_{c v \mathbf{k}} \sum_{c' v' \mathbf{k}'}$$

$$M_{vc\mathbf{k}}(\mathbf{G} + \mathbf{q}) \left[\sum_f \frac{\langle 0 | \hat{c}_{v\mathbf{k}}^\dagger \hat{c}_{c(\mathbf{k}+\mathbf{q})} | f \rangle \langle f | \hat{c}_{c'(\mathbf{k}'+\mathbf{q})}^\dagger \hat{c}_{v'\mathbf{k}'} | 0 \rangle}{\omega - E_f + i\eta} \right] M_{v'c'\mathbf{k}'}^*(\mathbf{G} + \mathbf{q}). \tag{3.26}$$

In the quasiparticle approximation, the double-differential cross section is therefore determined by the matrix elements $\chi_{cv\mathbf{k},c'v'\mathbf{k}'}^{R1}(\mathbf{q}, \omega)$ of Eq. 2.28 between transitions $v\mathbf{k} \to c(\mathbf{k} + \mathbf{q})$ and $v'\mathbf{k}' \to c'(\mathbf{k}' + \mathbf{q})$. The details of the matrix representation are discussed in Appendix A. Equation 3.26 then becomes

$$\frac{d^2\sigma}{d\Omega_2 d\omega_2} = -\frac{1}{\pi} \left(\frac{d\sigma}{d\Omega_2} \right)_{Th} \text{Im} \sum_{c v \mathbf{k}} \sum_{c' v' \mathbf{k}'} M_{vc\mathbf{k}}(\mathbf{G} + \mathbf{q}) \chi_{cv\mathbf{k},c'v'\mathbf{k}'}^{R1}(\mathbf{q}, \omega) M_{v'c'\mathbf{k}'}(\mathbf{G} + \mathbf{q}). \tag{3.27}$$

3.3 Electron Energy-Loss Spectroscopy

The non-resonant inelastic x-ray scattering is closely related to the scattering of high-energy electrons [169, 174], as probed in electron energy-loss spectroscopy (EELS). Instead of considering the total Hamiltonian of the electronic system and the photonic field of

Eq. 3.4, we start with the Hamiltonian for the electronic system with an additional fast-moving electron in a plane-wave state with momentum $\mathbf{K}$:

$$
\begin{aligned}
\hat{H} &= \hat{H}_0 + \sum_j \frac{1}{|\mathbf{r} - \mathbf{r}_j|} + \frac{\mathbf{K}^2}{2} \\
&= \hat{H}_0 + \hat{H}_i + \hat{H}_e,
\end{aligned}
\tag{3.28}
$$

where $\hat{H}_0$ is the Hamiltonian of the electronic system, $\hat{H}_e = \frac{\mathbf{K}^2}{2}$ is the Hamiltonian of the probing electron with momentum $\mathbf{K}$, and $\hat{H}_i = \sum_j 1/|\mathbf{r} - \mathbf{r}_j|$ is the interaction Hamiltonian with $\mathbf{r}$ being the position of the probing electron. Here, we assume that the probing electron is scattered from the initial plane-wave state $|\mathbf{K}_1\rangle$ to the final plane-wave one $|\mathbf{K}_2\rangle$, such that the wavefunctions of both states are known. To first order, the transition rate of Eq. 3.14 of scattering is given by

$$
w = 2\pi \sum_F \left| \langle F|\hat{H}_i|I\rangle \right|^2 \delta(E_I - E_F).
\tag{3.29}
$$

Since the wavefunction of the probing, high-energy electron $|\mathbf{K}_1\rangle = \frac{1}{\sqrt{V}} e^{i\mathbf{K}_1\mathbf{r}}$ is known, we can express the expectation value of the interaction Hamiltonian as

$$
\begin{aligned}
\langle F|\hat{H}_i|I\rangle &= \frac{1}{V}\langle f| \sum_j \langle \mathbf{K}_1| \frac{1}{|\mathbf{r} - \mathbf{r}_j|} |\mathbf{K}_0\rangle |i\rangle \\
&= \frac{1}{V}\langle f| \sum_j \int d^3r \frac{e^{i\mathbf{Q}\mathbf{r}}}{|\mathbf{r} - \mathbf{r}_j|} |i\rangle = \frac{4\pi}{V\mathbf{Q}^2} \langle f| \sum_j e^{i\mathbf{Q}\mathbf{r}_j} |i\rangle,
\end{aligned}
\tag{3.30}
$$

where we have inserted the Fourier transform of the Coulomb potential in the last line of Eq. 3.30. To obtain the double-differential cross section for electron scattering, we insert the dispersion of the electronic state, $E_2(\mathbf{K}_2) = \frac{\hbar^2\mathbf{K}_2^2}{2m}$, and the initial current of electrons $j_1 = \frac{N_0}{V} \frac{\hbar K_1}{m}$ into Eq. 3.3. This yields

$$
\frac{d^2\sigma}{d\Omega_2 d\omega_2} = \left(\frac{d\sigma}{d\Omega_2} \right)_R \sqrt{\frac{\omega_1}{\omega_2}} \sum_f \sum_{jj'} \langle i|e^{-i\mathbf{Q}\mathbf{r}_j}|f\rangle\langle f|e^{i\mathbf{Q}\mathbf{r}_{j'}}|i\rangle \delta(\omega - E_f),
\tag{3.31}
$$

with $\left(\frac{d\sigma}{d\Omega_2} \right)_R = \frac{4}{\mathbf{Q}^4}$. Comparing Eqs. 3.31 and 3.18, it becomes apparent that electron energy-loss spectroscopy and non-resonant inelastic x-ray scattering probe the same electronic excitations, albeit with different pre-factors which originate from the different interaction Hamiltonians. As such, we can use the derivation of the previous section to express the EELS cross section in terms of the inverse dielectric function, analogously to the expression

found in Eq. 3.24:

$$\frac{\mathrm{d}^2\sigma}{\mathrm{d}\Omega_2\mathrm{d}\omega_2} = -\frac{1}{\pi}\left(\frac{\mathrm{d}\sigma}{\mathrm{d}\Omega_2}\right)_R \sqrt{\frac{\omega_2}{\omega_1}} v_G^{-1}(\mathbf{q})\mathrm{Im}\,\epsilon_{GG}^{-1}(\mathbf{q},\omega). \tag{3.32}$$

A main difference between NRIXS and EELS arises from the $\mathbf{Q}$-dependence of the prefactors: For $\mathbf{Q} = 0$, the NRIXS signal vanishes, since $\left(\frac{\mathrm{d}\sigma}{\mathrm{d}\Omega_2}\right)_{Th} v_{G=0}^{-1}(\mathbf{q} = 0) = 0$, while for the EELS signal $\left(\frac{\mathrm{d}\sigma}{\mathrm{d}\Omega_2}\right)_R v_G^{-1}(\mathbf{q}) \propto \mathbf{Q}^{-2}$. As such, the forward-scattering rate in EELS does not vanish.
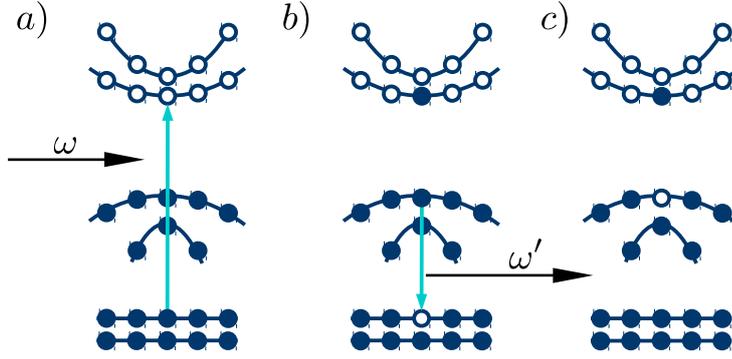
Figure 3.1: Schema of RIXS processes described by Eq. 5.7: The a) absorption of an x-ray photon with energy ω_1 leads to b) an excited state with a core hole, which through the emission of an x-ray photon with energy ω_2 yields c) an excited state with a valence hole. Filled and open circles represent occupied and unoccupied states, respectively. Blue lines indicate transitions, while black lines denote x-ray absorption and emission.

3.4 Resonant Inelastic X-ray Scattering

In the previous section, only the non-resonant part of the Kramers-Heisenberg formula in Eq. 3.17 was considered. If the excitation energy ω_1 is in resonance with an excitation energy E_n of the electronic system[2], the resonant term of Eq. 3.17 dominates. In this case, the non-resonant part can be neglected and we obtain

$$\frac{\mathrm{d}^2\sigma}{\mathrm{d}\Omega_2\mathrm{d}\omega_2} = \alpha^4 \left(\frac{\omega_2}{\omega_1}\right) \sum_f \left| \sum_n \frac{\langle f|\hat{T}^\dagger(\mathbf{e}_2, \mathbf{K}_2)|n\rangle\langle n|\hat{T}(\mathbf{e}_1, \mathbf{K}_1)|i\rangle}{\omega_1 - E_n + \mathrm{i}\eta} \right|^2 \delta(\omega_1 - \omega_2 - E_f), \quad (3.33)$$

where we define here the transition operator $\hat{T}(\mathbf{e}, \mathbf{K}) = \sum_j \mathbf{e} \cdot \mathbf{p}_j \exp\left(i\mathbf{K}\mathbf{r}_j\right)$. The microscopic resonant scattering process is schematically shown in Fig. 3.1 for a semiconducting or insulating system: The absorption of the initial x-ray photon with energy ω_1 excites a core electron into the conduction band, leaving a core hole behind. The intermediate system, after the excitation, is in an excited many-body state $|n\rangle$ in Eq. 3.33. The core hole can now be filled by a valence electron, which loses the energy ω_2 by emitting a x-ray photon. In the final many-body state $|f\rangle$, a hole is present in a valence state and an excited electron in a conduction state. While both the absorbed and emitted photon have energies in the x-ray region, the difference between them, *i.e.* the energy loss $\omega_1 - \omega_2$, is typically in the range of several eV. The final excited many-body states of the RIXS process correspond to the excited states of optical absorption. The schema of the RIXS process in Fig. 3.1 completely

---

[2]Note that throughout this thesis, $E_0 = 0$ for the electronic groundstate without loss of generality.

neglects many-body effects, *i.e.* the relaxation of the electronic system due to the presence of the excited electron and the hole, as well as the quantum-mechanical interaction of the excited electron and the core hole. This inherent complexity of the microscopic RIXS process poses challenges for any theoretical description, as both the effects of electron-hole interaction, as well as the coherence of the RIXS process have to be included.
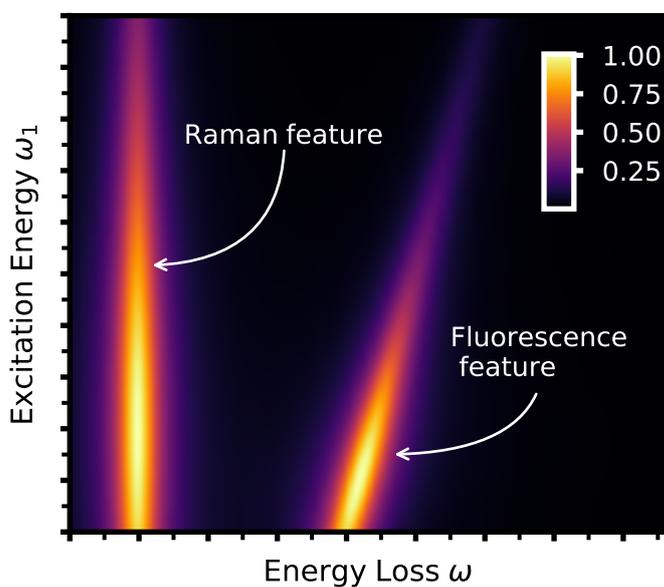
3.4.1 Raman and Fluorescence Features in RIXS

Figure 3.2: Schematical RIXS double-differential cross section as a function of the energy loss ω and excitation energy ω_1. Prototypical Raman and fluorescence features are shown.

The double differential cross section $d^2\sigma/d\Omega_2 d\omega_2$ is a function of both the excitation energy ω_1 and the energy loss $\omega = \omega_1 - \omega_2$. Alternatively, the cross section can be expressed as a function of the excitation energy ω_1 and the emission energy ω_2. Generally, two different groups of features in the RIXS cross section, denoted *Raman* and *Fluorescence* features, can be identified [175–177]. Raman features occur at an energy loss ω independent of the excitation energy ω_1. As such, they appear as vertical features in the $\omega - \omega_1$ plane in Fig. 3.2. The constant energy loss implies that the Raman features are due to scattering processes to the same final state independent of the excitation energy. For fluorescence features, on the other hand, the energy loss ω increases linearly with the excitation energy ω_1 in Fig. 3.2. Fluorescence features occur at constant emission energy $\omega_2 = \omega_1 - \omega$ with increasing excitation energy. We note that the schematics in Fig. 3.2 is highly idealized. For both Raman and fluorescence features, the intensity of the features can be a function of the excitation energy. Fluorescence with non-linear dispersion have been observed in the RIXS spectra of solids [178]. Additionally, the features can have fine structures that depend on both the excitation energy and the energy loss. The non-linear dispersion, the change of intensity, and the fine structure can hamper the distinction between Raman and fluorescence features.
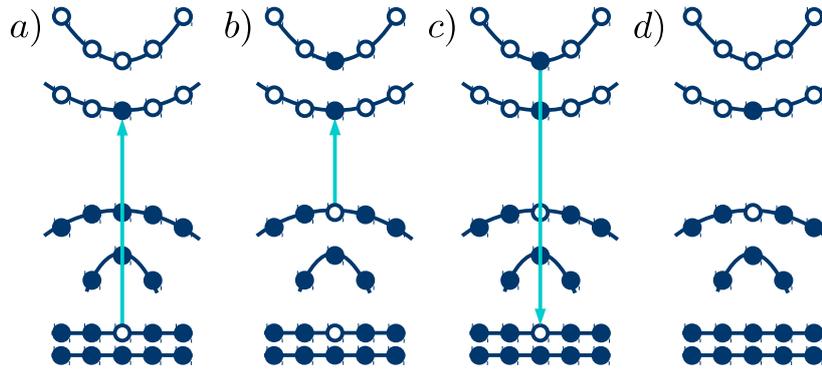
Figure 3.3: Schema of the indirect RIXS process: The a) absorption of an x-ray photon leads to b) an excitation of the core electron to a high-energy conduction state. Through scattering with the core-hole potential, a valence electron-hole pair is created. The c) subsequent de-excitation of the excited electron fills the core-hole. The d) final state of the scattering contains the valence electron-hole pair.

3.4.2 Direct and Indirect RIXS

The schema of RIXS presented in Fig. 3.1 ignores any effects of electron-hole interaction, both for the intermediate and the final state of the resonant scattering. This interaction of the excited electron and the core hole in the intermediate state renormalizes the energy E_n of the intermediate state in Eq. 3.33, the interaction between the excited electron and the valence hole that of the final state E_f. Additionally, the oscillator strength of the scattering is renormalized due to the electron-hole correlation. The excitation from the core state generates an intermediate many-body state where the excited electron is distributed in the conduction band, but due to the electron-hole interaction it is not in a well-defined single-particle state. The subsequent de-excitation of a valence electron yields the final state, which contains the excited electron distributed in the conduction bands and the hole distributed in the valence band. As in the intermediate many-body state, the electron and the valence hole do not occupy a well-defined single-particle state due to the electron-hole interaction. We denote resonant scattering that follows this schema as *direct RIXS* [175]. The direct RIXS requires that both the excitation from the core state to the conduction band, as well as the de-excitation from the valence band to the core state are dipole-allowed.

While the direct RIXS occurs already in the independent-particle approximation (IPA), a qualitatively different kind of resonant scattering is induced by the electron-hole interaction in the intermediate state. In this process, schematically shown in Fig. 3.3, the electron is excited to a high-energy conduction band by the absorption of the initial x-ray photon. In the intermediate state, the strong electron-core-hole interaction leads to the creation of an electron-hole pair where the electron is found in a low-energy conduction band and the

hole in the valence band. As such, the intermediate state contains two electron-hole pairs. The final state of the scattering is reached by the de-excitation of the high-energy electron, which fills the core hole. The final state again contains a valence electron-hole pair. This kind of resonant scattering is denoted as *indirect RIXS* [175, 179]. Indirect RIXS occurs mainly, when the transitions from the core state to the bottom of the conduction band are dipole-forbidden. It has been observed for example at the Mn K edge $LaMnO_3$ [180] and the Ni K edge in NiO and $NiCl_2$ [179].

Part II

Method Development and Implementation

CHAPTER 4

A Brief History of BSE Calculations

The Bethe-Salpeter equation (BSE) was first derived for excitations in solids by Sham and Rice in 1966 [181], providing an *ab initio* foundation for previous semi-empirical models. It was successively employed for the calculation of exciton binding energies in core [182, 183] and optical [184–187] spectra of model systems, and of real materials using tight-binding models [187–190]. The first fully *ab initio* results for exciton binding energies were presented in 1995 for sodium clusters by Onida and coworkers [58] and for crystalline Li_2O by Albrecht and coworkers [59]. Full *ab initio* optical absorption spectra were first calculated by Albrecht and coworkers [141, 191], Benedict and coworkers [139, 142], and Rohlfing and Louie [61, 138]. Shortly afterwards, BSE calculations of the optical absorption spectra and exciton binding energies were performed for molecular crystals [192–201]. Later, the approach was extended to determine excitations in molecules [199, 202]. The first core-level excitation spectra for solids were calculated within the BSE formalism by Shirley [203], Soinen [204], and Rehr [205]. This approach was later extended to describe x-ray scattering spectroscopy as well [206]. A BSE approach to RIXS has been presented by Shirley and co-workers [206–208] and by Vinson [209–211].

Most implementations of the BSE formalism make use of a plane-wave basis representation for the underlying electronic structure [212–221], where the wavefunctions and energies for the valence and conduction bands are explicitly calculated, while the effects of the remaining strongly-bound core states are implicitly included in the so-called *pseudopotential* [222–224]. As such, the valence and conduction pseudowavefunctions from these calculation are not identical to their all-electron counterparts. The difference between the wavefunctions is especially pronounced close to the nuclear positions [225]. Therefore, the pseudopotential implementations require approximations to the all-electron wavefunctions to determine XANES and RIXS spectra. Most BSE calculations of XANES [203, 206, 226] and RIXS spectra [206, 210, 227] rely on approximations to the all-electron wavefunctions by the projector augmented wave (PAW) expansion [178, 228–230]. The core states are calculated from atomic-structure codes in the *frozen core* approximation [231], *i.e.* it is assumed that the core energies and wavefunctions in the solid are identical to the ones of the free atom.

All-electron full-potential methods on the other hand, in particular those employing the LAPW+lo basis [232–235], treat core and valence electrons on the same footing, *i.e.* the

energies and wavefunctions of all electronic states, from the core region to the conduction states, are obtained without any approximation to the crystal potential. The first implementation of the BSE approach in an all-electron LAPW+lo framework was presented in 2002 by Puschnig and Ambrosch-Draxl [225] for optical excitations. Subsequently, it was applied to determine optical [198, 201, 236, 237] and core absorption spectra [45, 238–245] in solids and molecular crystals. While, in principle, an all-electron full-potential implementation of the BSE approach can consistently generate optical and core excitation spectra, existing implementations have either treated core states as deep valence ones, and were thus limited to shallow core excitations [241], such as those from the beryllium $1s$ states [244], aluminium $2p$ states [243], lithium $1s$ states [241], or the oxygen $1s$ states [45]. Other all-electron studies have focused solely on core excitations [238, 239].

From a computational point of view, solving the BSE is a cumbersome problem (compare Section 2.2.1 and Chapter 6), and several approaches to reduce the numerical workload have been proposed. Iterative [142, 149, 246, 247] and evolution schemes [248] avoid the computationally expensive diagonalization, while other approaches employ the inherent structure of the BSE problem [146, 360] to reduce the computational effort. Due also to these important efforts, the BSE approach has become the state of the art for the calculation of neutral excitations in solids, and implementations are available in a number of codes. Plane-wave codes such as (in alphabetical order) `BerkeleyGW` [249], `EXC` [250] (also included in `Abinit` [251]), `WEST` [252], and `yambo` [215, 216] enable calculations of optical excitations, and `OCEAN` [226, 228] those of core-level excitations. All-electron implementations are available in `exciting` [253, 254] and `WIEN2k` [225]. Additionally, a number of codes allow BSE calculations for molecular systems, such as `FHI-aims` [255, 256], `FIESTA` [257], `molgw` [258], `rgwbs` [259], and `turbomol` [260].

In this thesis, we have generalized the existing BSE implementation [239, 253] in the all-electron full-potential code `exciting` [254] to enable consistent calculations of electronic excitations with arbitrary momentum transfer and arbitrary excitation energies from the hard x-ray to the optical region. The development is based on our previous all-electron full-potential BSE implementation for core excitations [239], and from the one of Benjamin Aurich for optical excitations at finite momentum transfer [261]. Our development provides several benefits: It allows for a consistent study of core and optical excitations in a given material, where inconsistencies or even misinterpretations due to different treatments of the electronic structures or the solution of the BSE in the two regimes are avoided. Additionally, it is a starting point for our all-electron full-potential implementation of resonant-inelastic x-ray scattering (RIXS). We have derived a novel expression of the RIXS cross section within many-body perturbation theory and implemented in an all-electron full-potential framework. This new expression provides a powerful analysis tool to resolve the origin and the making of a RIXS spectrum. It allows us to determine what the most important contributions are, how they interfere, why spectral features may be masked, and more. By offering an intuitive interpretation of the RIXS process, our formalism represents a significant step

forward in the overall understanding of RIXS.

In the following chapters, we describe how we have extended the range of the BSE approach within the all-electron framework: In Chapter 5, we derive the RIXS cross section including many-body effects. In Chapter 6, we present our novel all-electron full-potential BSE implementation for optical and x-ray absorption and scattering spectra. The latter chapter describes work performed in close collaboration with Benjamin Aurich, and the chapter itself is based on our joint publication [359]. In Chapter 7, we present our implementation for the RIXS cross section, based on the derivation of Chapter 5. We describe how it allows for accurate calculations of RIXS spectra in solids, while also providing an intuitive interpretation of the RIXS process. Finally, in Chapter 8, we demonstrate these capabilities with selected examples.

Many-body Approach to Resonant Scattering

In this chapter, we derive a novel expression for the RIXS cross section in terms of selected matrix elements of the polarizability. To do so, we first reconsider the RIXS cross section within the independent-particle approximation (IPA). The derivation within this approximation then informs our derivation that includes many-body effects in the scattering process. Finally, we show how the cross section of non-resonant x-ray emission spectroscopy (XES) is obtained as a limiting case of our RIXS expression.

5.1 Independent-particle Approximation

It is instructive to discuss the RIXS process within the independent-particle approximation (IPA) before the scattering in the fully interactive system is considered. In the independent-particle approximation, the many-body ground-state wavefunction is given by a single Slater determinant, and both the intermediate many-body state $|n\rangle$ and the final one $|f\rangle$ are singlet excitations of the groundstate without any relaxation of the system. We know *a priori* that the intermediate states contain a core hole $\mu\mathbf{k}$ and an excited electron in a conduction state $c(\mathbf{k}+\mathbf{q}_1)$, such that we can express them in second quantization as $|n\rangle = |c(\mathbf{k}+\mathbf{q}_1)\mu\mathbf{k}\rangle = \hat{c}^\dagger_{c(\mathbf{k}+\mathbf{q}_1)}\hat{c}_{\mu\mathbf{k}}|0\rangle$. These intermediate states have a total energy $E_n = \epsilon_{c(\mathbf{k}+\mathbf{q}_1)} - \epsilon_{\mu\mathbf{k}}$. Furthermore, the final states contain in the IPA an excited electron in a specific conduction state $c'(\mathbf{k}'+\mathbf{q}_2)$ and a valence hole in the state $v\mathbf{k}'$, such that $|f\rangle = |c'(\mathbf{k}'+\mathbf{q}_2)v\mathbf{k}'\rangle = \hat{c}^\dagger_{c'(\mathbf{k}'+\mathbf{q}_2)}\hat{c}_{v\mathbf{k}'}|0\rangle$ and $E_f = \epsilon_{c'(\mathbf{k}'+\mathbf{q}_2)} - \epsilon_{v\mathbf{k}'}$. Here, we have introduced the momentum transfers $\mathbf{q}_1$ and $\mathbf{q}_2$ as the projection of the photon momentum on the first Brillouin zone, *i.e.* $\mathbf{K}_1 = \mathbf{G}_1 + \mathbf{q}_1$ and $\mathbf{K}_2 = \mathbf{G}_2 + \mathbf{q}_2$, where $\mathbf{G}_1$ and $\mathbf{G}_2$ are reciprocal lattice vectors. We assume that the interme-

diate and the final states have the same lifetime broadening η. Then, Eq. 3.33 becomes

$$\frac{\mathrm{d}^2\sigma}{\mathrm{d}\Omega_2\mathrm{d}\omega_2}\bigg|_{IP} = \alpha^4 \left(\frac{\omega_2}{\omega_1}\right) \sum_{\underbrace{c'v\mathbf{k}'}_{f}} \left| \sum_{\underbrace{c\mu\mathbf{k}}_{n}} \frac{\langle c'(\mathbf{k}'+\mathbf{q}_2)v\mathbf{k}'|\hat{T}^\dagger(\mathbf{e}_2)|c(\mathbf{k}+\mathbf{q}_1)\mu\mathbf{k}\rangle\langle c(\mathbf{k}+\mathbf{q}_1)\mu\mathbf{k}|\hat{T}(\mathbf{e}_1)|0\rangle}{\omega_1 - (\epsilon_{c(\mathbf{k}+\mathbf{q}_1)} - \epsilon_{\mu\mathbf{k}}) + \mathrm{i}\eta} \right|^2 \times$$

$$\times \delta(\omega - (\epsilon_{c'(\mathbf{k}'+\mathbf{q}_2)} - \epsilon_{v\mathbf{k}'})), \tag{5.1}$$

where we have introduced the energy loss $\omega = \omega_1 - \omega_2$. In the following, we employ the *dipole approximation, i.e.* the momenta $\mathbf{K}_1$ and $\mathbf{K}_2$ of the incoming and scattered photon are assumed to be small compared to the momenta of the electrons involved in the absorption and emission process. This approximation is typically employed in the calculation of x-ray absorption and emission spectroscopy. The approximation allows us to express the transition operator of Eq. 3.33 as $\hat{T}(\mathbf{e}) = \mathbf{e}\sum_j \mathbf{p}_j \exp(\mathrm{i}\mathbf{K}\mathbf{r}) \approx \mathbf{e}\sum_j \mathbf{p}_j$, where the summation over j includes all electrons in the system. We now insert the expression for the transition operator $\hat{T}$ in second quantization, analogously to the scattering operator $\hat{D}$ in Eq. 3.19:

$$\hat{T} = \mathbf{e}_1 \sum_{mn} \sum_{\mathbf{k}\mathbf{k}'} \langle m\mathbf{k}|\mathbf{p}|n\mathbf{k}'\rangle \hat{c}_{m\mathbf{k}}^\dagger \hat{c}_{n\mathbf{k}'} = \mathbf{e}_1 \sum_{mn} \sum_{\mathbf{k}\mathbf{k}'} \langle m\mathbf{k}|\mathbf{p}|n\mathbf{k}'\rangle_{V_0} \delta_{\mathbf{k}\mathbf{k}'} \hat{c}_{m\mathbf{k}}^\dagger \hat{c}_{n\mathbf{k}'}$$

$$= \sum_{mn} \sum_{\mathbf{k}} \mathbf{e}_1 \cdot \mathbf{P}_{mn\mathbf{k}} \hat{c}_{m\mathbf{k}}^\dagger \hat{c}_{n\mathbf{k}}, \tag{5.2}$$

where we have introduced the momentum matrix elements $\mathbf{P}_{mn\mathbf{k}} = \langle m\mathbf{k}|\mathbf{p}|n\mathbf{k}\rangle_{V_0}$. Inserting Eq. 5.2 into Eq. 3.33, we obtain

$$\frac{\mathrm{d}^2\sigma}{\mathrm{d}\Omega_2\mathrm{d}\omega_2}\bigg|_{IP} = \sum_{c'v\mathbf{k}'} \left| \sum_{c\mu\mathbf{k}} \sum_{mn\mathbf{k}''} \sum_{pq\mathbf{k}'''} \left[\mathbf{e}_2^* \cdot \mathbf{P}_{mn\mathbf{k}''}\right] \times \right.$$

$$\times \frac{\langle c'v\mathbf{k}'|\hat{c}_{m\mathbf{k}''}^\dagger \hat{c}_{n\mathbf{k}''}|c\mu\mathbf{k}\rangle\langle c\mu\mathbf{k}|\hat{c}_{p\mathbf{k}'''}^\dagger \hat{c}_{q\mathbf{k}'''}|0\rangle}{\omega_1 - (\epsilon_{c\mathbf{k}} - \epsilon_{\mu\mathbf{k}}) + \mathrm{i}\eta} \left[\mathbf{P}_{pq\mathbf{k}'''} \cdot \mathbf{e}_1\right] \Bigg|^2 \times \tag{5.3}$$

$$\times \delta(\omega - (\epsilon_{c'\mathbf{k}'} - \epsilon_{v\mathbf{k}'})).$$

We note that the summations over p and q in Eq. 5.3 are not restricted to either core, valence, or conduction states. Restrictions to these indices can be inferred from to the matrix elements of the creation and annihilation operators. We find that

$$\langle c\mu\mathbf{k}|\hat{c}_{p\mathbf{k}'''}^\dagger \hat{c}_{q\mathbf{k}'''}|0\rangle = \langle 0|\hat{c}_{\mu\mathbf{k}}^\dagger \hat{c}_{c\mathbf{k}}\hat{c}_{p\mathbf{k}'''}^\dagger \hat{c}_{q\mathbf{k}'''}|0\rangle = \delta_{\mu q}\delta_{cp}\delta_{\mathbf{k}\mathbf{k}'''}. \tag{5.4}$$

The term $\langle c'v\mathbf{k}'|\hat{c}_{m\mathbf{k}''}^\dagger \hat{c}_{n\mathbf{k}''}|c\mu\mathbf{k}\rangle$ requires a more careful treatment. We can write it as

$$\langle c'v\mathbf{k}'|\hat{c}_{m\mathbf{k}''}^\dagger \hat{c}_{n\mathbf{k}''}|c\mu\mathbf{k}\rangle = \langle 0| \left[\hat{c}_{v\mathbf{k}'}^\dagger \hat{c}_{c'\mathbf{k}'}\right] \left[\hat{c}_{m\mathbf{k}''}^\dagger \hat{c}_{n\mathbf{k}''}\right] \left[\hat{c}_{c\mathbf{k}}^\dagger \hat{c}_{\mu\mathbf{k}}\right] |0\rangle \tag{5.5}$$

Using Wick's theorem [125], we can evaluate the expectation value and obtain:

$$\langle c'v\mathbf{k}|\hat{c}^{\dagger}_{m\mathbf{k}''}\hat{c}_{n\mathbf{k}''}|c\mu\mathbf{k}'\rangle = \underbrace{\delta_{v\mu}\delta_{cn}\delta_{c'm}\delta_{\mathbf{k}\mathbf{k}'}\delta_{\mathbf{k}\mathbf{k}''}}_{(a)} + \underbrace{\delta_{c'c}\delta_{mn}\delta_{v\mu}\delta_{\mathbf{k}\mathbf{k}'}\delta_{\mathbf{k}\mathbf{k}''}}_{(b)} - \underbrace{\delta_{c'c}\delta_{\mu m}\delta_{vn}\delta_{\mathbf{k}\mathbf{k}'}\delta_{\mathbf{k}\mathbf{k}''}}_{(c)} . \quad (5.6)$$

Inserting Eq. 5.6 into Eq. 5.3 yields the cross section as a sum of three terms with additional cross terms, since the cross section is given by the square of the sum. Ignoring interference terms, the double differential cross section in the IPA has the following contributions,

$$\frac{\mathrm{d}^2\sigma}{\mathrm{d}\Omega_2\mathrm{d}\omega_2}\bigg|_{IP} = \alpha^4 \left(\frac{\omega_2}{\omega_1}\right) \begin{cases} \sum_{c'\mu\mathbf{k}} \left|\sum_c \frac{\mathbf{e}_2^*\cdot\mathbf{P}_{c'c\mathbf{k}}\mathbf{P}_{c\mu\mathbf{k}}\cdot\mathbf{e}_1}{\omega_1-(\epsilon_{c\mathbf{k}}-\epsilon_{\mu\mathbf{k}})+\mathrm{i}\eta}\right|^2 \delta(\omega-(\epsilon_{c'\mathbf{k}}-\epsilon_{\mu\mathbf{k}})) & (a) \\[2.5ex] + \sum_{c\mu\mathbf{k}} \left|\sum_m \frac{\mathbf{e}_2^*\cdot\mathbf{P}_{mm\mathbf{k}}\mathbf{P}_{c\mu\mathbf{k}}\cdot\mathbf{e}_1}{\omega_1-(\epsilon_{c\mathbf{k}}-\epsilon_{\mu\mathbf{k}})+\mathrm{i}\eta}\right|^2 \delta(\omega-(\epsilon_{c\mathbf{k}}-\epsilon_{\mu\mathbf{k}})) & (b) \\[2.5ex] + \sum_{cv\mathbf{k}} \left|\sum_\mu \frac{\mathbf{e}_2^*\cdot\mathbf{P}_{\mu v\mathbf{k}}\mathbf{P}_{c\mu\mathbf{k}}\cdot\mathbf{e}_1}{\omega_1-(\epsilon_{c\mathbf{k}}-\epsilon_{\mu\mathbf{k}})+\mathrm{i}\eta}\right|^2 \delta(\omega-(\epsilon_{c\mathbf{k}}-\epsilon_{v\mathbf{k}})) & (c) \end{cases} \quad (5.7)$$

each of the them corresponding to different physical processes. In the following, we will demonstrate that only one of them represents the RIXS process.

The physical process of term (a) in Eq. 5.7 is schematically shown in Fig. 5.1. The cross section has poles at excitation energies $\omega_1 = \epsilon_{c\mathbf{k}} - \epsilon_{\mu\mathbf{k}}$, where a core state $\mu\mathbf{k}$ is excited to a conduction state $c\mathbf{k}$. The poles in the emission energy occur at $\omega_2 = \epsilon_{c'\mathbf{k}} - \epsilon_{c\mathbf{k}}$, with the transition $c'\mathbf{k} \to c\mathbf{k}$ of the excited electron $c\mathbf{k}$ to a different conduction state $c'\mathbf{k}$ at the same $\mathbf{k}$-point. The final state contains a core hole in state $\mu\mathbf{k}$, which is created by the initial excitation, and the excited electron has scattered to a different conduction state $c'\mathbf{k}$. This process, shown in Fig. 3.1, does not correspond to RIXS. The final state still contains the initial core hole $\mu\mathbf{k}$, and the emission energy is typically within a few eV, due to the energy difference between two conduction electrons, such that the energy loss $\omega = \omega_1 - \omega_2$ is in the x-ray region.

The term (b) in Eq. 5.7 can be neglected, since it does not correspond to a resonant scattering process. Poles occur at excitation energies $\omega_1 = \epsilon_{c\mathbf{k}} - \epsilon_{\mu\mathbf{k}}$ and at emission energies $\omega_2 = 0$. The emission of photon occurs due to transitions $m\mathbf{k} \to m\mathbf{k}$ in Eq. 5.7b), where the sum over m includes all valence and conduction states. For each state $m\mathbf{k}$, the momentum matrix $P_{mm\mathbf{k}}$ vanishes, i.e. $P_{mm\mathbf{k}} = 0$, since the occupation factor $f_{m\mathbf{k}}$ has to be included in the matrix elements, such that $P_{mm\mathbf{k}} = f_{m\mathbf{k}}(1 - f_{m\mathbf{k}})\langle m\mathbf{k}|\mathbf{p}|m\mathbf{k}\rangle_{V_0}$. Both for valence electrons ($f_{m\mathbf{k}} = 1$) and for conduction electrons ($f_{m\mathbf{k}} = 0$), the matrix elements vanish.

The physical process of term (c) in Eq. 5.7 is schematically shown in Fig. 5.1. The cross section has poles at excitation energies $\omega_1 = \epsilon_{c\mathbf{k}} - \epsilon_{\mu\mathbf{k}}$ and at emission energies $\omega_2 = \epsilon_{v\mathbf{k}} - \epsilon_{\mu\mathbf{k}}$. This corresponds to an excitation $\mu\mathbf{k} \to c\mathbf{k}$ and subsequent de-excitation $v\mathbf{k} \to \mu\mathbf{k}$, where valence electron $v\mathbf{k}$ fills the core hole in $\mu\mathbf{k}$. In the final state, the system contains the
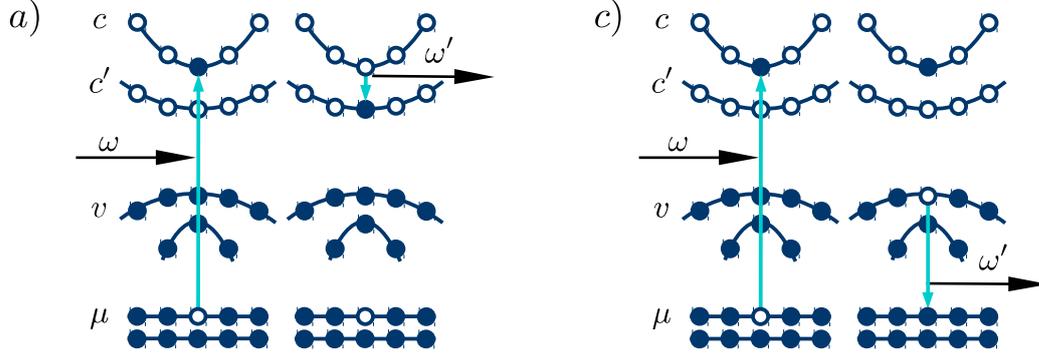
Figure 5.1: Schema of the processes that contribute to the RIXS cross section in Eq. 5.7. Filled and open circles represent occupied and unoccupied states, respectively. Vertical light blue lines indicate dipole transitions, while horizontal black lines indicates x-ray absorption and emission.

valence hole in the state $v\mathbf{k}$ and the excited electron in state $c\mathbf{k}$. Thus, this term corresponds to the RIXS process, as the initial core hole $\mu\mathbf{k}$ is filled. If the valence state $v\mathbf{k}$ is close to the Fermi energy, both the initial excitation energy ω_1 and the emission energy ω_2 are in the x-ray region, while the energy loss $\epsilon_{c\mathbf{k}} - \epsilon_{v\mathbf{k}}$ corresponds to an optical excitation energy.

This physical analysis of the cross sections resulting from the sum in Eq. 5.6 demonstrates that only one term yields the RIXS process. Neglecting cross terms, we can thus write

$$\langle cv\mathbf{k}|\hat{c}^{\dagger}_{m\mathbf{k}''}\hat{c}_{n\mathbf{k}''}|c'\mu\mathbf{k}'\rangle \approx -\delta_{cc'}\delta_{\mu m}\delta_{vn}\delta_{\mathbf{k}\mathbf{k}'}\delta_{\mathbf{k}\mathbf{k}''}. \tag{5.8}$$

The analysis also justifies why we neglect the cross terms in Eq. 5.7, because the different contributions have poles in vastly different energy regions. Finally, the expression for the RIXS double-differential cross section within the IPA is obtained as

$$\frac{\mathrm{d}^2\sigma}{\mathrm{d}\Omega_2\mathrm{d}\omega_2}\bigg|_{\mathrm{IP}} = \alpha^4\left(\frac{\omega_2}{\omega_1}\right)\sum_{cv\mu\mathbf{k}}\left|\frac{\mathbf{e}_2^* \cdot \mathbf{P}_{\mu v\mathbf{k}}\mathbf{P}_{c\mu\mathbf{k}} \cdot \mathbf{e}_1}{\omega_1 - (\epsilon_{c\mathbf{k}} - \epsilon_{\mu\mathbf{k}}) + i\eta}\right|^2 \delta(\omega - (\epsilon_{c\mathbf{k}} - \epsilon_{v\mathbf{k}})). \tag{5.9}$$

Furthermore, we employ Eq. 3.21 to express the δ-function that enforces the overall energy conservation with a finite Lorentzian broadening η, and obtain

$$\frac{\mathrm{d}^2\sigma}{\mathrm{d}\Omega_2\mathrm{d}\omega_2}\bigg|_{\mathrm{IP}} = -\frac{\alpha^4}{\pi}\left(\frac{\omega_2}{\omega_1}\right)\mathrm{Im}\sum_{cv\mathbf{k}}\frac{\left|\sum_{\mu}\frac{\mathbf{e}_2^*\cdot\mathbf{P}_{\mu v\mathbf{k}}\mathbf{P}_{c\mu\mathbf{k}}\cdot\mathbf{e}_1}{\omega_1-(\epsilon_{c\mathbf{k}}-\epsilon_{\mu\mathbf{k}})+i\eta}\right|^2}{\omega - (\epsilon_{c\mathbf{k}} - \epsilon_{v\mathbf{k}}) + i\eta}. \tag{5.10}$$

The equation above has been widely applied in the literature to calculate the RIXS cross

section in solids [262–267].

5.2 Many-body Formalism

In the previous section, we have derived a compact expression for the RIXS cross section within the IPA. Within this approximation, it is possible to enumerate all possible intermediate $|n\rangle$ and final many-body states $|f\rangle$ in Eq. 3.33 as each of these states is described as a singlet excitation above the ground state with no relaxation of the electronic system. It is known, however, that electron-hole interaction, which is neglected in the IPA, significantly alters the intermediate many-body states, which contain a core hole and an excited electron, and the final states, which contain a valence hole and an excited electron. This electron-hole interaction is the reason for the poor performance of the IPA for optical and x-ray excitation spectra in crystalline semiconductors and insulators. A more accurate approach is provided by many-body perturbation theory based on solutions of the BSE [55, 57, 103]. This approach has become the state of the art in the last decades to determine the optical [55, 56, 58–61] and x-ray absorption spectra [45, 226, 228, 237–245, 268–270] in solids. In order to describe many-body effects in RIXS within many-body perturbation theory, the cross section of Eq. 3.33 has to be expressed in quantities that can be obtained from the solution of the Bethe-Salpeter equation 1.33, more specifically the polarizability χ defined in Eq. 2.19.

Following Refs. [206, 209], we define an intermediate many-body state as

$$|Y(\omega_1)\rangle = \sum_n \frac{|n\rangle\langle n|}{\omega_1 - E_n} \hat{T}(\mathbf{e}_1)|0\rangle. \tag{5.11}$$

Similar intermediate states have been defined as *response vectors* in the context of non-linear spectroscopy in molecular systems [271, 272]. Inserting these intermediate states into Eq. 3.33, the RIXS cross section becomes

$$
\begin{aligned}
\frac{\mathrm{d}^2\sigma}{\mathrm{d}\Omega_2\mathrm{d}\omega_2} &= \alpha^4 \left(\frac{\omega_2}{\omega_1}\right) \sum_f |\langle f|\hat{T}^\dagger(\mathbf{e}_2)|Y(\omega_1)\rangle|^2 \delta(\omega - E_f) \\
&= \alpha^4 \left(\frac{\omega_2}{\omega_1}\right) \sum_f \langle Y(\omega_1)|\hat{T}(\mathbf{e}_2)|f\rangle\langle f|\hat{T}^\dagger(\mathbf{e}_2)|Y(\omega_1)\rangle \delta(\omega - E_f).
\end{aligned}
\tag{5.12}
$$

The intermediate states $|Y(\omega_1)\rangle$ contain the information about all possible excitation processes and can be understood as the excited many-body states produced by the absorption

of a photon with energy ω. Using Eq. 3.21, the cross section becomes

$$\frac{\mathrm{d}^2\sigma}{\mathrm{d}\Omega_2\mathrm{d}\omega_2} = \alpha^4\left(\frac{\omega_2}{\omega_1}\right)\mathrm{Im}\sum_f \frac{\langle Y(\omega_1)|\hat{T}(\mathbf{e}_2)|f\rangle\langle f|\hat{T}^\dagger(\mathbf{e}_2)|Y(\omega_1)\rangle}{\omega - E_f + \mathrm{i}\eta}. \tag{5.13}$$

We now introduce a crucial approximation for the many-body treatment of the RIXS process by assuming the intermediate and final many-body states to be represented completely in terms of singlet excitations of the groundstate, *i.e.* both intermediate and final state contain *only one* electron hole pair. Thus, we can approximate unity as

$$\mathbb{1} \approx \sum_{i\mathbf{k}}\sum_{j\mathbf{k}'} \hat{c}_{j\mathbf{k}'}^\dagger\hat{c}_{i\mathbf{k}}|0\rangle\langle 0|\hat{c}_{i\mathbf{k}}^\dagger\hat{c}_{j\mathbf{k}'}. \tag{5.14}$$

We note that this approximation does not imply that the excited electron and the hole are in a specific single-particle state, but rather assume that the interacting many-body states can be expressed as linear combinations of singlet excitations. This approximation is identical to the Tamm-Dancoff approximation in Eq. 1.60, such that Eq. 5.14 does not introduce an additional level of approximation if the polarizability is obtained in the Tamm-Dancoff approximation. Due to the limitation to singlet excitations, indirect RIXS can not be described, as it explicit requires the presence of two electron-hole pairs in the intermediate state (compare Section 3.4.2). Inserting Eq. 5.14 into Eq. 5.13 yields

$$\frac{\mathrm{d}^2\sigma}{\mathrm{d}\Omega_2\mathrm{d}\omega_2} = \alpha^4\left(\frac{\omega_2}{\omega_1}\right)\mathrm{Im}\sum_f\sum_{ij\mathbf{k}}\sum_{l\mathbf{k}'',m\mathbf{k}'''}\sum_{n\mathbf{k}^{IV},o\mathbf{k}^V}\sum_{pq\mathbf{k}^{VI}}$$

$$\left[\mathbf{e}_2^*\cdot\mathbf{P}_{ij\mathbf{k}}\right]^*\langle Y(\omega_1)|\hat{c}_{j\mathbf{k}}^\dagger\hat{c}_{i\mathbf{k}}\hat{c}_{m\mathbf{k}'''}^\dagger\hat{c}_{l\mathbf{k}''}|0\rangle\frac{\langle 0|\hat{c}_{l\mathbf{k}''}^\dagger\hat{c}_{m\mathbf{k}'''}|f\rangle\langle f|\hat{c}_{o\mathbf{k}^V}^\dagger\hat{c}_{n\mathbf{k}^{IV}}|0\rangle}{\omega - E_f + \mathrm{i}\eta}\times \tag{5.15}$$

$$\times\langle 0|\hat{c}_{n\mathbf{k}^{IV}}^\dagger\hat{c}_{o\mathbf{k}^V}\hat{c}_{p\mathbf{k}^{VI}}^\dagger\hat{c}_{q\mathbf{k}^{VI}}|Y(\omega_1)\rangle\left[\mathbf{e}_2^*\cdot\mathbf{P}_{pq\mathbf{k}^{VI}}\right].$$

We can insert the matrix elements of the polarizability of Eq. 2.28 and obtain

$$\frac{\mathrm{d}^2\sigma}{\mathrm{d}\Omega_2\mathrm{d}\omega_2} = \alpha^4\left(\frac{\omega_2}{\omega_1}\right)\mathrm{Im}\sum_{ij\mathbf{k}}\sum_{l\mathbf{k}'',m\mathbf{k}'''}\sum_{n\mathbf{k}^{IV},o\mathbf{k}^V}\sum_{pq\mathbf{k}^{VI}}$$

$$\left[\mathbf{e}_2^*\cdot\mathbf{P}_{ij\mathbf{k}}\right]^*\langle Y(\omega_1)|\hat{c}_{j\mathbf{k}}^\dagger\hat{c}_{i\mathbf{k}}\hat{c}_{m\mathbf{k}'''}^\dagger\hat{c}_{l\mathbf{k}''}|0\rangle\chi_{m\mathbf{k}'''l\mathbf{k}'',n\mathbf{k}^{IV}o\mathbf{k}^V}(\omega)\times \tag{5.16}$$

$$\times\langle 0|\hat{c}_{n\mathbf{k}^{IV}}^\dagger\hat{c}_{o\mathbf{k}^V}\hat{c}_{p\mathbf{k}^{VI}}^\dagger\hat{c}_{q\mathbf{k}^{VI}}|Y(\omega_1)\rangle\left[\mathbf{e}_2^*\cdot\mathbf{P}_{pq\mathbf{k}^{VI}}\right].$$

While this reformulation does not appear to simplify the problem, we note that the summation over the final many-body states $|f\rangle$ is now implicitly included in the polarizability.

Equation 5.16 yields an expression for the RIXS cross section in terms of the polarizability $\chi(\omega)$ evaluated at the energy loss $\omega = \omega_2 - \omega_1$, once the intermediate states $|Y(\omega_1)\rangle$ are known. In the quasiparticle approximation of Eq. 1.58, the summations over indices for creation and annihilation operators acting directly on the groundstate are restricted to conduction and valence states, respectively. Thus, the expression in Eq. 5.15 simplifies, and one obtains

$$
\begin{aligned}
\frac{\mathrm{d}^2\sigma}{\mathrm{d}\Omega_2\mathrm{d}\omega_2} =& \alpha^4 \left(\frac{\omega_2}{\omega_1}\right) \mathrm{Im} \sum_{ijk} \sum_{ck_c,vk_v} \sum_{c'k'_c,v'k'_v} \sum_{lmk'} \left[\mathbf{e}_2^* \cdot \mathbf{P}_{ijk}\right]^* \times \\
& \times \langle Y(\omega_1)|\hat{c}_{jk}^\dagger \hat{c}_{ik} \hat{c}_{ck_c}^\dagger \hat{c}_{vk_v}^\dagger|0\rangle \chi_{ck_cvk_v,c'k'_cv'k'_v}(\omega) \times \\
& \times \langle 0|\hat{c}_{v'k'_v}^\dagger \hat{c}_{c'k'_c} \hat{c}_{lk'}^\dagger \hat{c}_{mk'}|Y(\omega_1)\rangle \left[\mathbf{e}_2^* \cdot \mathbf{P}_{lmk'}\right].
\end{aligned}
\tag{5.17}
$$

The summations over the single-particle indices (ijk) and (lmk') are not restricted to either occupied or unoccupied states, since the corresponding creation and annihilation operators do not act on the ground state directly. To evaluate the expectation values $\langle Y(\omega_1)|\hat{c}_{jk}^\dagger \hat{c}_{ik} \hat{c}_{ck_c}^\dagger \hat{c}_{vk_v}^\dagger|0\rangle$ and $\langle 0|\hat{c}_{v'k'_v}^\dagger \hat{c}_{c'k'_c} \hat{c}_{lk'}^\dagger \hat{c}_{mk'}|Y(\omega_1)\rangle$, the explicit form of $|Y(\omega_1)\rangle$ has to be known. Similar to the treatment of Eq. 5.3, we also use our *a priori* knowledge that the intermediate many-body state $|n\rangle$ is supposed to contain a core hole. As such, we express the approximation to the unity operator in Eq. 5.14 in terms of electron-core hole pairs, where the electron is in the state $c\mathbf{k}$ and the core hole in the state $\mu\mathbf{k}$. Inserting the projection operator in Eq. 5.11 yields

$$
\begin{aligned}
|Y(\omega_1)\rangle &= \sum_n \sum_{c\mu k} \sum_{c'\mu'k'} \hat{c}_{ck}^\dagger \hat{c}_{\mu k}|0\rangle \frac{\langle 0|\hat{c}_{\mu k}^\dagger \hat{c}_{ck}|n\rangle\langle n|\hat{c}_{c'k'}^\dagger \hat{c}_{\mu'k'}|0\rangle}{\omega_1 - E_n} \left[\mathbf{e}_1 \cdot \mathbf{P}_{c'\mu'k'}\right] \\
&= \sum_{c\mu k} \sum_{c'\mu'k'} \hat{c}_{ck}^\dagger \hat{c}_{\mu k}|0\rangle \chi_{c\mu k,c'\mu'k'}(\omega_1) \left[\mathbf{e}_1 \cdot \mathbf{P}_{c'\mu'k'}\right].
\end{aligned}
\tag{5.18}
$$

This expression for the intermediate many-body state $|Y(\omega_1)\rangle$ allows us to evaluate the expectation values in Eq. 5.17, and we obtain

$$
\begin{aligned}
&\langle Y(\omega_1)|\hat{c}_{jk''}^\dagger \hat{c}_{ik''} \hat{c}_{c'''k'''}^\dagger \hat{c}_{v'''k'''}^\dagger|0\rangle \\
&= \sum_{cvk} \sum_{c'v'k'} \chi_{c\mu k,c'\mu'k'}^*(\omega_1) \left[\mathbf{e}_1 \cdot \mathbf{P}_{c'\mu'k'}\right]^* \langle 0|\hat{c}_{\mu k}^\dagger \hat{c}_{ck} \hat{c}_{jk''}^\dagger \hat{c}_{ik''} \hat{c}_{c'''k'''}^\dagger \hat{c}_{v'''k'''}^\dagger|0\rangle \\
&= -\sum_{c\mu k} \sum_{c'\mu'k'} \chi_{c\mu k,c'\mu'k'}^*(\omega_1) \left[\mathbf{e}_1 \cdot \mathbf{P}_{c'\mu'k'}\right]^* \delta_{cc'''}\delta_{v'''j}\delta_{\mu i}\delta_{\mathbf{k}\mathbf{k}'''}\delta_{\mathbf{k}\mathbf{k}''}
\end{aligned}
\tag{5.19}
$$

where in the last line, Eq. 5.8 is used to obtain an analytical expression for the expectation

value. Finally, this yields the double-differential cross section as

$$
\frac{d^2\sigma}{d\Omega'd\omega'} = \alpha^4 \left(\frac{\omega_2}{\omega_1}\right) \text{Im} \sum_{c,c',c'',c'''} \sum_{\mu,\mu',\mu'',\mu'''} \sum_{v,v'} \sum_{\mathbf{k}\mathbf{k}'\mathbf{k}''\mathbf{k}'''} \left[\left[\mathbf{e}_2^* \cdot \mathbf{P}_{\mu v \mathbf{k}}\right] \chi_{c\mu\mathbf{k},c'\mu'\mathbf{k}'}(\omega_1) \left[\mathbf{e}_1 \cdot \mathbf{P}_{c'\mu'\mathbf{k}'}\right] \right]^*
$$

$$
\chi_{cv\mathbf{k},c''v'\mathbf{k}''}(\omega) \left[\left[\mathbf{e}_2^* \cdot \mathbf{P}_{\mu''v'\mathbf{k}''}\right] \chi_{c''\mu''\mathbf{k}'',c'''\mu'''\mathbf{k}'''}(\omega_1) \left[\mathbf{e}_1 \cdot \mathbf{P}_{c'''\mu'''\mathbf{k}'''}\right] \right].
$$
(5.20)

Equation 5.20 represents the main result of this section: The RIXS cross section is expressed solely in terms of the polarizability χ. The polarizability is evaluated twice, once at the x-ray excitation energy ω_1, and once at the energy loss $\omega = \omega_1 - \omega_2$. The cumbersome summations over all intermediate and final many-body states are thus included in the polarizability, and Eq. 5.20 does not include explicit summations over many-body states.

5.3 Non-resonant X-ray Emission Spectroscopy

Non-resonant x-ray emission spectroscopy (XES) is a widely used technique to study the valence electronic system, thus complementing x-ray absorption spectroscopy, which reveals the conduction electronic structure. From a theoretical viewpoint, XES is a special case of RIXS, where the excitation energy is chosen high above the absorption edge, and the emission spectrum from the valence-core transitions is observed. In order to avoid the explicit calculation of the polarizability for high energies above the absorption edge, we employ the fact that the excited electron is in a conduction state high above the Fermi energy. Both the correlation between the excited electron and the core hole, and the correlation between the excited electron and the final valence hole, can be neglected in this case. Thus, we can employ the cross section in the independent particle approximation from Eq. 5.9 as

$$
\left.\frac{d^2\sigma}{d\Omega_2 d\omega_2}\right|_{\text{IP}} = \alpha^4 \left(\frac{\omega_2}{\omega_1}\right) \sum_{cv\mu\mathbf{k}} \left| \frac{\mathbf{e}_2^* \cdot \mathbf{P}_{\mu v \mathbf{k}} \mathbf{P}_{c\mu\mathbf{k}} \cdot \mathbf{e}_1}{\omega_1 - (\epsilon_{c\mathbf{k}} - \epsilon_{\mu\mathbf{k}}) + i\eta} \right|^2 \delta(\omega - (\epsilon_{c\mathbf{k}} - \epsilon_{v\mathbf{k}})).
$$
(5.21)

Furthermore, we assume a fixed excitation energy resonant to a specific independent-particle excitation, *i.e.* $\omega_1 = \epsilon_{c\mathbf{k}} - \epsilon_{\mu\mathbf{k}}$. Then, the δ-function becomes $\delta(\omega - (\epsilon_{c\mathbf{k}} - \epsilon_{v\mathbf{k}})) = \delta(\epsilon_{v\mathbf{k}} - \epsilon_{\mu\mathbf{k}} - \omega_2)$ and the cross section becomes a function of the emission energy ω_2 alone. As we have fixed the excitation energy to a specific core excitation, all terms depending on the conduction state $c\mathbf{k}$ yield only a constant factor to the cross section. Focussing on the dependence on the emission energy, we then write the cross section as

$$
\frac{d^2\sigma}{d\Omega_2 d\omega_2}|_{IP} \propto \sum_{v\mu\mathbf{k}} \left|\mathbf{e}_2 \cdot \mathbf{P}_{\mu v \mathbf{k}}\right|^2 \delta(\epsilon_{v\mathbf{k}} - \epsilon_{\mu\mathbf{k}} - \omega_2) \propto \text{Im} \sum_{\mu v} \frac{\left|\mathbf{e}_2 \cdot \mathbf{P}_{\mu v \mathbf{k}}\right|^2}{\omega_2 - (\epsilon_{v\mathbf{k}} - \epsilon_{\mu\mathbf{k}}) + i\eta}
$$
(5.22)

where we consider it only as a function of the emission energy ω_2. Equation 5.22 is identical to expressions in literature [273, 274] used to calculate XES spectra. Within our approximation, there are no effects of electron-hole correlation on the x-ray emission spectra, and the spectrum is thus given by single-particle energy differences, $\epsilon_{v\mathbf{k}} - \epsilon_{\mu\mathbf{k}}$, and the transition matrix elements $\mathbf{P}_{\mu v\mathbf{k}}$, fully determined by the electronic band structure. As such, the XES yields direct insight into the valence electronic structure.

Absorption and Non-resonant Scattering in `exciting`

In this chapter, we present the implementation of the BSE formalism in `exciting` [254]. In general, BSE calculations require the knowledge of the quasiparticle energies for the construction of Eq. 6.26 which can be obtained from the *GW* approach of MBPT. Existing all-electron implementations of *GW* typically adopt a basis set that is optimized to represent products of all-electron wavefunctions, know as *product basis* [275–277]. Details on the *GW* implementation in the `exciting` code within the product basis representation can be found in Refs. [254, 277, 278]. For the BSE implementation, the plane-wave representation for the non-local operators is chosen, which provides a description of the optical properties [225] at lower computational cost. Since momentum and plane-wave matrix elements are central quantities, they are discussed in detail in this section.

The work described in this chapter was developed in close collaboration with Benjamin Aurich [261], extending the existing implementation in the `exciting` [253, 279]. Benjamin Aurich implemented optical BSE calculations for finite momentum transfer and optical BSE calculations beyond the Tamm-Dancoff approximation, while we have combined the implementations for the calculations of optical excitations with the one for core excitations [239]. This consistent implementation is the starting point for our code development to determine the RIXS cross section (compare Chapter 7). This chapter in large parts follows the corresponding sections in Ref. [359].

6.1 Linearized Augmented Plane-wave Basis

`exciting` employs the (L)APW+lo basis set [232–235] for the Kohn-Sham equations Eq. 1.7 to compute valence and conduction states. These states subsequently enter the expressions of the matrix elements of the BSE Hamiltonian. To obtain the basis functions, the unit cell is divided into non-overlapping muffin-tin (MT) spheres centered at the atomic positions and the *interstitial* region between the spheres. Different functions are employed in the two regions in order to account for both the rapid variation of the Kohn-Sham wavefunctions close to the nuclei and the smoother behavior in the interstitial region. In the MT sphere

surrounding an atom α, the wavefunctions are expanded in atomic-like basis functions $u_l^\alpha(r)Y_{lm}(\hat{r})$, while plane waves $e^{-i(G+k)r}$ are used in the interstitial region. As such, the basis functions ϕ_{k+G} are expressed as

$$\phi_{k+G}(\mathbf{r}) = \begin{cases} \frac{1}{\sqrt{V_0}}e^{-i(G+k)\mathbf{r}} & \mathbf{r} \in I \\ \sum_{lm,p} A_{lm}^{k+G} u_{l,p}^\alpha(r)Y_{lm}(\hat{r}) & \mathbf{r} \in MT. \end{cases} \tag{6.1}$$

Here, V_0 is the unit-cell volume and $A_{lm,p}^{k+G}$ are expansion coefficients that ensure that the basis functions are continuous at the boundaries of the MT spheres. The radial functions $u_{l,p}^\alpha(r)$ are obtained from the solutions of the radial Schrödinger equation using the spherically averaged Kohn-Sham potential. The index p denotes p-th derivative with respect to the energy, *i.e.* $u_{l,p}^\alpha = \frac{\partial^p u_l^\alpha}{\partial \epsilon^p}$. For $p = 0$, we recover the APW+lo basis set [235], while the summation up to $p = 1$ yields the LAPW+lo basis set [232, 233]. Higher-order derivatives of the radial functions can also be included. In order to increase the variational degrees of freedom in the MT spheres, local orbitals (LOs) [235] $\phi_v(\mathbf{r})$ are used to complement the basis. These basis function are expressed as

$$\phi_v(\mathbf{r}) = \begin{cases} 0 & \mathbf{r} \in I \\ \delta_{\alpha\alpha_v}\delta_{ll_v}\delta_{mm_v} \sum_p B_{v,p} u_{l,p}^\alpha(r)Y_{lm}(\hat{r}) & \mathbf{r} \in MT \end{cases}. \tag{6.2}$$

The local orbitals vanish outside of the MT spheres and the coefficients $B_{v,p}$ ensure that they are continuous and smooth at the MT-sphere boundary. As the LOs are added for specific MT spheres and (lm)-channels, they allow for a systematic improvement of the basis. For a review on the family of (L)APW+lo basis sets, see Ref. [254]. The eigenstates ψ_{ik} of the Kohn-Sham Hamiltonian in Eq. 1.9 are expressed in the LAPW+lo basis as

$$\psi_{ik}^{KS}(\mathbf{r}) = \sum_G C_{i(k+G)}\phi_{k+G}(\mathbf{r}) + \sum_v C_{ivk}\phi_v(\mathbf{r}) = \begin{cases} \frac{1}{\sqrt{V_0}}\sum_G C_{i(k+G)}e^{-i(G+k)\mathbf{r}} & \mathbf{r} \in I \\ \sum_{lm} u_l^{ik}(r)Y_{lm}(\hat{r}) & \mathbf{r} \in MT \end{cases} \tag{6.3}$$

where the radial functions are defined as

$$u_l^{ik} = \sum_p \sum_G C_{i(k+G)}A_{lm,p}^{k+G}u_{l,p}^\alpha(r) + \sum_v C_{ivk}B_{v,p}u_{l,p}^\alpha(r). \tag{6.4}$$

$C_{i(k+G)}$ and C_{ivk} are the expansion coefficients, obtained from the diagonalization of the Kohn-Sham Hamiltonian.

While the expansion in this basis is convenient for the extended valence and conduction states, the highly localized core states $\psi_{\alpha,\kappa,M}^{KS}$ require a different treatment. These states are fully localized in the muffin-tin sphere of the atom α. As spin-orbit coupling can play
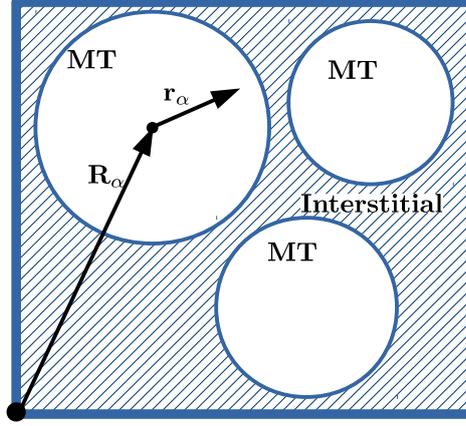
Figure 6.1: Schematics of a unit cell in the LAPW framework.

a dominant role for these states, they are obtained from the solution of the radial Dirac equation in the respective spherically symmetrized crystal potential. The spinor solutions $\psi^{KS}_{\alpha,\kappa,M}$ of these equations can be written as

$$\psi^{KS}_{\alpha,\kappa,M}(\mathbf{r}) = \begin{pmatrix} u_{\alpha,\kappa}(r)\Omega_{\kappa,M}(\hat{r}) \\ -iv_{\alpha,\kappa}(r)\Omega_{-\kappa,M}(\hat{r}) \end{pmatrix}, \tag{6.5}$$

where we have introduced a unique index κ for a core state $^{2S+1}L_J$, such that

$$\kappa = \begin{cases} -L-1 & \text{for } J = L + \frac{1}{2} \\ L & \text{for } J = L - \frac{1}{2} \end{cases}. \tag{6.6}$$

The spherical part of the core wavefunctions $\psi^{KS}_{\alpha,\kappa,M}$ is given by the spin spherical harmonics $\Omega_{L,S,J,M}(\hat{r})$, defined as

$$\Omega_{L,\frac{1}{2},L+\frac{1}{2},M}(\hat{r}) = \begin{pmatrix} \sqrt{\frac{L+M+\frac{1}{2}}{2L+1}}Y_{L,M-\frac{1}{2}}(\hat{r}) \\ \sqrt{\frac{L-M+\frac{1}{2}}{2L+1}}Y_{L,M+\frac{1}{2}}(\hat{r}) \end{pmatrix}, \tag{6.7}$$

and

$$\Omega_{(L,\frac{1}{2})L-\frac{1}{2},M}(\hat{r}) = \begin{pmatrix} -\sqrt{\frac{L-M+\frac{1}{2}}{2L+1}}Y_{L,M-\frac{1}{2}}(\hat{r}) \\ \sqrt{\frac{L+M+\frac{1}{2}}{2L+1}}Y_{L,M+\frac{1}{2}}(\hat{r}) \end{pmatrix}. \tag{6.8}$$

As such, the core wavefunctions $\psi^{KS}_{\alpha,\kappa}$ in Eq. 6.5 are four-dimensional Dirac vectors com-

posed of the two-dimensional spinors of the large and small component. The radial functions $u_{\alpha,\kappa}(r)$ for the large component and $-iv_{\alpha,\kappa}(r)$ for the small component, respectively, are given by the coupled radial Dirac equations

$$\frac{\partial u_{\alpha,\kappa}}{\partial r} = \frac{1}{c}\left(v_{eff}^{\alpha} - \epsilon_{\alpha,\kappa}\right)v_{\alpha,\kappa} + \left(\frac{\kappa-1}{r}\right)u_{\alpha,\kappa} \qquad (6.9)$$

$$\frac{\partial v_{\alpha,\kappa}}{\partial r} = -\frac{\kappa+1}{r}v_{\alpha,\kappa} + 2c\left[1 + \frac{1}{2c^2}\left(\epsilon_{\alpha,\kappa} - v_{eff}^{\alpha}\right)\right], \qquad (6.10)$$

In the calculation of matrix elements between core states and conduction states, the small component is neglected, and we obtain the core wavefunction $\psi_{\alpha,\kappa,M}^{KS}$ at an atomic site α:

$$\psi_{\alpha,\kappa,M}^{KS}(\mathbf{r}) = \begin{cases} u_{\alpha,\kappa}(r_\alpha)\Omega_{\kappa,M}(\hat{r}_\alpha) & \text{for } r_\alpha \leq R_{MT} \\ 0 & \text{else} \end{cases}. \qquad (6.11)$$

More details about the treatment of core states in the (L)APW+lo basis can be found in Ref. [239].

6.2 Momentum and Plane-wave Matrix Elements

The momentum matrix elements $P_{nm\mathbf{k}}^{j} = \langle n\mathbf{k}| - i\nabla_j|m\mathbf{k}\rangle$ between conduction and valence states, where j represents the polarization direction of the incoming light, are expanded in the (L)APW+lo basis

$$\begin{aligned} P_{nm\mathbf{k}}^{j} = & \sum_{\mathbf{GG'}} C_{n(\mathbf{k}+\mathbf{G})}^* C_{m(\mathbf{k}+\mathbf{G})} P_{\mathbf{GG'k}}^{j} + \sum_{\mathbf{G}v} C_{n(\mathbf{k}+\mathbf{G})}^* C_{mv\mathbf{k}} P_{\mathbf{G}v\mathbf{k}}^{j} \\ & + \sum_{v'\mathbf{G'}} C_{mv'\mathbf{k}}^* C_{n(\mathbf{k}+\mathbf{G})} P_{v'\mathbf{G'k}}^{j} + \sum_{v'v} C_{mv'\mathbf{k}}^* C_{nv\mathbf{k}} P_{v'v\mathbf{k}}^{j}. \end{aligned} \qquad (6.12)$$

$C_{i\mathbf{k}}$ and $C_{iv\mathbf{k}}$ are the coefficients of Eq. 6.3, and $P_{\mathbf{GG'k}}^{j}$, $P_{\mathbf{G}v\mathbf{k}}^{j}$, $P_{v'\mathbf{G'k}}^{j}$, and $P_{v'v}^{j}$ are LAPW-LAPW, LAPW-LO, LO-LAPW, and LO-LO momentum matrix elements, respectively, which are defined as

$$\begin{aligned} P_{\mathbf{GG'k}}^{j} &= \langle \phi_{\mathbf{k}+\mathbf{G}}| - i\nabla_j|\phi_{\mathbf{k}+\mathbf{G'}}\rangle \\ P_{\mathbf{G}v\mathbf{k}}^{j} &= \langle \phi_{\mathbf{k}+\mathbf{G}}| - i\nabla_j|\phi_v\rangle \\ P_{v'\mathbf{G'k}}^{j} &= \langle \phi_{v'}| - i\nabla_j|\phi_{\mathbf{k}+\mathbf{G'}}\rangle \\ P_{v'v}^{j} &= \langle \phi_{v'}| - i\nabla_j|\phi_v\rangle. \end{aligned} \qquad (6.13)$$

These matrix elements of the general form P_{ab}^{j} can be decomposed into contributions from the MT spheres $P_{ab}^{j,MT}$ and from the interstitial region $P_{ab}^{j,MT}$, such that we can write all plane-wave matrix elements as $P_{ab}^{j} = P_{ab}^{j,MT} + P_{ab}^{j,I}$. Since the local orbitals vanish in the interstitial region, only $P_{GG'}^{j}$ have a non-vanishing contribution. The interstitial contribution of the matrix elements is calculated analytically, as the action of the nabla-operator on plane waves can be determined analytically. In the MT spheres, the action of the nabla-operator is expanded in terms of spherical harmonics, $\nabla_j \left[u_{lp}^{\alpha}(r) Y_{lm}(\hat{r}) \right] = \sum_{l'm'} u_{lmp,l'm'}^{\alpha,j} Y_{l'm'}(\hat{r})$. This expansion allows for the analytic evaluation of the spherical integral, while the radial integration within the MT spheres is performed numerically on a grid.

Plane-wave matrix elements $M_{mn\mathbf{k}}(\mathbf{G}, \mathbf{q}) = \langle m\mathbf{k} | e^{-i(\mathbf{G}+\mathbf{q})\mathbf{r}} | n(\mathbf{k}+\mathbf{q}) \rangle$ are calculated accordingly:

$$
\begin{aligned}
M_{mn\mathbf{k}}(\mathbf{G}, \mathbf{q}) = &\sum_{\mathbf{G}'\mathbf{G}''} C_{m(\mathbf{k}+\mathbf{G}')}^{*} C_{n(\mathbf{k}+\mathbf{q}+\mathbf{G}'')} M_{\mathbf{G}'\mathbf{G}''\mathbf{k}}(\mathbf{G}, \mathbf{q}) \\
&+ \sum_{\mathbf{G}'\nu'} C_{m(\mathbf{k}+\mathbf{G}')}^{*} C_{n\nu'\mathbf{k}} M_{\mathbf{G}'\nu'\mathbf{k}}(\mathbf{G}, \mathbf{q}) \\
&+ \sum_{\nu\mathbf{G}'} C_{m\nu'\mathbf{k}}^{*} C_{n(\mathbf{k}+\mathbf{q}+\mathbf{G}')} M_{\nu\mathbf{G}'\mathbf{k}}(\mathbf{G}, \mathbf{q}) \\
&+ \sum_{\nu\nu'} C_{m\nu'\mathbf{k}}^{*} C_{n\nu\mathbf{k}+\mathbf{q}} M_{\nu\nu'\mathbf{k}}(\mathbf{G}, \mathbf{q}),
\end{aligned}
\tag{6.14}
$$

where the LAPW-LAPW, LAPW-LO, LO, LAPW-LO, and LO-LO plane-wave matrix elements are given by

$$
\begin{aligned}
M_{\mathbf{G}'\mathbf{G}''\mathbf{k}}(\mathbf{G}, \mathbf{q}) &= \langle \phi_{\mathbf{k}+\mathbf{G}'} | e^{-i(\mathbf{G}+\mathbf{q})\mathbf{r}} | \phi_{\mathbf{k}+\mathbf{q}+\mathbf{G}''} \rangle \\
M_{\mathbf{G}'\nu\mathbf{k}}(\mathbf{G}, \mathbf{q}) &= \langle \phi_{\mathbf{k}+\mathbf{G}'} | e^{-i(\mathbf{G}+\mathbf{q})\mathbf{r}} | \phi_{\nu} \rangle \\
M_{\nu'\mathbf{G}'\mathbf{k}}(\mathbf{G}, \mathbf{q}) &= \langle \phi_{\nu'} | e^{-i(\mathbf{G}+\mathbf{q})\mathbf{r}} | \phi_{\mathbf{k}+\mathbf{q}+\mathbf{G}'} \rangle \\
M_{\nu'\nu}(\mathbf{G}, \mathbf{q}) &= \langle \phi_{\nu'} | e^{-i(\mathbf{G}+\mathbf{q})\mathbf{r}} | \phi_{\nu} \rangle.
\end{aligned}
\tag{6.15}
$$

Equivalently to the case of the momentum-matrix elements, the plane-wave matrix elements are decomposed into an interstitial and a MT part. The integration in the interstitial part is performed analytically. In the MT spheres, we employ the Rayleigh expansion of plane waves in products of spherical harmonics and spherical Bessel functions of first kind $j_l(r)$, i.e. $e^{-i(\mathbf{G}+\mathbf{q})\mathbf{r}} = 4\pi \sum_{lm} (-i)^l j_l((G+q)r) Y_{lm}(\hat{r}) Y_{lm}(\widehat{G+q})$. As in the case of the momentum matrix elements, the spherical integral is performed analytically, while a numerical integration is performed on the radial grid. More details on the calculation of momentum and plane-wave matrix elements in the (L)APW+lo basis can be found in Refs. [239, 279].

We furthermore define modified plane-wave matrix elements $N_{nm\mathbf{k}}(\mathbf{G}, \mathbf{q})$ as

$$
N_{mn\mathbf{k}}(\mathbf{G}, \mathbf{q}) = \langle m\mathbf{k} | e^{-i(\mathbf{G}+\mathbf{q})\mathbf{r}} | \left(n(\mathbf{k}+\mathbf{q}) \right)^{*} \rangle,
\tag{6.16}
$$

that are employed to evaluate plane-wave matrix elements of states at $-(\mathbf{k} + q)$, *i.e.* $|n - (\mathbf{k} + \mathbf{q})\rangle = |\big(n(\mathbf{k} + \mathbf{q})\big)^*\rangle$. They are expressed in the (L)APW+lo basis as

$$
\begin{aligned}
N_{mn\mathbf{k}}(\mathbf{G}, \mathbf{q}) = &\sum_{\mathbf{G}'\mathbf{G}''} C^*_{m(\mathbf{k}+\mathbf{G}')} C^*_{n(\mathbf{k}+\mathbf{q}+\mathbf{G}'')} N_{\mathbf{G}'\mathbf{G}''\mathbf{k}}(\mathbf{G}, \mathbf{q}) \\
&+ \sum_{\mathbf{G}'\nu'} C^*_{m(\mathbf{k}+\mathbf{G}')} C^*_{n\nu'\mathbf{k}} N_{\mathbf{G}'\nu'\mathbf{k}}(\mathbf{G}, \mathbf{q}) \\
&+ \sum_{\nu\mathbf{G}'} C^*_{m\nu'\mathbf{k}} C^*_{n(\mathbf{k}+\mathbf{q}+\mathbf{G}')} N_{\nu\mathbf{G}'\mathbf{k}}(\mathbf{G}, \mathbf{q}) \\
&+ \sum_{\nu\nu'} C^*_{m\nu'\mathbf{k}} C^*_{n\nu\mathbf{k}+\mathbf{q}} N_{\nu\nu'\mathbf{k}}(\mathbf{G}, \mathbf{q}).
\end{aligned}
\tag{6.17}
$$

Analogously to the calculation of the plane-wave matrix elements in Eq. 6.15, we define modified plane-wave matrix elements between basis functions as

$$
\begin{aligned}
N_{\mathbf{G}'\mathbf{G}''\mathbf{k}}(\mathbf{G}, \mathbf{q}) &= \langle \phi_{\mathbf{k}+\mathbf{G}'} | e^{-i(\mathbf{G}+\mathbf{q})\mathbf{r}} | \phi^*_{\mathbf{k}+\mathbf{q}+\mathbf{G}''} \rangle \\
N_{\mathbf{G}'\nu\mathbf{k}}(\mathbf{G}, \mathbf{q}) &= \langle \phi_{\mathbf{k}+\mathbf{G}'} | e^{-i(\mathbf{G}+\mathbf{q})\mathbf{r}} | \phi^*_\nu \rangle \\
N_{\nu'\mathbf{G}'\mathbf{k}}(\mathbf{G}, \mathbf{q}) &= \langle \phi_{\nu'} | e^{-i(\mathbf{G}+\mathbf{q})\mathbf{r}} | \phi^*_{\mathbf{k}+\mathbf{q}+\mathbf{G}'} \rangle \\
N_{\nu'\nu}(\mathbf{G}, \mathbf{q}) &= \langle \phi_{\nu'} | e^{-i(\mathbf{G}+\mathbf{q})\mathbf{r}} | \phi^*_\nu \rangle.
\end{aligned}
\tag{6.18}
$$

The LAPW-LAPW matrix elements $N_{\mathbf{G}'\mathbf{G}''\mathbf{k}}$, LAPW-LO elements $N_{\mathbf{G}'\nu\mathbf{k}}$, LO-LAPW elements $N_{\nu'\mathbf{G}'\mathbf{k}}$, and LO-LO elements $N_{\nu'\nu}$ are calculated equivalently to those of Eq. 6.15, where we employ the analytic property $Y^*_{lm}(\hat{r}) = Y_{l(-m)}(\hat{r})$ for the MT contributions.

For additional details regarding the calculation of the plane-wave matrix elements in the (L)APW+lo basis of `exciting`, we refer the readers to Refs. [225, 253]. For additional information on matrix elements between states in the (L)APW+lo basis and core states, we refer to Ref. [239].

6.3 BSE in Matrix Form

Since the quantities $L(1, 2; 1', 2')$ and $L_0(1, 2; 1', 2')$ in the BSE (Eq. 2.24) depend on four points in space and time, they can be represented in a basis of non-local functions $\Upsilon_\alpha(\mathbf{r}, \mathbf{r}')$, where α is a generic index. The matrix elements $A_{\alpha\beta}$ of a generic non-local function $A(\mathbf{r}_1, \mathbf{r}'_1, \mathbf{r}_2, \mathbf{r}'_2)$ are defined as

$$
A_{\alpha\beta} = \int \int \int \int d^3 r_1 \, d^3 r'_1 \, d^3 r_2 \, d^3 r'_2 \, \Upsilon^*_\alpha(\mathbf{r}_1, \mathbf{r}'_1) A(\mathbf{r}_1, \mathbf{r}'_1, \mathbf{r}_2, \mathbf{r}'_2) \Upsilon_\beta(\mathbf{r}_2, \mathbf{r}'_2),
\tag{6.19}
$$

and the full function can be constructed from the matrix elements via

$$A(\mathbf{r}_1, \mathbf{r}_1', \mathbf{r}_2, \mathbf{r}_2') = \sum_{\alpha\beta} \Upsilon_\alpha(\mathbf{r}_1, \mathbf{r}_1') A_{\alpha\beta} \Upsilon_\beta^*(\mathbf{r}_2, \mathbf{r}_2'). \tag{6.20}$$

Typically, products of quasiparticle wavefunctions are chosen as basis representation. This choice of basis is motivated by the Lehman representation of the independent-particle correlation function $L_0(\mathbf{q}, \omega)$ in Eq. B.6. This basis is split into the *resonant* part, *i.e.* transitions from occupied to unoccupied states with positive transition energies, and the *anti-resonant* part, *i.e.* transitions from unoccupied to occupied states with negative transition energy. Here, we define such a basis with the functions Υ^r and Υ^a [140, 359] for the resonant and anti-resonant space, respectively:

$$\Upsilon_{\alpha,\mathbf{q}}^r(\mathbf{r}, \mathbf{r}') = \phi_{o\mathbf{k}_+}(\mathbf{r})\phi_{u\mathbf{k}_-}^*(\mathbf{r}') \tag{6.21}$$

and

$$\Upsilon_{\alpha,\mathbf{q}}^a(\mathbf{r}, \mathbf{r}') = \phi_{u(-\mathbf{k}_-)}(\mathbf{r})\phi_{o(-\mathbf{k}_+)}^*(\mathbf{r}'), \tag{6.22}$$

with the index o (u) denoting occupied (unoccupied) states, and the $\mathbf{k}$-point set chosen such that $\mathbf{k}_\pm = \mathbf{k} \pm \frac{\mathbf{q}}{2}$. α is a combined index $\alpha \leftrightarrow \{o, u, \mathbf{k}\}$ which, together with the index $\mathbf{q}$, uniquely labels independent-particle transitions from $\phi_{o\mathbf{k}_+}$ to $\phi_{u\mathbf{k}_-}$. This specific choice of basis functions allows us to exploit the symmetry properties $\phi_{n\mathbf{k}}(\mathbf{r}) = \phi_{n(-\mathbf{k})}^*(\mathbf{r})$ and $\epsilon_{n\mathbf{k}} = \epsilon_{n(-\mathbf{k})}$ of the Bloch states under time-reversal, such that [140, 261]

$$\Upsilon_{\alpha,\mathbf{q}}^a(\mathbf{r}, \mathbf{r}') = \Upsilon_{\alpha,\mathbf{q}}^r(\mathbf{r}', \mathbf{r}). \tag{6.23}$$

The matrix elements of L in this basis are obtained as

$$L_{ij}(\mathbf{q}) = \int d^3r_1 d^3r_1' d^3r_2 d^3r_2' \, \Upsilon_{i\mathbf{q}}^*(\mathbf{r}_1, \mathbf{r}_1') L(\mathbf{r}_1, \mathbf{r}_2, \mathbf{r}_1', \mathbf{r}_2') \Upsilon_{j\mathbf{q}}(\mathbf{r}_2', \mathbf{r}_2), \tag{6.24}$$

where i and j combine the indices of the transition (α) and of the resonant or anti-resonant subspace (r or a). As L_0 is diagonal in this representation, the inverse L_0^{-1} takes the form

$$\mathsf{L}_0^{-1}(\mathbf{q}, \omega) = -\left[\begin{pmatrix} \Delta\epsilon^{\mathrm{IP}}(\mathbf{q}) & 0 \\ 0 & \Delta\epsilon^{\mathrm{IP}}(\mathbf{q}) \end{pmatrix} - \omega \begin{pmatrix} \mathbb{1} & 0 \\ 0 & -\mathbb{1} \end{pmatrix}\right], \tag{6.25}$$

where

$$\Delta\epsilon_{\alpha,\alpha'}^{\mathrm{IP}}(\mathbf{q}) = \left(\epsilon_{u\mathbf{k}_-} - \epsilon_{o\mathbf{k}_+}\right)\delta_{\alpha,\alpha'} \tag{6.26}$$

contains the quasiparticle energies $\epsilon_{o/u\mathbf{k}_\pm}$.

We now write Eq. 2.24 as a matrix equation in the basis of Eqs. 6.21 and 6.22, and obtain

$$L(\mathbf{q}, \omega) = \left[L_0^{-1}(\mathbf{q}, \omega) - \Xi(\mathbf{q}) \right]^{-1}. \tag{6.27}$$

Inserting the explicit form of L_0 (Eq. 6.25) into this equation, we arrive at

$$L(\mathbf{q}, \omega) = - \left[H(\mathbf{q}) - \omega \Delta \right]^{-1}, \tag{6.28}$$

where $H(\mathbf{q})$ includes all frequency-independent terms and $\Delta = \begin{pmatrix} \mathbb{1} & 0 \\ 0 & -\mathbb{1} \end{pmatrix}$. The matrix $H(\mathbf{q})$ represents an effective Hamiltonian, the *BSE Hamiltonian*, the eigenstates of which are also eigenstates of L. Using time-reversal symmetry [140] and making use of the symmetry property of Eq. 6.23, the Hamiltonian becomes hermitian and takes the form:

$$H(\mathbf{q}) = \begin{pmatrix} A(\mathbf{q}) & B(\mathbf{q}) \\ B(\mathbf{q}) & A(\mathbf{q}) \end{pmatrix}, \tag{6.29}$$

with the diagonal block expressed by

$$A(\mathbf{q}) = E^{ip}(\mathbf{q}) + 2\gamma_x V^{rr}(\mathbf{q}) - \gamma_c W^{rr}(\mathbf{q}) \tag{6.30}$$

and the coupling block being

$$B(\mathbf{q}) = 2\gamma_x V^{rr}(\mathbf{q}) - \gamma_c W^{ra}(\mathbf{q}). \tag{6.31}$$

Here, we introduce the resonant-resonant and resonant-antiresonant screened Coulomb interaction as $W^{rr}(\mathbf{q})$ and $W^{ra}(\mathbf{q})$, respectively, as well as the resonant-resonant exchange interaction $V^{rr}(\mathbf{q})$.

6.4 Spin Structure of the BSE Hamiltonian

For non-spin-polarized systems where the spin-orbit coupling can be neglected, the BSE Hamiltonian of Eq. 6.29 has a particular spin structure, which can be exploited to reduce the size of the BSE problem. Let us consider a minimal example of a system with two valence states $v\mathbf{k}\uparrow$ and $v\mathbf{k}\downarrow$ and two conduction states $c\mathbf{k}\uparrow$ and $c\mathbf{k}\downarrow$ in the long-wavelength limit, *i.e.* $\mathbf{q} = 0$. Since the system is non-spin-polarized, we impose that the electronic wavefunction does not depend on the spin, *i.e.* $\psi_{i\mathbf{k}\uparrow}(\mathbf{r}) = \psi_{i\mathbf{k}\downarrow}(\mathbf{r})$. In the basis of the transitions $\{|v \uparrow c \uparrow \mathbf{k}\rangle, |v \uparrow c \downarrow \mathbf{k}\rangle, |v \downarrow c \uparrow \mathbf{k}\rangle, |v \downarrow c \downarrow \mathbf{k}\rangle\}$, the resonant BSE Hamiltonian

$A(\mathbf{q} = 0)$ then becomes [138, 280, 281]

$$A = \begin{pmatrix} E^{ip} - W^{rr} + V^{rr} & 0 & 0 & V^{rr} \\ 0 & E^{ip} - W^{rr} & 0 & 0 \\ 0 & 0 & E^{ip} - W^{rr} & 0 \\ V^{rr} & 0 & 0 & E^{ip} - W^{rr} + V^{rr} \end{pmatrix}. \tag{6.32}$$

The Hamiltonian decouples into two blocks: The *singlet excitations* are defined by the spin state $\frac{1}{\sqrt{2}}(|v \uparrow c \uparrow \mathbf{k}\rangle + |v \downarrow c \downarrow \mathbf{k}\rangle)$ determined by the singlet Hamiltonian $A^S = E^{ip} - W^{rr} + 2V^{rr}$. The *triplet excitations* are given by $\{|v \uparrow c \downarrow \mathbf{k}\rangle, |v \downarrow c \uparrow \mathbf{k}\rangle, \frac{1}{\sqrt{2}}(|v \uparrow c \uparrow \mathbf{k}\rangle - |v \downarrow c \downarrow \mathbf{k}\rangle)\}$ and are determined by the triplet Hamiltonian $A^T = E^{ip} - W^{rr}$. The results of the model can be generalized, and we obtain the singlet BSE Hamiltonian as

$$A^S(\mathbf{q}) = E^{ip}(\mathbf{q}) + 2V^{rr}(\mathbf{q}) - W^{rr}(\mathbf{q}) \tag{6.33}$$

and

$$B^S(\mathbf{q}) = 2V^{rr}(\mathbf{q}) - W^{ra}(\mathbf{q}), \tag{6.34}$$

while the triplet Hamiltonian is determined by

$$A^T(\mathbf{q}) = E^{ip}(\mathbf{q}) - W^{rr}(\mathbf{q}) \tag{6.35}$$

and

$$B^T(\mathbf{q}) = -W^{ra}(\mathbf{q}). \tag{6.36}$$

Since spin flips are forbidden by the optical selection rules, only singlet excitations are observed in absorption spectroscopy. In this case, only the singlet Hamiltonian needs to de diagonalized, which reduces the size of the problem to 25% of the original problem. Note that for system with non-negligible spin-orbit coupling, this separation is not possible, since in this case spin is not a good quantum number any more. In these systems, the full Hamiltonian of Eq. 6.29 needs to be considered.

6.5 Ambiguity of the Matrix Formulation

We note that the choice of basis functions in Eqs. 6.21 and 6.22 is not unique, even if only basis functions are considered where L_0 is diagonal. This ambiguity occurs since $L_0(1, 2; 1^+, 2^+)$ is a time-ordered quantity that depends on the energy difference $t_1 - t_2$. As such, we can define a time difference as $\tau^{(1)} = t_1 - t_2$ or as $\tau^{(2)} = t_2 - t_1$. For retarded quantities, such as the retarded polarizability, the time direction $\tau^{(1)}$ is unique, since $\chi^R(\tau^{(1)} < 0) = 0$, as the response of the system at t_1 has to follow the perturbation at t_2 to

preserve causality. As the time-ordered polarizability includes both the information of the retarded and the advanced response, no time direction is unique.

The two different choices of time-direction, either $\tau^{(1)} = t_1 - t_2$ or $\tau^{(2)} = t_2 - t_1$, yield two different Lehmann representations and thus two distinct sets of basis functions. The basis functions in Eqs. 6.21 and 6.22 are obtained from the Lehmann representation of L_0 with respect to $\tau^{(2)}$ (see Appendix B for more details). A different set of basis functions is obtained from the Lehmann representation with respect to $\tau^{(1)} = t_1 - t_2$, shown in Eq. B.6.

The two possible product-basis representations and their connection to the retarded polarizability is discussed in detail in Appendix B, where we show that both basis representations can be used to obtain the retarded polarizability. In the following, we will drop the superscript (1), which denotes the matrix representation in the basis functions of Eqs. 6.21 and 6.22, such that $\chi_{\alpha,\alpha'} \equiv \chi^{(1)}_{\alpha,\alpha'}$ and $\left[L_0\right]_{\alpha,\alpha'} \equiv \left[L_0\right]^{(1)}_{\alpha,\alpha'}$.

6.6 Matrix Elements of the BSE Hamiltonian

The matrix elements of the exchange interaction in Eqs. 6.30 and 6.31 are given by

$$V^{rr}_{\alpha\beta}(\mathbf{q}) = \int d^3r d^3r' \; \Upsilon^*_{\alpha,\mathbf{q}}(\mathbf{r},\mathbf{r})v(\mathbf{r},\mathbf{r}')\Upsilon_{\beta,\mathbf{q}}(\mathbf{r}',\mathbf{r}'). \tag{6.37}$$

We introduce the Fourier transform of the bare Coulomb potential

$$v(\mathbf{r},\mathbf{r}') = \sum_{\mathbf{G},\mathbf{q}} \underbrace{\frac{1}{V}\frac{4\pi}{|\mathbf{G}+\mathbf{q}|^2}}_{=v_{\mathbf{G}}(\mathbf{q})} e^{i(\mathbf{G}+\mathbf{q})(\mathbf{r}-\mathbf{r}')}, \tag{6.38}$$

where V denotes the crystal volume. The matrix elements $V^{rr}_{\alpha\beta}$ of Eqs. 6.30 and 6.31 are computed in reciprocal space as

$$V^{rr}_{\alpha\beta}(\mathbf{q}) = \frac{1}{V} \sum_{\mathbf{G}} v_{\mathbf{G}}(\mathbf{q}) M^*_{u o \mathbf{k}_-}(\mathbf{G},\mathbf{q}) M_{u'o'\mathbf{k}'_-}(\mathbf{G},\mathbf{q}). \tag{6.39}$$

The matrix elements of the screened Coulomb interaction are given by

$$W_{\alpha\beta}(\mathbf{q}) = \iint d^3r d^3r' \; \Upsilon^*_{\alpha,\mathbf{q}}(\mathbf{r},\mathbf{r}')w(\mathbf{r},\mathbf{r}')\Upsilon_{\alpha',\mathbf{q}}(\mathbf{r},\mathbf{r}'). \tag{6.40}$$

The statically screened Coulomb potential is given by

$$w(\mathbf{r}, \mathbf{r}') = \int d^3 r'' \, v(\mathbf{r}, \mathbf{r}'') \varepsilon^{-1}(\mathbf{r}'', \mathbf{r}', \omega = 0). \tag{6.41}$$

Again, we make use of its Fourier representation

$$w(\mathbf{r}, \mathbf{r}') = \sum_{\mathbf{G}\mathbf{G}'} \sum_{\mathbf{q}} e^{i(\mathbf{G}+\mathbf{q})\mathbf{r}} \, w_{\mathbf{G}\mathbf{G}'}(\mathbf{q}, \omega = 0) \, e^{-i(\mathbf{G}'+\mathbf{q})\mathbf{r}'}, \tag{6.42}$$

where the Fourier components are given by

$$w_{\mathbf{G}\mathbf{G}'}(\mathbf{q}) = v_{\mathbf{G}}(\mathbf{q}) \varepsilon_{\mathbf{G}\mathbf{G}'}^{-1}(\mathbf{q}, \omega = 0). \tag{6.43}$$

Here, the dielectric function is computed in the random-phase approximation (RPA) [282] as

$$\varepsilon_{\mathbf{G}\mathbf{G}'}^{RPA}(\mathbf{q}, \omega) = \delta_{\mathbf{G}\mathbf{G}'} - \frac{1}{V_0} v_{\mathbf{G}'}(\mathbf{q}) \sum_{ij\mathbf{k}} \frac{f(\epsilon_{j\mathbf{k}+\mathbf{q}}) - f(\epsilon_{i\mathbf{k}})}{\epsilon_{j\mathbf{k}+\mathbf{q}} - \epsilon_{i\mathbf{k}} - \omega} \times \times \left[M_{ij}^{\mathbf{G}}(\mathbf{k}, \mathbf{q}) \right]^* M_{ij}^{\mathbf{G}'}(\mathbf{k}, \mathbf{q}), \tag{6.44}$$

where $f(\epsilon_{i\mathbf{k}})$ are the occupation factors of the single-particle state with energy $\epsilon_{i\mathbf{k}}$. In terms of the plane-wave matrix elements, the resonant-resonant block of Eq. 6.40 can be rewritten as

$$W_{\alpha\alpha'}^{\mathrm{rr}}(\mathbf{q}) = \frac{1}{V} \sum_{\mathbf{G}\mathbf{G}'} w_{\mathbf{G}\mathbf{G}'}(\mathbf{k} - \mathbf{k}') M_{o'o\mathbf{k}'_+}^*(\mathbf{G}, \mathbf{k} - \mathbf{k}') M_{u'u\mathbf{k}_-}(\mathbf{G}', \mathbf{k} - \mathbf{k}'). \tag{6.45}$$

The elements of the resonant-anti-resonant block can be computed as

$$W_{\alpha\alpha'}^{\mathrm{ra}}(\mathbf{q}) = \frac{1}{V} \sum_{\mathbf{G}\mathbf{G}'} w_{\mathbf{G}\mathbf{G}'}(-\mathbf{k}' - \mathbf{k}) N_{uo'\mathbf{k}_-}^*(\mathbf{G}, -\mathbf{k}' - \mathbf{k}) N_{ou'\mathbf{k}_+}(\mathbf{G}', -\mathbf{k}' - \mathbf{k}). \tag{6.46}$$

6.7 BSE as an Eigenvalue Problem

The resolvent $L(\mathbf{q}, \omega) = -\left[H(\mathbf{q}) - \omega\Delta \right]^{-1}$ of Eq. 6.28 can be found using the solutions of the generalized eigenvalue problem (the index $\mathbf{q}$ is dropped for simplicity)

$$H \begin{pmatrix} X_\lambda \\ Y_\lambda \end{pmatrix} = E_\lambda \Delta \begin{pmatrix} X_\lambda \\ Y_\lambda \end{pmatrix}, \tag{6.47}$$

where, according to Ref. [283],

$$\left[\mathsf{H} - \omega\Delta\right]^{-1} = \sum_\lambda \frac{1}{E_\lambda - \omega} \begin{pmatrix} \mathbf{X}_\lambda \\ \mathbf{Y}_\lambda \end{pmatrix} \begin{pmatrix} \mathbf{X}_\lambda \\ \mathbf{Y}_\lambda \end{pmatrix}^\dagger + \frac{1}{E_\lambda + \omega} \begin{pmatrix} \mathbf{Y}_\lambda \\ \mathbf{X}_\lambda \end{pmatrix} \begin{pmatrix} \mathbf{Y}_\lambda \\ \mathbf{X}_\lambda \end{pmatrix}^\dagger. \tag{6.48}$$

For the solution of the full BSE, a direct diagonalization scheme is adopted in `exciting`. This scheme [140, 283] maps the generalized eigenvalue problem of Eq. 6.47 onto an auxiliary eigenvalue problem of half its size. The auxiliary Hamiltonian is constructed as

$$\mathsf{S} = \left(\mathsf{A} - \mathsf{B}\right)^{\frac{1}{2}} \left(\mathsf{A} + \mathsf{B}\right) \left(\mathsf{A} - \mathsf{B}\right)^{\frac{1}{2}}, \tag{6.49}$$

and the solutions of

$$\mathsf{S}\mathbf{Z}_\lambda = E_\lambda^2 \mathbf{Z}_\lambda \tag{6.50}$$

are used to reconstruct eivenvalues and eigenvectors of Eq. 6.47. As long as $\mathsf{A} - \mathsf{B}$ and $\mathsf{A} + \mathsf{B}$ are positive definite, the solutions of Eq. 6.47 are given by

$$\mathbf{X}_\lambda + \mathbf{Y}_\lambda = \left(\mathsf{A} - \mathsf{B}\right)^{\frac{1}{2}} \frac{1}{\sqrt{E_\lambda}} \mathbf{Z}_\lambda \tag{6.51}$$

and

$$\mathbf{X}_\lambda - \mathbf{Y}_\lambda = \left(\mathsf{A} - \mathsf{B}\right)^{\frac{1}{2}} \sqrt{E_\lambda} \mathbf{Z}_\lambda. \tag{6.52}$$

For an analysis of the BSE eigenstates, we define the (resonant) exciton valence weight $w_{v\mathbf{k}}^\lambda$ and exciton conduction weight $w_{c\mathbf{k}}^\lambda$ as

$$\begin{aligned} w_{v\mathbf{k}}^\lambda &= \sum_c |X_{cv\mathbf{k},\lambda}|^2 \\ w_{c\mathbf{k}}^\lambda &= \sum_v |X_{cv\mathbf{k},\lambda}|^2. \end{aligned} \tag{6.53}$$

The valence and conduction weight represent the distribution of the hole and excited electron for a given eigenstate $\mathbf{X}_\lambda$, respectively.

6.8 Dielectric Properties from the Solutions of the BSE

From the eigenvalues E^λ and eigenvectors X_λ, the retarded polarizability is obtained following Eq. B.54 as

$$\chi_{(-\mathbf{G})(-\mathbf{G})}^R(-\mathbf{q}, \omega) = \sum_\lambda \frac{t_\lambda(\mathbf{G}, \mathbf{q}) \left[t_\lambda(\mathbf{G}, \mathbf{q})\right]^*}{\omega - E^\lambda(\mathbf{q}) + i\eta} - \frac{t_\lambda(\mathbf{G}, \mathbf{q}) \left[t_\lambda(\mathbf{G}, \mathbf{q})\right]^*}{\omega + E^\lambda(\mathbf{q}) + i\eta}, \tag{6.54}$$

where the oscillator strength $t_\lambda(\mathbf{G}, \mathbf{q})$ is defined as in Eq. B.53:

$$t_\lambda(\mathbf{G}, \mathbf{q}) = \frac{1}{\sqrt{V}} \left(X_\lambda + Y_\lambda\right)^T M(\mathbf{G}, \mathbf{q}). \tag{6.55}$$

These terms represent a sum of weighted plane-wave transition matrix elements, where the weights are computed from the corresponding BSE eigenvectors. We then obtain the macroscopic dielectric function $\varepsilon_M(\mathbf{G} + \mathbf{q}, \omega)$ following Eq. 2.15 as

$$\varepsilon_M(\mathbf{G} + \mathbf{q}, \omega) = \frac{1}{1 + v_{\mathbf{G}}(\mathbf{q}) \chi_{\mathbf{GG}}^R(\mathbf{q}, \omega)} \tag{6.56}$$

In the optical limit, *i.e.* for $\mathbf{G} = 0$ and $\mathbf{q} \to 0$, we obtain the macroscopic dielectric function as

$$\varepsilon_M(\mathbf{q} \to 0, \omega) = \frac{1}{\lim_{\mathbf{q}\to 0} \varepsilon_{00}^{-1}(\mathbf{q}, \omega)}. \tag{6.57}$$

Alternatively, an *effective polarizability* $\bar{\chi}^R$ can be employed to obtain the macroscopic dielectric tensor directly [103, 140, 261]. Details of the effective polarizability are provided in Appendix B. We obtain the dielectric tensor as

$$\epsilon_M^{ij}(\omega) = \delta_{ij} - 4\pi \sum_\lambda \left(\frac{\left[t_{\lambda,i}\right]^* t_{\lambda,j}}{\omega - E_\lambda + i\eta} + \frac{\left[t_{\lambda,i}\right]^* t_{\lambda,j}}{-\omega - E_\lambda - i\eta} \right), \tag{6.58}$$

where the oscillator strength is given in Eq. B.60 as

$$t_{\lambda,i} = \frac{1}{\sqrt{V}} \left(X_\lambda + Y_\lambda\right)^T \frac{P_i}{\Delta\epsilon}, \tag{6.59}$$

where $\mathbf{P} = \langle c\mathbf{k}|\hat{\mathbf{p}}|v\mathbf{k}\rangle$ are the momentum matrix elements and $\Delta\epsilon = \epsilon_{c\mathbf{k}} - \epsilon_{v\mathbf{k}}$.

6.9 Tamm-Dancoff Approximation

In the *Tamm-Dancoff approximation* (TDA), the coupling between resonant and antiresonant transition in the BSE Hamiltonian in Eq. 6.29 is neglected ($B(\mathbf{q}) = 0$). As such, the resonant and anti-resonant part of the Hamiltonian decouple and the eigenstates X_λ and Y_λ are identical [261]. Thus, only the reduced eigenvalue problem

$$H^{\text{TDA}}\mathbf{X}_\lambda = A\mathbf{X}_\lambda = E_\lambda\mathbf{X}_\lambda \tag{6.60}$$

has to be solved. We finally obtain the Fourier transform of the polarizability following Eq. 6.54, where the oscillator strength t_λ^{TDA} in the Tamm-Dancoff approximation is given by

$$t_\lambda^{\text{TDA}}(\mathbf{G}, \mathbf{q}) = \frac{1}{\sqrt{V}} X_\lambda^T M(\mathbf{G}, \mathbf{q}). \tag{6.61}$$

In the optical limit, the oscillator strength of Eq. 6.62 reduces in the TDA to

$$t_{\lambda,i}^{\text{TDA}} = \frac{1}{\sqrt{V}} X_\lambda^T \frac{P_i}{\Delta\epsilon}, \tag{6.62}$$

6.10 BSE Formalism for Core Spectroscopy

The procedure described above naturally applies also in the case of core spectroscopy, where the BSE is solved for transitions between core and conduction states. In this case, the initial states are naturally selected among the core levels of Eq. 6.11. Since the spin-orbit coupling of the core states is generally non-negligible, the full BSE Hamiltonian of Eq. 6.29 has to be constructed even for non-spin-polarized systems, where the spin-orbit coupling can be neglected for valence and conduction states. To reduce the size of the BSE Hamiltonian, we introduce an approximation to the spin state of the conduction electrons, such that a spinor state $\psi^{spinor}(\mathbf{r})$ is given by

$$\psi_{i\mathbf{k}}^{spinor}(\mathbf{r}) = \frac{1}{\sqrt{2}} \begin{pmatrix} 1 \\ 1 \end{pmatrix} \psi_{i\mathbf{k}}^{KS}(\mathbf{r}), \tag{6.63}$$

where $\psi_{i\mathbf{k}}^{KS}$ is the Kohn-Sham wavefunction in Eq. 6.3 obtained from a non-spin-polarized calculation. In Eq. 6.63, we thus assume that a given state of a non-spin-polarized calculation occupies the spin-up and spin-down channel equally. The approximation reduces the size of the BSE Hamiltonian by 50%.

Following the approximation above, the implementation of the momentum and plane-wave matrix elements of Eqs. 6.12 and 6.65 are modified to include core states. For the matrix elements between a core state (κ, M) and a conduction state i at $\mathbf{k}$, the interstitial contribution vanishes, and the plane-wave matrix element is given by

$$P_{(\alpha,\kappa M),i\mathbf{k}}^{j} = -\mathrm{i} \int d\Omega \; \Omega_{\kappa,M}^*(\hat{r}_\alpha) \int_{R_{MT}^\alpha} dr \; r^2 u_{\kappa,\alpha}^*(r_\alpha) \nabla_j \psi_{i\mathbf{k}}^{spinor}$$

$$= -\mathrm{i} \sum_{lm} \int d\Omega \; \frac{1}{\sqrt{2}} \Omega_{\kappa,M}^*(\hat{r}_\alpha) \begin{pmatrix} 1 \\ 1 \end{pmatrix} \int_{R_{MT}^\alpha} dr \; r^2 u_{\kappa,\alpha}^*(r_\alpha) \nabla_j \left[u_l^{i\mathbf{k}}(r) Y_{lm}(\hat{\mathbf{r}}) \right], \tag{6.64}$$

where we have used in the second line the general form of the Kohn-Sham wavefunctions of Eq. 6.3. Analogous to the MT contributions of the matrix elements between conduction and valence states, the spherical integration is performed analytically, while the radial integration is performed numerically on a grid. Plane-wave matrix elements between core and conduction states are expressed as

$$
M_{(\alpha,\kappa M),i\mathbf{k}}(\mathbf{G},\mathbf{q}) = 4\pi \sum_{lm} \sum_{l'm'} Y_{l'm'}(\widehat{G+q}) \times
$$

$$
\times \int d\Omega \, \frac{1}{\sqrt{2}} \Omega^*_{\kappa,M}(\hat{r}) \begin{pmatrix} 1 \\ 1 \end{pmatrix} Y_{l'm'}(\hat{r}) Y_{lm}(\hat{r}) \int_{R_{MT}} dr \, u^*_{\alpha,\kappa}(r) j_{l'}((G+q)r) u^{i\mathbf{k}}_l(r).
$$

(6.65)

More details about the determination of core states and the calculation of core-conduction matrix elements are given in Ref. [239].

Due to the localized nature of the excited core states, the Bethe-Salpeter formalism can be simplified for core-level excitations. We consider an unit cell with M atomic sites $\{\alpha_1, \ldots, \alpha_M\}$. Since the core wave functions are localized at a specific atomic site (see Eq. 6.11), the momentum matrix elements between any two core-wavefunctions $(\alpha_i, \kappa, M)\mathbf{k}$ and $(\alpha_j, \kappa', M')\mathbf{k}$ at different atomic sites $i \neq j$ vanishes, *i.e.*

$$
M_{(\alpha_i,\kappa,M)(\alpha_j,\kappa',M')\mathbf{k}} = \langle (\alpha_i, \kappa, M)\mathbf{k}|e^{-i(\mathbf{G}+\mathbf{q})\mathbf{r}}|(\alpha_j, \kappa', M')\rangle = 0.
$$

(6.66)

As a consequence of Eq. 6.66, the matrix elements of the direct interaction W^{rr} in Eq. 6.45 vanish, if excitations from different atomic sites are involved. The same is not true for the exchange interaction in Eq. 6.39, as the matrix elements between the core states at the different atoms and the conduction states do not vanish. Nevertheless, the exchange interaction between core excitations at different atomic sites are assumed to be small and have, to the best of our knowledge, not been considered so far. In this approximation, the BSE Hamiltonian in Eq. 6.29 takes a block-diagonal form:

$$
H^{BSE} = \begin{pmatrix} H^{BSE}_{\alpha_1} & & 0 \\ & \ddots & \\ 0 & & H^{BSE}_{\alpha_M} \end{pmatrix},
$$

(6.67)

where the matrix elements $\left[H^{BSE}_{\alpha_i} \right]_{o(\alpha_i,\kappa,M)\mathbf{k}}$ describe the excitations of the core state $(\alpha_i, \kappa, M)\mathbf{k}_+$ to the conduction state $c\mathbf{k}_-$ at the atomic site α_i. Due to the block-diagonal form of Eq. 6.67, the dielectric function is successively expressed as a sum of atomic contributions, and Eq. 6.58 becomes

$$
\varepsilon^{ij}_M(\omega) = 1 + \sum_n^M \varepsilon^{ij}_{\alpha_n}(\omega),
$$

(6.68)

where the atomic contribution $\varepsilon_{\alpha_n}^{ij}$ is given by

$$\varepsilon_{\alpha_n}^{ij}(\omega) = -4\pi \sum_{\lambda} \left(\frac{\left[t_{\lambda,i}^{\alpha_n} \right]^* t_{\lambda,j}^{\alpha_n}}{\omega - E_\lambda + i\delta} + \frac{\left[t_{\lambda,i}^{\alpha_n} \right]^* t_{\lambda,j}^{\alpha_n}}{-\omega - E_\lambda - i\delta} \right). \tag{6.69}$$

The transition coefficients $t_{\lambda,i}^{\alpha_n}$ are obtained following Eq. 6.59 considering only the eigenstates of the block Hamiltonian $H_{\alpha_i}^{BSE}$.

CHAPTER 7

Resonant Inelastic Scattering in BRIXS

The implementation of RIXS in an all-electron many-body framework requires to infer the polarizability as calculated from the solution of the BSE in Eq. B.45 into the expression Eq. 5.20 for the RIXS cross section. The double differential cross section for the RIXS process is given by

$$
\frac{d^2\sigma}{d\Omega_2 d\omega_2} = \alpha^4 \left(\frac{\omega_2}{\omega_1} \right) \text{Im} \sum_{c,c',c'',c'''} \sum_{\mu,\mu',\mu'',\mu'''} \sum_{v,v'} \sum_{\mathbf{k}\mathbf{k}'\mathbf{k}''\mathbf{k}'''}
$$

$$
\left[\left[\mathbf{e}_2^* \cdot \mathbf{P}_{\mu v \mathbf{k}} \right] \chi_{c\mu\mathbf{k},c'\mu'\mathbf{k}'}(\omega_1) \left[\mathbf{e}_1 \cdot \mathbf{P}_{c'\mu'\mathbf{k}'} \right] \right]^* \chi_{cv\mathbf{k},c''v'\mathbf{k}''}(\omega) \times
$$

$$
\times \left[\left[\mathbf{e}_2^* \cdot \mathbf{P}_{\mu''v'\mathbf{k}''} \right] \chi_{c''\mu''\mathbf{k}'',c'''\mu'''\mathbf{k}'''}(\omega_1) \left[\mathbf{e}_1 \cdot \mathbf{P}_{c'''\mu'''\mathbf{k}'''} \right] \right]
$$

$$
= \alpha^4 \left(\frac{\omega_2}{\omega_1} \right) \text{Im} \sum_{cv\mathbf{k}} \sum_{c''v'\mathbf{k}''} \left[\sum_{c'\mu'\mathbf{k}'} \sum_{\mu} \left[\mathbf{e}_2^* \cdot \mathbf{P}_{\mu v \mathbf{k}} \right] \chi_{c\mu\mathbf{k},c'\mu'\mathbf{k}'}(\omega_1) \left[\mathbf{e}_1 \cdot \mathbf{P}_{c'\mu'\mathbf{k}'} \right] \right]^* \chi_{cv\mathbf{k},c''v'\mathbf{k}''}(\omega) \times
$$

$$
\times \left[\sum_{c'''\mu'''\mathbf{k}'''} \sum_{\mu''} \left[\mathbf{e}_2^* \cdot \mathbf{P}_{\mu''v'\mathbf{k}''} \right] \chi_{c''\mu''\mathbf{k}'',c'''\mu'''\mathbf{k}'''}(\omega_1) \left[\mathbf{e}_1 \cdot \mathbf{P}_{c'''\mu'''\mathbf{k}'''} \right] \right].
$$

$$(7.1)$$

The many-body nature of the coherent excitation and emission process in RIXS are contained in the matrix-elements $\chi_{c\mu\mathbf{k},c'\mu'\mathbf{k}'}(\omega_1)$ and $\chi_{cv\mathbf{k},c''v'\mathbf{k}''}(\omega)$, which contain the sums over all possible neutral excitations of the many-body system (compare Eqs. 2.28 and 2.29). The implementation of Eq. 7.1 requires explicit access to both the matrix elements $\chi_{cv\mathbf{k},c'v'\mathbf{k}'}(\omega)$ in the basis of valence-conduction transitions, and matrix elements $\chi_{c\mu\mathbf{k},c'\mu'\mathbf{k}'}(\omega_1)$ in the basis of core-conduction transitions, but not cross terms of the form $\chi_{cv\mathbf{k},c'\mu'\mathbf{k}'}(\omega_1)$. Thus, the determination of all matrix elements of the polarizability can be separated into two independent calculations, one for the core-conduction excitations and one for the valence-conduction ones. Furthermore, momentum matrix elements $\mathbf{P}_{c\mu\mathbf{k}}$ between core and conduction states and $\mathbf{P}_{\mu v\mathbf{k}}$ between valence and core states describe the excitation and de-excitation process, respectively. The coherence between core and valence excitations in the RIXS process is apparent in Eq. 7.1 from the combined summations over $\mathbf{k}'$ and $\mathbf{k}'''$,

which enforce that core and valence excitations are calculated on the same $\{\mathbf{k}\}$-grids. The coherence occurs, since the absorption and emission processes conserve the crystal momentum $\mathbf{k}$ [284].

7.1 Polarizability Matrix Elements

At the center of our novel expression for the RIXS cross section presented in this work are the resonant matrix elements of the (longitudinal) polarizability, as obtained from many-body perturbation theory. First introduced in Chapter 2 in Eqs. 2.28 and 2.29, their explicit expression obtained from solutions of the BSE is given by Eq. B.19 in the transition space basis. Within the Tamm-Dancoff approximation, the resonant matrix elements $\chi^{R,R}_{ij\mathbf{k},i'j'\mathbf{k}'}(\omega, \mathbf{q} = 0)$ of the retarded polarizability are given by

$$\chi^{R,R}_{ij\mathbf{k},i'j'\mathbf{k}'}(\omega, \mathbf{q} = 0) = \sum_\lambda \frac{\left[X_{ij\mathbf{k},\lambda}\right]^* X_{i'j'\mathbf{k}',\lambda}}{\omega - E^\lambda + i\eta}, \tag{7.2}$$

where $X_{ij\mathbf{k},\lambda}$ and E^λ are the BSE eigenstates and -values of Eq. 6.60. Inserting the polarizability in the Tamm-Dancoff approximation is consistent with the application of the TDA as defined in Eq. 1.59 in the derivation of RIXS cross section in Eq. 7.1. Note that the polarizability in Eq. 7.2 is transposed with respect to the one for the polarizability in Eq. 6.48. Here, we consider matrix elements of the *retarded polarizability*, while in Chapter 6 matrix elements of the time-ordered ones are provided as obtained from the Lehmann representation with respect to $\tau^{(1)}$. For the relationship between them, see Appendix B. As shortly discussed in Section 3.4, the polarizability is evaluated in the RIXS cross section for two very different energy scales, once for the excitation energy ω_1, which is typically in the hard x-ray region, and then for the energy loss $\omega = \omega_1 - \omega_2$, which is typically in the range of eV or tens of eV. Since transitions mix in the Bethe-Salpeter equation only over a limited range of energy [63], the mixing of core transitions $\mu\mathbf{k} \to c\mathbf{k}$ and valence transitions $v\mathbf{k} \to c\mathbf{k}$, which are typically separated by several hundred eV, can be neglected. This allows us to neatly separate the transitions in Eq. 7.1 into valence and core transitions. Note that due the presence of momentum matrix elements $\mathbf{P}_{\mu v\mathbf{k}}$ in Eq. 7.1, any expression for the RIXS DDCS cannot be written in the transition space of valence and core excitations alone, but furthermore contains terms that connect the two spaces.

7.2 Oscillator Strength and Excitation Pathways

The implementation of Eq. 7.1 appears as a daunting task, since it requires four summations over conduction and core states and two sums over valence states. However, employing the structure of the summations and inserting the explicit form of the polarizability in Eq. 7.2 yields a much more compact expression for the RIXS cross section, which furthermore allows for an intuitive interpretation of the many-body process.

First, we consider the last bracket of Eq. 7.1 and insert Eq. 7.2:

$$
\sum_{c'''\mu'''\mathbf{k}'''} \sum_{\mu''} \left[\mathbf{e}_2^* \cdot \mathbf{P}_{\mu''v'\mathbf{k}''} \right] \chi_{c''\mu''\mathbf{k}'',c'''\mu'''\mathbf{k}'''}(\omega_1) \left[\mathbf{e}_1 \cdot \mathbf{P}_{c'''\mu'''\mathbf{k}'''} \right]
$$

$$
= \sum_{c'''\mu'''\mathbf{k}'''} \sum_{\mu''} \sum_{\lambda_c} \left[\mathbf{e}_2^* \cdot \mathbf{P}_{\mu''v'\mathbf{k}''} \right] \frac{\left[X_{c''\mu''\mathbf{k}'',\lambda_c} \right]^* X_{c'''\mu'''\mathbf{k}''',\lambda_c}}{\omega_1 - E^{\lambda_c} + i\eta} \left[\mathbf{e}_1 \cdot \mathbf{P}_{c'''\mu'''\mathbf{k}'''} \right] \qquad (7.3)
$$

$$
\equiv \sum_{\mu''} \sum_{\lambda_c} \left[\mathbf{e}_2^* \cdot \mathbf{P}_{\mu''v'\mathbf{k}''} \right] \frac{\left[X_{c''\mu''\mathbf{k}'',\lambda_c} \right]^* t_{\lambda_c}^{(1)}}{\omega_1 - E^{\lambda_c} + i\eta},
$$

where E^{λ_c} and $X_{c\mu,\lambda_c}$ are the eigenvalues and eigenvectors of the core-level BSE Hamiltonian. In the last line of Eq. 7.3, we have defined the *core excitation oscillator strength* $t_{\lambda_c}^{(1)}$ as

$$
t_{\lambda_c}^{(1)} = \sum_{c'''\mu'''\mathbf{k}'''} X_{c'''\mu'''\mathbf{k}''',\lambda_c} \left[\mathbf{e}_1 \cdot \mathbf{P}_{c'''\mu'''\mathbf{k}'''} \right]. \qquad (7.4)
$$

Note that the oscillator strength is closely related to the transition coefficients $t^{\lambda_c}(\mathbf{G} = 0, \mathbf{q} \to 0)$ in Eq. 6.55. The core single-particle energies are typically much larger than those of the conduction states, *i.e.* $|\epsilon_{\mu\mathbf{k}}| \gg \epsilon_{c\mathbf{k}}$, and are independent of momentum, *i.e.* $\epsilon_{\mu\mathbf{k}} = \epsilon_\mu$ as the core wavefunctions are fully localized at an atomic site. Then, the energy difference $\epsilon_{c\mathbf{k}} - \epsilon_{\mu\mathbf{k}}$ is approximately constant for all transitions, and the transition coefficient is connected to the oscillator strength $t_{\lambda_c}(\mathbf{G}, \mathbf{q})$ of core excitations as $t_{\lambda_c}^{(1)} \propto t_{\lambda_c}^*(\mathbf{G} = 0, \mathbf{q} = \mathbf{e}_1)$. These two quantities are closely related, as $t_{\lambda_c}^{(1)}$ describes the absorption step in the RIXS process.

Inserting Eq. 7.3 into Eq. 7.1 yields

$$
\frac{\mathrm{d}^2\sigma}{\mathrm{d}\Omega_2\mathrm{d}\omega_2} = \alpha^4 \left(\frac{\omega_2}{\omega_1}\right) \mathrm{Im} \sum_{\lambda_c,\lambda_c',\lambda_o} \sum_{c,c''} \sum_{v,v'} \sum_{\mathbf{k}\mathbf{k}''}
$$

$$
\left[\sum_{\mu} \frac{t_{\lambda_c'}^{(1)} \left[X_{c\mu\mathbf{k},\lambda_c'}\right]^* \left[\mathbf{e}_2^* \cdot \mathbf{P}_{\mu v\mathbf{k}}\right]}{\omega_1 - E^{\lambda_c'} + i\eta}\right]^* \frac{\left[X_{cv\mathbf{k},\lambda_o}\right]^* X_{c''v'\mathbf{k}''',\lambda_o}}{\omega - E^{\lambda_o} + i\eta} \left[\sum_{\mu''} \frac{\left[\mathbf{e}_2^* \cdot \mathbf{P}_{\mu''v'\mathbf{k}''}\right] \left[X_{c''\mu''\mathbf{k}'',\lambda_c}\right]^* t_{\lambda_c}^{(1)}}{\omega_1 - E^{\lambda_c} + i\eta}\right],
$$

$$
(7.5)
$$

where Eq. 7.2 is used to write the matrix elements $\chi_{cv\mathbf{k},c''v'\mathbf{k}'}(\omega)$ in terms of the eigenvectors $X_{cv\mathbf{k},\lambda_o}$ and eigenvalues E^{λ_o} of the BSE Hamiltonian of valence-conduction transitions. Here, we discern the index of the valence-conduction excitations, λ_o, from the index λ_c of the core-conduction ones.

The shape of Eq. 7.5 suggests to define the *excitation pathway* $t_{\lambda_o,\lambda_c}^{(2)}$ as

$$
t_{\lambda_o,\lambda_c}^{(2)} = \sum_{cv\mathbf{k}} \sum_{\mu} X_{cv\mathbf{k},\lambda_o} \left[\mathbf{e}_2^* \cdot \mathbf{P}_{\mu v\mathbf{k}}\right] \left[X_{c\mu\mathbf{k},\lambda_c}\right]^*, \tag{7.6}
$$

which can be inserted in Eq. 7.5 to obtain

$$
\frac{\mathrm{d}^2\sigma}{\mathrm{d}\Omega_2\mathrm{d}\omega_2} = \alpha^4 \left(\frac{\omega_2}{\omega_1}\right) \mathrm{Im} \sum_{\lambda_o} \frac{\left|\sum_{\lambda_c} \frac{t_{\lambda_o,\lambda_c}^{(2)} t_{\lambda_c}^{(1)}}{\omega_1 - E^{\lambda_c} + i\eta}\right|^2}{(\omega_1 - \omega_2) - E^{\lambda_o} + i\eta}. \tag{7.7}
$$

We define the *RIXS oscillator strength* $t_{\lambda}^{(3)}(\omega_1)$ as

$$
t_{\lambda_o}^{(3)}(\omega_1) = \sum_{\lambda_c} \frac{t_{\lambda_o,\lambda_c}^{(2)} t_{\lambda_c}^{(1)}}{\omega_1 - E^{\lambda_c} + i\eta}. \tag{7.8}
$$

Using the definition of the oscillator strength $t_{\lambda_c}^{(1)}$ in Eq. 7.4 and the excitation pathway $t_{\lambda_o,\lambda_c}^{(2)}$ in Eq. 7.6 allows for the compact expression for the RIXS cross section as

$$
\frac{\mathrm{d}^2\sigma}{\mathrm{d}\Omega_2\mathrm{d}\omega_2} = \alpha^4 \left(\frac{\omega_2}{\omega_1}\right) \mathrm{Im} \sum_{\lambda_o} \frac{|t_{\lambda_o}^{(3)}(\omega)|^2}{(\omega_1 - \omega_2) - E^{\lambda_o} + i\eta}, \tag{7.9}
$$

which strongly resembles the expression for the optical absorption spectrum in Eq. 6.58. The dependence of the cross section on the energy loss $\omega = \omega_1 - \omega_2$ is given explicitly, while that on the excitation energy is contained in the oscillator strength $t_{\lambda_o}^{(3)}(\omega_1)$. The cross
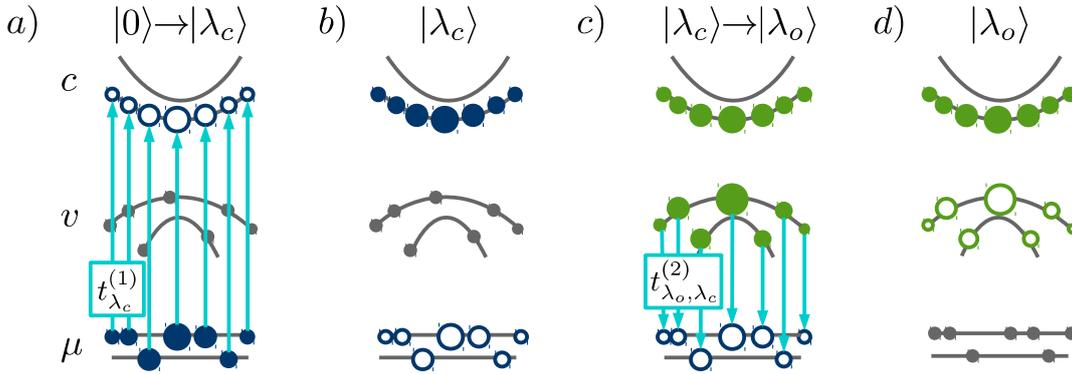
Figure 7.1: Schema of RIXS process taken from Ref. [361]: a) A core excitation yields b) the intermediate many-body state $|\lambda_c\rangle$. c) The subsequent de-excitation leads to d) the final state $|\lambda_o\rangle$. The distribution of the excited electron is shown as filled circles, those of the hole in open circles. Blue circles indicate the intermediate state, green ones the final one. Cyan arrows show dipole transitions.

section has poles in energy loss at the optical excitation energies E^{λ_o} of the system, independent of the excitation energy, while the oscillator strength of each of these excitations depends on the excitation energy. Furthermore, the definition of the oscillator strength in Eq. 7.8 gives further insight into the many-body processes that occur in RIXS. Schematically, these processes are shown in Fig. 7.1. The rate of the initial x-ray absorption event is given by $t^{(1)}_{\lambda_c}$, combined with the energy conservation rule (the denominator $\omega_1 - E^{\lambda_c} + i\eta$ in Eq. 7.8). The absorption leads to an intermediate core-excited state, characterized by the excitation index λ_c (schematically shown in Fig. 7.1). The final RIXS spectrum is then given by the rate of the absorption combined with the pathway $t^{(2)}_{\lambda_o,\lambda_c}$ that describes the many-body transition $|\lambda_c\rangle \rightarrow |\lambda_o\rangle$ (see Fig. 7.1). These pathways are far from obvious, for the mixing between $t^{(1)}_{\lambda_c}$ and $t^{(2)}_{\lambda_o,\lambda_o}$ can develop in destructive or constructive interference, attesting the many-body character of such process.

7.3 Coherence in Reciprocal Space

The expression for the RIXS cross sections through the core oscillator strength and excitation pathway involves sums over all possible excitation and emission pathways in the system. From early RIXS experiments, it has been observed that independent-particle calculations following Eq. 5.10 only explains a fraction of the observed spectra, the so-called *coherent scattering* [170]. This coherent contribution originates from processes, where both the absorption and the emission process occur at one **k**-point in reciprocal space. The coherent scattering is schematically shown in Fig. 7.2. In this process, the crystal momentum

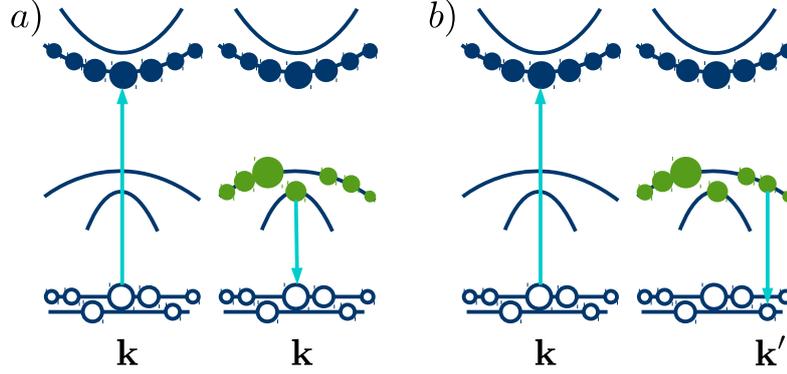**Figure 7.2:** a) Coherent RIXS process: Both the excitation of the core state and the de-excitation of the valence state occur at the same point **k** in reciprocal space. b) Incoherent RIXS process: The core electron is excited at point **k**. The electron-core hole pair scatters to the point **k'**, where the core hole is filled through the de-excitation of a valence electron.

k is conserved, as required within the IPA. The *incoherent scattering* originates from processes where the absorption occurs at a point **k** in reciprocal space, while the emission occurs at a different point **k'**. The incoherent scattering can only occur if the excited electron and the core hole are distributed over several **k**-points due to either electron-phonon or electron-hole scattering. The contribution of the incoherent scattering has been estimated to be around 40% for the RIXS cross section at the carbon K edge in diamond [262] and the silicon $L_{2,3}$ edge in silicon [285]. While *ab initio* methods have been developed to account for the incoherent contribution due to electron-phonon interaction [210, 227], the incoherent contribution due to electron-hole interaction has not been determined so far. In this chapter, we show how our novel *ab initio* approach to RIXS allows us to disentangle the coherent and incoherent contributions and to estimate how strongly the electron-hole interaction affects the coherence in reciprocal space.

Both coherent and incoherent scattering are included in the RIXS cross section in Eq. 5.20. The latter is contained in Eq. 5.20 solely due to electron-hole scattering as electron-phonon interaction are neglected in our calculations. To separate coherent and incoherent contributions, we first make the summations over **k**-points in Eq. 7.8 explicit:

$$
\begin{aligned}
t_{\lambda_o}^{(3)}(\omega) &= \sum_{\lambda_c} \frac{t_{\lambda_o,\lambda_c}^{(2)} t_{\lambda_c}^{(1)}}{\omega - E^{\lambda_c} + \mathrm{i}\delta} \\
&= \sum_{\lambda_c} \sum_{cv,\mu} \sum_{\mathbf{k}} \sum_{c'\mu'} \sum_{\mathbf{k'}} \frac{X_{cv\mathbf{k},\lambda_o} \left[\mathbf{e}_2^* \cdot \mathbf{P}_{\mu v\mathbf{k}} \right] \left[X_{c\mu\mathbf{k},\lambda_c} \right]^* X_{c\mu\mathbf{k'},\lambda_c} \left[\mathbf{e}_1 \cdot \mathbf{P}_{c\mu\mathbf{k'}} \right]}{\omega - E^{\lambda_c} + \mathrm{i}\eta}.
\end{aligned}
$$

(7.10)

In Eq. 7.10, the excitation into the excited state $|\lambda_c\rangle$ occurs at $\mathbf{k}'$, since this is where the momentum matrix element $\mathbf{P}_{c\mu\mathbf{k}'}$ is evaluated. The de-excitation occurs at $\mathbf{k}$, where the momentum matrix element $\mathbf{P}_{\mu v\mathbf{k}}$ is evaluated. These two $\mathbf{k}$-points do not have to be identical if the BSE eigenstate $X_{c\mu\mathbf{k},\lambda_c}$ has non-negligible contributions at both $\mathbf{k}'$ and at $\mathbf{k}$. Reformulating the summation over $\mathbf{k}'$ and $\mathbf{k}'$ as $\sum_{\mathbf{k},\mathbf{k}'} = \sum_{\mathbf{k}} + \sum_{\mathbf{k}} \sum_{\mathbf{k}'\neq\mathbf{k}}$, we can disentangle coherent and incoherent processes (see Fig. 7.2), where we identify the first term to represent the coherent scattering, the second one to represent the incoherent scattering. With this separation, we obtain

$$t_{\lambda_o}^{(3)}(\omega) = \sum_{\lambda_c} \frac{t_{\lambda_o,\lambda_c}^{\mathrm{coh}} + t_{\lambda_o,\lambda_c}^{\mathrm{incoh}}}{\omega - E^{\lambda_c} + \mathrm{i}\delta}, \tag{7.11}$$

where the *coherent contribution* $t_{\lambda_o,\lambda_c}^{\mathrm{coh}}$ is defined as

$$t_{\lambda_o,\lambda_c}^{\mathrm{coh}} = \sum_{cv,\mu} \sum_{c'v',\mu'} \sum_{\mathbf{k}} X_{cv\mathbf{k},\lambda_o} \left[\mathbf{e}_2^* \cdot \mathbf{P}_{\mu v\mathbf{k}} \right] \left[X_{c\mu\mathbf{k},\lambda_c} \right]^* X_{c\mu\mathbf{k},\lambda_c} \left[\mathbf{e}_1 \cdot \mathbf{P}_{c\mu\mathbf{k}} \right] \tag{7.12}$$

and represents all the contributions, where absorption and emission occur at the same $\mathbf{k}$-point. The *incoherent contribution* $t_{\lambda,\lambda'}^{\mathrm{incoh}}$ is given by

$$t_{\lambda_o,\lambda_c}^{\mathrm{incoh}} = \sum_{cv,\mu} \sum_{c'v',\mu'} \sum_{\mathbf{k}} \sum_{\mathbf{k}'\neq\mathbf{k}} X_{cv\mathbf{k},\lambda_o} \left[\mathbf{e}_2^* \cdot \mathbf{P}_{\mu v\mathbf{k}} \right] \left[X_{c\mu\mathbf{k},\lambda_c} \right]^* X_{c\mu\mathbf{k}',\lambda_c} \left[\mathbf{e}_1 \cdot \mathbf{P}_{c\mu\mathbf{k}'} \right] \tag{7.13}$$

and represents RIXS processes, where the absorption occurs at $\mathbf{k}'$, while the emission occurs at $\mathbf{k}$.

7.4 Atomic Coherence

For a system with M inequivalent atoms $\gamma_1, .., \gamma_M$, each with multiplicity N_γ, any summations over core excitations γ_c can be separated into atomic contributions, *i.e.* $\sum_{\lambda_c} = \sum_\gamma^M N_\gamma \sum_{\lambda_{c,\gamma}}$, where $\lambda_{c,\gamma}$ are the core excitations of atom γ. With this separation of the core excitations in atomic contributions, which is discussed in Section 6.10 in more detail, the RIXS oscillator strength in Eq. 7.8 becomes

$$t_{\lambda_o}^{(3)}(\omega_1) = \sum_\gamma N_\gamma \sum_{\lambda_{c,\gamma}} \frac{t_{\lambda_o,\lambda_{c,\gamma}}^{(2)} t_{\lambda_{c,\gamma}}^{(1)}}{\omega_1 - E^{\lambda_{c,\gamma}} + \mathrm{i}\eta} = \sum_\gamma N_\gamma t_{\lambda_o,\gamma}^{(3)}(\omega_1). \tag{7.14}$$

Here, we have introduced the atomic RIXS oscillator strength $t^{(3)}_{\lambda_o,\gamma}(\omega)$ as

$$t^{(3)}_{\lambda_o,\gamma}(\omega_1) = \sum_{\lambda_c,\gamma} \frac{t^{(2)}_{\lambda_o,\lambda_c,\gamma} t^{(1)}_{\lambda_c,\gamma}}{\omega_1 - E^{\lambda_c,\gamma} + i\eta} \tag{7.15}$$

While the RIXS oscillator strength is a sum of the atomic contributions, interference terms occur in the RIXS cross section, since $\frac{d^2\sigma}{d\Omega_2 d\omega_2} \propto |t^{(3)}(\omega_1)|^2$. Equivalent atoms in the unit cell do not contribute to the interference terms, since the excitonic eigenstates and eigenenergies of equivalent atoms are identical (compare Section 6.10). We can then define the atomic double-differential cross section as

$$\frac{d^2\sigma_\gamma}{d\Omega_2 d\omega_2} = \alpha^4 \left(\frac{\omega_2}{\omega_1}\right) \text{Im} \sum_{\lambda_o} \frac{\left|t^{(3)}_{\lambda_o,\gamma}(\omega_1)\right|^2}{\omega - E^{\lambda_o} + i\eta}, \tag{7.16}$$

which represents the RIXS double-differential cross section at the specific atom γ. The total RIXS cross section is then the sum of all atomic terms and the interference term $d^2\sigma_{\text{interf}}/d\Omega_2 d\omega_2$, such that

$$\frac{d^2\sigma}{d\Omega_2 d\omega_2} = \sum_\gamma N_\gamma^2 \frac{d^2\sigma_\gamma}{d\Omega_2 d\omega_2} + \frac{d^2\sigma_{\text{interf}}}{d\Omega_2 d\omega_2}. \tag{7.17}$$

To quantify the contribution of an atom γ to the RIXS spectrum at a given excitation energy ω_1, we define the relative atomic contribution $\Delta\sigma_\gamma(\omega_1)$ as

$$\Delta\sigma_\gamma(\omega_1) = \frac{N_\gamma^2 \int \frac{d^2\sigma_\gamma}{d\Omega_2 d\omega_2} d\omega}{\int \frac{d^2\sigma}{d\Omega_2 d\omega_2} d\omega}, \tag{7.18}$$

which obey $\sum_\gamma \Delta\sigma_\gamma(\omega_1) + \Delta\sigma_{\text{interf}}(\omega_1) = 1$ for each excitation energy ω_1.

7.5 Limitations of Transition-Space Representation

The core oscillator strength $t^{(1)}_{\lambda_c}$, the excitation pathways $t^{(2)}_{\lambda_o,\lambda_c}$, and the RIXS oscillator strength $t^{(3)}_{\lambda_o}(\omega)$ can readily be calculated once the excitonic eigenstates of the valence excitations $X_{cv\mathbf{k},\lambda_o}$ and of the core excitations $X_{c\mu\mathbf{k},\lambda_c}$, and the corresponding excitation energies E^{λ_o} and E^{λ_c}, are obtained from two BSE calculations. Yet, the combination of the valence- and the core-level BSE calculations requires a transformation between matrix representations in different vector spaces. In Section 6.3, the transition space is introduced, such that

a one-dimensional transition-space index α represents the combination of a valence-state index v, a conduction-state c, and a $\mathbf{k}$-point, *i.e.* $\alpha \leftrightarrow \{o, u, \mathbf{k}\}$. With this *transition-space* representation, the Bethe-Salpeter equation can be expressed as a two-dimensional matrix equation. More explicitly, we define a bijective function f_T that provides a transition index α for each combination $(c, v, \mathbf{k})$ of a conduction state $(c\mathbf{k})$ and a valence state $(v\mathbf{k})$, such that

$$f_T(c, v, \mathbf{k}) = \alpha \quad f_T^{-1}(\alpha) = (c, v, \mathbf{k}). \tag{7.19}$$

For any three-dimensional array A with entries $A[c, v, \mathbf{k}]$, there is a corresponding column-vector $\hat{A}$ in transition space, such that $\hat{A}[\alpha, 1] = \hat{A}[f_T(c, v, \mathbf{k}), 1]$. Equivalently, for any four-dimensional array B with entries $B[c, v, \mathbf{k}, \lambda]$, there is a corresponding 2-dimensional array $\hat{B}$, such that $\hat{B}[\alpha, \lambda] = B[f_T(c, v, \mathbf{k}), \lambda]$. Using this notation, the column vector of core excitation oscillator strength $\hat{t}^{(1)}$ of Eq. 7.4 is obtained as

$$\hat{t}^{(1)} = \hat{X}^c \times \left[\mathbf{e}_1 \cdot \mathbf{P} \right], \tag{7.20}$$

where $\hat{X}^c$ is the eigenvector matrix $\hat{X}^c_{\alpha, \alpha'} = X_{c\mu\mathbf{k}, \lambda_c}$ of the core excitations. As such, the oscillator strength $t^{(1)}$ is calculated as a vector in the transition space of the core-conduction BSE Hamiltonian. For the excitation pathway $t^{(2)}$, a calculation within the transition space of the core-conduction or the valence-conduction BSE Hamiltonian is not possible, as these pathways connect the transition spaces. We therefore define an intermediate matrix I as

$$I = \left[X^c \right]^* \times \left[\mathbf{e}_2^* \cdot \mathbf{P} \right]. \tag{7.21}$$

The matrix multiplication in Eq. 7.21 is performed for each $\mathbf{k}$-point and core excitation index λ_c, such that matrix elements are given in single-particle space as

$$I_{c, v, \mathbf{k}, \lambda_c} = \sum_{\mu} \left[\mathbf{e}_2^* \cdot \mathbf{P}_{\mu, v, \mathbf{k}} \right] \left[X^c_{c, \mu, \mathbf{k}, \lambda_c} \right]^*. \tag{7.22}$$

The 4-dimensional matrix I is subsequently transformed to a two-dimensional matrix $\hat{I}$ in the transition space of the valence-conduction BSE Hamiltonian, with matrix elements $\hat{I}_{f_T(c, v, \mathbf{k}), \lambda_c}$. The matrix $\hat{t}^{(2)}$ is then obtained as $\hat{I}$

$$\hat{t}^{(2)} = \left[\hat{X}^o \right]^T \times \hat{I}. \tag{7.23}$$

Finally, the RIXS oscillator strength is obtained as

$$\hat{t}^{(3)}(\omega) = \hat{t}^{(2)} \times \left[\Delta E^{-1}(\omega) \right] \times t^{(1)}, \tag{7.24}$$

where we have defined the matrix ΔE^{-1} as

$$\Delta E^{-1}(\omega)_{\lambda\lambda'} = \frac{\delta_{\lambda\lambda'}}{(\omega - E^\lambda + i\eta)}. \tag{7.25}$$

The RIXS cross section is finally obtained from $\hat{t}^{(3)}$ through a Lorentzian convolution as seen in Eq. 7.7.

7.6 Block Matrix Formulation

Generally, the matrix sizes of both the oscillator strength and the excitation pathway are considerable. The size of the transition space for the core calculation is given by $N_{\text{core}} = n_c \times n_\mu \times n_{\mathbf{k}}$, where n_c is the number of conduction bands, n_μ the number of core states, and $n_{\mathbf{k}}$ the number of $\mathbf{k}$-points in the calculation. The corresponding size of the valence transition space is given by $N_{\text{optics}} = n_c \times n_v \times n_{\mathbf{k}}$, where n_v is the number of valence bands. Considering the example of the C K edge RIXS of diamond in Section 8.2, the matrix sizes are $N_{\text{core}} \approx 176,000$ and $N_{\text{optics}} \approx 88,000$. Therefore, the memory-intensive matrix-matrix multiplications become the bottleneck of the calculations. As such, explicit matrix-matrix multiplication is avoided in the implementation. Rather, we separate every matrix in transition space into N_{blocks} smaller rectangle block matrices. Any matrix-matrix multiplication $\hat{C} = \hat{A} \times \hat{B}$ is then replaced by the expression for a block $\hat{C}_{ij}$, as $\hat{C}_{ij} = \sum_k^{N_{\text{blocks}}} \hat{A}_{ik} \times \hat{B}_{kj}$. Thus, each multiplication is replaced by N_{blocks} multiplications of matrices with smaller size. This way, a block $\hat{t}_i^{(1)}$ of the core oscillator strength is given as

$$\hat{t}_i^{(1)} = \sum_k^{N_{\text{blocks}}} \left[\hat{X}_{ki}\right]^T \times \left[\mathbf{e}_1 \cdot \mathbf{P}\right]_k. \tag{7.26}$$

The pathway $t^{(2)}$ cannot be obtained by algebraic operations in the transition space of the optical or the core transitions, since the pathway connects the excitations by the transitions $v \rightarrow \mu$ that are not included in either transition space. For each excitation λ_c and $\mathbf{k}$-point, the block matrix $\tilde{I}_{:,:,\mathbf{k},i}$ is obtained by matrix multiplication as

$$\tilde{I}_{:,:,\mathbf{k},\lambda_c} = \left[\tilde{X}_{:,:,\mathbf{k},\lambda_c}\right]^* \times \left[\mathbf{e}_2^* \cdot \tilde{\mathbf{P}}\right]_{:,:,\mathbf{k}}^T, \tag{7.27}$$

where $(:,:)$ indicates that $\tilde{I}$, $\left[\mathbf{e}_2^* \cdot \tilde{\mathbf{P}}\right]$, and $\tilde{X}$ are matrices with the dimensionality of (n_c, n_v), and (n_c, n_μ), respectively, for each $\mathbf{k}$-point and excitation λ_c. Typically, the number of transitions at each $\mathbf{k}$-point is small enough both for the core and optical transitions, such that the matrix multiplication in Eq. 7.27 can be performed directly. Each entry of $\tilde{I}_{c,v,\mathbf{k},\lambda_c}$ can be

mapped to an entry $I_{(cv\mathbf{k}),\lambda_c}$ in the optical transition space. Then, blocks of the excitation pathway $t_{ij}^{(2)}$ are obtained as

$$t_{ij}^{(2)} = \sum_{k,l}^{N_{\text{blocks}}} \left[X_{ki} \right]^T \times I_{kj}.$$

(7.28)

Finally, blocks $t_{ij}^{(3)}(\omega_1)$ of the RIXS oscillator strength are obtained as

$$t_{ij}^{(3)}(\omega) = \sum_{kl}^{N_{\text{blocks}}} t_{ik}^{(2)} \times \left[\Delta E^{-1}(\omega_1) \right]_{kl} \times t_l^{(1)}.$$

(7.29)

Note that only the oscillator strength in Eq. 7.29 depends on the excitation energy ω_1 through the matrix elements of ΔE^{-1} defined in Eq. 7.25, such that $t^{(1)}$ and $t^{(2)}$ can be calculated only once and then written to file.

7.7 The BRIXS and pyBRIXS Codes

```
bse_output.h5
└── eigvec-singlet-TDA-BAR-full
    └── 0001
        ├── parameters
        │   ├── koulims(4, Nk)
        │   ├── smap(3, Nλtotal)
        │   └── ensortidx(Nλtotal)
        ├── evals(Nλ)
        ├── evalsIP(Nλtotal)
        └── indexλ(2, Nλtotal)
```
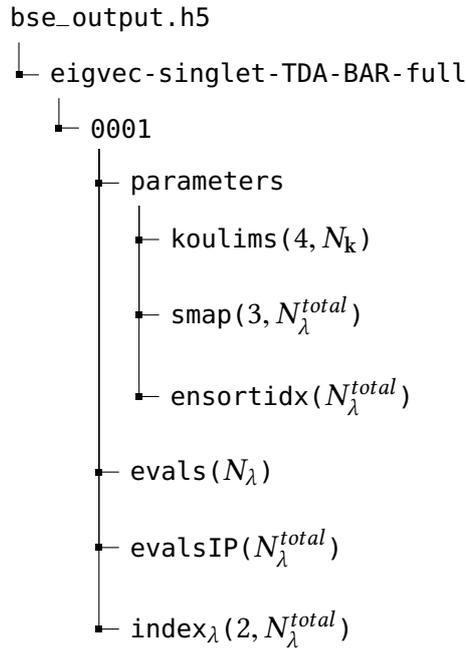
Figure 7.3: Expected structure of the HDF5 output file *bse_output.h5* of a BSE calculation.

The block-matrix formalism described in the previous section is implemented in the FORTRAN90 code **BRIXS** (**B**SE Calculations for **RIXS**). The code takes the output of two BSE calculations, where one determines the eigenstates $X_{cv\mathbf{k},\lambda_o}$ and energies E^{λ_o} of the optical excitations, the other the corresponding eigenstates $X_{c\mu\mathbf{k},\lambda_c}$ and energies E^{λ_c} for the core excitations at a specific absorption edge for a given atom in the unit cell, and calculates the core excitation oscillator strength $t^{(1)}$, the excitation pathway matrix $t^{(2)}$, and finally the RIXS oscillator strength $t^{(3)}(\omega)$. A calculation with BRIXS requires the execution of two independent programs: The first one, named BRIXS-pathway determines the matrices $t^{(1)}$ and $t^{(2)}$ and

writes them to file. The second one, BRIXS-oscstr takes the output of the previous program and generates the matrix $t^{(3)}(\omega)$ and writes it to file. The separation is beneficial since BRIXS-pathway does not require the excitation frequency ω as the input. As such, it can be executed once and the output can be employed to calculate $t^{(3)}(\omega)$ for any set of excitation energies, without performing redundant calculations. As the determination of the double-differential cross section $\frac{\mathrm{d}^2\sigma}{\mathrm{d}\Omega_2\mathrm{d}\omega_2}$ from the RIXS oscillator strength following Eq. 7.7 is trivial, the BRIXS code does not generate the final RIXS spectrum. The RIXS spectra can then be generated for arbitrary values of the energy loss $\omega_1 - \omega_2$ and with arbitrary values for the lifetime broadening η from the output of the BRIXS code. A convenient way to generate RIXS spectra is provided by the pyBIRXS module, which contains objects that store the results of the BRIXS calculations, generate RIXS spectra, and provide several ways to visualize results. In this section, we will describe the structure of the BRIXS code and discuss the structure of the input and output files. Additionally, we present the objects contained in the pyBRIXS module.

7.7.1 Structure of Input and Output Files

BRIXS requires the output of two BSE calculations performed with the exciting code [359, 254]. The code parses the output of the BSE calculations, one for the optical and one for the core excitations, provided in the Hierarchical Data Format, version 5 (HDF5) [286], and the output of BRIXS is generated in the same file format. The code requires four input files: files named *core_output.h5* and *optical_output.h5* contain the output of the corresponding BSE calculations, the momentum matrix elements are provided in the file *pmat.h5*. Finally, the text-file *input.cfg* contains additional input parameters for the RIXS calculation, which are described in more detail in Section 7.7.2. The files *optical_output.h5* and *core_output.h5* have the same structure shown in Fig. 7.3. Let us consider a BSE calculation on a grid of $N_\mathbf{k}$ $\mathbf{k}$-points, where the BSE Hami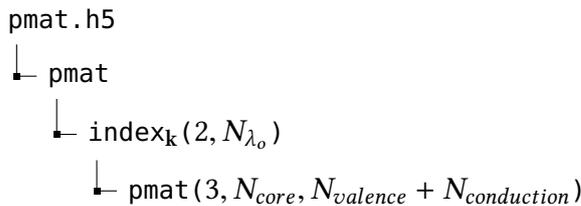ltonian has a size of N_λ^{total}. A smaller number $N_\lambda \leq N_\lambda^{total}$ of BSE eigenvectors and eigenvalues are stored to files. The output file *bse_output.h5* is required to contain a group named "parameters" containing the following 3 arrays (compare Fig. 7.3): "koulims" is an integer array of shape $(4, N_\mathbf{k})$, which, for each $\mathbf{k}$-point, contains the index of low-

```
pmat.h5
└─ pmat
    └─ index_k(2, N_{λ_o})
        └─ pmat(3, N_core, N_valence + N_conduction)
```

Figure 7.4: Structure of the file pmat.h5 that contains the momentum matrix elements.

est conduction state [koulims$(1, \mathbf{k})$], the highest conduction state [koulims$(2, \mathbf{k})$], the lowest valence state [koulims$(3, \mathbf{k})$], and the highest valence state [koulims$(4, \mathbf{k})$] of the BSE Hamiltonian. The array "smap" is an integer array containing the transition-space map

defined in Eq. 7.19 between the transition space and the single-particle indices, such that $smap(:, \alpha) = f_T^{-1}(\alpha) = (c, v, \mathbf{k})$. Finally, the integer array "ensortidx" contains all transition space indices α, sorted such that the energy-differences $\Delta\epsilon(\alpha) = \epsilon_{c\mathbf{k}} - \epsilon_{v\mathbf{k}}$ are increasing. The latter is required to calculate the RIXS cross section in the IPA. The main data are the BSE eigenvalues E^λ stored in the real-valued dataset "evals", the IPA eigenvalues $E_{IP}^\alpha = \epsilon_{c\mathbf{k}} - \epsilon_{v\mathbf{k}}$ in the real-valued dataset "evalsIP", and the BSE eigenstates, which each have their own dataset.

```
data.h5
├── t(1)(2, N_{λ_c})
├── t(2)(2, N_{λ_o}, N_{λ_c})
└── evals(N_{λ_c})
```
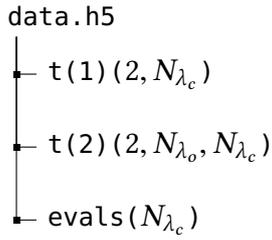
Figure 7.5: Structure of the HDF5 file *data.h5* that contains intermediate output of a BRIXS calculation.

Each BSE eigenstate is stored in an individual dataset, the name of which is generated as an 8-digit string with leading zeros of the excitation index λ, *i.e.* the file contains datasets 00000001, 00000002, and so forth, each containing an excitonic eigenstate. The names of the datasets are denoted as index_λ in Fig. 7.3, as the names are generated from the λ-index. Due to this naming convention, no more than 10^8 excitonic eigenstates can be stored. Each of the datasets contains a vector that has the length of the full transition-space size N_λ^{total}. Since the HDF5 format does not have datatype for complex numbers, the additional dimension of size 2 contains the real and imaginary part for each entry. The file *pmat.h5* contains both the momentum matrix elements $\mathbf{P}_{\mu v\mathbf{k}}$ between the core and valence states, as well as the matrix elements $\mathbf{P}_{\mu c\mathbf{k}}$ between core and conduction states, as defined in Eq. 6.64. The file contains a number of groups, the name of which is a 8-digit string generated from the index of the $\mathbf{k}$-points, *i.e* the groups are named 00000001, 00000002, and so forth. We note that this naming convention limits the $\mathbf{k}$-grid to 10^8 $\mathbf{k}$-points. Each of these groups contains a dataset named pmat of dimension $(3, N_{core}, N_{valenc} + N_{conduction})$, where N_{core} is the number of core states, $N_{valence}$ is the number of valence states, and $N_{conduction}$ is the number of the conduction states. Note that these numbers refer to the DFT calculations for the electronic structure underlying the BSE calculations, and more states might be included than are contained in the BSE Hamiltonian.
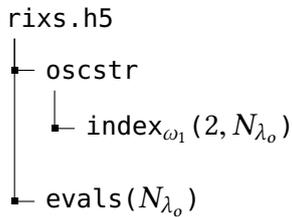
```
rixs.h5
├── oscstr
│   └── index_{ω_1}(2, N_{λ_o})
└── evals(N_{λ_o})
```

Figure 7.6: Structure of the HDF5 file *rixs.h5*, which contains the main output of the BRIXS calculation.

The program BRIXS-pathway generates the HDF5 file *data.h5*, the structure of which is shown in Fig. 7.5. The file contains three datasets containing the arrays $t^{(1)}$ and $t^{(2)}$, while the third array stores the BSE eigenvalues E_{λ_c} of the core BSE calculation. The size of the arrays depends on the number of BSE eigenstates that are provided in the files *core_output.h5* and *optical_output.h5*. Consider that N_{λ_c} core BSE eigenstates and N_{λ_o} optical BSE eigenstates are provided. The array $t^{(1)}$ in *data.h5* then contains N_{λ_c} entries, the array $t^{(2)}$ $N_{\lambda_o} \times N_{\lambda_c}$ entries. As both $t^{(1)}$ and $t^{(2)}$ are complex-valued, an additional dimension describes the real and complex part. The output of

the program BRIXS-oscstr is contained in the file "rixs.h5" shown in Fig. 7.6. It contains the real-valued array "evals", which stores the BSE eigenvalues E^{λ_o}. A group "oscstr" contains the RIXS oscillator strength $t^{(3)}(\omega_1)$. For a calculation with N_ω values for the excitation energy ω_1 defined in the file "input.cfg", the group contains N_ω datasets, where the name of the dataset is generated from the index of the ω_1 entry as a four-digit string, *e.g.* the datasets are named 0001, 0002, and so forth. The naming convention limits the number of excitation energies that can be computed in one calculation to 1000. Each of the dataset has dimension $2 \times N_{\lambda_o}$, where the first dimension occurs since $t^{(3)}$ is complex-valued.

7.7.2 BRIXS Implementation

The BRIXS requires a number of parameters, which are provided to the program in a file named *input.cfg*.

- **omega**: Comma-separated list of values for the excitation energies ω_1 in eV.

- **nstato**: Number N_{λ_o} of core-conduction eigenstates included in the BRIXS calculation counted from the BSE eigenstate with the lowest eigenvalue. The number must be smaller or equal to the number of eigenstates contained in the file *optical_output.h5*.

- **nstatc**: Number N_{λ_c} of BSE valence-conduction eigenstates included in the BRIXS calculation counted from the BSE eigenstate with the lowest eigenvalue. The number must be smaller or equal to the number of eigenstates contained in the file *core_output.h5*.

- **broad**: Value of the lifetime broadening of the intermediate state in eV.

- **pol**: Polarization vector $\mathbf{e}_1$ of the initial photon, where currently, $\mathbf{e}_1 = \mathbf{e}_2$ is assumed, *i.e.* the code does not allow one to calculate the effects of dichroism.

- **nblocks**: Number of blocks N_{blocks}.

The algorithm of BRIXS-pathway is shown in Algorithm 1. Due to block-wise formulation, the calculation of the vector $t^{(1)}$ requires a two-fold nested summation over the N_{blocks} blocks, while the calculation of $t^{(2)}$ requires a three-fold nested summation over the blocks. As such, the runtime increases with increasing numbers of blocks. On the other hand, the size of the $t^{(1)}$ blocks decreases with N_{blocks}^{-1}, that of the $t^{(2)}$ with N_{blocks}^{-2}. Therefore, the memory consumption decreases with increasing number of blocks, because the Algorithm 1 does not require any array of the size of the original BSE Hamiltonian. The same block-wise formalism is employed in the Algorithm 2 for the program BRIXS-oscstr, and as such a two-fold loop over N_{blocks} is required. Here, additionally a loop over the excitation energies ω_1 occurs.

Algorithm 1 Algorithm for the block-wise calculation of the core excitation oscillator strength and excitation pathways.

1: **procedure** BRIXS-PATHWAY
2:     **for all** N_{blocks} **do**
3:         Read block of E^{λ_c} from file
4:         Write block of E^{λ_c} to file
5:         Initialize block of $t^{(1)}_{\lambda_c} = 0$
6:         **for all** N_{blocks} **do**
7:             Read block of X_{λ_c} from file
8:             Generate block of $\left[\mathbf{e}_1 \cdot \mathbf{P}\right]$
9:             Add to block of $t^{(1)} = t^{(1)} + \left[X\right]^T \times \left[\mathbf{e}_1 \cdot \mathbf{P}\right]$ ▷ See Eq. 7.20
10:         **end for**
11:         Write block of $t^{(1)}_{\lambda_c}$ to file
12:     **end for**
13:     **for all** N_{blocks} **do**
14:         **for all** N_{blocks} **do**
15:             Initialize block of $t^{(2)}_{\lambda_o,\lambda_c} = 0$
16:             **for all** N_{blocks} **do**
17:                 Read block of eigvecs X_{λ_o} from file
18:                 Read block of eigvecs X_{λ_c} from file
19:                 generate block $\left[\mathbf{e}_2^* \cdot \tilde{\mathbf{P}}\right]^T_{\lambda_c}$ ▷ See Eq. 7.21
20:                 generate block of I_{λ_c} ▷ See Eq. 7.21
21:                 add to block of $t^{(2)} = t^{(2)} + \left[X\right]^T \times I$ ▷ See Eq. 7.23
22:             **end for**
23:             Write block of $t^{(2)}_{\lambda_o,\lambda_c}$ to file
24:         **end for**
25:     **end for**
26: **end procedure**

Algorithm 2 Algorithm for the block-wise calculation of the RIXS oscillator strength.

---

    procedure BRIXS-OSCSTR
2:      **for all** N_{blocks} **do**
          Read block of E^{λ_o} from file
4:          Write block of E^{λ_o} to file
          for all ω_1 **do**
6:             Initialize block of $t^{(3)}_{\lambda_o}(\omega_1) = 0$
             for all N_{blocks} **do**
8:                Read block of E^{λ_c} from file
                Read block of $t^{(1)}_{\lambda_c}$ from file
10:              Read block of $t^{(2)}_{\lambda_o,\lambda_c}$ from file
                Generate block of $\left[\Delta E^{-1}(\omega_1)\right]_{\lambda_o}$ ▷ See Eq. 7.25
12:              Add to block of $t^{(3)}(\omega_1) = t^{(3)}(\omega_1) + t^{(2)} \cdot \left[\Delta E^{-1}(\omega_1)\right] \cdot t^{(1)}$ ▷ See Eq. 7.29
             end for
14:             Write block of $t^{(3)}_{\lambda_o}(\omega_1)$ to file
          end for
16:      **end for**
    end procedure

7.7.3 Post-processing with pyBRIXS

The RIXS double-differential cross section is constructed from the output of the BRIXS code following Eq. 7.7. A robust and convenient way to generate spectra and visualize them is provided by the pyBRIXS module, written in the programming language python. The module offers objects that store the output of the BRIXS calculation, generates the RIXS spectrum, and provides convenient ways to visualize the results. The object pyBRIXS.rixs is generated with the output contained in the *rixs.h5* file. Provided with an array of values for the energy loss $\omega = \omega_1 - \omega_2$ and the value for the final-state lifetime broadening η, the object calculates the RIXS spectrum. The object furthermore stores the emission energies $\omega_2 = \omega_1 - \omega$. It also stores the RIXS cross section $t^{(3)}(\omega_1)$ for more advanced post-processing, such as the summation over atomic contributions. More advanced visualization are accessible through the object pyBRIXS.analysis, which is generated from the pyBRIXS.rixs object. The pyBRIXS.analysis object interpolates the RIXS spectrum on the excitation-loss grid ($\omega_1 - \omega$) and on the excitation-emission grid ($\omega_1 - \omega_2$). The interpolation is performed using established algorithms of the *numpy* and *scipy* packages [287–289]. The pyBRIXS.analysis object furthermore allows the user to store the interpolated RIXS spectrum to file. The attributes of the object are structured such that they can readily be visualized using the *matplotlib* package [290]. All visualization of RIXS spectra shown in this thesis are generated using the pyBRIXS code.

7.7.4 Scaling Tests

Due to the large number of BSE eigenstates and the even larger size of the transition space in the BSE calculations for the optical and core excitations, an efficient parallelized execution of the BRIXS code is required. It therefore employs a combination of the shared-memory Open Multi-Processing (OpenMP) [291] and Message-Passing Interface (MPI) [292] standard. In both BRIXS-pathway and BRIXS-oscstr, the outer summation over N_{blocks} is distributed over MPI ranks, while OMP parallelization is implicitly used for each matrix-matrix multiplication, as they are performed by subroutines of the LAPACK library [293].

In the following, we determine the scaling of the BRIXS-pathway (compare Algorithm 1) and BRIXS-oscstr (compare Algorithm 2) with respect to the number of threads in the OpenMP and ranks in the MPI parallelization. To do so, we perform BRIXS calculations starting from BSE calculations for the core and optical excitations, where the transition spaces of both include 1280 transitions. For the BRIXS-pathway code, the runtime and speed-up are shown in Fig. 7.7. We find that the MPI parallelization yields a strong speed-up for a wide range of MPI ranks. For increasing number of MPI ranks, however, the speed-up deviates from the ideal speed-up as the effort of distributing it over a large number of ranks outweighs
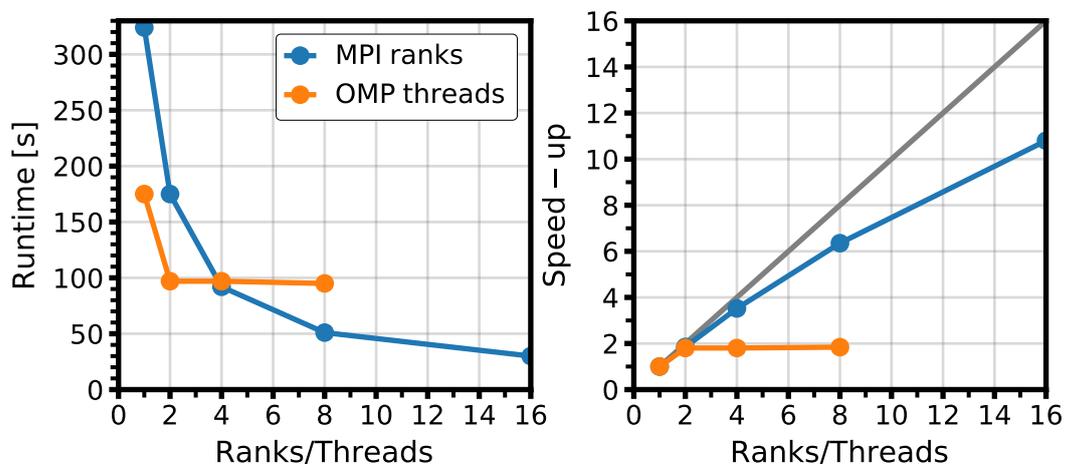
Figure 7.7: Runtime (left) and speed-up (right) for BRIXS-pathway calculations with increasing number of MPI ranks (blue) with one OpenMP thread and increasing number of OpenMP threads with two MPI ranks (orange). The ideal speed-up is shown as a gray line.
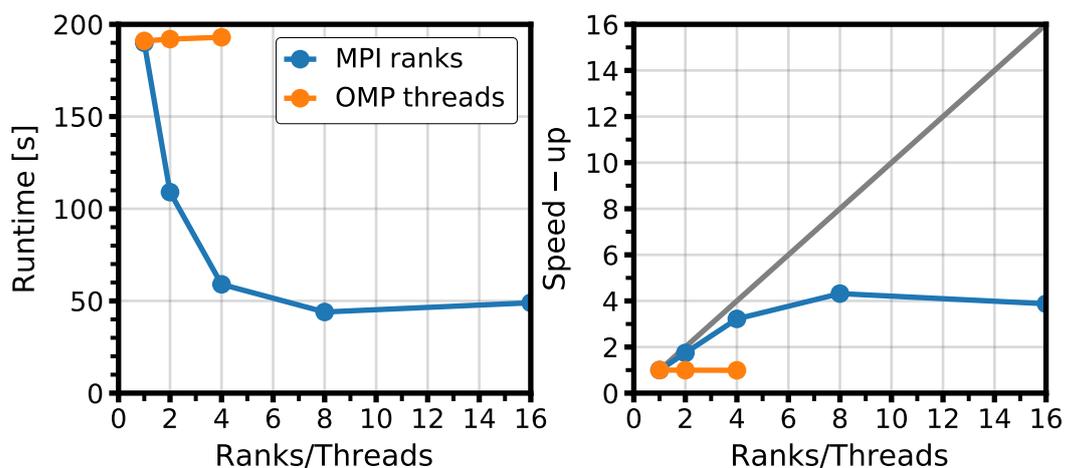

Figure 7.8: Runtime (left) and speed-up (right) for BRIXS-oscstr calculations with increasing number of MPI ranks (blue) with one OpenMP thread and increasing number of OpenMP threads with one MPI rank (orange). The ideal speed-up is shown as a gray line.

the benefit of performing the matrix operations in parallel. Considering the OpenMP parallelization in Fig. 7.7, a speed-up is only observed up to two OpenMP threads. This is due to the small matrix sizes in these calculations, which limits the benefit of shared-memory

parallelization. The scaling tests of the `BRIXS-oscstr` code, shown in Fig. 7.8, shows significant speed-up only up to 8 MPI ranks, while the increase of OpenMP threads does not yield any noticeable change in runtime. The bottleneck of the `BRIXS-oscstr` is the reading from the HDF5 file data.h5 and writing to rixs.h5, especially for the small matrix sizes considered in the scaling calculations. As these operations are not affected by OpenMP parallelization, it does not reduce the runtime. As the data input and output is parallelized over MPI ranks, however, an increased number of MPI ranks yields a speed-up of the calculations, which is limited due to the small size of the matrices in the scaling tests, as in the case of the MPI scaling of the `BRIXS-pathway`.

CHAPTER 8

Examples

8.1 Ce $N_{4,5}$ Edge NRIXS in CeO$_2$

To demonstrate the capabilities of our many-body perturbation theory approach to NRIXS, we consider the Ce $N_{4,5}$ edge in CeO$_2$. The electronic structure of this rare-earth oxide CeO$_2$ is characterized by the presence of highly localized Ce $4f$ states and the resulting large overlap of the Ce $4d$ and Ce $4d$ states leads to a considerable $4d - 4f$ interaction. Particularly the strong exchange interaction, introduces so called *multiplet features* in the Ce $4d \rightarrow 4f$ transitions, *i.e.* the Ce $N_{4,5}$ edge. These multiplet features are due excitations to atomic-like final states from the Ce $4d^9 4f$ ground state, which not be described in a single-particle approach [294, 295]. The accurate calculation of such multiplet features remains a challenge even within the many-body perturbation theory approach, as was previously shown for the multiplets in Ti $L_{2,3}$ [238, 268] and Ca $L_{2,3}$ [239] edge XANES. Furthermore, the multiplets only appear as weak pre-edge features in the Ce $N_{4,5}$ XANES [295, 296], as most of the transitions are dipole-forbidden. These features only become visible in the NRIXS spectra at high momentum transfer $\mathbf{q}$ [297].

To obtain a good starting point for the calculation of the NRIXS spectra, Hubbard corrections [299–301] are employed in the determination of the electronic structure of CeO$_2$. These corrections account parametrically for the self-interaction of the localized Ce $4f$ states, which is underestimated in DFT calculations with semilocal functionals [302, 303]. The electronic structure of CeO$_2$ is shown in Fig. 8.1: The top of the valence band is predominantly formed by oxygen p states, while the de-localized conduction bands are mostly formed by Ce d states. The onset of the conduction region is dominated by a group of weakly dispersing bands composed of the Ce $4f$ states, which introduce a strong peak in the DOS. As the electrons at the cerium sites are in a Ce $4d^{10} 4f^0$ configuration [297, 304], the Ce $4f$ peak is found above the band gap. The calculated electronic structure agrees well with the experimental one [298], with the only exception being the underestimated band gap due to the semilocal functional [304]. A more accurate band gap is obtained from $G_0 W_0$ calculations [302, 303]. To obtain reliable transition energies for the cerium $N_{4,5}$ edge, not only the band gap, but also the relative positions of the cerium $4d$ states have to be known. While *GW* calculations of the valence electronic structure are nowadays routinely employed, few studies have presented corrections for states farther from the band
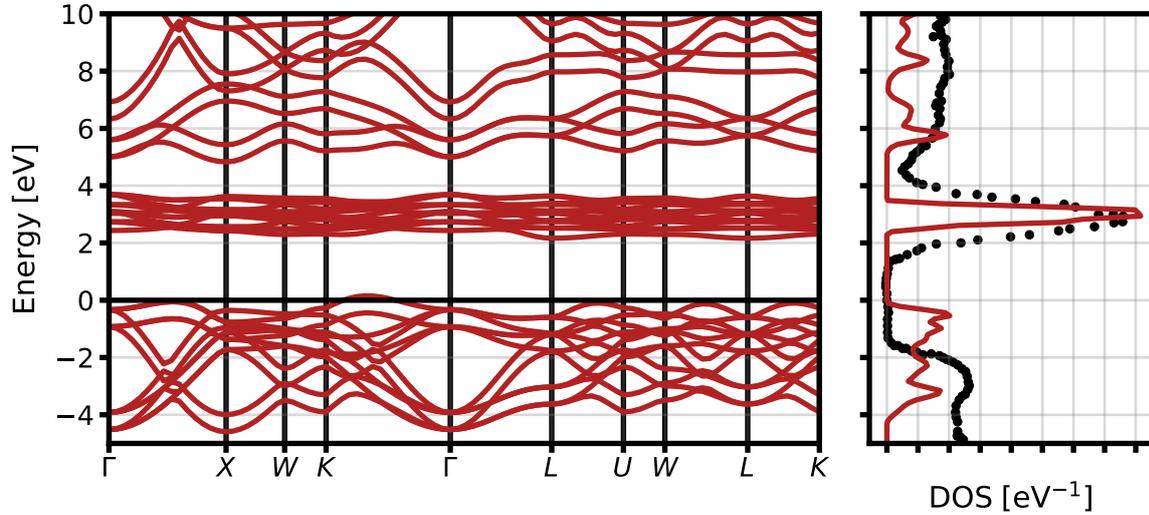
Figure 8.1: Band structure (left) and density of states (right) of CeO$_2$. The calculated results are shown in red, the experimental x-ray photoemission spectra [298] in black. The calculated electronic structure is aligned to the experimental one at the Ce 4f peak.

gap [305, 306]. As such, it is still common practice to apply scissors operators to align calculated and experimental core excitation spectra [238, 239, 268]. Here, we shifted the calculated NRIXS spectra by $\Delta\omega$ = 4.25 eV, such that the main peak in the experimental and calculated spectrum for the momentum transfer $|\mathbf{q}|$ = 8.6 Å, where the multiplets are most pronounced, are aligned. We note that we use the same scissors operator for all spectra at different momentum transfer.

The calculated Ce N$_{4,5}$ edge NRIXS spectrum at low momentum loss $|\mathbf{q}|$ = 1.6Å^{-1} in Fig. 8.2 resembles the DOS shown in Fig. 8.1. It displays an intense peak at around 137 eV, while the experimental spectrum shows a similar feature at 130 eV, although broader than the calculated one. With increasing momentum transfer, two new peaks at 109 and 112 eV emerge with increasing relative intensity. The main peak at 137 eV is nearly vanished for a momentum transfer of $|\mathbf{q}|$ = 8.6Å^{-1}. Our analysis of the BSE eigenvalues and eigenstates reveals that the low energy peaks are due to bound excitons with binding energies up to 2.77 eV. These bound excitons can be interpreted as atomic-like Ce 4$d^9$4f^1 multiplets. As the transitions from the Ce 4d^{10}4f^0 ground state to several of these multiplets are dipole forbidden, they only become visible in the spectrum for significant momentum transfer. Previous many-body atomic calculations [297] of Ce^{4+} support our analysis of the low-energy excitations. However, in these calculations the nature of the high-energy peak at 137 eV could not be resolved. It was assumed that the peak is due to a multiplet excitation that is shifted upwards in energy due to the repulsive exchange interaction. The large broadening of the feature is assumed to originate from the hybridization of the multiplet
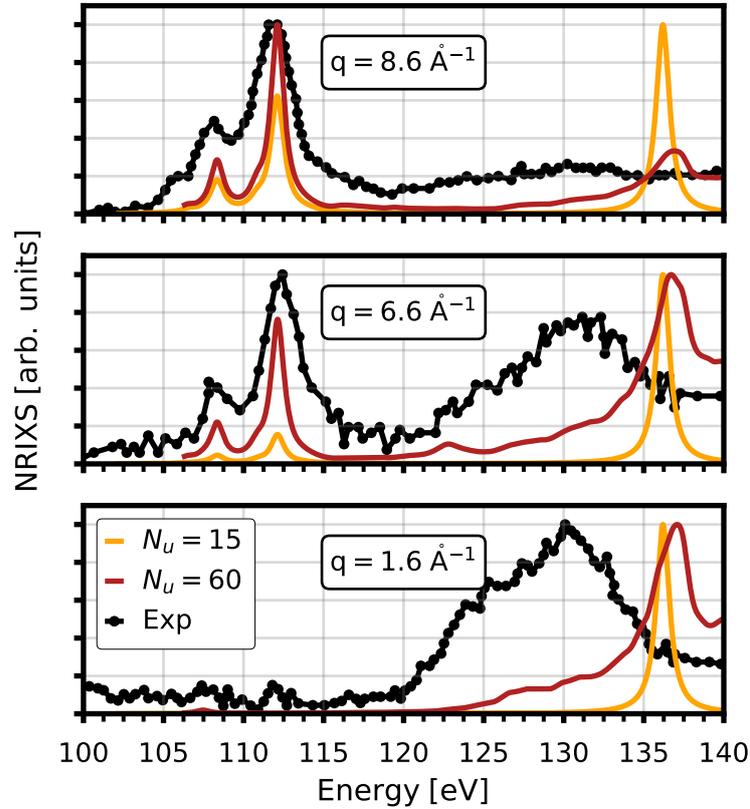
Figure 8.2: Ce N$_{4,5}$ edge NRIXS spectra of CeO$_2$ for increasing values of the momentum transfer **q**. Calculated pectra with $N_u = 15$ (yellow) and $N_u = 60$ (red) conduction bands are compared to experimental spectra from Ref. [297]. For each momentum transfer, all spectra are normalized to the intensity of the maximum.

excitation with the transitions from the Ce $4d$ states to the continuum states. To analyze the origin feature, we additionally show the result of a BSE calculation with a reduced number of bands (orange lines) in Fig. 8.2. This calculation shows a similar spectrum, but the high-energy peak at 137 eV is more pronounced, has approximately the same linewidth as the low-energy peaks, and does not lose relative intensity with increasing momentum transfer. This indicates that a dipole-allowed multiplet excitation, originating from transitions to the Ce $4f$ states at the onset of the conduction bands, is shifted upwards in energy due to the exchange interactions and forms the strong peak at 137 eV. The broadening of the peak and the decrease of its relative intensity with increasing momentum transfer only occurs in the calculation with a larger number of unoccupied bands. It is therefore due to the hybridization of this atomic-like excitations with the high-energy excitations of the Ce $4d$ states to the continuum. Our calculations present the first *ab initio* calculations to confirm the hybridization of multiplet excitations with continuum ones for the Ce N$_{4,5}$ edge and
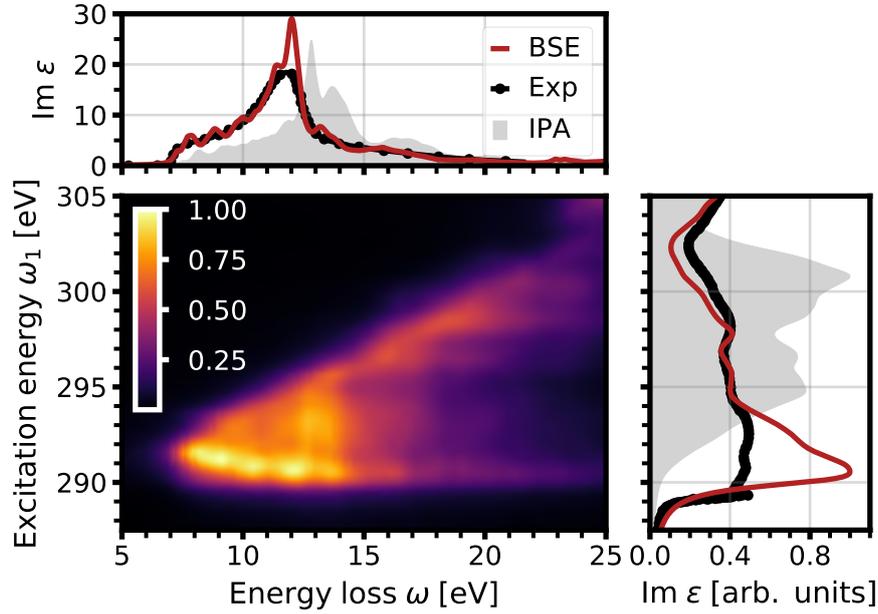
confirm earlier assumptions [297].

Figure 8.3: Center: Normalized carbon K edge RIXS double-differential cross section of diamond as a function of excitation energy and energy loss. Top: Optical absorption spectrum obtained from BSE calculation (red) and independent-particle approximation (gray) compared to the experimental spectrum (black) from Ref. [307]. Right: Carbon K edge absorption spectrum in diamond. The experimental spectrum (black) is taken from Ref. [308]

8.2 Carbon K Edge RIXS in Diamond

As a first demonstration of our RIXS implementation, we consider the RIXS spectra at the carbon K edge in diamond. Both the optical [142, 307, 309–311] and the carbon K edge [204, 308, 312] absorption spectra have been investigated intensively before. Experimental [262, 308] and theoretical [206, 209] RIXS results for the carbon K edge RIXS are also available. As such, this material acts as a good example to demonstrate our approach and benchmark the resulting spectra.

In a first step, the optical and carbon K edge absorption spectra, shown in Fig. 8.3, are calculated starting from a DFT calculation using a semilocal GGA functional [77]. Our calculations yield an indirect band gap of 4.04 eV and a direct band gap of 5.55 eV, well below the corresponding experimental values of 5.48 eV [313] and 7.3 eV [314]. We employ a scissors operator of $\Delta\omega = 1.9$ eV, to increase the optical band gap of 5.55 eV to the experimental one of 7.3 eV [314].
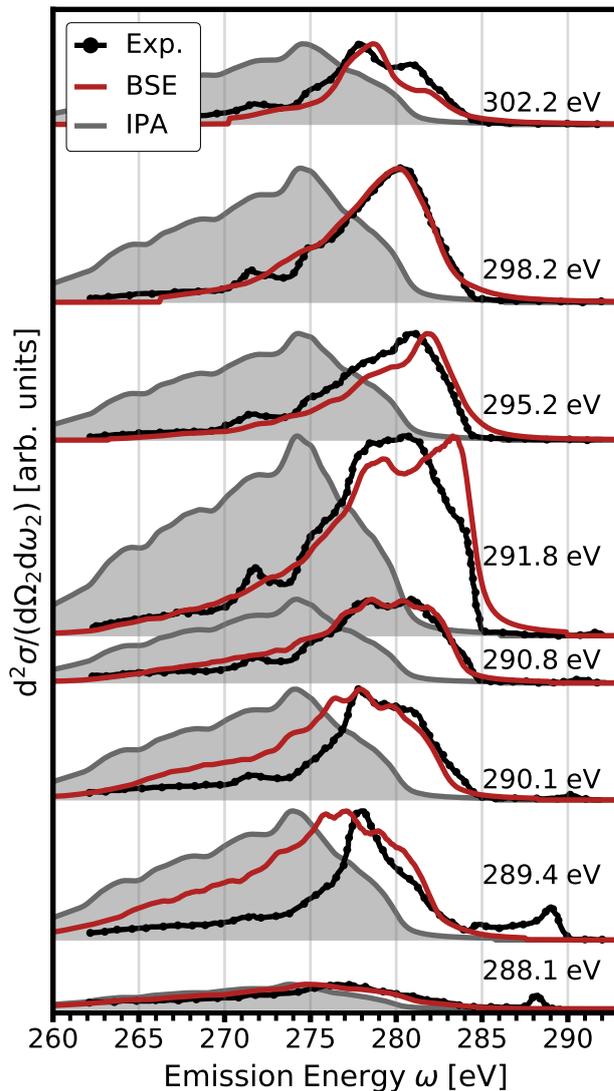
This scissors operator yields an absorption spectrum in good agreement with experiment, but overestimates the indirect band gap, indicating that *GW* corrections do not only increase the band gap, but furthermore alter the band dispersion.

For the carbon K edge spectrum, not only the band gap but also the position of the carbon 1*s* level has to be corrected. We choose a scissors operator $\Delta\omega_1 = 22$ eV, such that the onset of the experimental and calculated spectrum are aligned. Both scissors operators together furthermore define the scissors operators used for the RIXS spectra: The excitation energies are shifted by $\Delta\omega_1$, the energy loss by $\Delta\omega$, and the emission energy by $\Delta\omega_2 = \Delta\omega_1 - \Delta\omega$. As such, there are no free parameters for the RIXS spectra once the optical and core-edge absorption spectra are aligned.

The calculated RIXS spectra are shown in Fig. 8.3. Following Eqs. 7.7 and 7.8, it is obvious to display the RIXS double-differential cross section $\frac{d^2\sigma}{d\Omega_2 d\omega_2}$ as a function of the excitation energy ω_1 and energy loss $\omega = \omega_1 - \omega_2$. Equivalently, the cross section can be displayed as a function of excitation energy ω_1 and emission energy ω_2, which corresponds to the way the RIXS spectra are experimentally recorded. For excitation energies below the carbon K edge absorption edge at approximately 290 eV (see Fig. 8.3 right), the RIXS cross section is negligible, since the excitation energy is not in resonance with any carbon 1*s* excitation. Once the excitation energy reaches resonance with the absorption edge, the RIXS cross section increases considerably. The emission occurs over a wide

Figure 8.4: Calculated RIXS DDCS (red) for several excitation energies. Spectra are shifted upwards for clarity. Experimental spectra from Ref. [308] are shown in black, the results obtained within the IPA in gray.
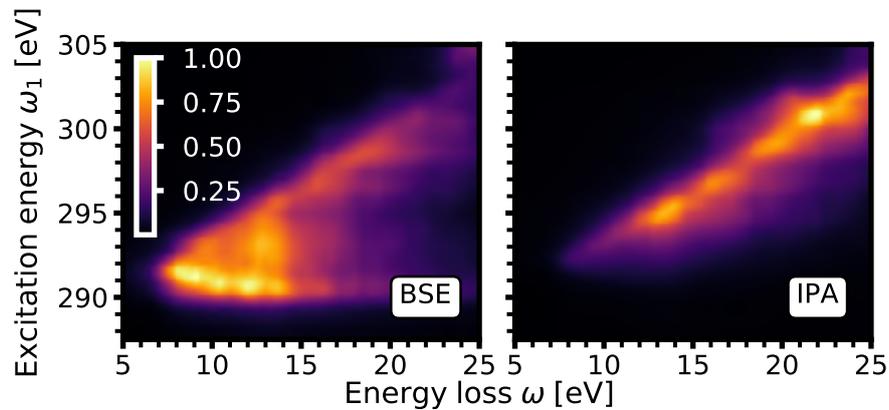
Figure 8.5: RIXS double-differential cross section calculated within BSE (left) and IPA (right). Both colormaps employ the same scale to allow for a direct comparison.

range of energy loss up to around 20 eV, but is strongest at low emission at the onset of optical absorption (compare Fig. 8.3 top). With increasing excitation energy, the emission reduces due to the reduced rate of absorption beyond the onset. Furthermore, the emission at low energy loss vanishes as the excitation energy increases. At an excitation energy of 295 eV, no emission with an energy loss below approximately 12 eV is observed; at an excitation energy of 300 eV, no emission with a loss below 20 eV. Due to this linear dispersion of the energy loss with the excitation energy, the emission energies stay more or less constant, as can be seen in Fig. 8.4, where the RIXS cross section is shown as a function of the emission energy for selected excitation energies. Even though we have selected excitation energies within a window of 12 eV in Fig. 8.4, the emission occurs consistently between 285 and 275 eV. We observe that our calculations agree well with experimental spectra, for the emission spectrum at a given excitation energy as well as for the change in emission due to different excitation energies.

In Fig. 8.3, we furthermore show the RIXS cross section within the IPA following Eq. 5.10. The IPA results are overall blue shifted compared to the experimental spectra, *i.e.* the energy loss is overestimated. The blue shifts originates from the red shift of the IPA absorption spectra, which can be seen in Fig. 8.4. Especially for lower excitation energies, the IPA emission spectra furthermore have a different spectral shape than the experimental ones. The intensity at higher emission energies is underestimated, and spectra are too broad. Both the shift and the different broadening are due to the neglect of electron-hole interaction: Both in the optical and the carbon K edge absorption spectra, the electron-hole interaction leads to an increase of intensity at low energies and a sharper onset. This effect is especially pronounced for the core excitations (Fig. 8.4). For emission spectra at higher excitation energy, the discrepancy between IPA and BSE results decreases and the spectral shape is correctly reproduced within IPA, while spectra are still blue-shifted (Fig. 8.3). For excitations with

higher energy, both in the intermediate and in the final state, the role of electron-hole interaction decreases and thus the quality of IPA calculations increases. The underestimation of the RIXS intensity at low energy loss in the IPA is clearly seen, when we compare the calculated BSE and IPA spectra in Fig. 8.5 directly. While the IPA reproduces the general dispersion of the RIXS spectrum, the intensity at the onset is completely underestimated, and the main spectral features at the onset are missing. Our analysis shows that a careful treatment of the electron-hole interaction is paramount for an accurate description of the RIXS spectra.
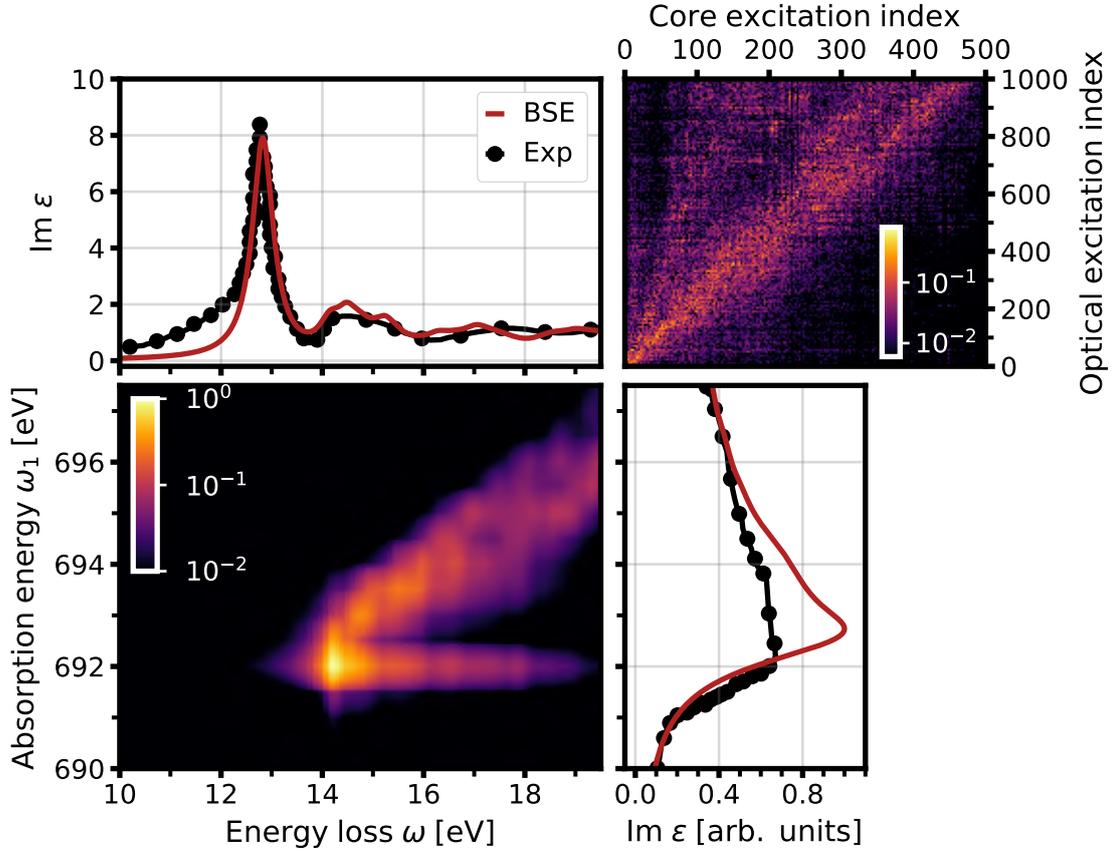
Figure 8.6: Lower left: Normalized F K edge RIXS of LiF as a function of the excitation energy and energy loss Lower right: F K edge absorption spectrum obtained from BSE calculations (red) and experiment (black) [315]. Upper left: Optical absorption spectrum of LiF from BSE calculations (red) and experiment (black). Upper right: Normalized $|t^{(2)}|^2$ matrix elements between the first 500 core excitations and first 1000 optical excitations.

8.3 Flouride K Edge RIXS in LiF

As a second demonstration of our RIXS approach, we present in the following results for the F K edge of LiF. This section closely follows our work in Ref. [361]. Due to its large band gap, strong effects of electron-hole interaction occur in the electronic excitations of LiF, as indicated by the presence of bound excitons in both the valence and the core regimes. Our approach allows for a deeper analysis of the RIXS spectra, the results of which are shown in Fig. 8.6. For excitation energies below the absorption onset of the core edge, i.e., at approximately 691.8 eV, the cross section is small, since the F $1s$ states are not excited reso-

nantly. Nevertheless, resonant scattering also occurs below the absorption onset, and this case will be discussed later. When the excitation energy is in resonance with the absorption onset, the spectrum changes abruptly. The oscillator strength increases tremendously and is focussed on a distinct loss peak at 14.6 eV. For higher absorption energies, this peak shows a linear dispersion. The feature loses oscillator strength and widens with increasing excitation energy.

As the shape of the RIXS spectrum is determined by the excitation pathways, we now have a closer look at the $t^{(2)}$-matrix. The top right of Fig. 8.6 shows this matrix for the first 500 core and 1000 optical excitations that determine the RIXS cross sections for excitation energies between 680.1 and 696.7 eV and energy losses between 12.8 and 18.3 eV. It shows a pronounced band-matrix form, *i.e.* the largest contributions are observed along the diagonal. From Eq. 7.6, two contributions can be inferred that lead to considerable matrix elements. First, transitions from the valence hole distribution of the final state to the core hole have to be dipole-allowed, and second, the distributions of the excited electron of the intermediate and final state have to be similar. For core excitations with increasing energy, the excited electron is distributed farther from the band gap, and the same holds true for optical excitations with increasing energy. This similarity leads to the band-matrix form of $t^{(2)}$. Moreover, we find that for core excitations at higher energies, pathways to more and more valence excitations are possible, and therefore the shoulder at higher loss is getting more pronounced.

Although the elements of $t^{(2)}$ yield insight into the origin of the features in the RIXS spectrum, they do not solely define it. While the pathway between the lowest excitations in the optical and core spectrum is very strong, surprisingly, the excitonic peak that dominates the optical absorption spectrum at 12.7 eV is not observed in the RIXS spectrum. This strongly bound exciton is formed by a complicate interplay of transitions from the top of the valence band, formed by the F p states, to the bottom of the conduction band, dominated by the Li s states.[220] In the corresponding RIXS spectrum, the initial excitations from the F $1s$ states to the Li s states at the bottom of the conduction band is not possible, as $s \rightarrow s$ transitions are dipole-forbidden. As such, the bound exciton in the F K edge spectrum is dark. While the $t^{(2)}$ matrix elements between the dark exciton in the F K edge and the bound exciton in the optical spectrum are considerable, the $t^{(1)}$ entries vanish, as the initial excitation of the dark exciton is prohibited. We note that in the literature, this peak has been ascribed to transitions from the exciton in the F K edge spectrum to that in the optical spectrum [315]. Our first-principles approach shows that RIXS spectrum at the core onset is more complex and requires in-depth analysis to be unraveled.

Plotting in Fig. 8.7 the calculated RIXS spectra as a function of the emission energies for selected excitation energies allows for a comparison with the experimental spectra [315]. We first consider the spectra beyond 689.9 eV, where the RIXS signal is considerable: For an excitation energy of 690.8 eV, below the absorption onset of approximately 691.8 eV, the
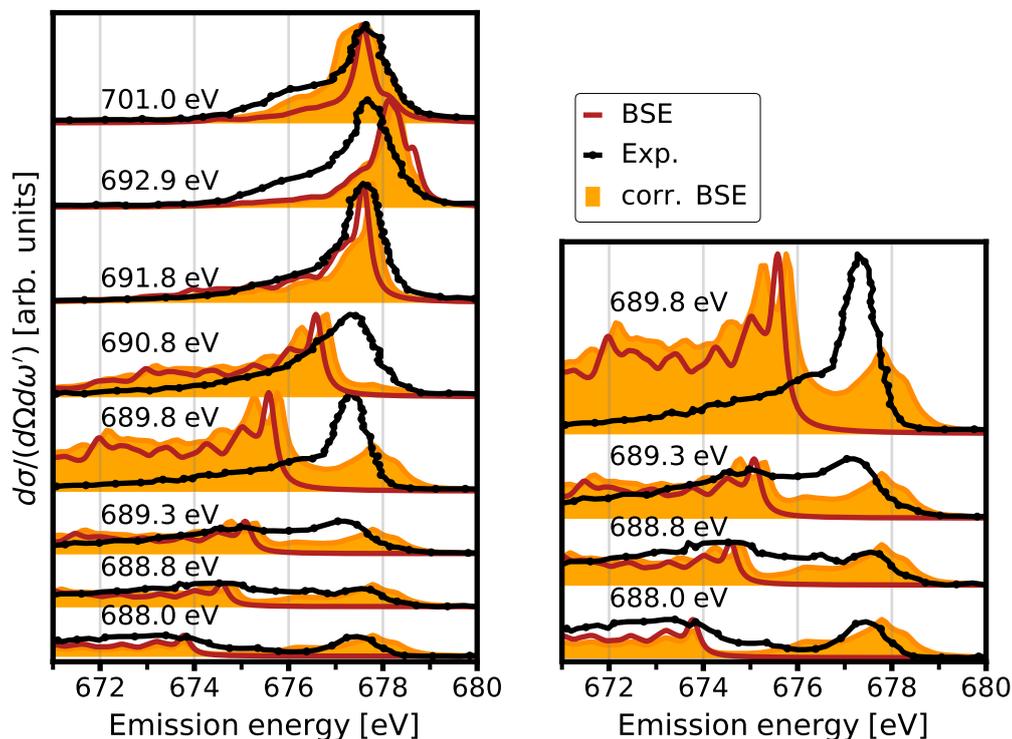
Figure 8.7: Left: F K edge RIXS spectra for selected excitation energies computed from our BSE approach (red), corrected BSE spectra including stray-light correction (orange) and experimental spectra from Ref. [315]. Right: Zoom of the RIXS spectra for excitation energies below the F K absorption onset.

calculated spectrum has a peak at 676.8 eV, which slowly decays at lower emission energies, *i.e.* the maximum of the scattering occurs at a loss of 14 eV, with considerable contributions at higher energy loss. With increasing excitation energy, the peak becomes narrower and moves to slightly higher emission energy. The broad feature at lower emission energy is strongly suppressed for excitations of approximately 691.8 eV, while a shoulder in the emission appears for even higher excitation energies. The calculated spectra at a given excitation energy, as well as the change as a function of the excitation energy are in good agreement with their experimental counterparts [315].

Experimental spectra have also reported for excitations energies below the absorption onset, and we display the calculated spectra on the right side of Fig. 8.7. In this excitation region, the calculated BSE spectra disagree qualitatively from the experimental ones: A strong, non-dispersive peak at emission energies of approximately 677.3 eV is completely missing in our calculations, which predict that emission only occurs at considerably higher energy loss, *i.e.* lower emission energies. For excitations in this energy region, none of the

core excitation is excited resonantly, and the spectrum is formed by the life-time tails of many excitations over a wide energy range. In the calculated spectra, the loss occurs predominantly at 14 eV, independently of the excitation energy yielding the broad emission feature in Fig. 8.7. The presence of linearly dispersive broad absorption features at constant energy loss in the sub-threshold RIXS spectrum have been observed for LiF [315], Cu, and Ni [316] before. They occur, since no core excitation is in resonance with the incoming x-ray energy, and as such no core excitation is strongly favored over the others. As a result, the emission spectrum does not strongly depend on the absorption energy and thus reflects the shape of the optical absorption spectrum. The experimental spectra, on the other hand, show an additional peak at approximately 677.4 eV for all excitation energies below the onset. With increasing excitation energy, the peak becomes more dominant until, at 689.8 eV, it completely dominates the experimental spectrum.

If we consider the excitation at 688 eV, the initial peak at 677.4 eV corresponds to an energy loss of around 10.6 eV, well below the optical absorption onset (see lower panel in Fig. 8.6). This indicates that the emission does not originate from the absorption of an x-ray photon with an energy of 688.0 eV, but rather of a photon with higher energy, such that the energy loss is actually higher. This can occur if the incoming x-ray beam is not perfectly monochromatic, but rather has a finite linewidth [315, 317]. For a given excitation energy, we then have to consider the scattering of x-ray photons within a range of energies around the given excitation energy. Following Ref. [315], we express the double-differential cross section as a function of the excitation energy ω_1 and emission energy ω_2 and obtain

$$\frac{\mathrm{d}^2\sigma(\omega_1, \omega_2)}{\mathrm{d}\Omega_2\mathrm{d}\omega_2} = \int d\omega_3 \frac{\mathrm{d}^2\sigma_{\mathrm{BSE}}(\omega_3, \omega_2)}{\mathrm{d}\Omega_3\mathrm{d}\omega_3} \cdot \eta(\omega_3 - \omega_1), \tag{8.1}$$

where $\mathrm{d}^2\sigma_{\mathrm{BSE}}(\omega_3, \omega_2)/\mathrm{d}\Omega_3\mathrm{d}\omega_3$ is the DDCS calculated from BSE for an excitation energy ω_3 and emission energy ω_2, while $\eta(\omega_3 - \omega_1)$ describes the linewidth of the excitation energy. In the derivation of the DDCS, we assume $\eta(\omega_3 - \omega_1) \to \delta(\omega_3 - \omega_1)$. Now, we extend the assumption by an additional Lorentzian background with a width Δ and a relative intensity ξ, such that

$$\eta(\omega_3 - \omega_1) = \delta(\omega_3 - \omega_1) + \xi \frac{\Delta^2}{\Delta^2 + (\omega_3 - \omega_1)^2}. \tag{8.2}$$

The second term is called the *stray-light contribution*. In Fig. 8.7, we show the stray-light corrected BSE spectra, using a distribution of $\Delta = 20$ eV and $\xi = 0.001$, corresponding to the parameters of Ref. [315]. The stray-light contribution correctly introduces the peak at high emission energies, but our calculations yield a peak at slightly overestimated emission energies. Our analysis shows that the peak originates from the strong RIXS signal that occurs at an excitation energy of 692 eV and an energy loss of 14 eV. Due to the linewidth of the excitation energy, even at considerably lower excitation energies below the absorption onset, some initial x-ray photons have an energy of 692 eV and are scattered such that the
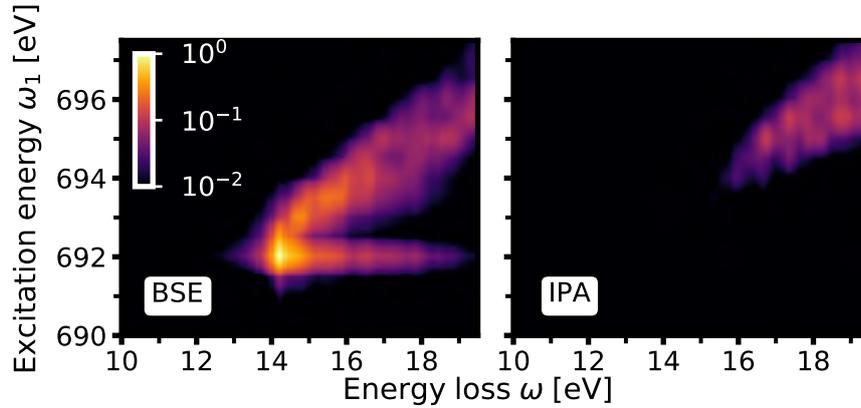
Figure 8.8: F K edge RIXS of LiF spectra obtained from BSE (left) and IPA (right) calculations. The spectra are normalized to the intensity of the most intense peak.

emitted photon has an energy of 678 eV. Due to the low signal of the scattering rate for x-ray photons with energies below the absorption onset, the peak at 678 eV is strong. We find that the agreement is better at lower excitation energies than at 689.8 eV. The frequency-dependency of $\eta(\omega'' - \omega')$ depends on the set-up of the measurement, and it appears that at higher excitation energies it does not have a Lorentzian shape.

Finally, we demonstrate the importance of electron-hole interaction by comparing in Fig. 8.8 the RIXS spectra obtained by the BSE with those from the independent-particle approximation (IPA). For low excitation energies, a broad emission spectrum is predicted in the IPA, missing the pronounced peak found in both the experimental spectra and our BSE calculations. At an excitation energy of 701 eV, the agreement between the IPA and BSE spectra improves, because the effect of electron-hole interaction decreases with increasing excitation energy. Comparing in Fig. 8.7 the RIXS cross sections obtained from the two calculations, one notices that the strong peak at the excitation energy of 691.8 eV and the loss of 14.8 eV is completely missing within the IPA. This comparison demonstrates that the renormalization of the RIXS spectra due to electron-hole interaction is crucial at low excitation energies and low energy loss.

Part III

Excitations in Ga$_2$O$_3$

CHAPTER 9

Geometry and Electronic Structure

9.1 Geometry of Ga$_2$O$_3$ Polymorphs

Several polymorphs of Ga$_2$O$_3$ have been identified, yet the symmetry and structure of some of these phases is still debated. Even the number of polymorphs is unclear to date. Commonly, six of them, named $\alpha-$, $\beta-$, $\gamma-$, $\delta-$, $\epsilon-$, and $\kappa-$Ga$_2$O$_3$, have been determined in experimental [7, 318–321] and theoretical [41] studies. All of these polymorphs consist of networks of gallium atoms at the center of either distorted tetrahedra or octahedra, the corners of which are formed by the nearest oxygen atoms [322, 323]. All studies confirm that the β-phase is the thermodynamically stable phase, but samples of the other polymorphs have been produced with suitable substrates and growth techniques [7]. Recently, the $\delta-$phase has been identified as a mixture of $\beta-$ and $\epsilon-$Ga$_2$O$_3$ [321], and it has been argued that the κ- and $\epsilon-$phases might be identical [324]. In this work, we focus on the thermodynamically stable β-phase, which we compare to the metastable α-phase. For selected properties, where experimental results are available, we also include the ϵ-phase in our comparison. The γ-polymorph is not considered here, due to its defective spinel structure that requires one to consider different atomic configurations in computationally expensive super-cell calculations. As an example, 14 configurations of unit cells with 40 atoms each were considered in Ref. [41] in order to determine the geometry of γ-Ga$_2$O$_3$.

The primitive unit cell of rhombohedral α-Ga$_2$O$_3$ (space group $R\bar{3}c$) is defined by the lattice vectors

$$
\mathbf{a}_1 = \left(a \cdot \cos\left(\frac{\alpha}{2}\right), -a \cdot \sin\left(\frac{\alpha}{2}\right), 0 \right),
$$
$$
\mathbf{a}_2 = \left(a \cdot \cos\left(\frac{\alpha}{2}\right), a \cdot \sin\left(\frac{\alpha}{2}\right), 0 \right),
$$
$$
\mathbf{a}_3 = \left(a \cdot \frac{\cos(\alpha)}{\cos\left(\frac{\alpha}{2}\right)}, 0, a \cdot \sqrt{1 - \frac{\cos^2(\alpha)}{\cos^2(\frac{\alpha}{2})}} \right),
$$

(9.1)

with the experimental lattice parameters $a = 5.321$ Å and $\alpha = 55.795°$ [28, 325]. The unit
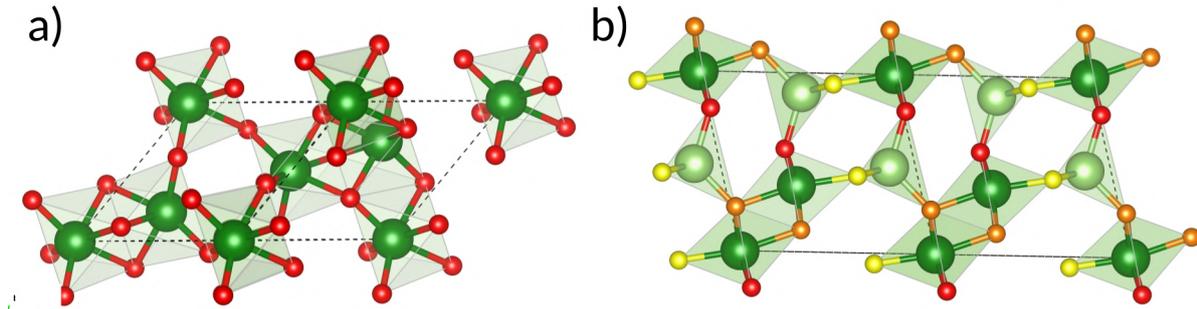
a)

b)

Figure 9.1: Primitive unit cell of a) α- and b) β-Ga$_2$O$_3$. Dark green atoms indicate octahedrally coordinated gallium atoms, light green atoms tetrahedrally coordinated ones. Red, orange, and yellow atoms indicate the inequivalent oxygen atoms. The dashed lines show the borders of the primitive unit cells.

cell shown in Fig. 9.1 contains 10 atoms, where the two gallium atoms (dark green) are equivalent and all three oxygen atoms in the unit cell (red) are equivalent to each other. All gallium atoms are octahedrally coordinated. Commonly, a non-primitive hexagonal unit cell is reported [28], with the hexagonal axis $\mathbf{c} = \mathbf{a}_1 + \mathbf{a}_2 + \mathbf{a}_3$.

The primitive unit cell of monoclinic β-Ga$_2$O$_3$ (space group $C2/m$) is given by the lattice vectors

$$\mathbf{a}_1 = (a/2, b/2, 0),$$
$$\mathbf{a}_2 = (-a/2, b/2, 0), \tag{9.2}$$
$$\mathbf{a}_3 = (c \cdot \cos \beta, 0, c \cdot \sin \beta),$$

with lattice parameters of $a = 12.233$ Å, $b = 3.038$ Å, $c = 5.807$ Å, and $\beta = 103.82°$ [325]. With this choice of primitive unit cell, the crystal axis $\mathbf{a}$ is positioned along the x-axis, the axis $\mathbf{b}$ along the y-axis, and the $\mathbf{c}$-axis lies in the xz-plane. The primitive unit cell shown in Fig. 9.1 contains 10 atoms, with two inequivalent gallium sites and 3 inequivalent oxygen ones. We label the octahedrally and tetrahedrally coordinated gallium atoms as Ga$_1$ (dark green) and Ga$_2$ (light green), respectively. In the $\beta-$phase, the ratio between octahedrally and tetrahedrally coordinated gallium atoms is 1 : 1 (compare Fig. 9.1). The three inequivalent oxygen atoms differ in their bonding to the inequivalent gallium atoms: the atoms O$_1$ (orange) share two bonds with Ga$_1$, one bond with Ga$_2$. The atoms O$_2$ (dark red) share three bonds with Ga$_1$ and one with Ga$_2$. The atoms O$_3$ (yellow) share one bond with Ga$_1$ and three bonds with Ga$_2$. Our color scheme is consistent with the one suggested in Ref. [34]. The low crystallographic symmetry of the monoclinic phase results in a strong anisotropy of the electronic and optical properties [21], which will be a focus of the present and following chapters.

The orthorhombic $\epsilon-$phase (space group $Pna2_1$), shown in Fig. 9.2, is defined by the lattice

vectors

$$\mathbf{a}_1 = (a, 0, 0),$$
$$\mathbf{a}_2 = (0, b, 0),$$
$$\mathbf{a}_3 = (0, 0, c),$$

(9.3)

with the lattice parameters a = 5.0566 Å, b = 8.6867 Å, and c = 9.3035 Å [28]. The primitive unit cell contains 40 atoms. There 16 gallium atoms are distributed over four inequivalent sites in the unit cell, each four-fold degenerate. One of these sites is tetrahedrally coordinated, three are octahedrally coordinated. As such, the ratio between octahedrally and tetrahedrally coordinated gallium atoms is 4 : 1. The 24 oxygen atoms are distributed over 6 inequivalent oxygen sites, each four-fold degenerate. As in the case of the β-phase, the inequivalent oxygen sites differ in the number of bonds they share with either octahedrally or tetrahedrally coordinated gallium atoms.

Figure 9.2: Crystal structure of ϵ-Ga$_2$O$_3$. Gallium atoms are shown in green, oxygen atoms in red. The dashed line indicates the boundary of the primitive unit cell.

Geometry, composition and bonding environment in the three polymorphs α-, $\beta-$ and ϵ-Ga$_2$O$_3$ are similar, where the main difference is the ratio between octahedrally and tetrahedrally coordinated gallium atoms [322, 323]. The influence of these subtle difference in the geometry on the electronic and optical properties will be the topic of the following chapters.

9.2 Electronic Structure

The similarities in the structure and bonding environment of the different polymorphs of Ga$_2$O$_3$ leads to similar electronic structures. Generally, the valence-band maximum (VBM) of all Ga$_2$O$_3$ polymorphs is formed predominantly by O p states, while the conduction band minimum (CBm) is formed mostly by hybridized O s and Ga s states. Yet, differences in the electronic structure arise due to the different symmetries and especially the varying ratio of tetrahedrally and octahedrally coordinated gallium atoms. We therefore discuss the electronic structure of the α- and β-polymorph in great detail. We complement the discussion by comparing these phases to the ϵ-phase.

First, we consider the band structure and density of states (DOS) of the α-polymorph shown in Fig. 9.3. The highest valence bands are predominantly formed by O p states, while the lowest conduction bands are formed by hybridized Ga s and O s states.
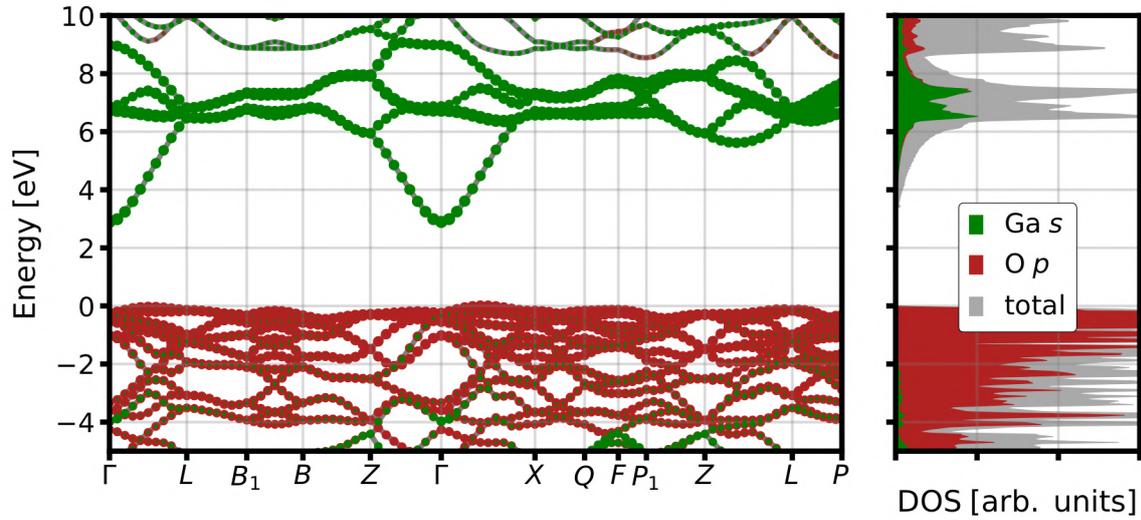
Figure 9.3: Electronic structure and DOS of α-Ga$_2$O$_3$. The high-symmetry path follows the standard of Ref. [326]. The projection on Ga s states are displayed in green, the ones of O p in red. The VBM is set to zero.
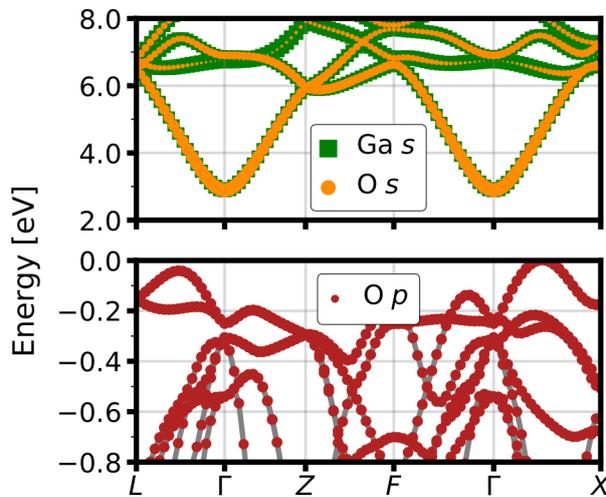

Figure 9.4: Band structure of α-Ga$_2$O$_3$ focusing on sections of the high-symmetry path around the optical band gap at Γ. The energy of the VBM is set to zero.

Due to the delocalization of the lowest conduction states, the corresponding band is strongly dispersive with the conduction-band minimum (CBm) at the Γ point. Within the first 3 eV beyond the CBm , the band structure is solely formed by this band. In contrast, the topmost valence bands display only weak dispersion (note the different energy scale), leading to high effective hole masses. We note that, due to the symmetry of the α-phase, the highest occupied band is twofold degenerate at the Γ-point, while the lowest conduction band is not degenerate. Our calculations yield an indirect Kohn-Sham band gap of 2.89 eV, as the valence band maximum (VBM) is displaced slightly from the Γ-point. Due to the low 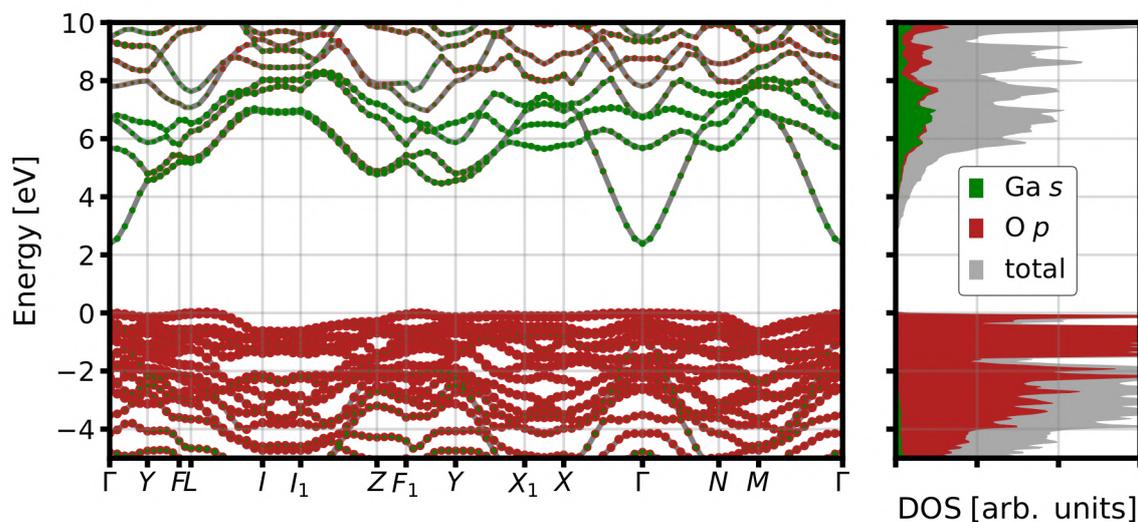dispersion and the high density of valence bands, the density of states at the VBM is sharp with an abrupt onset. The density of states at the CBm shows the expected $\sqrt{\epsilon}$ behavior, as the band structure is formed by a single

Figure 9.5: Electronic structure and DOS of β-Ga$_2$O$_3$. The projection on the Ga s are displayed in green in both the band structure and the DOS, the ones of the O p in red. The high-symmetry path follows the standard of Ref. [326].

parabolic band. For the optoelectronic properties, the electronic structure in the vicinity of the direct band gap is of special importance. In the next sections, we will therefore employ a reduced band-structure path focussing mainly on the vicinity of the Γ-point. The band structure is shown in Fig. 9.4, where we also visualize the projection onto the Ga s and O s states for the conduction bands, and the O p for the valence states. Figure 9.4 demonstrates that the Ga s and O s state contribute to the CBm equally. While the contributions of the Ga s are often discussed in the literature, it is equally important to consider those of the O s states to understand the optoelectronic properties of Ga$_2$O$_3$.

The band structure of the β-phase, shown in Fig. 9.5 closely resembles that of the α-phase. As in the latter, the valence bands have predominantly O p character and are only weakly dispersing, while the lowest conduction band is formed by hybridized Ga and O s states and displays a parabolic dispersion around the Γ-point. We obtain an indirect band gap of 2.39 eV, although the difference of the direct and indirect band gap is very small, since the highest valence bands are nearly flat. Focusing on the electronic structure in the vicinity of the band gap, as shown in Fig. 9.6, we observe that the topmost valence bands are predominantly formed by O p states, yet the inequivalent oxygen sites contribute differently to these bands. The highest valence band is formed mostly by O$_3$ p states, except around the L-point where O$_2$ and O$_3$ contribute nearly equivalently. We note that O$_3$ shares the highest number of bonds to the tetrahedral gallium site. The contributions of O$_1$ to the top of the valence band are negligible, and the first significant contributions occur about 0.7 eV below the VBM. For the CBm, however, the s states of Ga$_1$ and Ga$_2$ contribute equivalently. The

hybridization with O s is considerable, where the atomic contributions of the O_1, O_2, and O_3 are similar. Only at about 6 eV above the VBM, when the parabolic band is intersected by the other conduction bands, the contributions of the inequivalent gallium sites differ. This is especially pronounced for the second-lowest conduction band at Γ, which is solely formed by Ga_2 s states, while the lowest conduction band at the X point is formed predominantly by Ga_1 s states.
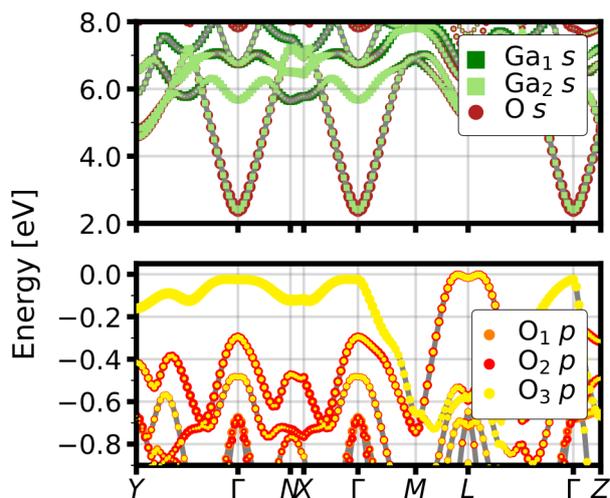

Figure 9.6: Band structure of β-Ga_2O_3 focusing on sections of the high-symmetry path around the optical band gap at Γ. The VBM is set to zero.

We have seen so far that the electronic structures of the α- and β-phase are similar. Differences occur mainly due to the reduced symmetry of the β-phase, which leads to distinguishable contributions of the inequivalent oxygen sites to different valence bands. For a direct comparison, Fig. 9.7 shows the DOS for the α-, β-, and ϵ-polymorph, projected on the Ga s and p, and O s and p states. The main difference between the three is the electronic structure at the VBM: While the α-phase shows a smooth onset, the β- and ϵ-phase show a distinct peak, which is more pronounced in the ϵ- than in the β-phase. The feature originates from oxygen p states of oxygen sites predominantly bonded to tetrahedrally coordinated gallium atoms. These sites do not occur in th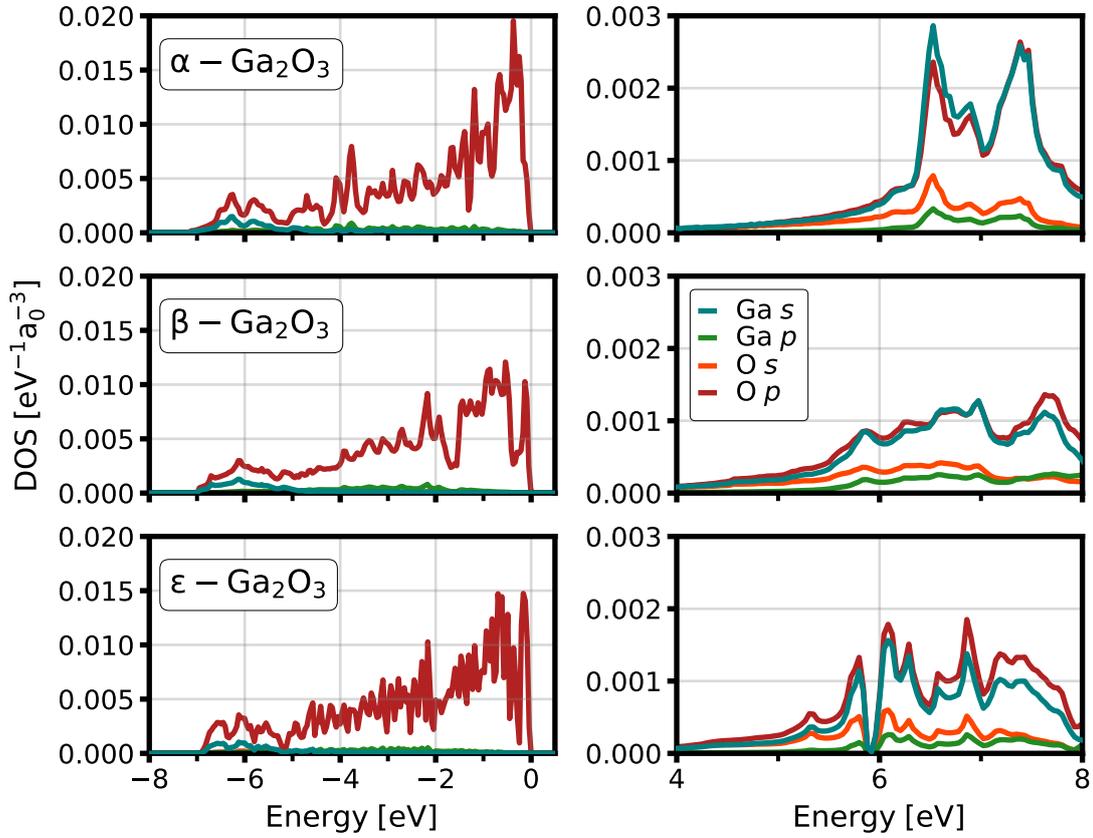e α-phase, such that there is no such peak here. For the ϵ-phase, the ratio of tetrahedral to octahedral gallium atoms is higher, which explains the stronger relative intensity of the peak.

Our results for the electronic structure are in good agreement with previous *ab-initio* calculations with semilocal functionals, as shown in Table 9.1. As expected, the Kohn-Sham band gaps are considerably smaller than the experimental ones. Better agreement is obtained from calculations with hybrid functionals. The application of the G_0W_0 approach on top of HSE calculations [28] gives an even larger band gap, beyond the experimental value. Comparison with G_0W_0 calculations starting from LDA [327] and PBE [328] band structures, which yield considerably smaller band gaps, indicate that there is a strong starting-point dependence. Recent results of quasiparticle-selfconsistent GW calculations [329] indicate that a high band gap of 5.3 eV, close to the one obtained from G_0W_0@HSE calculations is reasonable, since the lattice screening, which is ignored in all calculations shown in Table 9.1 reduces the band gap by up to 0.5 eV [329].

Figure 9.7: Projected valence (left) and conduction DOS (left) of α- (top), β- (middle), and ϵ-Ga_2O_3. The energy of the VBM is set to zero.

	α-Ga_2O_3	β-Ga_2O_3
this work	2.89 eV	2.39 eV
PBE	2.83 eV [28]	2.36 eV [28]
HSE	5.26 eV [330]	4.69 eV [330], 4.87 eV [331], 5.01 eV [328]
GW@LDA		4.24 eV [327]
GW@PBE		4.49 eV [328]
GW@HSE	5.39 [28]	5.04 eV [28]
QSGW		5.33 [329]
Exp.	5.72 eV [332](o), 5.3 eV [333]	4.9 eV [334, 335]

Table 9.1: Summary of the theoretical and experimental band gaps for α- and β-Ga_2O_3. All fundamental band gaps are indirect. For α-Ga_2O_3, only the experimental optical gap is reported, the value is marked by (o).

While the computationally expensive methods yield good results for the band gaps, it has been shown that their effect on the electronic structure is basically a rigid upward shift of the conduction bands [35], affecting the effective masses and other properties derived from the curvature of the band structure only little [28, 328]. Therefore, we employ DFT band structures to calculate the excitations in the following chapters using the semilocal PBE functional [76] and employ a scissors operator to match the experimental band gap.

CHAPTER 10

Optical Spectroscopy

10.1 Absorption Spectroscopy

Generally, the dielectric function is not a scalar, but a tensor of rank two. However, the number of unique components of the dielectric tensor depend on the crystal symmetries. For the rhombohedral α-phase, the dielectric tensor can be reduced to a non-degenerate parallel component $\varepsilon_M^{\parallel}$ along the hexagonal axis $\mathbf{c} = \mathbf{a}_1 + \mathbf{a}_2 + \mathbf{a}_3$ and a two-fold degenerate perpendicular component $\varepsilon_M^{\perp}$ [28, 155], *i.e.*

$$\varepsilon_M(\omega) = \begin{pmatrix} \varepsilon_M^{\perp}(\omega) & 0 & 0 \\ 0 & \varepsilon_M^{\perp}(\omega) & 0 \\ 0 & 0 & \varepsilon_M^{\parallel}(\omega) \end{pmatrix}. \tag{10.1}$$

The entries are shown in Fig. 10.1. The parallel and orthogonal components are similar, both display a sharp peak at the onset of optical absorption. The main peak in both components occurs at approximately 9 eV. A shoulder is observed in the perpendicular component at 6.4 eV, which is not visible in the parallel one. In the latter, on the other hand, the low-energy peak is more pronounced and slightly blue-shifted by about 0.8 eV. The low-energy peak in both components lies below the onset of independent-particle transitions (compare Fig. 10.1), which indicates that the features originate from bound valence excitons. Our calculations yield a series of bound excitons with binding energies below 182 meV. In $\varepsilon_M^{\perp}$, the excitons with the largest binding energy have the strongest oscillator strength. In $\varepsilon_M^{\parallel}$, these excitons have vanishing oscillator strength and the excitonic peak originates from bound excitons with binding energies of around 100 meV, and the peak is therefore found around 80 meV higher in energy. Experimentally, only the perpendicular component of the dielectric tensor has been determined [155]. We find that our calculations yield the position of the low-energy peak and the shoulder in excellent agreement with the experimental spectrum, while the position of the calculated main peak is underestimated by approximately 0.7 eV. Our calculations also agree with previous ones on the same level of theory [28].

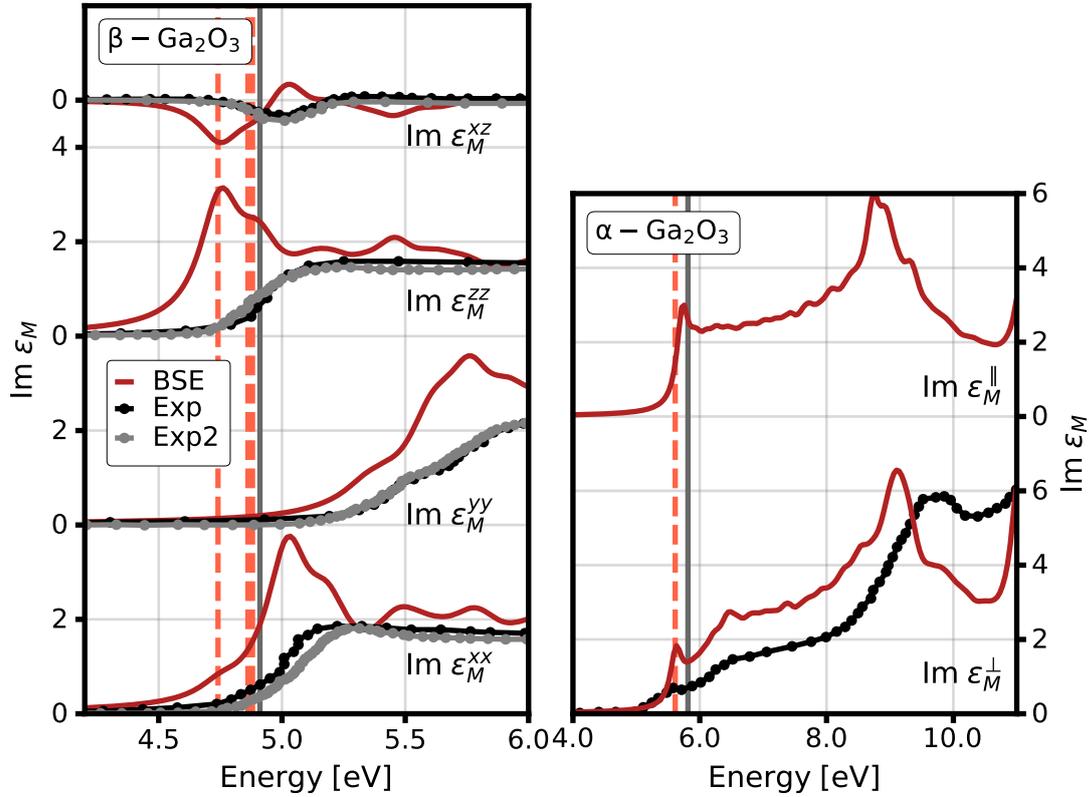For the β-phase, the macroscopic dielectric tensor $\varepsilon_M(\omega)$ consists of four distinct entries

Figure 10.1: Non-vanishing entries of the dielectric tensor of β- (left) and α-Ga$_2$O$_3$ (right). Calculated spectra (red) are compared to experimental ones obtained from Ref. [43] (black) and Ref. [44] (gray) for the β- and Ref. [155] for the α-phase. The optical band gap is marked by a gray vertical line, the position of the bound excitons by vertical red lines.

due to the low degree of symmetry, *i.e.*

$$\varepsilon_M(\omega) = \begin{pmatrix} \varepsilon_M^{xx}(\omega) & 0 & \varepsilon_M^{xz}(\omega) \\ 0 & \varepsilon_M^{yy}(\omega) & 0 \\ \varepsilon_M^{xz}(\omega) & 0 & \varepsilon_M^{zz}(\omega) \end{pmatrix}. \tag{10.2}$$

The non-vanishing entries are shown in Fig. 10.1. In the ε_M^{zz}-component, the calculated spectrum shows a strong peak at 4.76 eV below the direct band gap of 4.9 eV. This peak is introduced by a bound exciton with a considerable binding energy of approximately 230 meV. The shoulder at 4.89 eV is a introduced by bound excitons with lower binding energies. In the ε_M^{xx}-components, the excitonic peak is small, while the main peak appears at 5.03 eV, above the optical band gap. In the ε_M^{yy}-component, no significant absorption oc-

curs below the band gap, such that the first small feature is at 5.35 eV, 0.45 eV above the band gap, and the main peak at 5.76 eV. The anisotropy of the dielectric tensor follows from the anisotropy of the dipole matrix elements in Eq. 6.59. While the CBm has predominant contributions from the largely anisotropic Ga and O s states, the VBM is formed by the strongly anisotropic O p states, such that the matrix elements in the ε_M^{yy}-component vanish within 0.5 eV below the VBM [336]. As such, features originating from bound excitons are only observed in the ε_M^{xx}- and ε_M^{zz}-component, but not in the ε_M^{yy}-component. While the calculated absorption onsets in the different components agree with the experimental results [43, 44], our calculations yields a significantly more considerable absorption for lower energies than observed in experiment. A similar overestimation of the oscillator strength at low energies has been observed in previous calculations on the same level of theory [35], likely due to the strong effect of electron-phonon interaction. For β-Ga$_2$O$_3$, the formation of self-trapped excitons due to the strong interaction of the O $2p$ hole and lattice distortions have been reported in both experimental [337–339] and theoretical studies [30]. The self-trapping leads to a short lifetime of the excitations, which reduces the relative intensity of the excitonic peaks. This finding is corroborated by a electroreflectance study [53], which for β-Ga$_2$O$_3$ yields a lifetime broadening of bound excitons of up to 0.48 eV.

	This work		Experiment	
λ	E_λ [eV]	E_{bind}[meV]	E_λ [eV]	E_{bind} [meV]
		α-Ga_2O_3		
1	5.62	182	-	110 [332]
2	5.67	137	-	-
3	5.71	89	-	-
		β-Ga_2O_3		
1	4.81	170	4.73 [54], 4.57 [53]	250,410
2	4.86	49	4.81 [54], 4.71 [53]	170,280
3	4.88	30	4.88 [54], 4.96 [53]	92,20

Table 10.1: Transition energies E_λ and binding energies E_{bind} of bound excitons in α- and β-Ga_2O_3. The experimental exciton binding energies for α- [332] and transition energies for β-Ga_2O_3 [53, 54] are provided for comparison. The experimental binding energies for β-Ga_2O_3 are determined from the experimental transition energies using the experimental band gap of 4.88 eV.

10.2 Bound Excitons

As shown in Fig. 10.1, bound valence excitons dominate the low-energy absorption in α- and β-Ga_2O_3. For a more comprehensive analysis of the absorption onset, we perform BSE calculations with an increased **k**-sampling, while reducing the number of involved bands to those that are relevant (compare Appendix C). These calculations yield 8 two-fold degenerate bound excitons for α-Ga_2O_3 and 3 non-degenerate bound excitons for β-Ga_2O_3. The transition energies and binding energies of the three most strongly bound excitons of both polymorphs are shown in Table 10.1.

More details are inferred from the exciton weight (compare Eq. 6.53) that represent the distribution of the excited electron and the valence hole for a given excitonic eigenstates $X_{cv\mathbf{k},\lambda}$. As shown in Fig. 10.2, the valence hole and the excited electron are distributed around the Γ-point for the first three bound excitons in the α- and β-phase. The excited electron is distributed solely on the lowest conduction band in both phases, the hole mostly on the highest valence band. A major difference between the polymorphs occurs in the hole distribution: In the β-phase, the highest occupied band at Γ is separated from the second-highest one by around 270 meV. The contributions of other valence bands to the bound excitons are negligible. For the most strongly bound exciton, for example, the contributions of the second-highest valence bands are only 0.02% compared to the contributions of the highest valence band. In the α-phase, the highest valence band at the Γ point is two-fold degenerate and separated by the second-highest valence band (also two-fold degenerate) by only 54 meV. Therefore, contributions to the bound excitons arise from all four highest valence bands in the vicinity of the Γ point. The hole is distributed much more widely over

the valence band than in the β-phase. For the most strongly bound exciton, the second and third band still yield a contribution that is around 2% of that of the highest valence band. The contributions of lower valence bands increase with decreasing binding energy.
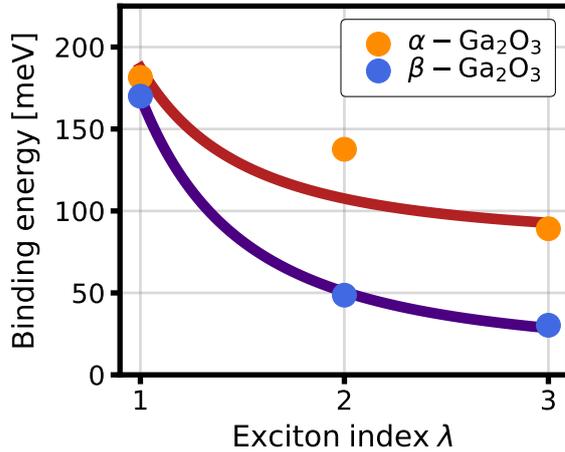

Figure 10.3: Binding energies of the first three excitons in α- (yellow symbols) and β-Ga_2O_3(blue symbols). The Wannier-Mott fit is shown for the β- (red line) and α-phase (blue line).

Generally, two pictures have been developed to understand (bound) excitons in condensed matter: For materials with large static dielectric function $\varepsilon_M \approx 10$, the binding energies are typically only few tens of meV [62, 340]. As such, the electron-hole pair is highly delocalized, *i.e.* their envelope function might extend over tens of unit cells. These excitons are commonly known as *Wannier-Mott excitons* [341, 342]. The binding energies of these excitons can be approximated by a hydrogenic model, assuming that these excitons are formed by transitions from a single parabolic valence band to a single parabolic conduction band. In this model, the bare Coulomb interaction between electron and hole is empirically reduced by the static dielectric constant $\vare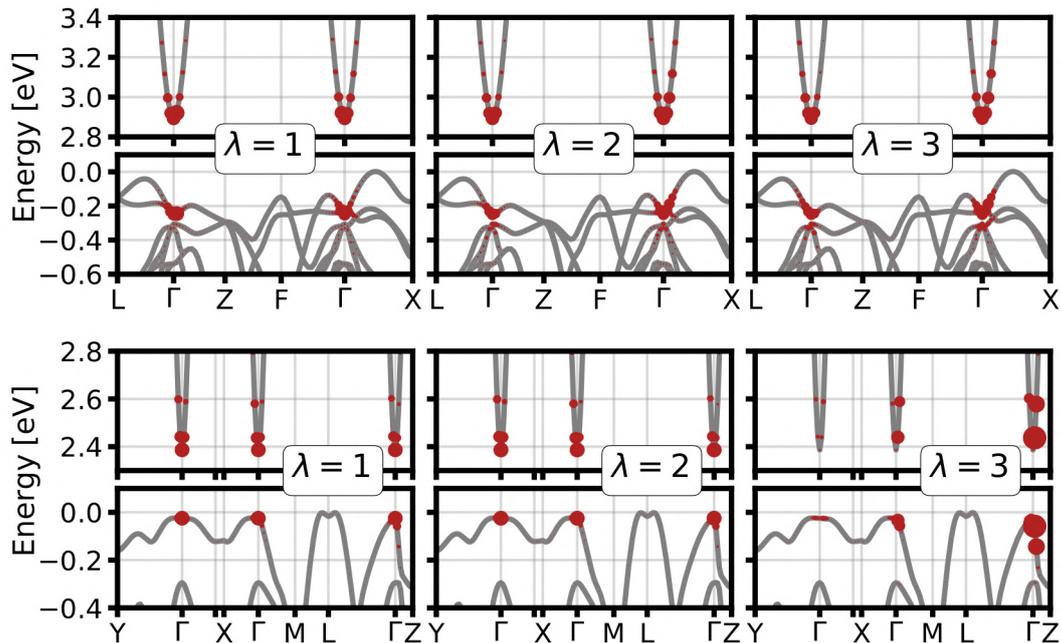psilon_\infty$ to include the screening in the solid. In the simplest approximation of the Wannier-Mott model, the exciton binding energy E_{bind} is given by [62]

$$E_{\text{bind}}(\lambda) = R_\infty \frac{\mu_{ex}}{\varepsilon_\infty^2} \frac{1}{\lambda^2}, \tag{10.3}$$

where $R_\infty = 13.605$ eV is the Rydberg energy, μ_{ex} is the effective mass of the exciton. In many semiconductors containing elements of the groups III − V, the exciton binding energies are in the range of several meV [62, 340] and are well described by the Wannier-Mott model.

For materials with narrow bands and low dielectric function, such as solid noble gases and alkali halides, the exciton binding energies at the absorption onset can be considerable. In solid Ne, for example, it is 4.2 eV [343], in LiF 0.8 eV [344]. In these cases, the electron-hole pairs are highly localized within a single unit cell or at an atomic site. These so-called *Frenkel excitons* are commonly described in terms of on-site excitations and hopping terms between atomic sites [62].

Coming back to Ga_2O_3, the computed binding energies of 170 and 182 for the α- and β-phase, respectively, lie between those of typical Frenkel and Wannier-Mott excitons. In

Figure 10.2: Exciton weight (compare Eq. 6.53) of the first three excitons ($\lambda = 1, 2$, and 3) in α- (top) and β-Ga$_2$O$_3$ (bottom). The size of the red markers indicate the contribution of the corresponding valence or conduction state to the excitonic wavefunction.

order to determine whether the binding energies can still be described by the Wannier-Mott model in Eq. 10.3, we fit the three exciton energies of the β-phase, and the first four in the α-phase with the trial function $E_\lambda = A \cdot \frac{1}{\lambda^2} + B$, where A and B are fit parameters. For β-Ga$_2$O$_3$, this yields an excellent fit ($R^2 = 0.9994$), while the agreement for α-Ga$_2$O$_3$ is significantly worse ($R^2 = 0.825$). From the binding energies and the Wannier-Mott fits shown in Fig. 10.3, it is obvious that the three bound excitons are well described as the Rydberg series of a Wannier-Mott exciton, while the same does not hold for the α-phase. One of the fundamental approximation of the Wannier-Mott approach is the so-called *two-band model*, *i.e.* that the exciton is formed solely by transitions from the highest valence band to the lowest conduction band [62, 345]. While this is a good approximation for the excitons in the β-phase, the mixing of transition from different valence bands in the α-phase is considerable (compare Fig. 10.2). As transitions from several valence bands to the lowest conduction band form the excitons in the α-phase, the binding energies of the excitons are not described well by the Wannier-Mott model.

Excitons in Ga$_2$O$_3$, especially in the β-phase, have been investigated in several recent experimental and theoretical studies. For β-Ga$_2$O$_3$, a series of three bound excitons have been obtained from polarized reflectance [54] and electroreflectance [53] studies. The transition energies are reported in Table 10.1. Our *ab initio* results provide an intuitive interpretation

of the three excitons consistently observed in β-Ga_2O_3, yet the binding energies appear underestimated. The underestimation is most likely due to the overestimation of the screening. In our BSE calculations, the screening is determined within the RPA, and as a result the static dielectric function is overestimated [52]. While RPA calculations [28] yield dielectric constants of $\varepsilon_\infty = 4.38$ for the α- and $\varepsilon_\infty = 4.12$ for the β−phase, respectively, these values are decreased to 3.8 for the α- and 3.56 for the β-phase, respectively, when quasiparticle corrections and electron-hole interactions are taken into account [28]. Model calculations with a static dielectric function that include the effects of electron-hole interaction yields exciton binding energies in closer agreement with experimental values [52].

CHAPTER 11

Oxygen K Edge Spectroscopy

11.1 Absorption Spectroscopy

The O K edge XANES is a widely used spectroscopic tool to investigate the unoccupied electronic structure in oxides [45, 346, 347]. Through the excitations of the localizes oxygen $1s$ electrons, the XANES spectra reveal the local unoccupied electronic structure and bonding environment of the absorbing atom. The calculated O K edge XANES for α-, β-, and ϵ-Ga_2O_3, displayed in Fig. 11.1, are dominated by two pronounced features: a sharp peak at the absorption onset and a second, broader feature approximately 5.5 eV beyond the onset. In the α-phase, between these two features a local minimum and a small peak occurs, approximately 3 eV above the first peak, while no local minimum is found in the spectra of the β- and ϵ-phases. For all three polymorphs, our calculations yield four dark bound excitons below the absorption onset. They are formed by transition from the O $1s$ states to the lowest conduction band, which are has predominantly by Ga s and O s character. As $s \rightarrow s$ transitions are dipole-forbidden, the oscillator strength of the bound excitons is weak, and they are barely visible in the absorption spectra. We obtain binding energies of up to 285 meV in the α-, 345 meV in the β-, and 323 meV in the ϵ-phase. Comparing the experimental [358] and calculated spectra in Fig. 11.1, we observe that the position of the two peaks and the overall spectral shape are excellently reproduced for the β- and ϵ-phase, but the energy distance between the two peaks is underestimated in the α-phase by approximately 1.4 eV. For all three polymorphs, our calculations overestimate the relative intensity of the initial peak. This overestimation is typically observed in BSE calculations of core excitations [348, 349]. It stems from inelastic losses, *i.e.* the response of the many-electron system to the sudden creation of the electron-core hole pair, which is described in our calculations by a constant broadening parameter. An improved description is obtained if the frequency-dependent broadening is determined from the imaginary part of the quasiparticle self energy Σ [350] or by a cumulant approach to the two-particle Green's function [348]. In our calculations, however, the lifetime broadening is approximated by a constant parameter.

As the orientation of the experimental samples is not known, the calculated spectra on the left side of Fig. 11.1 are obtained by averaging over all diagonal entries of the dielectric
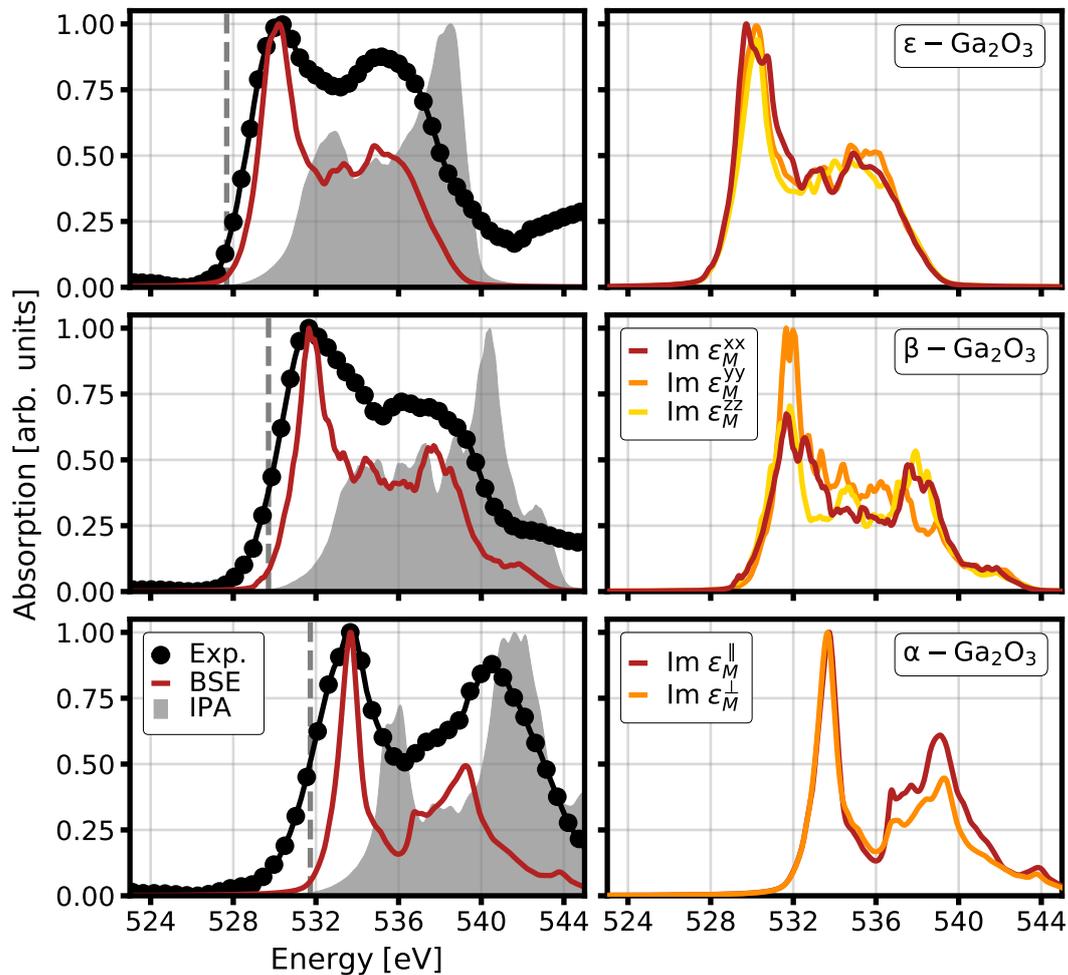
Figure 11.1: Left: Normalized O K edge XANES for α-, β-, and ϵ-Ga_2O_3 (from bottom) from BSE (red), IPA (gray), and experiment (black) [358]. We show Im ε_M averaged over the diagonal components of the dielectric tensor. The absorption onset in the IPA is marked by the dotted line, the IPA spectrum by the gray-shaded area. Right: Relative intensity of the diagonal components for the corresponding phase.

tensor. The parallel and perpendicular component of the α-phase and the diagonal components of the β- and ϵ-phase are shown on the right side of Fig. 11.1. They display only weak anisotropy for all three polymorphs. The anisotropy is most pronounced for the β-phase, where the low-energy peak is significantly stronger in the ε_M^{yy}-component than in the ε_M^{xx}- and ε_M^{zz}-components. The high-energy peak, on the other hand, is found in the ε_M^{xx}- and ε_M^{zz}-components, but not in the ε_M^{yy}-component. We note that this is different from the optical absorption (Fig. 10.1), where the absorption onset is more pronounced in the ε_M^{xx}- and ε_M^{zz}-component. In the α-phase, the pronounced peak at 538.8 eV is found in both $\varepsilon_M^{\parallel}$

and $\varepsilon_M^{\perp}$ with identical intensity. The features at 540 eV has more pronounced intensity in $\varepsilon_M^{\parallel}$ than in $\varepsilon_M^{\perp}$.
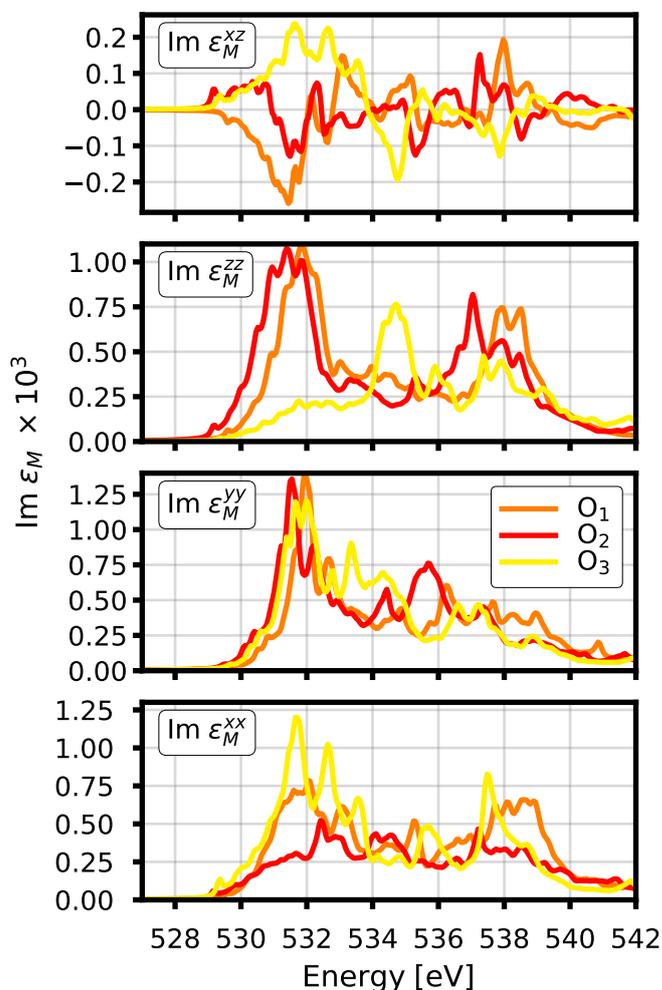
Figure 11.2: Contributions of the inequivalent oxygen atoms O_1 (orange), O_2 (red), and O_3 (yellow) to ε_M^{xx}, ε_M^{yy}, ε_M^{zz}, and ε_M^{xz} (from bottom to top) in β-Ga$_2$O$_3$.

To determine the influence of electron-hole interaction on the O K edge XANES spectra, we include the calculations within the independent-particle approximation (IPA) in Fig. 11.1. We mark the onset of transitions in the IPA with a vertical gray line. The electron-core hole interaction has two effects: the spectrum is red-shifted, *i.e.* absorption occurs at lower energies, and oscillator strength is shifted to excitations at lower energy. In all three polymorphs, the electron-hole interaction significantly alters the spectral shape. In the α- and ϵ-phase, the IPA spectrum already displays the two-peak structure, yet the initial peak has lower intensity than the higher-energy one. In the β-phase, no peak is present at the onset of the absorption spectrum in the IPA. Only when the electron-hole interaction is included in the calculations, the correct relative intensity of the peaks is obtained.

While the unit cell of α-Ga$_2$O$_3$ contains only one inequivalent oxygen atom (compare Chapter 9), the β-phase contains 3, the ϵ-phase 6 inequivalent oxygen atoms. Following Section 6.10, the absorption spectrum is obtained as the sum of the spectra of all inequivalent atoms. For the β-phase, we show the atomic contributions to the non-vanishing entries of the dielectric tensor. The ones of the atom O_1 and O_2 are similar in all components, yet there is a small shift between the spectra due to the shifts between O_1 $1s$ and O_2 $1s$ states. The similarity arises as both atoms share more bonds with the octahedral Ga atoms than with the tetrahedral ones. The atom O_3, on the other hand, shares more bonds with the tetrahedral Ga atom (compare Chapter 9). As such, the difference between the spectrum of
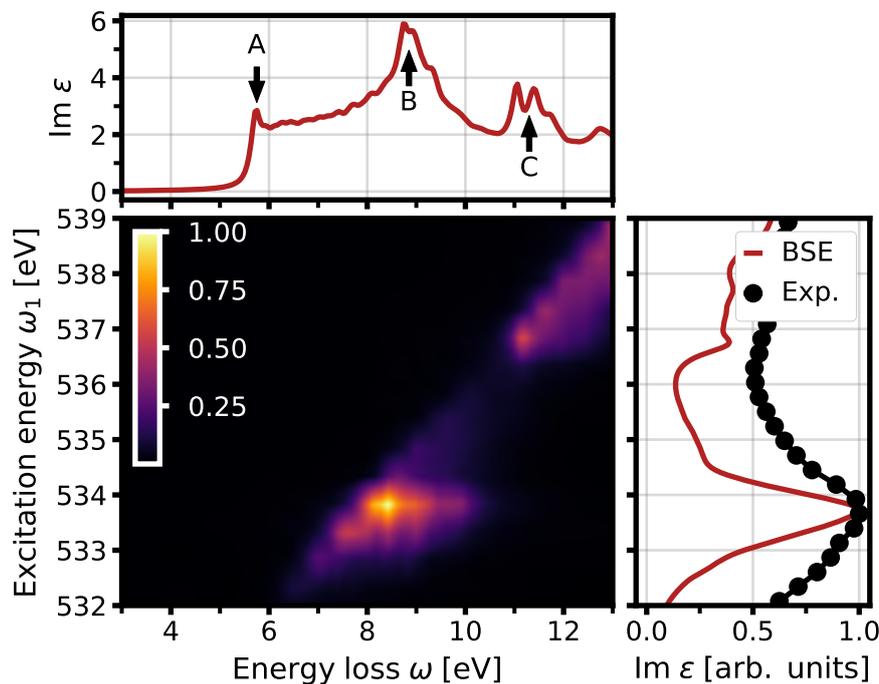
Figure 11.3: Center: O K edge RIXS cross section of α-Ga_2O_3 as a function of the excitation energy and the energy loss. The RIXS spectrum is normalized to the intensity of the most intense peak. Top: Optical absorption spectrum of α-Ga_2O_3. Left: O K edge absorption spectrum normalized to the most intense peak.

O_3 differs more from those of O_1 and O_2 than the spectrum of O_1 and O_2 differ from each other. We find that the initial peak at 532 eV occurs in the absorption spectrum of all three oxygen sites, while the feature at around 538 eV is more pronounced in the spectra of O_1 and O_2. In the spectrum of O_3, on the other hand, we find a peak at approximately 535 eV, which is not present in the spectra of the other atoms. This explains the local minimum observed in the spectrum of the α-phase, because all Ga atoms are octahedrally coordinated and the spectrum resembles that of O_3 in the β-phase. As such, the response at the high-energy feature is more pronounced, while the absorption between the initial and the high-energy peak is reduced. Our analysis of the atomic contributions corroborates previous calculations on the same level of theory [45]. However, the difference in the atomic spectra are small compared to the lifetime broadening of the spectra and thus the spectral differences of the three polymorphs are subtle.

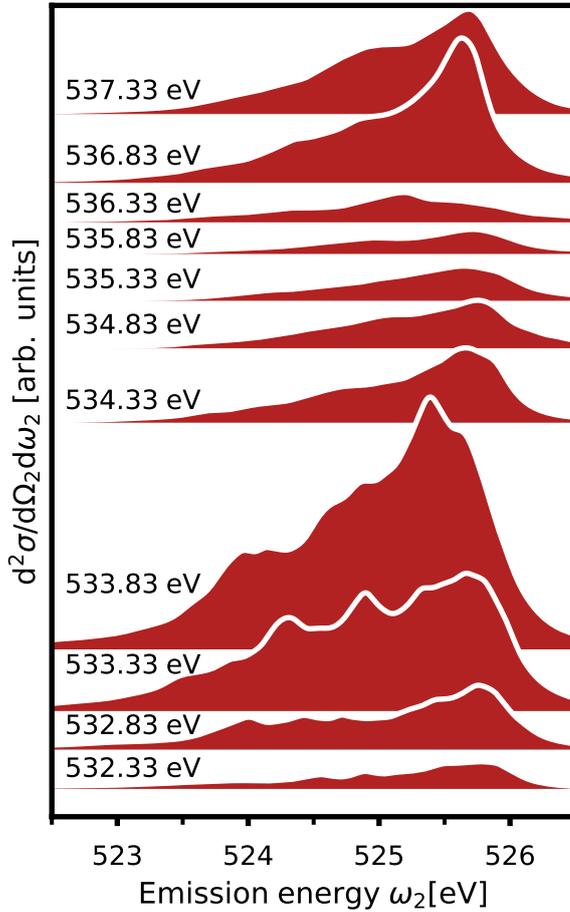## 11.2 Resonant Inelastic X-ray Scattering Spectroscopy

The O K edge RIXS spectra of α- and β-Ga$_2$O$_3$ contain the information on both the valence excitations, which are also studied by optical absorption spectroscopy (compare Chapter 10), and on the O 1s excitations (compare Section 11.1). We first consider the O K edge RIXS for the α-phase, shown in Fig. 11.3. The RIXS spectrum shows an intense peak at an excitation energy of approximately 533.5 eV and an energy loss of 8 eV, the latter being 3 eV above the onset of optical absorption. For excitation energies above 534 eV and energy losses above 9 eV, the RIXS signal decreases sharply as the O K edge absorption spectrum decreases. At excitation energies above 537 eV and higher energy loss of around 11 eV, the RIXS signal increases again.

Figure 11.3 shows that the RIXS spectrum has a pronounced fluorescence form as a function of the excitation energy ω_1 and energy loss ω, *i.e.* features occur at increasing energy loss with increasing excitation energy [176, 177]. In the $\omega - \omega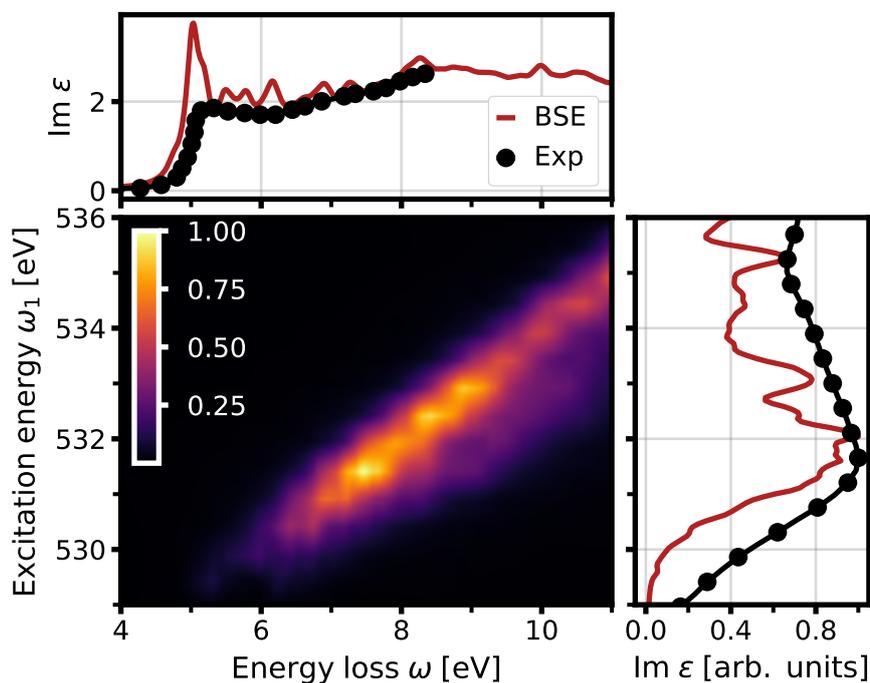_1$ plane, strong features occur mainly along the diagonal line. As a result, the peaks occur at constant emission energy $\omega_2 = \omega_1 - \omega$. This can be seen in Fig. 11.4, where the RIXS spectrum is shown as a function of the emission energy for selected excitation energies. The emission spectrum shows only a very weak dispersion, such that the emission occurs between 523 eV and 526 eV independent of the excitation energy. Nevertheless, the spectral shape changes considerably with the excitation energy. For low excitation energies below 533.5 eV, the spectrum is broad, with considerable contributions at higher loss, *i.e.* at lower emission energies. At an excitation energy of 533.83 eV, the spectrum shows a strong peak at higher emission energies. Increasing the excitation energy further, the overall RIXS signal decreases because the absorption is reduced (compare Fig. 11.3) and the relative intensity of the main peak decreases. For

Figure 11.4: O K edge RIXS in α-Ga$_2$O$_3$ as a function of the emission energy ω_2 for selected excitation energies. The excitation energies are listed in the text. The spectra are offset for clarity.

Figure 11.5: Center: O K edge RIXS cross section of β-Ga$_2$O$_3$ as a function of the excitation energy and the energy loss, normalized to the intensity of the most intense peak. Top: Optical absorption spectrum of α-Ga$_2$O$_3$. Left: O K edge absorption spectrum normalized to the most intense peak.

even higher excitation energies above 536.5 eV, the intensity increases again. While the main peak occurs consistently at an emission energy of approximately 535.5 eV, the final state of the scattering process depends on the excitation energy: For an excitation energy of 533.83 eV, the main peak occurs at an emission energy of 525.38 eV, *i.e.* at an energy loss of 8.45 eV. The peak in the RIXS spectrum thus corresponds to the peak B in the absorption spectrum in Fig. 11.3. For the excitation energy of 536.83 eV, the peak occurs at an emission energy of 525.63 eV, corresponding to an energy loss of 11.2 eV. Thus, the emission peak corresponds to the peak C in the optical absorption spectrum. In summary, the RIXS spectrum for different excitation energies probes different features in the optical excitation spectrum. Note that the excitonic peak A in the optical absorption spectrum can not be probed by O K edge RIXS spectroscopy. This peak originates from bound valence excitons, which are predominantly formed by O $p \rightarrow$ O s transitions (compare Chapter 10). These final states are inaccessible in O K edge RIXS, as O $1s \rightarrow$ O s transitions are dipole-forbidden.

For β-Ga$_2$O$_3$, the O K edge RIXS spectrum in Fig. 11.5 shows a similar fluorescence form. The features occur along the diagonal line in the $\omega - \omega_1$ plane, such that the main peak appears at a constant emission energy independent of the excitation energy. In contrast to

the α-phase, the change of the RIXS spectrum with excitation energy ω_1 is smaller, since features in the O K absorption spectrum are less pronounced.
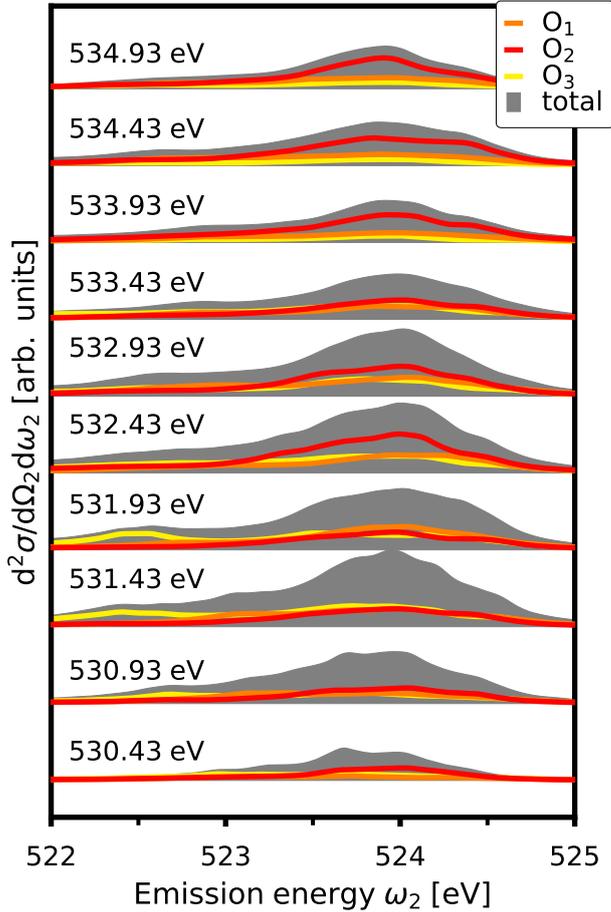

Figure 11.6: O K edge RIXS in β-Ga$_2$O$_3$ as a function of the emission energy ω_2 for selected excitation energies listed in the text. The spectra are offset for clarity.

The spectrum shows a main peak at an excitation energy of 531.4 eV and energy loss of 7.6 eV, while a slightly less intense peak occurs at a higher excitation energy of 532.3 eV and energy loss of 8.4 eV. Like in the α-phase, only a weak RIXS signal is observed for smaller energy loss at the optical absorption onset of 5 eV, as the RIXS transitions in this energy region are dipole-forbidden. Since there are three inequivalent oxygen atoms in the unit cell, the RIXS spectrum in Fig. 11.5 is the sum of three atomic terms and an interference term (compare Section 7.4). The atomic terms represent the RIXS spectrum of each of the inequivalent atoms, while the interference term accounts for the coherence between the atomic terms. In Fig. 11.6, the total RIXS spectrum and the atomic contributions are shown as a function of the emission energy for selected excitation energies. As already apparent in Fig. 11.5, the RIXS spectrum as a function of the emission energy does not show a strong dependence on the excitation energy. The spectrum is broad, with a peak at an emission energy of 524 eV.
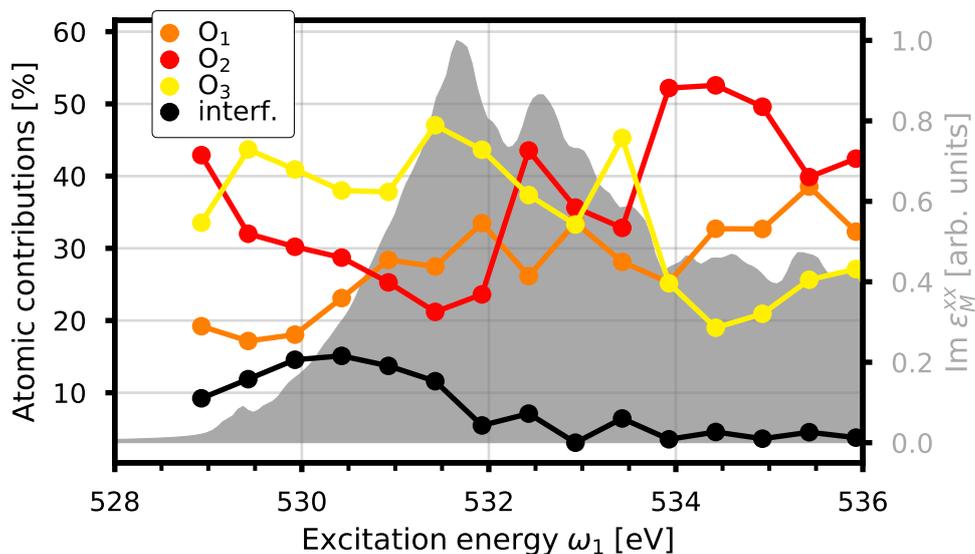
The atomic contributions to the RIXS spectrum, on the other hand, depend on the excitation energies: For excitation energies below 532 eV, the contributions of all three inequivalent oxygen atom are of comparable size. For higher excitation energies, the strongest contribution arises from O$_2$. The contributions for a given excitation energy ω_1 can be quantified using Eq. 7.18. The relative atomic contributions and interference term are shown in Fig. 11.7. At the onset of the O K edge, the contribution of O$_3$ is the largest, providing around 40% of the oscillator strength. With increasing excitation energy above 533.5 eV,

Figure 11.7: Contribution of O_1 (orange), O_2 (red), and O_3 (yellow) to the RIXS spectrum of β-Ga_2O_3 and the interference term (black). For comparison, the total O K edge absorption spectrum of the β-polymorph is shown.

the contribution of atom O_2 is largest. The difference in the atomic contributions is due to the different cross sections of the initial x-ray absorption: Considering the atomic absorption spectra for the different atoms in Fig. 11.2, one notices that the order of the atomic RIXS contributions resembles the difference in atomic absorption. Generally, the largest contribution yields around 50% of the oscillator strength, indicating that even when the response of one oxygen atom is the largest, the response of the other atoms cannot be neglected. The interference term, which originates from the coherent nature of the resonant scattering, contributes up to 15% of the total spectrum at the absorption onset of around 529 eV. With increasing excitation energy, it decreases quickly and, above 532 eV, it contributes only around 5-7%. Thus, the coherence between the atomic contributions is small for these excitation energies, and the RIXS spectrum is well described as a sum of atomic contributions.

Gallium L_2 Edge Spectroscopy

12.1 Absorption Spectroscopy

The excitations of the Ga $2p$ states, *i.e.* the Ga $L_{2,3}$ edge, yield important insight into the unoccupied electronic structure. Because the bottom of the conduction band is formed by Ga s states and $p \rightarrow s$ transitions are dipole-allowed, we expect strong signatures of these transitions in the spectrum. Before discussing the absorption spectrum, it is instructive to consider the Ga $2p$ states in this material: Our calculations yield a splitting of 27.66 eV between the Ga $2p_{1/2}$ and $2p_{3/2}$ states in both the α- and β-phase similar to that determined in previous calculations for the free Ga atom [351]. Due to the large splitting, the excitations from the Ga $2p_{1/2}$ (the Ga L_2 edge) and the Ga $2p_{3/2}$ (the Ga L_3 edge) decouple and can be calculated separately. Since the $2p_{1/2}$ states are fourfold degenerate, while the $2p_{3/2}$ states are eightfold degenerate, the number of transition at the L_2 edge is half of those at the L_3 edge. The spectral shape of the two sub-edges is identical, yet the L_3 edge spectrum is 50% more intense according to the ratio of initial states.

The Ga L_2 edge spectra for α- and β-Ga_2O_3, shown in Fig. 12.1, show a series of four distinct features, denoted as D, E, F, and G. At the onset at 1146.7 eV (1146.9 eV) in the α- (β-)phase, we find the distinct peak D. The feature E appears as a shoulder at 1150 eV in the α-polymorph, while it is a pronounced peak at 1149.3 eV in the β-phase. The sharp feature C, occurring at 1152 eV and 1151.3 eV in the α- and β-polymorphs, respectively, is more pronounced in the latter than in the former. At higher energies, the broad feature D appears at around 1158 eV (1156.7 eV) in the $\alpha(\beta)$-polymorph. A visible difference in the spectra of the two polymorphs is the relative intensity of peak E: While it is weak in the α-phase, it is more pronounced in the β-phase. To determine the origin of the peaks, the absorption spectra of the octahedrally coordinated atom Ga_1 and the tetrahedrally coordinated Ga_2 in the β-phase are calculated individually, and the total spectrum is obtained as the sum of the two. While peak D occurs in the spectrum of both atoms, the other peaks can be assigned to one of the gallium sites: E and C occur only in the spectrum of Ga_1, D only in that of Ga_2. The spectrum of Ga_2 shares more resemblance with the spectrum of the α-polymorph, since in the latter all gallium atoms are tetrahedrally coordinated.
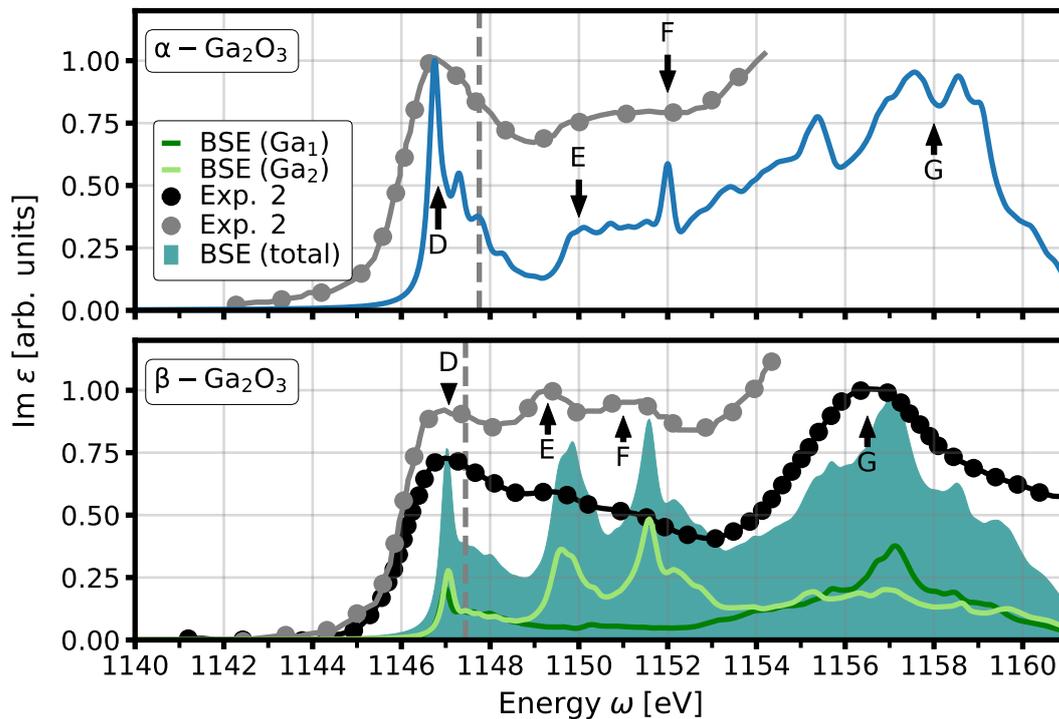
Figure 12.1: Ga L$_2$ edge spectra for α- (top) and β-Ga$_2$O$_3$ (bottom). The spectra are obtained as averages over the diagonal components of the dielectric tensor. For β-Ga$_2$O$_3$, the spectra of the octahedral atom Ga$_1$ (dark green) and the tetrahedral atom Ga$_2$ (light green), and the total spectrum (teal area) are displayed. The experimental spectra are extracted from Refs. [50] (black) and [51] (gray).

For both α- and β-Ga$_2$O$_3$, the peak D occurs below the onset of independent-particle transitions, *i.e.* it originates from bound excitons. We find two bound excitons in the α-phase with a maximum binding energy of 390 meV, four in the β-phase with a maximum binding energy of 460 meV for Ga$_1$, and 527 meV for Ga$_2$. Because of the two-fold degeneracy of the gallium $2p_{1/2}$ states, each exciton is two-fold degenerate. The distributions of the excited electron in the bound electrons in Fig. 12.2 show that the excited electron is completely contained in the lowest conduction band in the vicinity of the Γ-point. As for the optical spectrum (Fig. 10.2), the excited electron in the bound excitons with the highest binding energies ($\lambda = 1$ and $\lambda = 2$) are distributed at the Γ-point, while for those with smaller binding energies ($\lambda = 3$ and $\lambda = 4$), it is distributed predominately at slightly higher energies, along the $\Gamma - X$ path. For both the α- and β-phase, the bound excitons have considerable oscillator strength, since the lowest conduction band is predominantly formed by Ga s states, and Ga $2p_{1/2} \rightarrow$ Ga s transitions are dipole-allowed. As for the case of the optical spectrum (compare Chapter 10), we fit the series of bound excitons
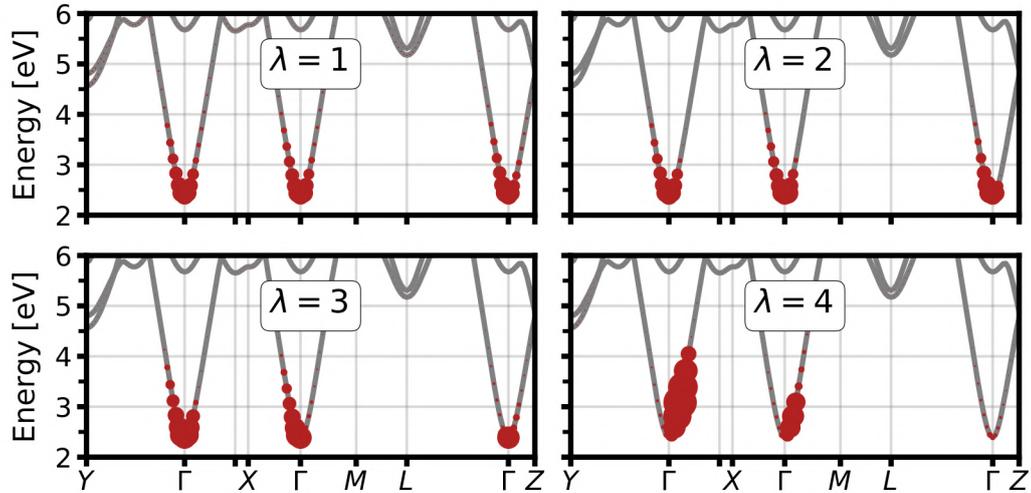
Figure 12.2: Distribution of the excited electron for the four bound excitons ($\lambda = 1, 2, 3, 4$) below the transition onset in the Ga_1 L_2 edge spectrum in β-Ga_2O_3. The size of the red circles denotes the relative contribution of the corresponding conduction state.

with a Wannier-Mott model following Eq. 10.3. The results for the β-phase are shown in Fig. 12.3. In the α-polymorph, no fitting can be performed, as a model with two parameters cannot be applied to only two bound excitons. The binding energies of the first exciton of the two inequivalent gallium atoms differ by approximately 70 meV, and this difference decreases to 12, 5 and 0.2 meV for the excitons with lower binding energies.
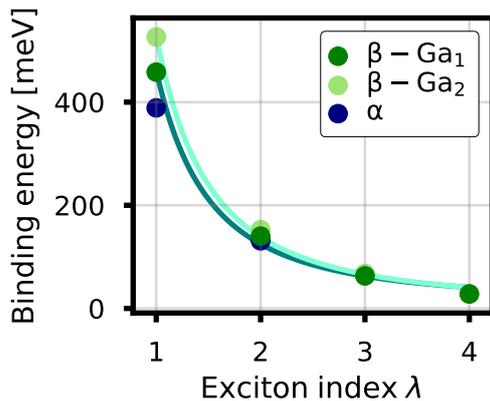

Figure 12.3: Binding energies of the bound excitons in the Ga L_2 edge spectrum of α- and β-Ga_2O_3. Additionally, the Wannier-Mott fit for the β-phase is shown.

We find that for the excitations of both atoms, the Wannier-Mott model yields an excellent fit ($R^2 = 0.996$ for Ga_1 and $R^2 = 0.998$ for Ga_2). This indicates that these bound excitons are well described by the Wannier-Mott model. Remember that for the bound excitons in the optical spectra of α- and β-Ga_2O_3, we discussed that the Wannier-Mott model assumes that the bound excitons are formed by transition from a non-degenerate occupied band to a non-degenerate conduction band. Since the excitons are formed by transition from the Ga $2p_{1/2}$ states to the non-degenerate lowest conduction band, the Wannier-Mott model explains the binding energies well.

Measurements of the Ga L_3 XANES of Ga_2O_3-

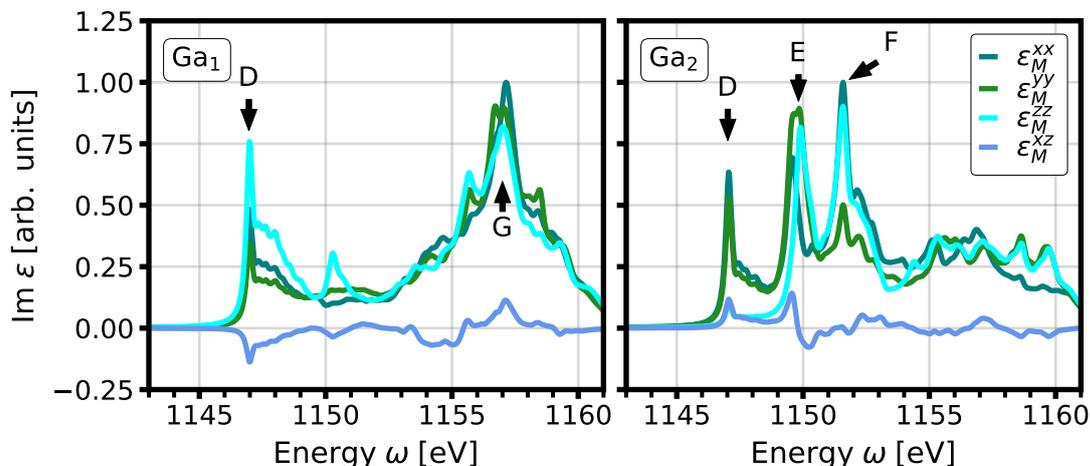**Figure 12.4:** Ga L$_2$ spectrum of the Ga$_1$ (left) and Ga$_2$ (right) atomic site in β-Ga$_2$O$_3$.

polymorphs have, to the best of our knowledge, not been reported so far. However, experimental Ga L$_2$ edge XANES for both α- [51] and β-Ga$_2$O$_3$ [50, 51] have been published. As the Ga L$_2$ and L$_3$ edge XANES are identical, up to a constant prefactor, we construct the former from the latter. To align the calculated and experimental spectra, we first shift the experimental XANES by the spin-orbit splitting of 27.66 eV, to obtain the Ga L$_3$ edge counterpart. Due to the finite precision in the energy calibration of the measurements, the experimental spectra of Refs. [51] and [50] are rigidly shifted with respect to each other. We have aligned the experimental spectra to the calculated one at the peak G. Generally, we find good agreement between the calculated and experimental results. In the α-phase, the pronounced peak G and the shoulder E are observed in both experimental and calculated spectra at identical positions. The peak F is hidden in the experimental spectrum due to the larger broadening. In the β-phase, the peaks D and G can clearly be observed in the experimental spectrum from Ref. [51], while the peaks E and F are barely visible due to the large broadening. The peaks E and F are much better visible in the experimental spectrum from Ref. [51] than in the one from Ref. [50]. The relative intensity of the features in the experimental spectra is well reproduced by our calculations.

Since in Fig. 12.1, the Ga L$_2$ edge spectra are displayed as the average over all diagonal entries of the dielectric tensor, the anisotropy of the spectra is hidden. In Fig. 12.4, we show the imaginary part of the diagonal components for both absorbing sites. For Ga$_1$, the peak D is stronger in the ε_M^{zz} component than in ε_M^{xx} and ε_M^{yy}, while the broad peak G does not display strong anisotropy. A small peak is visible in ε_M^{zz} at the position of peak E, which is not visible in the averaged spectrum in Fig. 12.1. For Ga$_2$, the initial peak D is more pronounced in the ε_M^{xx} and ε_M^{yy} components, where it has approximately the same relative intensities. In the ε_M^{zz} component, it occurs only with greatly reduced intensity. The peak

E and F occur all three components with comparable intensity.

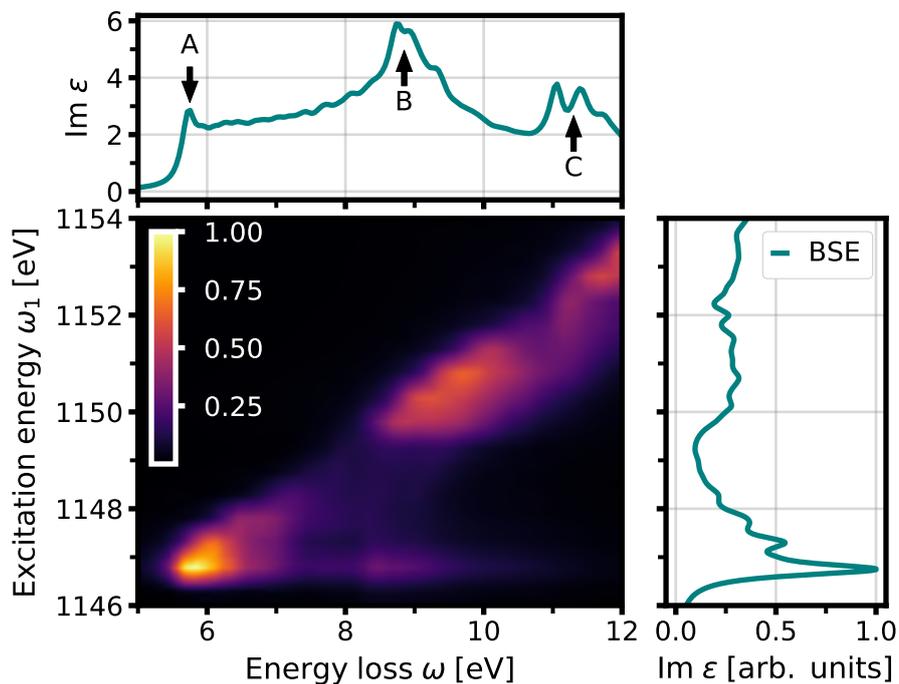**Figure 12.5:** Center: Normalized Ga L$_2$ edge RIXS cross section of α-Ga$_2$O$_3$ as a function of excitation energy and energy loss. Top: Optical absorption spectrum. Right: Normalized Ga L$_2$ edge absorption spectrum.

12.2 Resonant Inelastic X-ray Scattering Spectroscopy

In the previous section, we have shown that the Ga L$_2$ edge XANES spectra of both the α- and β-phase display a pronounced excitonic peak at the onset of the spectrum. The contributions of the inequivalent Ga atoms can clearly be separated, to the extent that several features originate solely in the response of a specific atom. We now turn to the RIXS spectra to determine how the Ga L$_2$ edge can provide insight into the nature of the valence excitations, especially the bound excitons already discussed in Chapter 10.

The spectrum of α-Ga$_2$O$_3$ in Fig. 12.5 shows a strong peak at the Ga L$_2$ absorption onset of 1146.75 eV and an energy loss of 5.8 eV, which is identical to that of peak A at the onset of the absorption spectrum. In Chapter 10, we have identified peak A to originate from bound excitons formed by transitions from the VBM to the CBm (compare Fig. 10.1). Equivalently, bound excitons introduce the pronounced peak at the onset of the Ga L$_2$ edge absorption spectrum (compare Fig. 12.1).
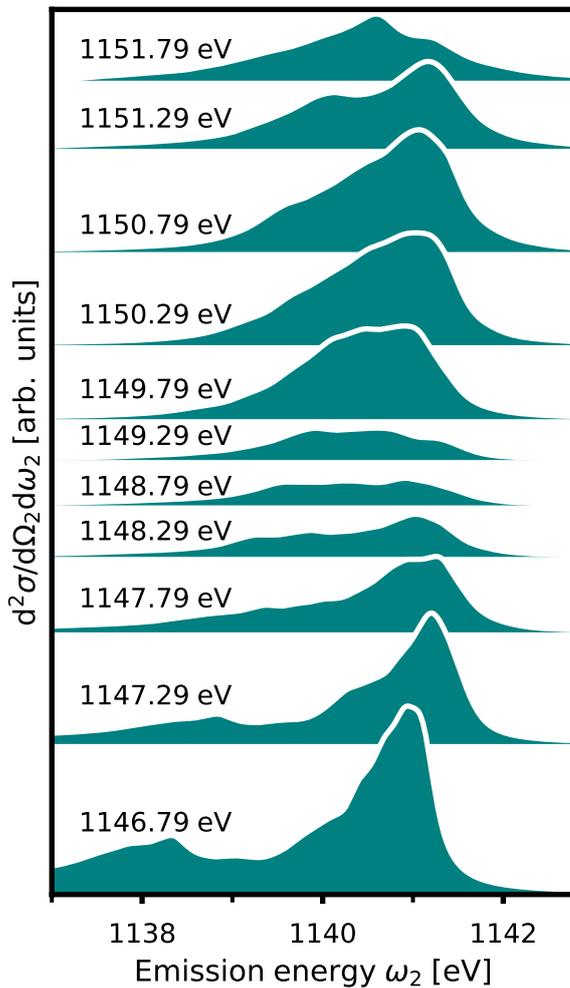
The intense peak in the RIXS spectrum therefore originates from the absorption of the x-ray photon with an energy of around 1146.75 eV, which leads to an intermediate state that contains a strongly bound core exciton. Transitions of a valence electron from the VBM fill the Ga $2p_{1/2}$ core hole and result in the formation of the bound valence exciton. The initial excitation is dipole-allowed, since the CBm has a strong Ga s contribution. The subsequent de-excitation from the VBM is also dipole-allowed, as it is formed by hybridized O p and Ga s states. Therefore, this scattering process leads to an intense peak in the RIXS spectrum. For the same excitation energy, a second, broader feature occurs at the energy loss of peak B in the optical spectrum. With increasing excitation energy, a linearly dispersive fluorescence feature occurs in the RIXS spectrum. Its intensity is low for excitation energies between 1148 and 1150 eV due to the low intensity of the initial absorption process. A second, broader feature is observed for excitation energies arou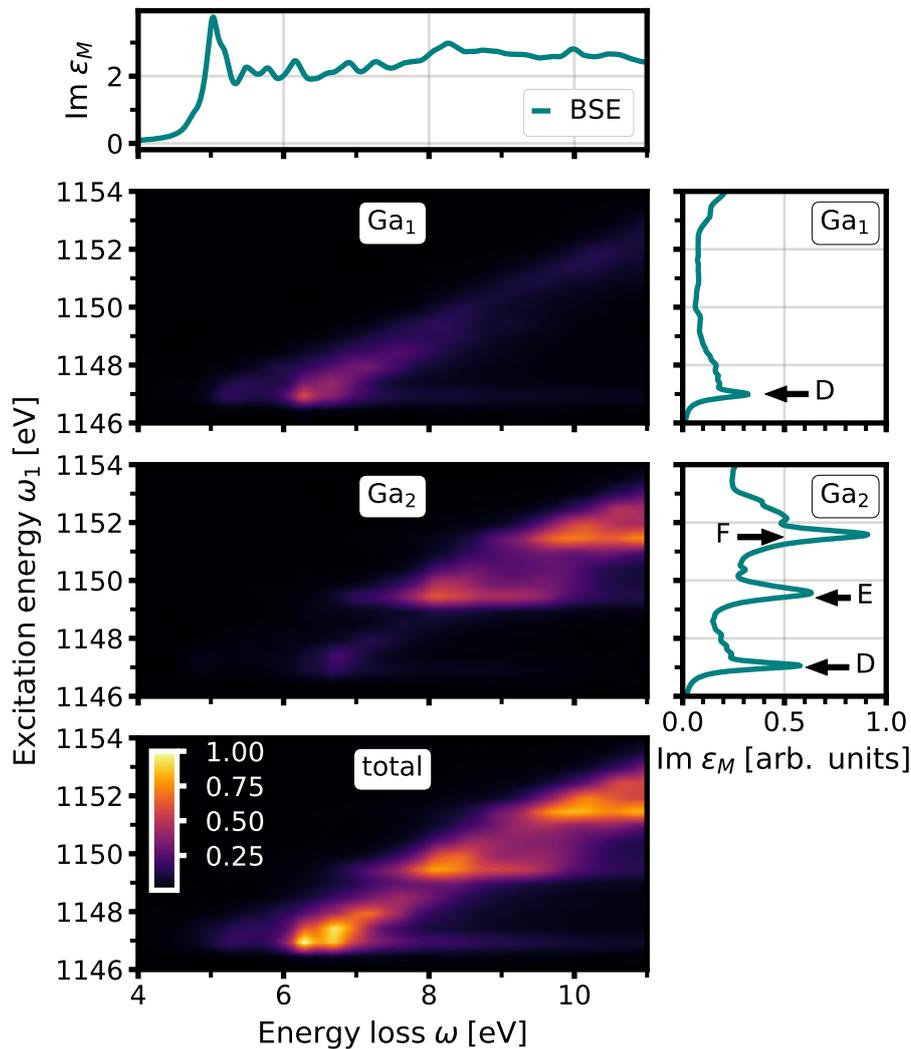nd 1151 eV and an energy loss of approximately 9.7 eV, corresponding to peak B. The presence of the feature indicates that the distribution of the excited electron for Ga $2p_{1/2}$ excitations around 1151 eV and for optical excitations around 9.7 eV is similar. The feature in the RIXS is broad compared to the peak at lower excitation energy, as the scattering process involves broad band transitions both in the excitation and emission process.

Due to its fluorescence shape, features of the RIXS spectrum occur at constant emission energy, which is shown for selected excitation energies in Fig. 12.6. The spectral shape, however, changes considerably with increasing excitation energy. At the absorption onset,

Figure 12.6: Ga L_2 edge RIXS spectrum for α-Ga_2O_3 as a function of the emission energy for selected excitation energies. The spectra are offset for clarity.

Figure 12.7: Ga L$_2$ edge RIXS cross section of Ga$_1$ (top) and Ga$_2$ (center) in β-Ga$_2$O$_3$ and the total RIXS cross section (bottom) as a function of excitation energy and energy loss. All RIXS spectra are normalized to the intensity of the maximum of the total Ga L$_2$ edge RIXS. Top: Optical absorption spectrum. Right: Normalized Ga L$_2$ edge absorption spectrum of Ga$_1$ and Ga$_2$, respectively.

the sharp excitonic peak is found at an emission energy of 1140.95 eV. With increasing excitation energy, the relative intensity of this peak decreases and the peak at around 1141 eV becomes broader. For intermediate excitation energies between 1147.8 and 1149.5 eV, the overall RIXS signal is weak (compare Fig. 12.5). Above 1149.5 eV, the signal increases, and the RIXS spectrum displays a broad peak at 1141 eV with a pronounced slope to lower emission energies.
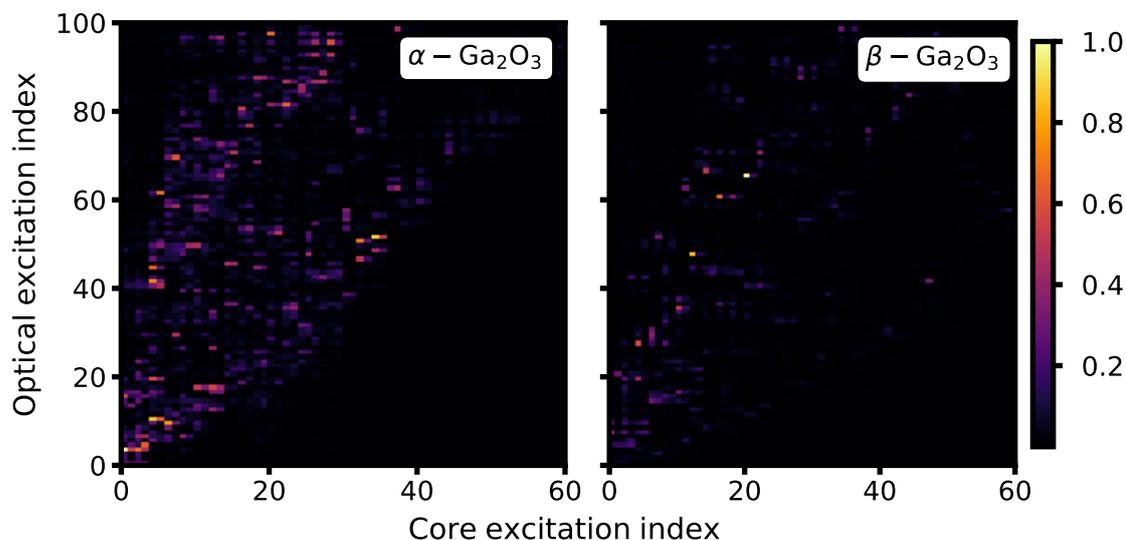
Figure 12.8: Absolute-squared matrix elements $|t^{(2)}|^2$ of the excitation pathway matrix for the $\alpha-$ (left) and β-phase (right). The elements between the first 60 core excitations and 100 first valence excitations are shown, normalized to the maximum value in that range.

We now turn to the RIXS spectra of the β-phase in Fig. 12.7. Since the core excitations strongly depend on the absorbing atomic site in β-Ga$_2$O$_3$ (compare Fig. 12.1), we expect that the resonant scattering will show a similar dependence. The total RIXS spectrum shows three distinct features. Each of them occurs for a narrow range of excitation energies, but a wide range of energy loss values and, as such, appear as horizontal lines in the $\omega - \omega_1$ plane. The first feature occurs at the absorption edge at 1146.25 eV, and the strongest oscillator strength is observed for an energy loss of about 6.3 eV. However, significant oscillator strength also occurs for energy losses of up to 8.8 eV. The excitation energy of this feature corresponds to that of feature D in the Ga L$_2$ absorption spectrum. For the second feature, the excitation energy of 1148 eV corresponds to that of feature E in the absorption spectrum, while the third feature appears at the excitation energy of peak F at 1150.9 eV and a range of energy loss around 10.3 eV.

The two features at higher excitation energies can be assigned to Ga$_2$, since peaks E and F only occur in the absorption spectrum of this atom. Both features are very broad as functions of the energy loss, such that an assignment of these features to peaks in the optical spectrum is not possible. This is due to the fact that the optical absorption spectrum shows only very weak spectral features at energy loss values above the absorption onset. Peak D occurs in the absorption spectrum of both atomic sites, yet the corresponding feature in

the RIXS spectrum occurs much more pronounced in the spectrum of Ga_1 than in that of Ga_2. As the intensity of peak D in the absorption spectra of both atoms is comparable, the difference in the RIXS spectrum has to originate from the different oscillator strengths of the de-excitation process. The energy loss of 6.4 eV is significantly higher than the absorption onset of 4.91 eV, such that the final state of the scattering is not a bound valence exciton, which occur in β-Ga_2O_3 at around 4.75 to 4.9 eV (compare Fig. 10.1). The energy loss is furthermore higher than that of the pronounced peak in the optical absorption at 5 eV. This indicates that the valence excitations at low energies, including the bound valence excitons, cannot be excited by the resonant scattering process due to the dipole selection rules. This is in contrast to the RIXS spectrum of the α-phase, where a strong signal for the scattering into the bound valence excitons is observed (compare Fig. 12.5).
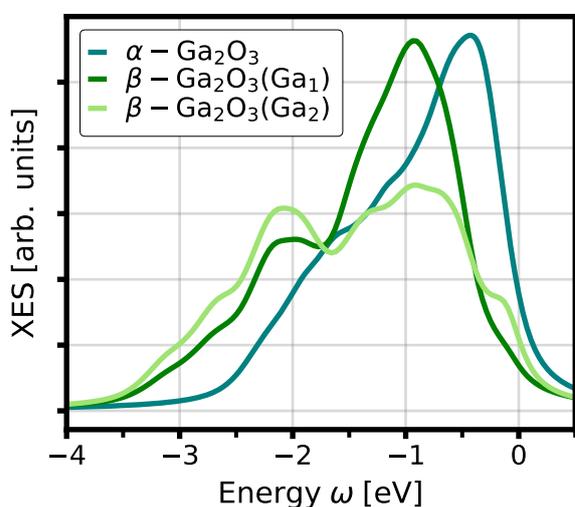

Figure 12.9: Ga L_2 edge non-resonant x-ray emission spectra (XES) for α-Ga_2O_3 (teal) and the atoms Ga_1 (dark green) and Ga_2 (light green) in β-Ga_2O_3. All spectra are aligned to the position of the valence band maximum.

A more detailed analysis of the RIXS onset, *i.e.* the scattering for low excitation energies and low energy loss, can be performed by considering the excitation pathways $t^{(2)}$ between the initial core and final valence excitations. These pathways, defined in Eq. 7.6, determine the rate of de-excitation from a many-body state with a core hole and an excited electron to a state containing a valence hole and an excited electron. The pathways for the first 60 intermediate states and 100 final states of both phases are shown in Fig. 12.8. The bound excitons corresponds to the first few indices for both the core and optical excitations, *i.e.* the lower-left corner of the plots. For both phases, the $t^{(2)}$ matrix shows a banded form, where non-zero entries for increasing core-excitation indices occur mostly for increasing optical-excitation indices. This banded form yields the linearly dispersive features in Figs. 12.5 and 12.7.

Nevertheless, the $t^{(2)}$ matrix elements for low core and optical excitation indices are distinct between the two phases. In the α-phase, strong pathway elements occur in the lower left corner of Fig. 12.8, *i.e.* for the low-energy core and optical excitations. In the β-phase, however, significant non-zero pathways occur for higher optical excitation indices, indicating that the pathways between low-energy core and optical excitations are negligible. As such, the Ga L_2 edge RIXS can access the bound valence excitons of the α-phase, but
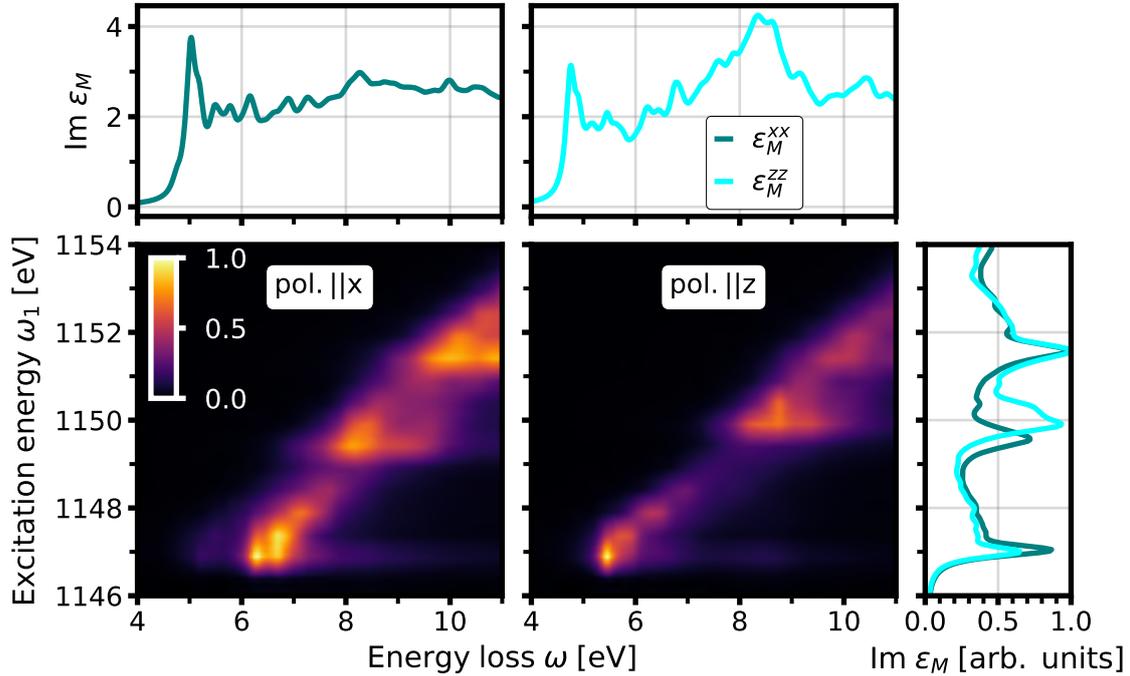
Figure 12.10: Normalized Ga L_2 edge RIXS of β-Ga_2O_3 for light polarizations along the x-axis (lower left) and along the z-axis (lower center). The corresponding components of the dielectric tensor in the optical region are shown in the top panels. The Ga L_2 edge XANES for both polarizations are shown on the left.

not those of β-Ga_2O_3. Fundamentally, this difference originates from the different degree of hybridization: De-excitation from low-energy core excitations to low-energy valence ones are due to the transition from the VBM to the Ga $2p_{1/2}$ core hole. Since the former has mostly O p character (compare Chapter 9), the amount of hybridization with the Ga s states determines whether the transitions are dipole-allowed. Since in both phases, the low-energy excitations occur predominantly in a small region of the Brillouin zone around the Γ-point (compare Fig. 10.2), the hybridization in that region specifically determines the rate of the de-excitation. In the α-phase, the hybridization of O p with Ga s states at the VBM is stronger than in the β-phase. This subtle difference in the hybridization can be further demonstrated by considering the non-resonant x-ray emission spectroscopy (XES), which yields information on the valence band structure through non-coherent de-excitations from valence states to the Ga $2p_{1/2}$ core hole (compare Section 5.3). In the α-phase, the Ga L_2 edge XES shows a pronounced peak around 0.4 eV below the onset of the valence band. For the β-phase, the peak occurs at lower emission energies, about 0.9 eV below the VBM. In the β-polymorph, the emission spectra of the two inequivalent gallium atoms differ significantly: The Ga_1 XES shows a distinct peak 0.9 eV below the VBM and a second, less

intense peak 2 eV below the VBM. For Ga$_2$, the peak 0.9 eV below the VBM is less intense, but a small shoulder at higher emission energy, 0.1 eV below the VBM, appears. These differences occur since the hybridization of the O p states with Ga s states at the VBM is more pronounced in the α- than in the β-phase. In the latter, the hybridization at the VBM is more pronounced for Ga$_1$ than for Ga$_2$. These subtle differences in the electronic structure lead to the significant difference in the Ga L$_2$ edge RIXS spectrum.

The Ga L$_2$ edge absorption spectrum displays a strong anisotropy, as shown in Fig. 12.4. This leads to a corresponding anisotropy of the Ga L$_2$ edge RIXS, which is shown in Fig. 12.10, where the spectra for β-Ga$_2$O$_3$ in x and z polarization are compared. Both spectra show the three distinct features, discussed above. The first feature appears for both polarizations at the absorption onset of 1146.3 eV. The energy loss of the first peak for z polarization is around 5.5 eV and, as such, 0.8 eV lower than for the x polarization. The second feature shifts slightly upward in excitation energy to 1149.2 eV in z polarization, as the second peak in the component ε_M^{zz} is around 0.5 eV higher than in ε_M^{xx}. Even though the first peak occurs at lower loss, it still occurs above the onset of the optical spectrum (at 4.75 eV for z polarization). This demonstrates that the bound valence excitons of β-Ga$_2$O$_3$ cannot be accessed by Ga L$_2$ edge RIXS, irrespective of the polarization direction.

CHAPTER 13

Gallium K Edge Spectroscopy

13.1 Absorption Spectroscopy

The excitations of the Ga 1s states, *i.e.* the Ga K edge, yield complementary information to the Ga L$_2$ edge described in Chapter 12, as both probe the local geometry and electronic structure of the absorbing gallium atom with a different cross section. As such, it has been employed in experimental studies to determine the electronic structure of different Ga$_2$O$_3$ polymorphs [47], the local structure of Ga$_2$O$_3$ nanostructures [46], the geometry of indium-gallium-oxide [48], and that of amorphous Ga$_2$O$_3$ [49]. These studies have, for instance, provided indications for distinctive contributions of inequivalent atoms in the β-phase. While first *ab initio* core-hole calculations for the β-phase [49] have presented promising results and provided a first analysis of the contributions of inequivalent atoms, a detailed first-principles analysis of the Ga K edge spectra is lacking so far. In Fig. 13.1, we display the Ga K edge spectra of α- and β-Ga$_2$O$_3$, averaged over all diagonal components of the dielectric tensor. The spectra of the α-phase displays two peaks: a broad peak L at 10375.5 eV and a less pronounced peak M at 10378 eV. The spectra of the β-phase, on the other hand, shows a series of three peaks, denoted H, L, and M. Our analysis shows that peak H at 10372.5 eV originates from transitions at Ga$_1$, while peak L at 10374.3 eV occurs in the spectra of both atomic sites. Peak M at 10376.7 eV occurs only in the spectrum of Ga$_2$. Comparing the β-phase with the α-phase, it is apparent that the spectrum of Ga$_1$ resembles that of the α-phase, since all Ga atoms in the latter are octahedrally coordinated. Figure 13.1 additionally shows experimental spectra extracted from Refs. [46] and [48]. The finite precision of the experimental energy calibration induces a rigid shift between the spectra from Refs. [46] and [48], and we align the experimental and calculated spectra at the most intense feature M. We find that our results are in excellent agreement with the experimental ones. From deconvolution analysis [47] and previous *ab initio* calculations [49], it has been proposed that peak H originates from transitions at octahedrally coordinated Ga atoms, while peak M originates from those at tetrahedrally coordinated Ga atoms, which is confirmed by our calculations. The distance between the peaks H and M of 4.2 eV is also in good agreement with the experimental values of 3.9 eV [47] and 4 eV [48].

Due to the strong anisotropy of the Ga$_2$O$_3$ polymorphs, the different components of the dielectric tensor have distinct spectral shapes. In Fig. 13.2, we compare the diagonal com-
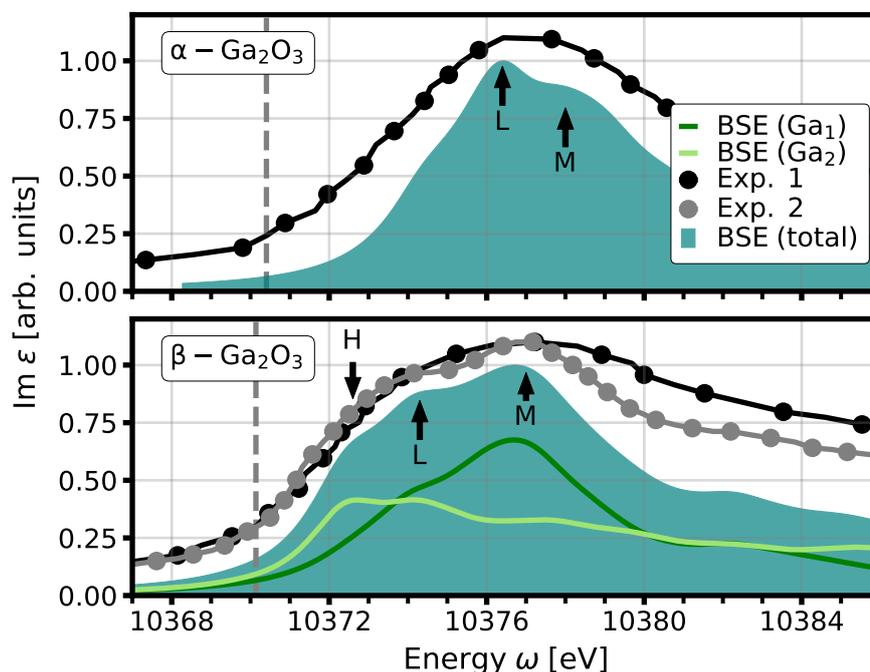
Figure 13.1: Calculated total Ga K edge XANES spectra (teal) of α- (top) and β-Ga$_2$O$_3$. For the β-phase, the contributions of the inequivalent atom Ga$_1$ (dark green) and Ga$_2$ (light green) are displayed. The experimental spectra are obtained from Refs. [46] (black) and [48].

ponents for Ga$_1$ and Ga$_2$. The figure demonstrates that the assignment of the peaks to the inequivalent atoms (compare Fig. 13.1) becomes more complex: For the spectrum of Ga$_1$, peak K occurs solely in ε_M^{zz}, which, in turn, does not display the dominant peak L of the averaged spectrum. The components ε_M^{xx} and ε_M^{yy} are similar, both showing the pronounced peak L. For Ga$_2$, peak H occurs strongly in ε_M^{xx}, and less distinct in ε_M^{yy}. Neither of these components displays peak K, and peak L is missing in ε_M^{xx} as well. In ε_M^{zz}, is less pronounced. While the polarization-dependence of the Ga K edge is complex, the spectral features along each of the components can be assigned to one of the inequivalent atoms. For the ε_M^{xx}- and ε_M^{yy}-components, the analysis we presented for the averaged spectra in Fig. 13.1 holds: The spectrum of Ga$_1$ is dominated by peak L, while that of Ga$_2$ shows a more pronounced peak H, where peak L is either weak or missing completely. For the component ε_M^{zz}, the difference between the atomic contribution is more subtle. For both atomic sites, K is the main peak. However, the spectrum of Ga$_2$ shows a much more pronounced peak L than the spectrum of Ga$_1$.
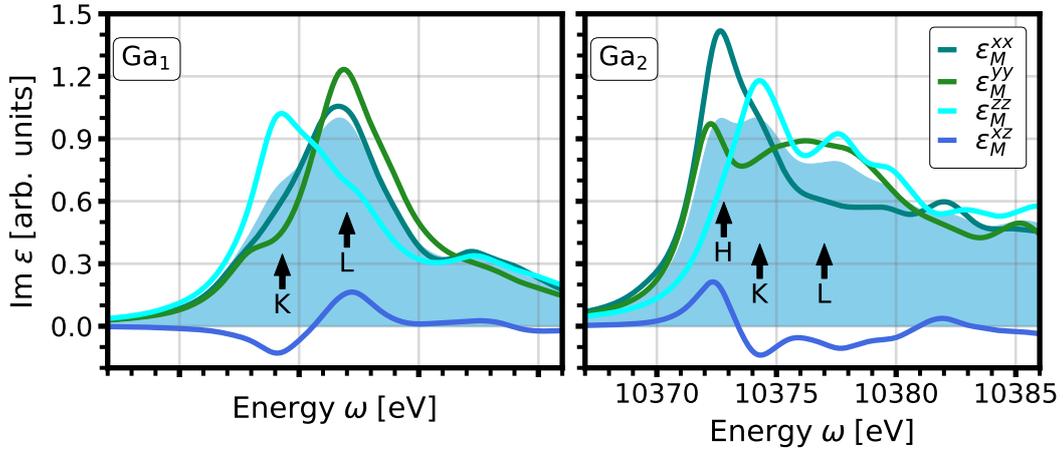
Figure 13.2: Components of the dielectric tensor at the Ga K edge for the atomic site Ga$_1$ (top) and Ga$_2$ (bottom). The components ε_M^{xx} (dark blue), ε_M^{yy} (dark green), ε_M^{zz} (cyan), and ε_M^{xz} (blue) are compared to the averaged spectrum (shaded area).

13.2 Resonant Inelastic X-ray Scattering Spectroscopy

We now turn to the Ga K edge RIXS. The spectrum of α-Ga$_2$O$_3$, shown in Fig. 13.3, displays a pronounced peak at the position of the Ga K edge absorption onset at 10376 eV. A less intense feature occurs at slightly lower excitation energies of around 10374 eV. These features occur at an energy loss of 10.0 and 12.1 eV, respectively, which is considerably above the onset of optical absorption of 5.8 eV. This indicates that excited states with energies below approximately 10.0 eV cannot be reached by the resonant x-ray scattering process at the Ga 1s states. This is due to the dipole-selection rules in this process: As discussed in Chapter 9, the bottom of the conduction band is predominantly formed by Ga and O s states. Therefore, transitions from the Ga 1s to the lowest conduction band are dipole-forbidden, and the onset of the Ga 1s excitations is formed by transitions to conduction bands at considerably higher energies, which exhibit increased Ga p character. Therefore, in the intermediate state of the resonant scattering process with an excitation energy of around 10374 eV, the excited electron is distributed in conduction bands considerably above the CBm. As the low-energy optical excitations originate from transitions from the VBM, predominantly formed by O p states, to the lowest conduction band, formed by Ga and O s states, they can not be reached by the x-ray emission from the intermediate state. Thus, we can deduce from the Ga K edge RIXS that the valence excitations between 5.8 and approximately 12.1 eV are formed by transitions to the conduction bands with predominant Ga s character.

Similarly, the onset of Ga K edge RIXS spectra of β-Ga$_2$O$_3$ in Fig. 13.4 occurs as excitation energies of approximately 10372 eV and an energy loss of more than 9 eV. While this excita-
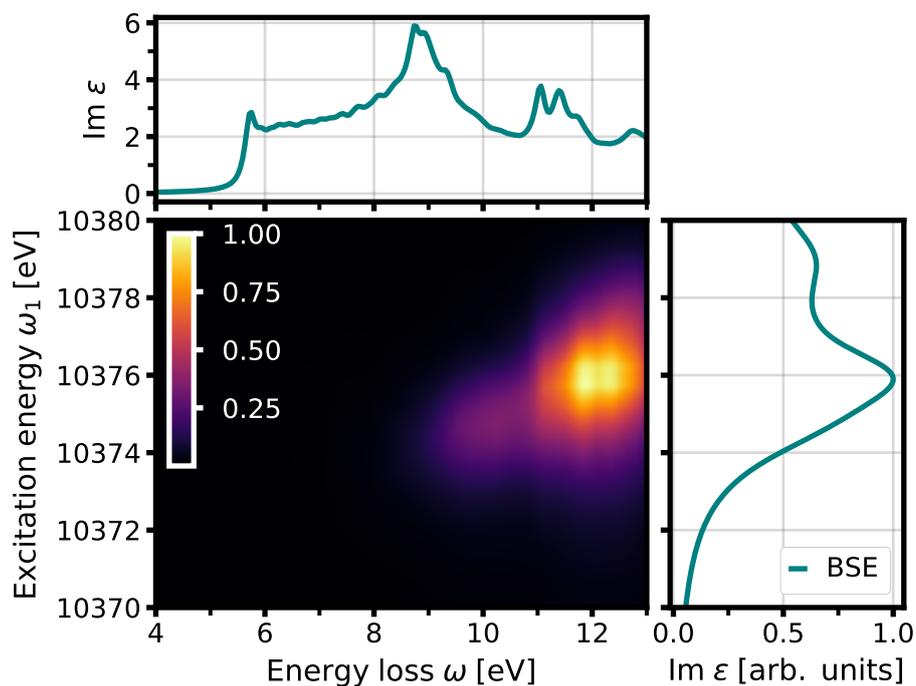
Figure 13.3: Normalized RIXS (center) and XANES (right) at the Ga K edge of α-Ga_2O_3. Top: Optical absorption spectrum. The light is polarized along the x-axis for all spectra.

tion energy corresponds to the Ga K edge absorption onset, the energy loss lies considerably above the optical absorption onset of around 5 eV. For the resonant scattering of the Ga_1 $1s$ states, the onset occurs at even higher the energy loss, as the Ga K edge absorption onset appears at higher excitation energies. The features in the RIXS spectra of both atomic sites are broad, both as a function of the excitation energy and the energy loss, due to the considerable lifetime broadening of the Ga $1s$ core hole of 1 eV. As for the α-polymorph, the Ga K edge RIXS indicates that the optical excitations between 5 and 9 eV are due to transitions to conduction bands with Ga s character. Above 9 eV, the hybridization with Ga p states increases, and excitations in that energy region can be reached by the Ga $1s$ resonant scattering process.
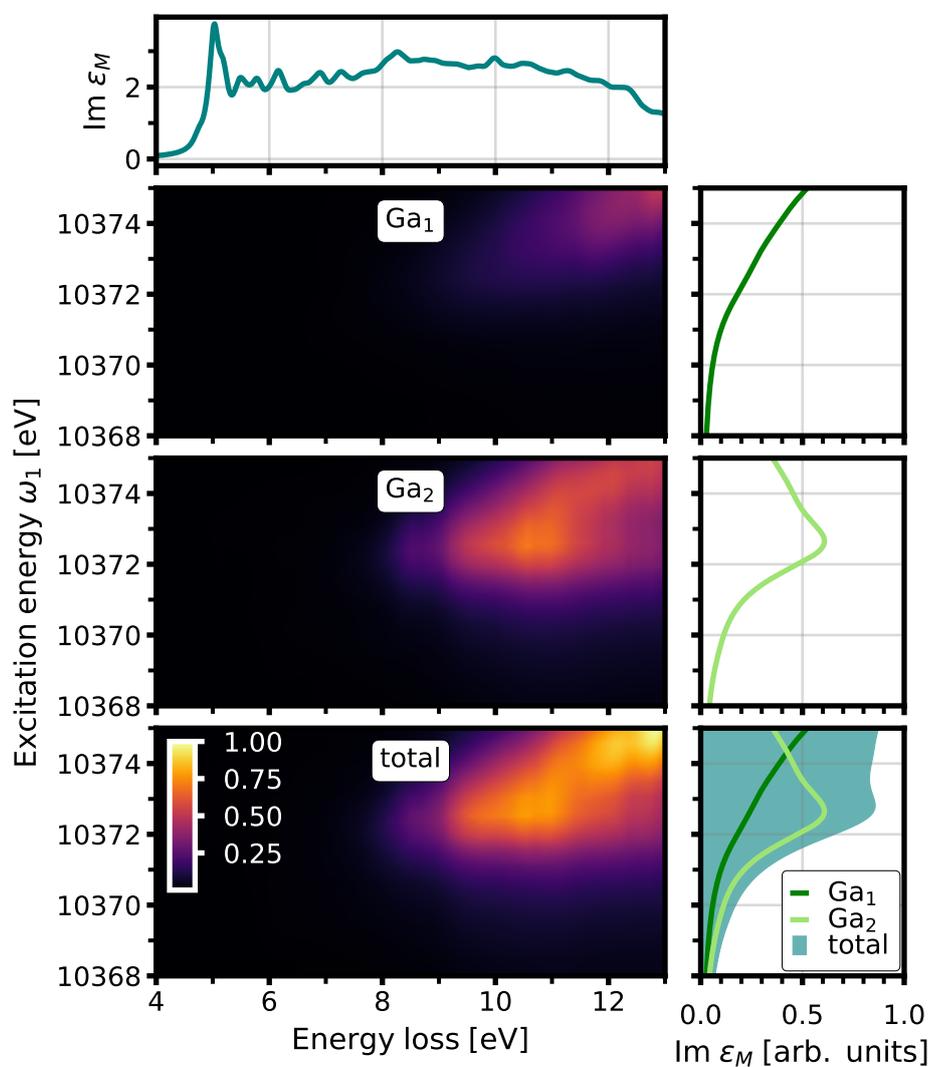
Figure 13.4: Optical absorption spectrum, normalized Ga K edge RIXS spectra of the atoms Ga_1 and Ga_2 and total RIXS spectrum of β-Ga_2O_3 (left column from the top). The Ga K absorption spectra of the corresponding Ga atoms and the total Ga K edge absorption spectrum are shown in the right column.

Part IV

Appendix

APPENDIX A

Fourier Transforms

A.1 Fourier Transform in Time

A function $f(t)$ and its Fourier transform in frequency $f(\omega)$ are connected by

$$f(t) = \frac{1}{2\pi} \int d\omega f(\omega) e^{i\omega t}, \tag{A.1}$$

and, inversely,

$$f(\omega) = \int dt f(t) e^{-i\omega t}. \tag{A.2}$$

A.2 Fourier Transforms in Space

A.2.1 Local and Nonlocal Functions

The Fourier components $f_G(\mathbf{q})$ of a local function $f(\mathbf{r})$ are given by

$$f_G(\mathbf{q}) = \frac{1}{V} \int_V d^3 r f(\mathbf{r}) e^{-i(G+q)\mathbf{r}}. \tag{A.3}$$

The function $f(\mathbf{r})$ can be recovered from the Fourier components as

$$f(\mathbf{r}) = \sum_{q,G} f_G(\mathbf{q}) e^{i(G+q)\mathbf{r}}. \tag{A.4}$$

For a non-local function $f(\mathbf{r}, \mathbf{r}')$, the Fourier components $f_{GG'}(\mathbf{q}, \mathbf{q}')$ are given by

$$f_{GG'}(\mathbf{q}, \mathbf{q}') = \frac{1}{V} \int_V \int_V d^3 r d^3 r' e^{-i(G+q)\mathbf{r}} f(\mathbf{r}, \mathbf{r}') e^{i(G'+q')\mathbf{r}'}, \tag{A.5}$$

and the function can be constructed from the Fourier components as

$$f(\mathbf{r}, \mathbf{r}') = \frac{1}{V} \sum_{\mathbf{q},\mathbf{G}} \sum_{\mathbf{q}',\mathbf{G}'} e^{i(\mathbf{G}+\mathbf{q})\mathbf{r}} f_{\mathbf{G}\mathbf{G}'}(\mathbf{q}, \mathbf{q}') e^{-i(\mathbf{G}'+\mathbf{q}')\mathbf{r}'}. \tag{A.6}$$

A.2.2 Periodic Functions

A local function that is periodic with respect to a lattice vector $\mathbf{R}$, *i.e.* $f(\mathbf{r} + \mathbf{R}) = f(\mathbf{r})$ has only Fourier components with $\mathbf{q} = 0$, and thus Eq. A.4 simplifies to

$$f(\mathbf{r}) = \sum_{\mathbf{G}} f_{\mathbf{G}}(0) e^{i\mathbf{G}\mathbf{r}}. \tag{A.7}$$

Analogously, for a periodic nonlocal function, which obeys $f(\mathbf{r} + \mathbf{R}, \mathbf{r}' + \mathbf{R}) = f(\mathbf{r}, \mathbf{r}')$, only Fourier components with $\mathbf{q} = \mathbf{q}'$ are non-vanishing, and Eq. A.6 reduces to

$$f(\mathbf{r}, \mathbf{r}') = \frac{1}{V} \sum_{\mathbf{q}} \sum_{\mathbf{G},\mathbf{G}'} e^{i(\mathbf{G}+\mathbf{q})\mathbf{r}} f_{\mathbf{G}\mathbf{G}'}(\mathbf{q}) e^{-i(\mathbf{G}'+\mathbf{q})\mathbf{r}'}. \tag{A.8}$$

A.2.3 Useful Properties

In this section, we present some useful properties of the Fourier transforms of periodic functions [280]. The integral of a complex exponential function over the total crystal volume V is given by

$$\int_V d^3r\, e^{i\mathbf{q}\mathbf{r}} = V \delta_{\mathbf{q},0}, \tag{A.9}$$

where $\mathbf{q}$ is a vector from the first Brillouin zone. Analogously, the integral of a complex exponential function over the unit cell volume V_0 is given by

$$\int_{V_0} d^3r\, e^{i\mathbf{G}\mathbf{r}} = V_0 \delta_{\mathbf{G},0}, \tag{A.10}$$

where $\mathbf{G}$ is a reciprocal lattice vector.

A.2.4 General Basis Representation

The representation of local and nonlocal functions in a Fourier transformation is not unique. Generally, local functions can be expanded in any set of complete basis functions $\{\Upsilon^\alpha(\mathbf{r})\}$.

Equivalently to Eqs. A.3 and A.4, the functions are related to their matrix elements f_α as

$$f_\alpha = \int_V d^3 r f(\mathbf{r}) \left[\Upsilon^\alpha(\mathbf{r}) \right]^*$$
$$f(\mathbf{r}) = \sum_\alpha f_\alpha \Upsilon_\alpha(\mathbf{r}). \tag{A.11}$$

The matrix elements are related to the Fourier components $f_G(\mathbf{q})$ as

$$f_G(\mathbf{q}) = \frac{1}{V} \sum_\alpha M_\alpha(\mathbf{G} + \mathbf{q}) f_\alpha, \tag{A.12}$$

where we define the plane-wave matrix elements $M_\alpha(\mathbf{G} + \mathbf{q})$ as

$$M_\alpha(\mathbf{G} + \mathbf{q}) = \int_V d^3 r \Upsilon^\alpha(\mathbf{r}) e^{-i(G+q)\mathbf{r}}. \tag{A.13}$$

Nonlocal functions are expanded in a set of complete nonlocal functions $\Upsilon^\alpha(\mathbf{r}, \mathbf{r}')$ such that

$$f_{\alpha\beta} = \int_V d^3 r \left[\Upsilon^\alpha(\mathbf{r}, \mathbf{r}) \right]^* f(\mathbf{r}, \mathbf{r}') \Upsilon_\beta(\mathbf{r}', \mathbf{r}') \quad f(\mathbf{r}, \mathbf{r}') = \sum_{\alpha\beta} \Upsilon^\alpha(\mathbf{r}, \mathbf{r}) f_{\alpha\beta} \left[\Upsilon^\beta(\mathbf{r}', \mathbf{r}') \right]^*. \tag{A.14}$$

The matrix elements $f_{\alpha\beta}$ are related to the Fourier components $f_{GG'}(\mathbf{q}, \mathbf{q}')$ by

$$f_{GG'}(\mathbf{q}, \mathbf{q}') = \frac{1}{V} \sum_{\alpha\beta} M_\alpha(\mathbf{G} + \mathbf{q}) f_{\alpha\beta} M_\beta^*(\mathbf{G}' + \mathbf{q}'), \tag{A.15}$$

where the plane-wave matrix elements for a non-local basis function are defined as

$$M_\alpha(\mathbf{G} + \mathbf{q}) = \int d^3 r \Upsilon^\alpha(\mathbf{r}, \mathbf{r}) e^{-i(G+q)\mathbf{r}}. \tag{A.16}$$

APPENDIX B

Lehmann Representations

B.1 Lehmann Representation of L^0

The Lehmann representation of the two-particle correlation function $L^0(1, 2; 1^+, 2^+)$ is of special importance in this work. It is employed to motivate the basis representation of the BSE for the polarizability and leads to the Lehmann representation for the polarizability shown below. Starting from the definition of the correlation function in Eq. 1.34, one obtains

$$
\begin{aligned}
L^0(1, 2; 1^+, 2^+) &= G(1, 2^+)G(2, 1^+) \\
&= -\langle 0|\hat{T}[\hat{\psi}(1)\hat{\psi}^\dagger(2)]|0\rangle\langle 0|\hat{T}[\hat{\psi}(2)\hat{\psi}^\dagger(1)]|0\rangle \\
&= \langle 0|e^{iHt_1}\hat{\psi}(\mathbf{r}_1)e^{-iH(t_1-t_2)}\hat{\psi}^\dagger(\mathbf{r}_2)e^{-iHt_2}|0\rangle\times \\
&\quad \times \langle 0|e^{iHt_1}\hat{\psi}^\dagger(\mathbf{r}_1)e^{-iH(t_1-t_2)}\hat{\psi}(\mathbf{r}_2)e^{-iHt_2}|0\rangle\Theta(t_1 - t_2) \\
&\quad + \langle 0|e^{iHt_2}\hat{\psi}^\dagger(\mathbf{r}_2)e^{-iH(t_2-t_1)}\hat{\psi}(\mathbf{r}_1)e^{-iHt_1}|0\rangle\times \\
&\quad \times \langle 0|e^{iHt_2}\hat{\psi}(\mathbf{r}_2)e^{-iH(t_2-t_1)}\hat{\psi}^\dagger(\mathbf{r}_1)e^{-iHt_1}|0\rangle\Theta(t_2 - t_1),
\end{aligned}
\tag{B.1}
$$

where we have evaluated the time-ordering operator explicitly. The Fourier transform following Eq. A.1 along two different time directions, $\tau^{(1)} = t_1 - t_2$ and $\tau^{(2)} = t_2 - t_1$, are possible, which lead to different Lehmann representations. For a Fourier transform along $\tau^{(1)}$ and inserting the unity operator $\mathbb{1} = \sum_N |N\rangle\langle N|$, where the summation includes all excited many-body states $|N\rangle$ with total energy E_N, we obtain [1]

$$
\begin{aligned}
L^0(\mathbf{r}_1, \mathbf{r}_2, \tau^1) &= \sum_{N,N'} \Big[\langle 0|\hat{\psi}(\mathbf{r}_1)|N\rangle\langle N|\hat{\psi}^\dagger(\mathbf{r}_2)|0\rangle\langle 0|\hat{\psi}^\dagger(\mathbf{r}_1)|N'\rangle\langle N'|\hat{\psi}(\mathbf{r}_2)|0\rangle\times \\
&\quad \times e^{-i(E_N+E_{N'})\tau^{(1)}}\Theta(\tau^{(1)}) \\
&\quad + \langle 0|\hat{\psi}^\dagger(\mathbf{r}_2)|N\rangle\langle N|\hat{\psi}(\mathbf{r}_1)|0\rangle\langle 0|\hat{\psi}(\mathbf{r}_2)|N'\rangle\langle N'|\hat{\psi}^\dagger(\mathbf{r}_1)|0\rangle\times \\
&\quad \times e^{i(E_N+E_{N'})\tau^{(1)}}\Theta(-\tau^{(1)}) \Big]
\end{aligned}
\tag{B.2}
$$

---

[1] In the following, we will set $E_0 = 0$ without loss of generality.

The equation above holds for any time-independent Hamiltonian $\hat{H}$, such as the Hamiltonian of a system of electrons in an external potential, shown in Eq. 1.2. The Fourier transform $L(\mathbf{r}_1, \mathbf{r}_2, \omega)$ is obtained as

$$L_{\tau^1}^0(\mathbf{r}_1, \mathbf{r}_2, \omega) = i \sum_{N,N'} \left[\frac{\langle 0|\hat{\psi}(\mathbf{r}_1)|N\rangle\langle N|\hat{\psi}^\dagger(\mathbf{r}_2)|0\rangle\langle 0|\hat{\psi}^\dagger(\mathbf{r}_1)|N'\rangle\langle N'|\hat{\psi}(\mathbf{r}_2)|0\rangle}{\omega - (E_N + E_{N'}) + i\eta} \right.$$
$$\left. - \frac{\langle 0|\hat{\psi}^\dagger(\mathbf{r}_2)|N\rangle\langle N|\hat{\psi}(\mathbf{r}_1)|0\rangle\langle 0|\hat{\psi}(\mathbf{r}_2)|N'\rangle\langle N'|\hat{\psi}^\dagger(\mathbf{r}_1)|0\rangle}{\omega + (E_N + E_{N'}) - i\eta} \right] . \tag{B.3}$$

Within the quasiparticle approximation, the expectation values $\langle n|\psi(\mathbf{r})|0\rangle$ and $\langle n|\psi^\dagger(\mathbf{r})|0\rangle$ can be evaluated explicitly as

$$\langle N|\psi(\mathbf{r})|0\rangle = \sum_{v\mathbf{k}} \psi_{v\mathbf{k}}(\mathbf{r}) \quad \langle N|\psi^\dagger(\mathbf{r})|0\rangle = \sum_{c\mathbf{k}} \psi_{c\mathbf{k}}^*(\mathbf{r}) \tag{B.4}$$

with corresponding total energies

$$E_N = -\epsilon_{v\mathbf{k}} \quad E_N = \epsilon_{c\mathbf{k}} . \tag{B.5}$$

This yields the Lehmann representation of L^0 as

$$L_{\tau^{(1)}}^0(\mathbf{r}_1, \mathbf{r}_2, \omega) = i \sum_{\mathbf{q}} \sum_{cv} \sum_{\mathbf{k}} \left[\frac{\phi_{c(\mathbf{k}+\mathbf{q})}(\mathbf{r}_1)\phi_{v\mathbf{k}}^*(\mathbf{r}_1)\phi_{c(\mathbf{k}+\mathbf{q})}^*(\mathbf{r}_2)\phi_{v\mathbf{k}}(\mathbf{r}_2)}{\omega - (\epsilon_{c(\mathbf{k}+\mathbf{q})} - \epsilon_{v\mathbf{k}}) + i\eta} \right.$$
$$\left. - \frac{\phi_{c\mathbf{k}}^*(\mathbf{r}_1)\phi_{v(\mathbf{k}+\mathbf{q})}(\mathbf{r}_1)\phi_{c\mathbf{k}}(\mathbf{r}_2)\phi_{v(\mathbf{k}+\mathbf{q})}^*(\mathbf{r}_2)}{\omega + (\epsilon_{c\mathbf{k}} - \epsilon_{v(\mathbf{k}+\mathbf{q})}) - i\eta} \right], \tag{B.6}$$

where we have employed the translational symmetry $L^0(\mathbf{r}_1 + \mathbf{R}, \mathbf{r}_2 + \mathbf{R}) = L^0(\mathbf{r}_1, \mathbf{r}_2)$ for each lattice vector $\mathbf{R}$. Equation B.6 implies that $L_{\tau^1}^0$ can be expanded in a basis $\Upsilon_\alpha(\mathbf{r}, \mathbf{r})$ following Eqs. 6.19 and 6.20. The shape of $L_{\tau^{(1)}}^0(\omega)$ infers that distinct basis functions should be employed for the first (resonant) and second (antiresonant) term. For a given $\mathbf{q}$, the resonant basis functions $\Upsilon_{\alpha,\mathbf{q}}^{r,1}(\mathbf{r}, \mathbf{r}; \mathbf{q})$ and antiresonant ones $\Upsilon_{\alpha,\mathbf{q}}^{a,1}(\mathbf{r}, \mathbf{r}; \mathbf{q})$ are then defined as

$$\Upsilon_{\alpha,\mathbf{q}}^{r,1}(\mathbf{r}_1, \mathbf{r}_2) = \phi_{v\mathbf{k}}^*(\mathbf{r}_1)\phi_{c(\mathbf{k}+\mathbf{q})}(\mathbf{r}_2) \quad \Upsilon_{\alpha,\mathbf{q}}^{a,1}(\mathbf{r}_1, \mathbf{r}_2) = \phi_{v\mathbf{k}}(\mathbf{r}_1)\phi_{c(\mathbf{k}+\mathbf{q})}^*(\mathbf{r}_2) \tag{B.7}$$

The transition space index $\alpha = (c, v\mathbf{k})$ combines the quasiparticle indices. The resonant matrix elements $L_{\alpha\beta}^{0,R1}$ of the correlation function are then given as

$$L_{\alpha,\alpha'}^{0,R1}(\mathbf{q}, \omega) = \frac{\delta_{cc'}\delta_{vv'}\delta_{\mathbf{k}\mathbf{k}'}}{\omega - \left(\epsilon_{c(\mathbf{k}+\mathbf{q})} - \epsilon_{v\mathbf{k}}\right) + i\eta}, \tag{B.8}$$

and the anti-resonant matrix elements $L^{0,A1}_{\alpha\beta}$ as

$$L^{0,A1}_{\alpha,\alpha'}(\mathbf{q}, \omega) = \frac{\delta_{cc'}\delta_{vv'}\delta_{\mathbf{kk'}}}{\omega + \left(\epsilon_{c\mathbf{k}} - \epsilon_{v(\mathbf{k+q})}\right) - \mathrm{i}\eta}, \tag{B.9}$$

respectively.

We now consider the Lehmann representation with respect to $\tau^{(2)}$. We obtain an equation similar to Eq. B.2 as

$$
\begin{aligned}
L^0(\mathbf{r}_1, \mathbf{r}_1, \tau^{(2)}) = \sum_{N,N'} \Big[& \langle 0|\hat{\psi}^\dagger(\mathbf{r}_2)|N\rangle\langle N|\hat{\psi}(\mathbf{r}_1)|0\rangle\langle 0|\hat{\psi}(\mathbf{r}_2)|N'\rangle\langle N'|\hat{\psi}^\dagger(\mathbf{r}_1)|0\rangle\times \\
& \times \mathrm{e}^{-\mathrm{i}(E_N + E_{N'})\tau^{(2)}}\Theta(\tau^{(2)}) \\
& + \langle 0|\hat{\psi}(\mathbf{r}_1)|N\rangle\langle N|\hat{\psi}^\dagger(\mathbf{r}_2)|0\rangle\langle 0|\hat{\psi}^\dagger(\mathbf{r}_1)|N'\rangle\langle N'|\hat{\psi}(\mathbf{r}_2)|0\rangle\times \\
& \times \mathrm{e}^{\mathrm{i}(E_N + E_{N'})\tau^{(2)}}\Theta(-\tau^{(2)}) \Big].
\end{aligned}
\tag{B.10}
$$

Note that while the complex exponentials in Eq. B.10 are identical to the ones in Eq. B.2, the order of the field operators is reversed due to the reversal in time-direction. We obtain a second Lehmann representation $L^0_{\tau^2}$ as

$$
L^0_{\tau^{(2)}}(\mathbf{r}_1, \mathbf{r}_2, \omega) = \mathrm{i}\sum_{N,N'} \left[\frac{\langle 0|\hat{\psi}^\dagger(\mathbf{r}_2)|N\rangle\langle N|\hat{\psi}(\mathbf{r}_1)|0\rangle\langle 0|\hat{\psi}(\mathbf{r}_2)|N'\rangle\langle N'|\hat{\psi}^\dagger(\mathbf{r}_1)|0\rangle}{\omega - (E_N + E_{N'}) + \mathrm{i}\eta} \right.
$$
$$
\left. + \frac{\langle 0|\hat{\psi}(\mathbf{r}_1)|N\rangle\langle N|\hat{\psi}^\dagger(\mathbf{r}_2)|0\rangle\langle 0|\hat{\psi}^\dagger(\mathbf{r}_1)|N'\rangle\langle N'|\hat{\psi}(\mathbf{r}_2)|0\rangle}{\omega + (E_N + E_{N'}) - \mathrm{i}\eta} \right].
\tag{B.11}
$$

Combining quasiparticle approximation in Eq. 1.58 and Tamm-Dancoff approximation in Eq. 1.60, the correlation function $L^0_{\tau^{(2)}}$ becomes

$$
L^0_{\tau^{(2)}}(\mathbf{r}_1, \mathbf{r}_2, \omega) = \mathrm{i}\sum_{\mathbf{q}}\sum_{cv}\sum_{\mathbf{k}} \left[\frac{\phi^*_{c\mathbf{k}}(\mathbf{r}_1)\phi_{v(\mathbf{k+q})}(\mathbf{r}_1)\phi_{c\mathbf{k}}(\mathbf{r}_2)\phi^*_{v(\mathbf{k+q})}(\mathbf{r}_2)}{\omega - (\epsilon_{c\mathbf{k}} - \epsilon_{v(\mathbf{k+q})}) + \mathrm{i}\eta} \right.
$$
$$
\left. - \frac{\phi_{c(\mathbf{k+q})}(\mathbf{r}_1)\phi^*_{v\mathbf{k}}(\mathbf{r}_1)\phi^*_{c(\mathbf{k+q})}(\mathbf{r}_2)\phi_{v\mathbf{k}}(\mathbf{r}_2)}{\omega + (\epsilon_{c(\mathbf{k+q})} - \epsilon_{v\mathbf{k}}) - \mathrm{i}\eta} \right].
\tag{B.12}
$$

This implies a different set of basis functions $\Upsilon^{r,2}_\alpha(\mathbf{r}_1, \mathbf{r}_2; \mathbf{q})$ and $\Upsilon^{a,2}_\alpha(\mathbf{r}_1, \mathbf{r}_2)$ defined as

$$\Upsilon^{r,2}_{\alpha,\mathbf{q}}(\mathbf{r}_1, \mathbf{r}_2) = \phi_{v(\mathbf{k+q})}(\mathbf{r}_1)\phi^*_{c\mathbf{k}}(\mathbf{r}_2) \quad \Upsilon^{a,2}_{\alpha,\mathbf{q}}(\mathbf{r}_1, \mathbf{r}_2) = \phi^*_{v\mathbf{k}}(\mathbf{r}_1)\phi_{c(\mathbf{k+q})}(\mathbf{r}_2). \tag{B.13}$$

It is now obvious that the two different Fourier transforms yield to two different Lehmann

representations in Eqs. B.3 and B.11, which in turn yield two different expressions for the basis in transition space shown in Eqs. B.7 and B.13, respectively. Note that the correlation function L^0 is diagonal both in the basis in Eq. B.7 and in the basis in Eq. B.13, but the matrix elements of the BSE that are derived from the Lehmann representation of L^0 are not identical. The ambiguity of the Lehmann representation and the resulting ambiguity of the basis representation is not a unique property of L^0, since it originates generally from expectation values of the form $\langle 0|\hat{T}[\hat{\psi}^\dagger(1)\hat{\psi}(2)]|0\rangle$, which occur in many observables in spectroscopy.

B.2 Lehmann Representation of χ

The Lehmann representation of the time-ordered polarizability χ is of central importance in this thesis, as it is employed to construct the macroscopic dielectric function, which in turn yields the x-ray and optical absorption spectra as well as the inelastic x-ray scattering spectra and electron energy loss spectra. We furthermore show that the resonant inelastic x-ray spectra can be expressed in terms of the polarizability as well. As discussed in the previous section for the correlation function L^0, we will show that two different Lehmann representations for χ can be obtained, and we will discuss how these Lehmann representations are related to the Lehmann representation of the retarded polarizability. The time-ordered polarizability is defined as

$$\chi(1,2) = iG_2(1,2;1^+,2^+) - iG(1,1^+)G(2,2^+). \tag{B.14}$$

For now, let us rewrite only the first term in Eq. B.14 as

$$
\begin{aligned}
iG_2(1,2;1^+,2^+) &= -i\langle 0|\hat{\psi}(1)\hat{\psi}(2)\hat{\psi}^\dagger(2)\hat{\psi}^\dagger(1)|0\rangle \\
&= -i\sum_n \Big[\langle 0|\hat{\psi}^\dagger(\mathbf{r}_1)\hat{\psi}(\mathbf{r}_1)|n\rangle\langle n|\hat{\psi}^\dagger(\mathbf{r}_2)\hat{\psi}(\mathbf{r}_2)|0\rangle e^{-iE_n(t_1-t_2)}\Theta(t_1-t_2) \\
&\quad + \langle 0|\hat{\psi}^\dagger(\mathbf{r}_2)\hat{\psi}(\mathbf{r}_2)|n\rangle\langle n|\hat{\psi}^\dagger(\mathbf{r}_1)\hat{\psi}(\mathbf{r}_1)|0\rangle e^{iE_n(t_1-t_2)}\Theta(-(t_1-t_2)) \Big].
\end{aligned}
\tag{B.15}
$$

Recall that we set $E_0 = 0$ without loss of generality. The term $n = 0$ in the summation in Eq. B.15 cancels exactly with the term $G(1,1^+)G(2,2^+)$ in Eq. B.14, such that we obtain

$$
\begin{aligned}
\chi(1,2) = -i\sum_{n\neq 0} \Big[&\langle 0|\hat{\psi}^\dagger(\mathbf{r}_1)\hat{\psi}(\mathbf{r}_1)|n\rangle\langle n|\hat{\psi}^\dagger(\mathbf{r}_2)\hat{\psi}(\mathbf{r}_2)|0\rangle e^{-iE_n(t_1-t_2)}\Theta(t_1-t_2) \\
+ &\langle 0|\hat{\psi}^\dagger(\mathbf{r}_2)\hat{\psi}(\mathbf{r}_2)|n\rangle\langle n|\hat{\psi}^\dagger(\mathbf{r}_1)\hat{\psi}(\mathbf{r}_1)|0\rangle e^{iE_n(t_1-t_2)}\Theta(-(t_1-t_2)) \Big].
\end{aligned}
\tag{B.16}
$$

The Fourier transform in $\tau^{(1)} = t_1 - t_2$ following Eqs. A.1 yields

$$\chi_{\tau^{(1)}}(\mathbf{r}_1, \mathbf{r}_2, \omega) = \sum_{N \neq 0} \left[\frac{\langle 0|\hat{\psi}^\dagger(\mathbf{r}_1)\hat{\psi}(\mathbf{r}_1)|N\rangle\langle N|\hat{\psi}^\dagger(\mathbf{r}_2)\hat{\psi}(\mathbf{r}_2)|0\rangle}{\omega - E_N + i\eta} \right.$$
$$\left. - \frac{\langle 0|\hat{\psi}^\dagger(\mathbf{r}_2)\hat{\psi}(\mathbf{r}_2)|N\rangle\langle N|\hat{\psi}^\dagger(\mathbf{r}_1)\hat{\psi}(\mathbf{r}_1)|0\rangle}{\omega + E_N - i\eta} \right]. \tag{B.17}$$

Combining the quasiparticle approximation in Eq. 1.58 and the Tamm-Dancoff approximation in Eq. 1.60, the Lehmann representation of the polarizability is obtained as

$$\chi_{\tau^{(1)}}(\mathbf{r}_1, \mathbf{r}_2, \omega) = \sum_{N \neq 0} \sum_{\mathbf{q}} \sum_{cv\mathbf{k}} \sum_{c'v'\mathbf{k}'}$$
$$\left[\phi^*_{v\mathbf{k}}(\mathbf{r}_1)\phi_{c(\mathbf{k}+\mathbf{q})}(\mathbf{r}_1)\phi^*_{c'(\mathbf{k}'+\mathbf{q})}(\mathbf{r}_2)\phi_{v\mathbf{k}'}(\mathbf{r}_2) \frac{\langle 0|\hat{c}^\dagger_{v\mathbf{k}}\hat{c}_{c(\mathbf{k}+\mathbf{q})}|N\rangle\langle N|\hat{c}^\dagger_{c'(\mathbf{k}'+\mathbf{q})}\hat{c}_{v'\mathbf{k}'}|0\rangle}{\omega - E_N + i\eta} \right.$$
$$\left. + \phi_{v(\mathbf{k}+\mathbf{q})}(\mathbf{r}_1)\phi^*_{c\mathbf{k}}(\mathbf{r}_1)\phi_{c'\mathbf{k}'}(\mathbf{r}_2)\phi^*_{v'(\mathbf{k}'+\mathbf{q})}(\mathbf{r}_2) \frac{\langle 0|\hat{c}^\dagger_{v'(\mathbf{k}'+\mathbf{q})}\hat{c}_{c'\mathbf{k}'}|N\rangle\langle N|\hat{c}^\dagger_{c\mathbf{k}}\hat{c}_{v(\mathbf{k}+\mathbf{q})}|0\rangle}{\omega + E_N - i\eta} \right]. \tag{B.18}$$

As for the correlation function L^0 in the previous section, the polarizability can be expressed in the transition space of Eq. B.7 and the resulting matrix elements $\chi^{R1}_{\alpha\beta}$ and $\chi^{A1}_{\alpha\beta}$ are shown in Eqs. 2.28 and 2.29, respectively. For clarity, let us recall the matrix elements here:

$$\chi^{R1}_{cv\mathbf{k},c'v'\mathbf{k}'}(\mathbf{q}, \omega) = \sum_{N \neq 0} \frac{\langle 0|\hat{c}^\dagger_{v\mathbf{k}}\hat{c}_{c(\mathbf{k}+\mathbf{q})}|N\rangle\langle N|\hat{c}^\dagger_{c'(\mathbf{k}'+\mathbf{q})}\hat{c}_{v'\mathbf{k}'}|0\rangle}{\omega - E_N + i\eta}, \tag{B.19}$$

and

$$\chi^{A1}_{vc\mathbf{k},v'c'\mathbf{k}'}(\mathbf{q}, \omega) = \sum_{N \neq 0} \frac{\langle 0|\hat{c}^\dagger_{v'(\mathbf{k}'+\mathbf{q})}\hat{c}_{c'\mathbf{k}'}|N\rangle\langle N|\hat{c}^\dagger_{c\mathbf{k}}\hat{c}_{v(\mathbf{k}+\mathbf{q})})|0\rangle}{\omega + E_N - i\eta}. \tag{B.20}$$

As for the correlation function L^0, the Lehmann representation is not unique, and the Fourier transform in $\tau^{(2)} = t_2 - t_1$ in quasiparticle approximation and Tamm-Dancoff ap-

proximation is

$$\chi_{\tau^{(2)}}(\mathbf{r}_1, \mathbf{r}_2, \omega) = \sum_{N \neq 0} \sum_{\mathbf{q}} \sum_{cv\mathbf{k}} \sum_{c'v'\mathbf{k}'}$$

$$\Bigg[\phi_{v(\mathbf{k}+\mathbf{q})}^*(\mathbf{r}_1) \phi_{c\mathbf{k}}^*(\mathbf{r}_1) \phi_{c'\mathbf{k}'}(\mathbf{r}_2) \phi_{v(\mathbf{k}'+\mathbf{q})}(\mathbf{r}_2) \frac{\langle 0|\hat{c}_{v'(\mathbf{k}'+\mathbf{q})}^\dagger \hat{c}_{c'\mathbf{k}'}|N\rangle \langle N|\hat{c}_{c\mathbf{k}}^\dagger \hat{c}_{v(\mathbf{k}+\mathbf{q})}|0\rangle}{\omega - E_N + i\eta} \tag{B.21}$$

$$+ \phi_{v\mathbf{k}}(\mathbf{r}_1) \phi_{c(\mathbf{k}+\mathbf{q})}(\mathbf{r}_1) \phi_{c'(\mathbf{k}'+\mathbf{q})}(\mathbf{r}_2) \phi_{v'\mathbf{k}'}^*(\mathbf{r}_2) \frac{\langle 0|\hat{c}_{c(\mathbf{k}+\mathbf{q})}^\dagger \hat{c}_{v\mathbf{k}}|N\rangle \langle N|\hat{c}_{v'\mathbf{k}'}^\dagger \hat{c}_{c'(\mathbf{k}'+\mathbf{q})}|0\rangle}{\omega + E_N - i\eta} \Bigg].$$

The matrix elements $\chi_{cv\mathbf{k},c'v'\mathbf{k}'}^{R2}$ and $\chi_{cv\mathbf{k},c'v'\mathbf{k}'}^{A2}$ in the basis of Eq. B.13 are now distinct from those in Eqs. B.19 and B.20, as they are given by

$$\chi_{\alpha,\alpha'}^{R2}(\mathbf{q}, \omega) = \sum_{N \neq 0} \frac{\langle 0|\hat{c}_{v'(\mathbf{k}'+\mathbf{q})}^\dagger \hat{c}_{c'\mathbf{k}'}|N\rangle \langle N|\hat{c}_{c\mathbf{k}}^\dagger \hat{c}_{v(\mathbf{k}+\mathbf{q})}|0\rangle}{\omega - E_N + i\eta}, \tag{B.22}$$

and

$$\chi_{\alpha,\alpha'}^{A2}(\mathbf{q}, \omega) = \sum_{N \neq 0} \frac{\langle 0|\hat{c}_{c(\mathbf{k}+\mathbf{q})}^\dagger \hat{c}_{v\mathbf{k}}|N\rangle \langle N|\hat{c}_{v'\mathbf{k}'}^\dagger \hat{c}_{c'(\mathbf{k}'+\mathbf{q})}|0\rangle}{\omega + E_N - i\eta}. \tag{B.23}$$

Comparing the matrix elements in Eqs. B.19 and B.20 with those in Eqs. B.22 and B.23, we note a common structure. The analytical dependence on the frequency ω can be used to write the matrix elements $\chi_{\alpha,\alpha'}^{Ri}(\mathbf{q}, \omega)$, where $i = 1, 2$ as

$$\chi_{\alpha,\alpha'}^{Ri}(\mathbf{q}, \omega) = \sum_{N \neq 0} \frac{\chi_{\alpha\alpha'}^{Ri}(\mathbf{q}; N)}{\omega - E_N + i\eta}. \tag{B.24}$$

The corresponding structure of the antiresonant matrix elements can be expressed as

$$\chi_{\alpha,\alpha'}^{Ai}(\mathbf{q}, \omega) = \sum_{N \neq 0} \frac{\chi_{\alpha\alpha'}^{Ai}(\mathbf{q}; N)}{\omega + E_N - i\eta}. \tag{B.25}$$

B.3 Lehmann Representation of χ^R

We have seen in the previous sections that the time-ordered quantities L^0 and χ can be expressed in two distinct Lehmann representations. These yield two distinct sets of basis functions for the transition space. Both representations are correct, and we will show that observables are unaffected by the choice of the basis representation (in systems with time-

reversal symmetry). Nevertheless, for many time-ordered quantities, specifically those that are correlation functions, a corresponding retarded quantity exists, which relates directly to experimentally measured observables [57, 63]. In the following, I will specifically focus on the retarded polarizability. The definition for the time-ordered polarizability in Eq. B.14 can be rewritten as

$$\chi(1, 2) = -i\langle 0 \left| \hat{T} \left[\Delta \left[\hat{\psi}^\dagger(1)\hat{\psi}(1) \right] \Delta \left[\hat{\psi}^\dagger(2)\hat{\psi}(2) \right] \right] \right| 0 \rangle, \tag{B.26}$$

where deviation operators $\Delta\hat{A}(1) = \hat{A}(1) - \langle 0|\hat{A}(1)|0\rangle$ are introduced. The corresponding retarded polarizability χ^R is defined by replacing the time-ordering operator $\hat{T}[\ldots]$ with the commutator $[.., ..]$ and we obtain

$$\chi^R(1, 2) = -i\langle 0 \left| \left[\Delta \left[\hat{\psi}^\dagger(1)\hat{\psi}(1) \right], \Delta \left[\hat{\psi}^\dagger(2)\hat{\psi}(2) \right] \right] \right| 0 \rangle \Theta(t_1 - t_2). \tag{B.27}$$

The Lehmann representation of χ^R is then given by

$$\chi^R(\mathbf{r}_1, \mathbf{r}_2; \omega) = \sum_{N \neq 0} \left[\frac{\langle 0|\hat{\psi}^\dagger(\mathbf{r}_1)\hat{\psi}(\mathbf{r}_1)|N\rangle\langle N|\hat{\psi}^\dagger(\mathbf{r}_2)\hat{\psi}(\mathbf{r}_2)}{\omega - E_N + i\eta} \right. $$
$$\left. - \frac{\langle 0|\hat{\psi}^\dagger(\mathbf{r}_2)\hat{\psi}(\mathbf{r}_2)|N\rangle\langle N|\hat{\psi}^\dagger(\mathbf{r}_1)\hat{\psi}(\mathbf{r}_1)}{\omega + E_N + i\eta} \right]. \tag{B.28}$$

For a more detailed analysis, let us consider the retarded polarizability in the quasiparticle approximation, which takes the form

$$\chi_R(\mathbf{r}_1, \mathbf{r}_2, \omega) = \sum_{\mathbf{q}} \sum_{cv\mathbf{k}} \sum_{c'v'\mathbf{k}'} \left[\phi^*_{v\mathbf{k}}(\mathbf{r}_1)\phi_{c(\mathbf{k}+\mathbf{q})}(\mathbf{r}_1)\chi^{R,R}_{cv\mathbf{k},c'v'\mathbf{k}'}(\mathbf{q}, \omega)\phi^*_{c'(\mathbf{k}'+\mathbf{q})}(\mathbf{r}_2)\phi_{v\mathbf{k}'}(\mathbf{r}_2) \right.$$
$$\left. + \phi_{v(\mathbf{k}+\mathbf{q})}(\mathbf{r}_1)\phi^*_{c\mathbf{k}}(\mathbf{r}_1)\chi^{R,A}_{cv\mathbf{k},c'v'\mathbf{k}'}(\mathbf{q}, \omega)\phi_{c'\mathbf{k}'}(\mathbf{r}_2)\phi^*_{v'(\mathbf{k}'+\mathbf{q})}(\mathbf{r}_2) \right], \tag{B.29}$$

where the resonant and anti-resonant matrix elements, $\chi^{R,R}(\mathbf{q}, \omega)$ and $\chi^{R,A}(\mathbf{q}, \omega)$ are given as

$$\chi^{R,R}_{cv\mathbf{k},c'v'\mathbf{k}'}(\mathbf{q}, \omega) = \sum_{n \neq 0} \frac{\langle 0|\hat{c}^\dagger_{v\mathbf{k}}\hat{c}_{c(\mathbf{k}+\mathbf{q})}|n\rangle\langle n|\hat{c}^\dagger_{c'(\mathbf{k}'+\mathbf{q})}\hat{c}_{v'\mathbf{k}'}|0\rangle}{\omega - E_n + i\eta}(\mathbf{q}, \omega) \tag{B.30}$$

and

$$\chi^{R,A}_{cv\mathbf{k},c'v'\mathbf{q}} = -\sum_{n \neq 0} \frac{\langle 0|\hat{c}^\dagger_{c'\mathbf{k}'}\hat{c}_{v'(\mathbf{k}'+\mathbf{q})}|n\rangle\langle n|\hat{c}^\dagger_{v(\mathbf{k}+\mathbf{q})}\hat{c}_{c\mathbf{k}}|0\rangle}{\omega + E_n + i\eta}. \tag{B.31}$$

B.4 Time-reversal Optimized Basis Functions

In the previous sections, we derived two sets of basis functions to represent the correlation function L_0 and the polarizability χ, shown in Eqs. B.7 and B.13. We repeat them here for clarity. The functions are given as

$$
\begin{aligned}
\Upsilon_{\alpha,\mathbf{q}}^{r,1}(\mathbf{r}_1,\mathbf{r}_2) &= \phi_{v\mathbf{k}}^*(\mathbf{r}_1)\phi_{c(\mathbf{k+q})}(\mathbf{r}_2) & \Upsilon_{\alpha,\mathbf{q}}^{a,1}(\mathbf{r}_1,\mathbf{r}_2) &= \phi_{v(\mathbf{k+q})}(\mathbf{r}_1)\phi_{c\mathbf{k}}^*(\mathbf{r}_2) \\
\Upsilon_{\alpha,\mathbf{q}}^{r,2}(\mathbf{r}_1,\mathbf{r}_2) &= \phi_{v(\mathbf{k+q})}(\mathbf{r}_1)\phi_{c\mathbf{k}}^*(\mathbf{r}_2) & \Upsilon_{\alpha,\mathbf{q}}^{a,2}(\mathbf{r}_1,\mathbf{r}_2) &= \phi_{v\mathbf{k}}^*(\mathbf{r}_1)\phi_{c(\mathbf{k+q})}(\mathbf{r}_1 2.
\end{aligned}
\tag{B.32}
$$

Employing the symmetry of Bloch functions under time reversal, allows us to define basis sets that simplify the BSE problem significantly. The time-reversal symmetry implies that for any given Bloch function $\phi_{i\mathbf{k}}$:

$$
\phi_{i(-\mathbf{k})}(\mathbf{r}) = \phi_{i\mathbf{k}}^*(\mathbf{r}) \quad \epsilon_{i(-\mathbf{k})} = -\epsilon_{i\mathbf{k}}
\tag{B.33}
$$

To utilize these symmetries, we define *time-reversal optimized basis functions* $\bar{\Upsilon}^{1,2}$ [140, 359, 261] as

$$
\begin{aligned}
\bar{\Upsilon}_{\alpha,\mathbf{q}}^{r,1}(\mathbf{r}_1,\mathbf{r}_2) &= \phi_{v(\mathbf{k}-\frac{\mathbf{q}}{2})}^*(\mathbf{r}_1)\phi_{c(\mathbf{k}+\frac{\mathbf{q}}{2})}(\mathbf{r}_2) & \bar{\Upsilon}_{\alpha,\mathbf{q}}^{a,1}(\mathbf{r}_1,\mathbf{r}_2) &= \phi_{v-(\mathbf{k}+\frac{\mathbf{q}}{2})}(\mathbf{r}_1)\phi_{c-(\mathbf{k}-\frac{\mathbf{q}}{2})}^*(\mathbf{r}_2) \\
\bar{\Upsilon}_{\alpha,\mathbf{q}}^{r,2}(\mathbf{r}_1,\mathbf{r}_2) &= \phi_{v(\mathbf{k}+\frac{\mathbf{q}}{2})}(\mathbf{r}_1)\phi_{c(\mathbf{k}-\frac{\mathbf{q}}{2})}^*(\mathbf{r}_2) & \bar{\Upsilon}_{\alpha,\mathbf{q}}^{a,2}(\mathbf{r}_1,\mathbf{r}_2) &= \phi_{v-(\mathbf{k}-\frac{\mathbf{q}}{2})}^*(\mathbf{r}_1)\phi_{c-(\mathbf{k}+\frac{\mathbf{q}}{2})}(\mathbf{r}_2).
\end{aligned}
\tag{B.34}
$$

Equation B.33 implies the following properties of the optimized basis functions:

$$
\bar{\Upsilon}_{\alpha,\mathbf{q}}^{a,(1,2)}(\mathbf{r}_1,\mathbf{r}_2) = \bar{\Upsilon}_{\alpha,\mathbf{q}}^{r,(1,2)}(\mathbf{r}_1,\mathbf{r}_2).
\tag{B.35}
$$

In this optimized basis representation, the BSE Hamiltonian becomes hermitian [140, 359, 261], and only the matrix elements V^{rr}, W^{rr}, and W^{ra} need to be computed. Another important symmetry follows from Eq. B.35: The resonant and antiresonant plane-wave matrix elements defined in Eq. A.16 are given by

$$
M_\alpha^{r,(1,2)}(\mathbf{G},\mathbf{q}) \int d^3r\, \bar{\Upsilon}_{\alpha,\mathbf{q}}^{r,(1,2)}(\mathbf{r},\mathbf{r})e^{-i(\mathbf{G}+\mathbf{q})\mathbf{r}} = \int d^3r\, \bar{\Upsilon} g_{\alpha,\mathbf{q}}^{a,(1,2)}(\mathbf{r},\mathbf{r})e^{-i(\mathbf{G}+\mathbf{q})\mathbf{r}} = M^{a,(1,2)}(\mathbf{G},\mathbf{q}).
\tag{B.36}
$$

Due to Eq. B.34, the resonant basis functions are related by

$$
\bar{\Upsilon}_{\alpha,\mathbf{q}}^{r2}(\mathbf{r}_1,\mathbf{r}_2) = \left[\phi_{v(\mathbf{k}+\frac{\mathbf{q}}{2})}^*(\mathbf{r}_1)\phi_{c(\mathbf{k}-\frac{\mathbf{q}}{2})}(\mathbf{r}_2)\right]^* = \left[\bar{\Upsilon}_{\alpha,-\mathbf{q}}^{r1}(\mathbf{r}_1,\mathbf{r}_2)\right]^*.
\tag{B.37}
$$

Equivalently, for the antiresonant basis functions, we obtain

$$
\bar{\Upsilon}_{\alpha,\mathbf{q}}^{a2}(\mathbf{r}_1,\mathbf{r}_2) = \left[\bar{\Upsilon}_{\alpha,-\mathbf{q}}^{a1}(\mathbf{r}_1,\mathbf{r}_2)\right]^*.
\tag{B.38}
$$

In the following, we will always employ the time-reversal optimized basis functions. To simplify the notation, we write $\Upsilon \equiv \bar{\Upsilon}$

B.5 Connection between Response Functions

The Lehmann representation of the retarded polarizability in Eq. B.29 closely resembles those of the time-ordered polarizabilities in Eqs. B.18 and B.21. Following Eqs. B.24 and B.25, we write the matrix elements of the retarded polarizability as

$$\chi_{\alpha\alpha'}^{R,R} = \sum_{N \neq 0} \frac{\chi_{\alpha\alpha}^{R,R}(\mathbf{q}; N)}{\omega - E_N + i\eta} \tag{B.39}$$

and

$$\chi_{\alpha\alpha'}^{R,A} = \sum_{N \neq 0} \frac{\chi_{\alpha\alpha}^{R,A}(\mathbf{q}; N)}{\omega + E_N + i\eta}. \tag{B.40}$$

We then find

$$\chi_{\alpha\alpha'}^{R,R}(\mathbf{q}; N) = \langle 0|\hat{c}_{v(\mathbf{k}-\frac{\mathbf{q}}{2})}^{\dagger}\hat{c}_{c(\mathbf{k}+\frac{\mathbf{q}}{2})}|n\rangle\langle n|\hat{c}_{c'(\mathbf{k}'+\frac{\mathbf{q}}{2})}^{\dagger}\hat{c}_{v'(\mathbf{k}'-\frac{\mathbf{q}}{2})}|0\rangle$$
$$= \chi_{\alpha\alpha'}^{R1}(\mathbf{q}; N) = \left[\chi_{\alpha\alpha'}^{R2}(-\mathbf{q}; N)\right]^{*} \tag{B.41}$$

and

$$\chi_{\alpha\alpha'}^{R,A}(\mathbf{q}; N) = \langle 0|\hat{c}_{c'(\mathbf{k}-\frac{\mathbf{q}}{2})}^{\dagger},\hat{c}_{v'(\mathbf{k}'+\frac{\mathbf{q}}{2})}|n\rangle\langle n|\hat{c}_{v(\mathbf{k}+\frac{\mathbf{q}}{2})}^{\dagger}\hat{c}_{c(\mathbf{k}-\frac{\mathbf{q}}{2})}|0\rangle$$
$$= \chi_{\alpha\alpha'}^{A1}(\mathbf{q}; N) = \left[\chi_{\alpha\alpha'}^{A2}(-\mathbf{q}; N)\right]^{*}. \tag{B.42}$$

We see that the matrix elements of the time-ordered polarizability using a Fourier transform in $\tau^{(1)}$ are identical to the ones of the retarded polarizability. Those matrix elements obtained from the Fourier transform in $\tau^{(2)}$, on the other hand, are the complex-conjugate of the corresponding matrix elements for the momentum transfer $-\mathbf{q}$.

Let us formulate a physical interpretation of this behavior: Using $\tau^{(1)}$ represents moving forward in time, as can be seen in the definition of the retarded polarizability in Eq. 2.18. We observe excitations and de-excitations in the time-ordered polarizability as we do in the retarded one. These excitations occur with a momentum transfer $\mathbf{q}$, *i.e.* transitions occur from $\mathbf{k} - \frac{\mathbf{q}}{2}$ to $\mathbf{k} + \frac{\mathbf{q}}{2}$. Using $\tau^{(2)}$ represents a time reversal, as increasing $\tau^{(2)}$ means moving backward in time. An excitation seen moving forward in time turns into a de-excitation, when moving backward. Since the momentum changes sign under time reversal, the Fourier components of the polarizability with respect to $\tau^{(2)}$ contains the information about excitations and de-excitations with momentum transfer $-\mathbf{q}$.

B.6 Consequences for BSE Implementations

In the following, we will show how the construction of the retarded polarizability differ in BSE implementations depending on which of the basis set representations in Eq. B.34 are employed. Due to the relationship between the basis functions in Eq. B.37 and B.37, the eigenstates $X_\lambda^{(1,2)}$ corresponding to an eigenvalue $E_\lambda^{(1,2)}$ in the two basis sets are related by

$$X_\lambda^{(2)}(\mathbf{q}) = \left[X_\lambda^{(1)}(-\mathbf{q}) \right]^* \quad Y_\lambda^{(2)}(\mathbf{q}) = \left[Y_\lambda^{(1)}(-\mathbf{q}) \right]^* \tag{B.43}$$

and the eigenvalues by

$$E_\lambda^{(1)}(\mathbf{q}) = E_\lambda^{(2)}(-\mathbf{q}). \tag{B.44}$$

B.6.1 Construction of the Polarizabiliy

Once the BSE eigenvalues $E^\lambda(\mathbf{q})$ and eigenstates $X_\lambda^{(1)}(\mathbf{q}), Y_\lambda^{(1)}(\mathbf{q})$ are obtained from the BSE Hamiltonian (Eq. 6.29) in the basis $\{\Upsilon_\alpha^{r1}, \Upsilon_\alpha^{a1}\}$, the retarded polarizability is calculated according to Ref. [283] as

$$\chi(\mathbf{q}, \omega) = - \left[H^{\text{BSE}}(\mathbf{q}) - \omega\Delta \right]^{-1} = \sum_\lambda \frac{\chi^{R1}(\mathbf{q}, \lambda, 1)}{\omega - E^\lambda + i\eta} - \frac{\chi^{A1}(\mathbf{q}, \lambda, 1)}{\omega - E^\lambda - i\eta}, \tag{B.45}$$

with

$$\chi^{R1}(\mathbf{q}; \lambda) = \begin{pmatrix} X_\lambda^{(1)}(\mathbf{q}) \left[X_\lambda^{(1)}(\mathbf{q}) \right]^\dagger & X_\lambda^{(1)}(\mathbf{q}) \left[Y_\lambda^{(1)}(\mathbf{q}) \right]^\dagger \\ Y_\lambda^{(1)}(\mathbf{q}) \left[X_\lambda^{(1)}(\mathbf{q}) \right]^\dagger & Y_\lambda^{(1)}(\mathbf{q}) \left[Y_\lambda^{(1)}(\mathbf{q}) \right]^\dagger \end{pmatrix}$$

$$\chi^{A1}(\mathbf{q}; \lambda, 1) = \begin{pmatrix} Y_\lambda^{(1)}(\mathbf{q}) \left[Y_\lambda^{(1)}(\mathbf{q}) \right]^\dagger & Y_\lambda^{(1)}(\mathbf{q}) \left[X_\lambda^{(1)}(\mathbf{q}) \right]^\dagger \\ X_\lambda^{(1)}(\mathbf{q}) \left[Y_\lambda^{(1)}(\mathbf{q}) \right]^\dagger & X_\lambda^{(1)}(\mathbf{q}) \left[X_\lambda^{(1)}(\mathbf{q}) \right]^\dagger \end{pmatrix}. \tag{B.46}$$

The Fourier components of the retarded polarizabiliy are given by as[2]

$$\chi_{\mathbf{GG'}}^R(\mathbf{q}, \omega) = \frac{1}{V} \left([M^{(1)}]^T(\mathbf{G}, \mathbf{q}) \quad [M^{(1)}]^T(\mathbf{G}, \mathbf{q}) \right) \chi^R(\mathbf{q}, \omega) \begin{pmatrix} \left[M^{(1)} \right]^*(\mathbf{G}, \mathbf{q}) \\ \left[M^{(1)} \right]^*(\mathbf{G}, \mathbf{q}) \end{pmatrix}, \tag{B.47}$$

---

[2]Here, we use the fact that $\Upsilon_\alpha^{(1,2)r}(\mathbf{r}, \mathbf{r}) = \Upsilon_\alpha^{(1,2)a}(\mathbf{r}, \mathbf{r})$ [261].

where $M^{(1)}(\mathbf{G}, \mathbf{q})$ are the plane-wave matrix elements defined in Eq. A.16 with respect to the basis $\Upsilon^{(1)}$. Finally, we obtain the compact expression

$$\chi^R_{GG}(\mathbf{q}, \omega) = \sum_\lambda \frac{\left[t^{(1)}_\lambda(\mathbf{q}) \right]^* t^{(1)}_\lambda(\mathbf{q})}{\omega - E^\lambda(\mathbf{q}) + i\eta} - \frac{t^{(1)}_\lambda(\mathbf{q}) \left[t^{(1)}_\lambda(\mathbf{q}) \right]^*}{\omega + E^\lambda(\mathbf{q}) + i\eta}, \tag{B.48}$$

where we have defined the oscillator strength $t^{(1)}_\lambda(\mathbf{q})$ as

$$t^{(1)}_\lambda(\mathbf{q}) = \frac{1}{\sqrt{V}} \left(X^{(1)}_\lambda(\mathbf{q}) + Y^{(1)}_\lambda(\mathbf{q}) \right)^\dagger \left[M^{(1)}(\mathbf{G}, \mathbf{q}) \right]^*. \tag{B.49}$$

Equations B.48 and B.49 show that the retarded polarizability can be obtained in a straightforward fashion from the eigenvalues and -states of the BSE in the basis set $\Upsilon^{(1)}$. To obtain an expression in terms of the eigenvalues and eigenstates obtained from a solution in the basis set Υ^2, we use that the plane-wave matrix elements $M^{(1)}$ and $M^{(2)}$ are related as

$$M^{(1)}_\alpha(\mathbf{G}, \mathbf{q}) = \int d^3 r \Upsilon^{(1)}_{\alpha, \mathbf{q}}(\mathbf{r}, \mathbf{r}) e^{-i(\mathbf{G}+\mathbf{q})\mathbf{r}} = \left[\int d^3 r \Upsilon^{(2)}_{\alpha, -\mathbf{q}}(\mathbf{r}, \mathbf{r}) e^{i(\mathbf{G}+\mathbf{q})\mathbf{r}} \right]^* = \left[M^{(2)}_\alpha(-\mathbf{G}, -\mathbf{q}) \right]^*, \tag{B.50}$$

where we have combined Eqs. B.37 and B.38. Using Eqs. B.43 and B.44, the retarded polarizability can be expressed in terms of solutions of the BSE in the basis $\Upsilon^{(2)}$ as

$$\chi^R_{GG}(\mathbf{q}, \omega) = \sum_\lambda \frac{\left| M^{(2)}(-\mathbf{G}, -\mathbf{q})^\dagger \left(X^{(2)}_\lambda(-\mathbf{q}) + Y^{(2)}_\lambda(-\mathbf{q}) \right)^* \right|^2}{\omega - E^\lambda(-\mathbf{q}) + i\eta}$$
$$- \frac{\left| M^{(2)}(-\mathbf{G}, -\mathbf{q})^\dagger \left(X^{(2)}_\lambda(-\mathbf{q}) + Y^{(2)}_\lambda(-\mathbf{q}) \right)^* \right|^2}{\omega + E^\lambda(-\mathbf{q}) + i\eta}. \tag{B.51}$$

Equivalently, the Fourier components $\chi^R_{(-G)(-G)}(-\mathbf{q}, \omega)$ can be obtained as

$$\chi^R_{(-G)(-G)}(-\mathbf{q}, \omega) = \sum_\lambda \frac{\left| M^{(2)}(\mathbf{G}, \mathbf{q})^\dagger \left(X^{(2)}_\lambda(\mathbf{q}) + Y^{(2)}_\lambda(\mathbf{q}) \right)^* \right|^2}{\omega - E^\lambda(\mathbf{q}) + i\eta}$$
$$- \frac{\left| M^{(2)}(\mathbf{G}, \mathbf{q})^\dagger \left(X^{(2)}_\lambda(\mathbf{q}) + Y^{(2)}_\lambda(\mathbf{q}) \right)^* \right|^2}{\omega + E^\lambda(\mathbf{q}) + i\eta}. \tag{B.52}$$

where we have used $E^\lambda(\mathbf{q}) = E^\lambda(-\mathbf{q})$ and $X_{\lambda,2}(\mathbf{q}) + Y_{\lambda,2}(\mathbf{q}) = X_{\lambda,2}(-\mathbf{q}) + Y_{\lambda,2}(-\mathbf{q})$. We then define the oscillator strength $t_\lambda^{(2)}(\mathbf{q})$ as

$$t_\lambda^{(2)}(\mathbf{q}) = \frac{1}{\sqrt{V}} \left(X_\lambda^{(2)}(\mathbf{q}) + Y_\lambda^{(2)}(\mathbf{q}) \right)^T M^{(2)}(\mathbf{G}, \mathbf{q}) \tag{B.53}$$

and obtain

$$\chi^R_{(-\mathbf{G})(-\mathbf{G})}(-\mathbf{q}, \omega) = \sum_\lambda \frac{t_\lambda^{(2)}(\mathbf{q}) \left[t_\lambda^{(2)}(\mathbf{q}) \right]^*}{\omega - E^\lambda(\mathbf{q}) + i\eta} - \frac{t_\lambda^{(2)}(\mathbf{q}) \left[t_\lambda^{(2)}(\mathbf{q}) \right]^*}{\omega + E^\lambda(\mathbf{q}) + i\eta}. \tag{B.54}$$

As such, we have shown in Eq. B.54 that the solutions of the BSE Hamiltonian in the basis $\Upsilon^{(2)}$ for a momentum transfer $\mathbf{Q} = \mathbf{G} + \mathbf{q}$ yield the retarded polarizability for the momentum transfer $-\mathbf{Q} = -\mathbf{G} - \mathbf{q}$.

B.6.2 Optical Limit

To obtain the macroscopic dielectric tensor $\epsilon_M^{ij}(\omega)$ in the optical limit, *i.e.* for $\mathbf{q} \to 0$ directly, an *effective retarded polarizability* $\bar{\chi}^R_{\mathbf{G}\mathbf{G}'}$ can be employed. With this, the dielectric tensor becomes

$$\varepsilon_M(\mathbf{G} + \mathbf{q}, \omega) = 1 - \frac{4\pi}{|\mathbf{G} + \mathbf{q}|^2} \bar{\chi}^R_{\mathbf{G}\mathbf{G}}(\mathbf{q}, \omega). \tag{B.55}$$

The effective polarizability $\bar{\chi}^R$ is connected to the retarded polarizability χ^R via $\bar{\chi}^R = \chi^R + \chi^R \bar{v} \bar{\chi}^R$, where $\bar{v}$ is given for a momentum transfer $\mathbf{Q} = \mathbf{G} + \mathbf{q}$, as

$$\bar{v}_{\mathbf{G}'}(\mathbf{q}') = \begin{cases} 0 & \mathbf{G}' = \mathbf{G} \quad \mathbf{q}' = \mathbf{q} \\ v_{\mathbf{G}'}(\mathbf{q}') & \text{else} \end{cases} \tag{B.56}$$

The effective polarizability is calculated by replacing the bare Coulomb potential in Eqs. 6.37 and 6.39 with $\bar{v}$. More details can be found in Refs. [103, 140, 261]. In the optical limit, Eq. B.55 becomes

$$\epsilon_M(\omega) = 1 - \lim_{q \to 0} \frac{4\pi}{q^2} \bar{\chi}^R_{0,0}(\mathbf{q}, \omega). \tag{B.57}$$

In order to evaluate the limit $\mathbf{q} \to 0$, we consider first the limit of the plane-wave matrix elements $M^{(2)}(0, -\mathbf{q})$:

$$\lim_{\mathbf{q} \to 0} M_\alpha^{(2)}(0, -\mathbf{q}) = \lim_{\mathbf{q} \to 0} \int d^3 r \Upsilon^{(2)}(\mathbf{r}, \mathbf{r}) e^{i\mathbf{q}\mathbf{r}} \approx i\mathbf{q} \int d^3 r \mathbf{r} \Upsilon^{(2)}(\mathbf{r}, \mathbf{r}) = \mathbf{q} \frac{P_\alpha^{(2)}}{\Delta\epsilon_\alpha}, \tag{B.58}$$

where we have used $\left[\hat{H}, \hat{r}\right] = -i\hat{p}$ to express the plane-wave matrix element in terms of the momentum matrix element $\mathbf{P}_\alpha$ and the energy difference $\Delta\epsilon_\alpha = \epsilon_{c\mathbf{k}} - \epsilon_{v\mathbf{k}}$. By separating the momentum vector $\mathbf{q} = |\mathbf{q}|\hat{\mathbf{q}}$, where $\hat{\mathbf{q}}$ is the unit vector in the direction of $\mathbf{q}$, we can now construct the macroscopic dielectric function as

$$\varepsilon_M(\omega) = 1 - 4\pi \sum_{i,j} \hat{q}_i \sum_{\lambda} \left(\frac{\left[t^{(2)}_{\lambda,i}\right]^* t_{\lambda,j}}{\omega - E_\lambda + i\eta} + \frac{\left[t^{(2)}_{\lambda,i}\right]^* t_{\lambda,j}}{-\omega - E_\lambda - i\eta} \right) \hat{q}_j. \tag{B.59}$$

In Eq. B.59, we have defined the oscillator strength at $\mathbf{q} = 0$ as

$$t^{(2)}_{\lambda,i} = \frac{1}{\sqrt{V}} \left(X^{(2)}_\lambda(\mathbf{q}) + Y^{(2)}_\lambda(\mathbf{q}) \right)^T \frac{P_i}{\Delta\epsilon} \tag{B.60}$$

We can now rewrite Eq. B.59 in matrix form to obtain the 3×3 dielectric tensor, the entries of which are given by

$$\varepsilon^{ij}_M(\omega) = \delta_{ij} - 4\pi \sum_{\lambda} \left(\frac{\left[t^{(2)}_{\lambda,i}\right]^* t^{(2)}_{\lambda,j}}{\omega - E_\lambda + i\eta} + \frac{\left[t^{(2)}_{\lambda,i}\right]^* t^{(2)}_{\lambda,j}}{-\omega - E_\lambda - i\eta} \right). \tag{B.61}$$

APPENDIX C

Numerical Convergence

The main parameters of BSE calculations in the `exciting` code are the $\mathbf{k}$-grid, the Fourier cut-off $|\mathbf{G} + \mathbf{q}|_{max}$ of matrix elements in Eqs. 6.39, 6.45, and 6.46, and the number of conduction and valence bands that are included in the construction of the BSE Hamiltonian. For all absorption spectra presented in this thesis, we have performed convergence test, where we have considered the full spectral shape as the convergence criterion. We have performed additional tests to ensure the convergence of exciton binding energies. For all core excitation spectra in Ga_2O_3 polymorphs, we consider only the convergence of the spectrum of one of the inequivalent atoms. All spectra in this chapter represent *raw computational spectra*, *i.e.* the spectra are not aligned to the experimental ones, and thus may differ from those provided in Chapters 10,11,12,13.

C.1 Ga_2O_3 Optical Absorption Spectra

The convergence behavior of the optical absorption spectra of α- and β-Ga_2O_3 is displayed in Fig. C.1. We find that the optical absorption of α-Ga_2O_3 changes little with increasing $\mathbf{k}$-grid, while the position and intensity of the peaks in the spectrum of the β-phase change strongly. For both polymorphs, the spectra change little with increasing cut-off off $|\mathbf{G} + \mathbf{q}|_{max}$. The optical absorption spectrum is converged for a $11 \times 11 \times 11$ $\mathbf{k}$-grid. We chose a cut-off $|\mathbf{G} + \mathbf{q}|_{max} = 2.0$ a_0^{-1} and 1.1 a_0^{-1} for α- and β-Ga_2O_3, respectively. As we analyze the bound excitons, we consider the convergence of the binding energy of the most strongly bound exciton in Fig. C.2. For both polymorphs, the binding energies converge slowly with respect to the size of the $\mathbf{k}$-grids. As the numerical cost of the BSE calculations increase tremendously with increasing numbers of $\mathbf{k}$-points, these tests are performed with a decreased number of conduction bands in the BSE Hamiltonian. From the exciton weights in Fig. 10.2 we anticipate that the excited electron is solely distributed over the lowest two conduction bands, while the hole is distributed over several valence bands. Therefore, for the convergence of the bound excitons, we consider transitions from the 9 and 10 highest valence bands in α and β-Ga_2O_3, respectively, to the 2 lowest conduction bands. We find that there is no significant change in the binding energy for β-Ga_2O_3. Generally, the binding energies decrease with increasing number of $\mathbf{k}$-points. The increase of $|\mathbf{G} + \mathbf{q}|_{max}$ does not
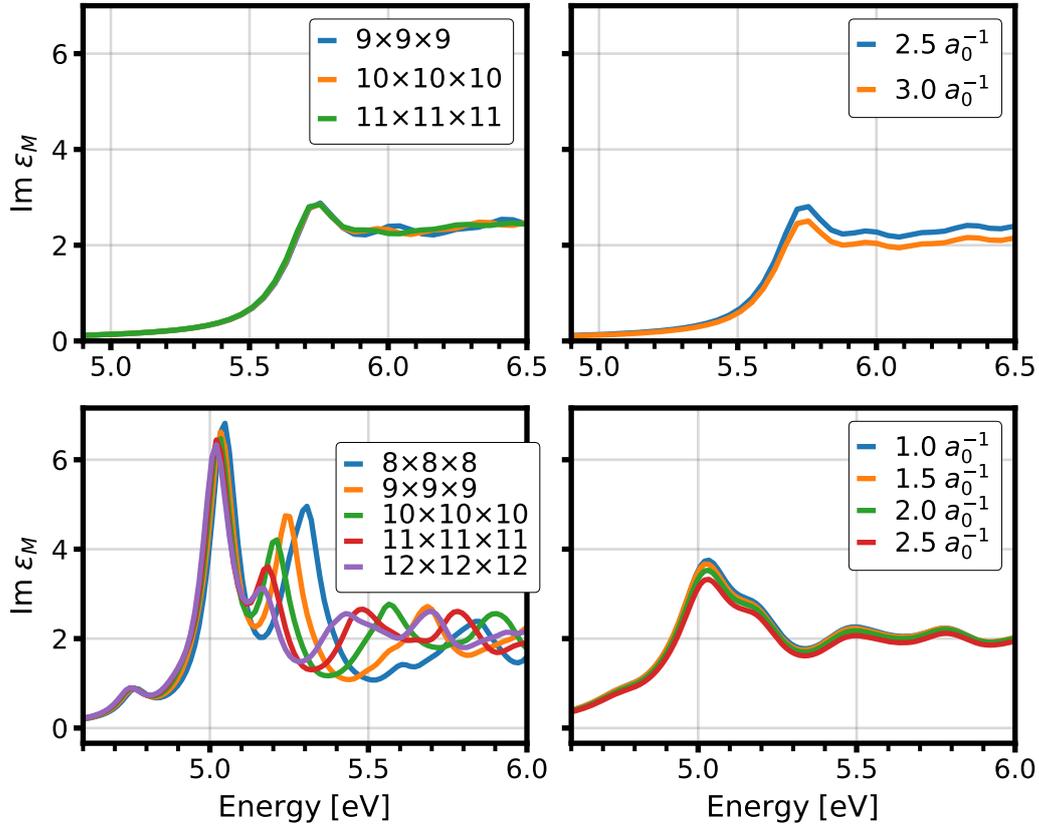
Figure C.1: Convergence of ε_M^{xx} of α- (top) and β-Ga$_2$O$_3$ (bottom) with respect to the **k**-grid (left) and the cut-off $|\mathbf{G} + \mathbf{q}|_{max}$.

change them significantly. Converged values are obtained with a $14 \times 14 \times 14$ **k**-grid and cut-off $|\mathbf{G} + \mathbf{q}|_{max} = 2.0\ a_0^{-1}$ for α-Ga$_2$O$_3$. For β-Ga$_2$O$_3$, the corresponding parameters are a $16 \times 16 \times 16$ **k**-grid and $|\mathbf{G} + \mathbf{q}|_{max} = 0.8\ a_0^{-1}$.

Figure C.2: Convergence of the exciton binding energy for the most strongly bound exciton in α- and β-Ga$_2$O$_3$ with respect to the number of **k**-points (left) and cut off $|\mathbf{G}+\mathbf{q}|_{max}$ (right). For the former, we show both the convergence of the full calculation and the onset calculation.
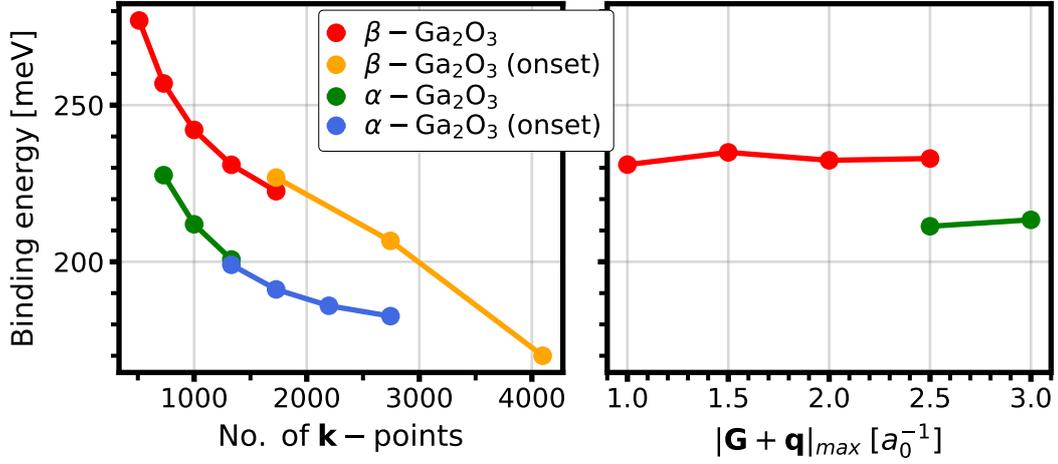
C.2 Ga$_2$O$_3$ Oxygen K Edge Spectra

The O K edge spectra of α-, β-, and ϵ-Ga$_2$O$_3$ converge rapidly both with respect to the number of **k**-points and the cut-off $|\mathbf{G}+\mathbf{q}|_{max}$. While Fig. C.3 only shows the results for ε_M^{xx} of the oxygen atom O$_1$ in each polymorph, we have verified that the other components and the spectra of all inequivalent atoms converge for the same numerical parameters. From the our convergence tests, we induce that converged spectra are obtained with a $9 \times 9 \times 9$ **k**-grid and $|\mathbf{G}+\mathbf{q}|_{max} = 3.0\ a_0^{-1}$ for α-Ga$_2$O$_3$, $10 \times 10 \times 10$ grid and $|\mathbf{G}+\mathbf{q}|_{max} = 1.0\ a_0^{-1}$ for β-Ga$_2$O$_3$, and $8 \times 8 \times 8$ grid and $|\mathbf{G}+\mathbf{q}|_{max} = 1.5\ a_0^{-1}$ for ϵ-Ga$_2$O$_3$.
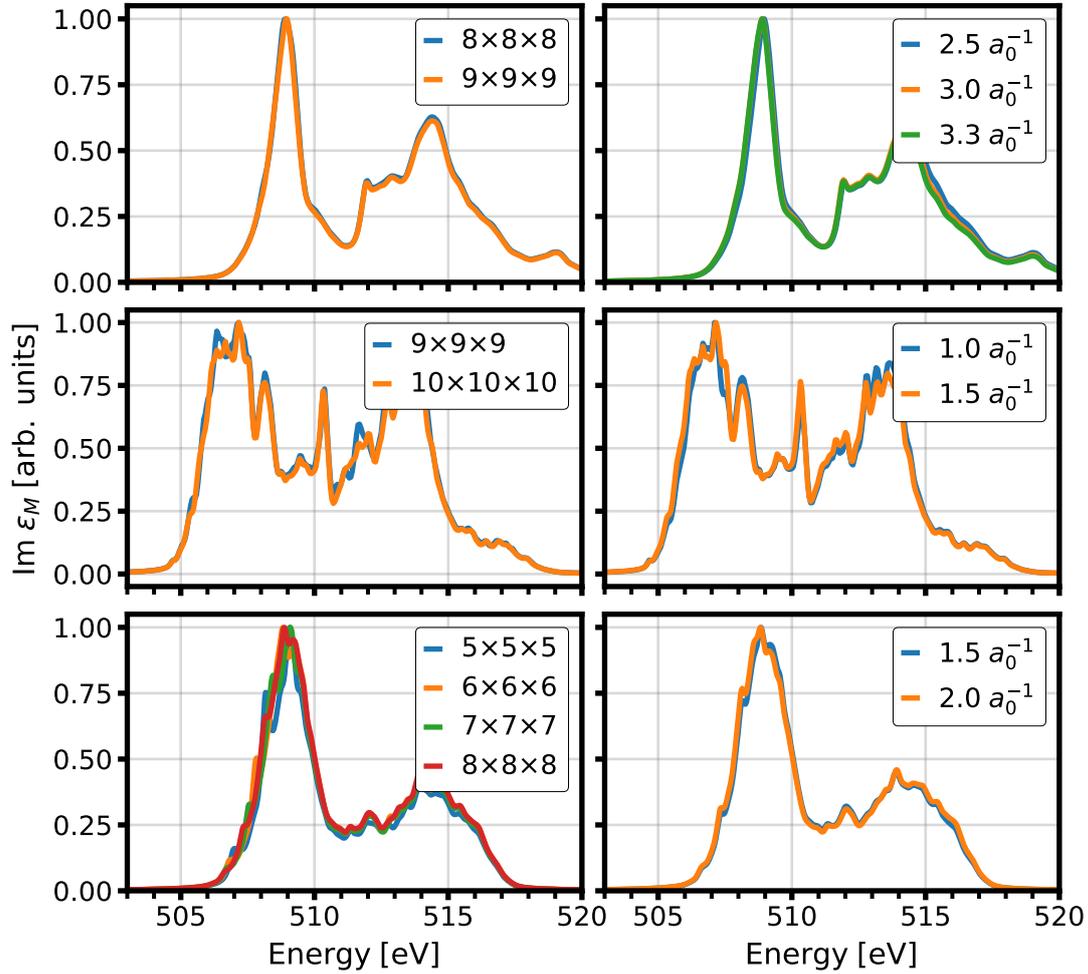
Figure C.3: Convergence of the O K edge spectrum for α- (top), β- (center), and ϵ-Ga$_2$O$_3$ (bottom) with respect to the **k**-grid (left) and the cut-off $|\mathbf{G} + \mathbf{q}|_{max}$ (right). The component ε_M^{xx} is shown for all polymorphs. All spectra are normalized to the most intense peak.

C.3 Ga$_2$O$_3$ Gallium L$_2$ Edge Spectra

The convergence behavior of the Ga L$_2$ edge spectra of both α- and β-Ga$_2$O$_3$ differs significantly from that of the optical and O K edge spectra. The spectra converge quickly with the **k**-grid, but the convergence with respect to the Fourier cut-off $|\mathbf{G}+\mathbf{q}|_{max}$ is very slow. With increasing cut-off, both the relative intensity and relative position of the low-energy excitonic peak in the spectrum changes. While the convergence is slow, the spectral changes are subtle and can not be deduced from Fig. C.4. We therefore introduce a measure for the

convergence of spectra. Given a spectrum $\varepsilon_a(\omega)$ and a converged spectrum $\varepsilon_b(\omega)$, we define the integrated difference $\Delta\varepsilon$ as

$$\Delta\varepsilon = \frac{\int d\omega \left|\mathrm{Im}\left[\varepsilon_a(\omega) - \varepsilon_b(\omega)\right]\right|}{\int d\omega \left|\mathrm{Im}\,\varepsilon_b(\omega)\right|}. \tag{C.1}$$

The integrated difference for the α- and β-phase shown in Fig. C.5 demonstrate that the spectra converge with increasing $|\mathbf{G} + \mathbf{q}|_{\mathrm{max}}$. For excitonic properties, the convergence is seen more clearly when the exciton binding energies are considered in Fig. C.6. These decreases slightly for calculations with increasing number of $\mathbf{k}$-points and we find that both the exciton binding energy and the absorption spectra are converged with $\mathbf{k}$-grids of $11 \times 11 \times 11$ and $10 \times 10 \times 10$ for α- and β-Ga$_2$O$_3$, respectively. The change with increasing $|\mathbf{G} + \mathbf{q}|_{max}$ is more significant. We find that the binding energy and absorption spectra are only converged for $|\mathbf{G} + \mathbf{q}|_{max} = 4.5\ a_0^{-1}$ for both polymorphs, a considerably higher cut-off than required for the calculation of the optical and O K edge absorption spectra.
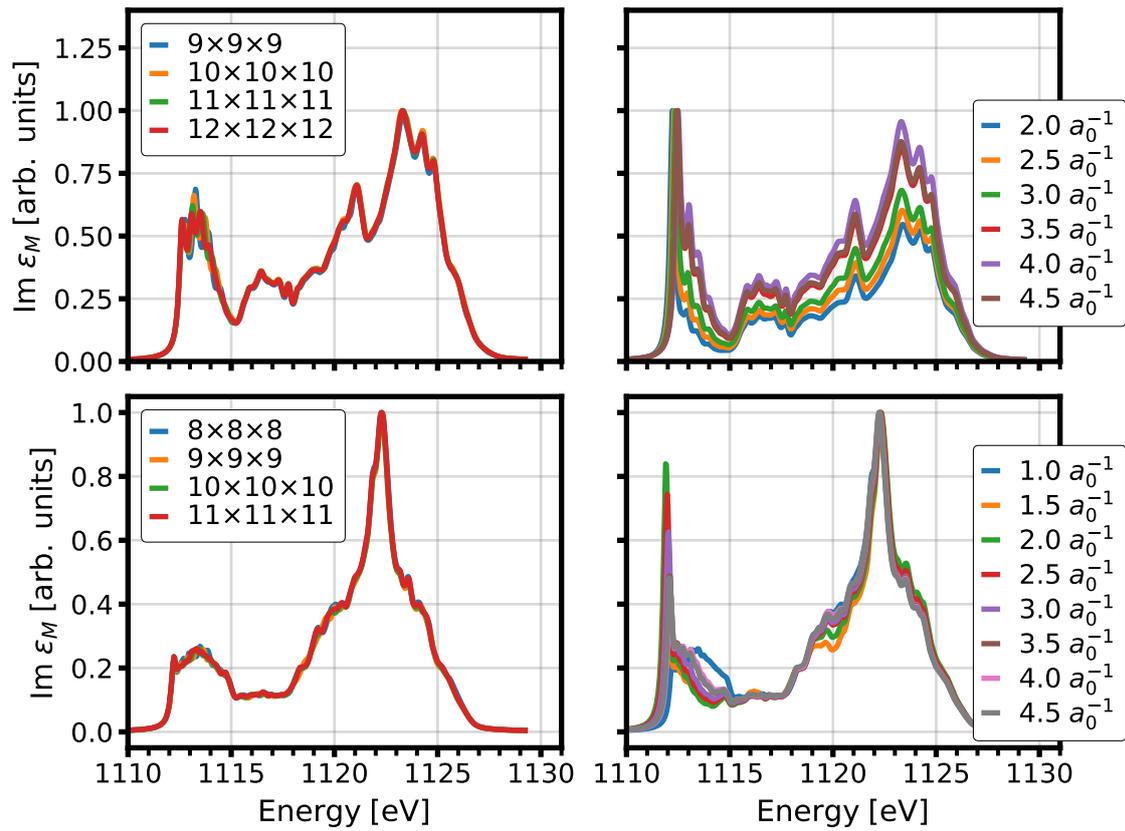
Figure C.4: Convergence of Ga L_2 edge absorption spectrum of α- (top) and β-Ga$_2$O$_3$ (bottom) with respect to the **k**-grid (left) and $|\mathbf{G} + \mathbf{q}|_{max}$ (right). We display the component ε_M^{xx}. All spectra are normalized to the most intense peak.
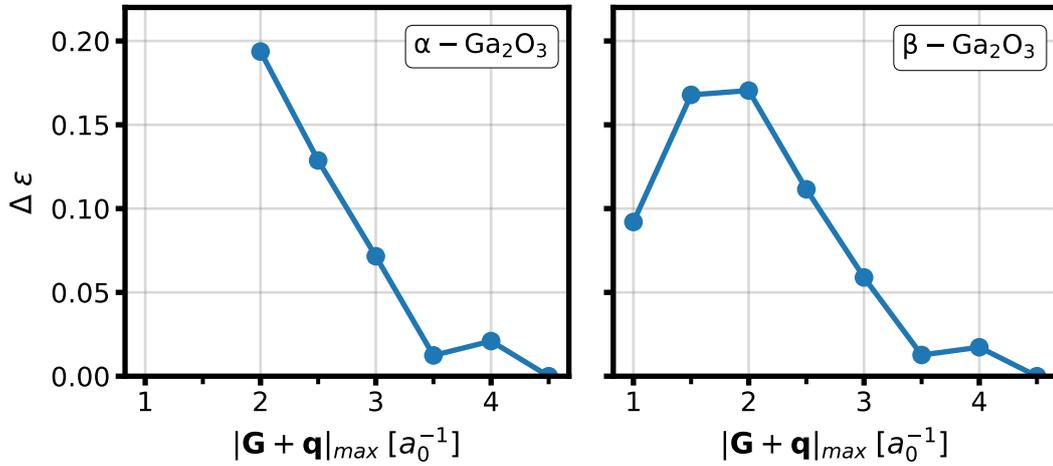
Figure C.5: Integrated difference following Eq. C.1 for the Ga L$_2$ edge XANES of α-(left) and β-Ga$_2$O$_3$ (right). For both polymorphs, we compare the spectra to the one with $|\mathbf{G} + \mathbf{q}|_{\max} = 4.5\ a_0^{-1}$.
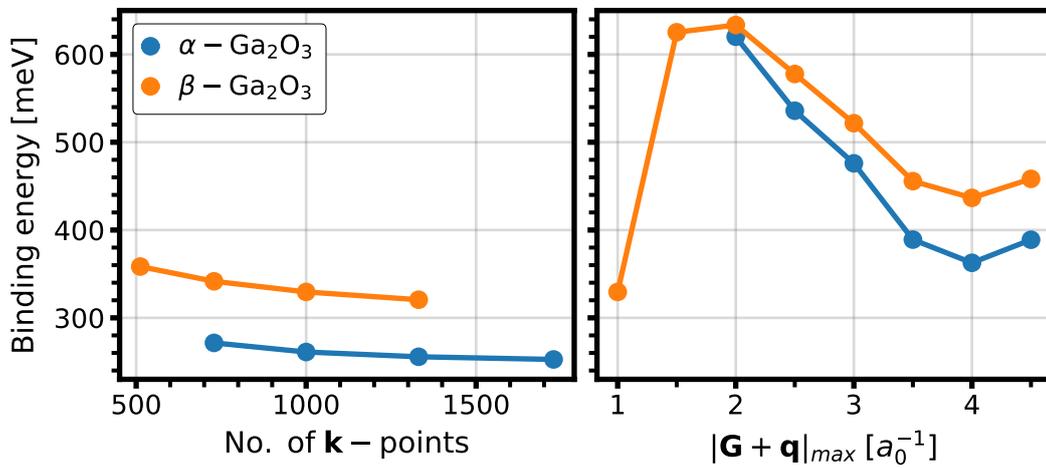
Figure C.6: Convergence of the binding energy of the most strongly-bound exciton in α- (blue) and β-Ga$_2$O$_3$ (orange) with respect to the number of $\mathbf{k}$-points (left) and the cut-off $|\mathbf{G} + \mathbf{q}|_{max}$.

C.4 Ga$_2$O$_3$ Gallium K Edge Spectra

The Ga K edge XANES of both α- and β-Ga$_2$O$_3$ converge rapidly with respect to both the **k**-grid and the cut-off $|\mathbf{G} + \mathbf{q}|_{max}$ for the screened and bare Coulomb potentials. For α-Ga$_2$O$_3$, a $9 \times 9 \times 9$ **k**-grid and a cut-off $|\mathbf{G} + \mathbf{q}|_{max} = 2.5 \ a_0^{-1}$ yields a correct spectral shape. For the β-phase, a $10 \times 10 \times 10$ **k**-grid and a cut-off $|\mathbf{G} + \mathbf{q}|_{max} = 3.0 a_0^{-1}$ is found to be sufficient.
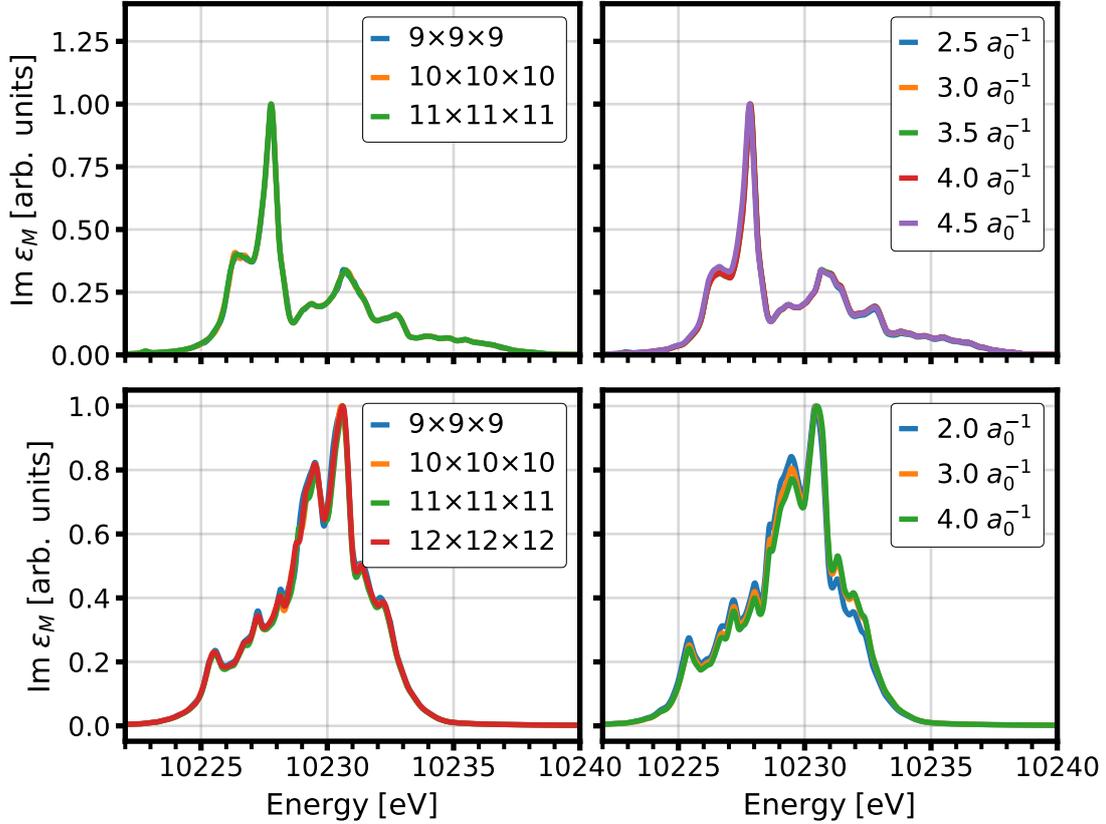
Figure C.7: Convergence of ε_M^{xx} at the Ga K edge of α- (top) and β-Ga$_2$O$_3$ (bottom) with respect to the **k**-grid (left) and the cut-off $|\mathbf{G}+\mathbf{q}|_{max}$. All spectra normalized to the intensity of the maximum.

C.5 Converged Parameters

C.5.1 DFT Calculations

Here, we summarize the numerical parameters for the DFT calculations from which the electronic-structure plots in this thesis are obtained, and which are the basis of the BSE calculations. The parameters of the latter are presented in the next section. All DFT calculations are performed with the all-electron full-potential `exciting` code [254]. Calculations with this code require the user to specify a number of numerical parameter, and in the following we only report the three most important ones: the **k**-grid describe the sampling of the first Brillouin zone, the product of the smallest muffin-tin radius R_{MT} and the plane-wave cutoff $|\mathbf{G}+\mathbf{k}|_{\max}$ describes size of the (L)APW+lo basis, and we report the exchange-correlation functional of the calculations. The remaining numerical parameters

can be obtained from the input and output files of the calculations, which we provide in Refs. [352–354] for diamond, LiF, and CeO$_2$, respectively, and in Refs. [355–357] for α-, β-, and ϵ-Ga$_2$O$_3$, respectively.

Material	k-grid	$R_{\mathrm{MT}}|\mathbf{G} + \mathbf{k}|_{\mathrm{max}}$	Functional $v_{xc}[n]$
Diamond	$9 \times 9 \times 9$	8.0	PBSEsol [77]
LiF	$8 \times 8 \times 8$	9.0	PBEsol
CeO$_2$	$8 \times 8 \times 8$	9.0	PBE [76]
α-Ga$_2$O$_3$	$8 \times 8 \times 8$	8.0	PBE
β-Ga$_2$O$_3$	$8 \times 8 \times 8$	8.0	PBE
ϵ-Ga$_2$O$_3$	$4 \times 4 \times 4$	10.0	PBE

Table C.1: Converged numerical parameters for all DFT calculations.

C.5.2 BSE Calculations

In this section, we summarize the numerical parameters of all BSE calculations that are included in this thesis. All calculations are performed using the exciting code [359, 254]. The relevant parameters are the k-grid, the number of conduction states N_{cond}(screen) included in the calculations of the RPA dielectric function, and the number N_{val} of valence and N_{cond}(bse) of the conduction states included in the construction of the BSE Hamiltonian. Finally, the lifetime broadening η used for the construction of the dielectric function. The input and output files of the BSE calculations can be found in Refs. [352–354] for diamond, LiF, and CeO$_2$, respectively, and in Refs. [355–357] for α-, β-, and ϵ-Ga$_2$O$_3$, respectively.

Material	Energy	$\mathbf{k}$-grid	N_{cond} (screen)	N_{val}	N_{cond} (bse)	$|\mathbf{G} + \mathbf{q}|_{max}$ $[a_0^{-1}]$	η [eV]
diamond	optics	$13 \times 13 \times 13$	100	4	10	3.5	0.15
	C K edge	$13 \times 13 \times 13$	100	2	40	5.5	0.5
LiF	optics	$9 \times 9 \times 9$	100	4	20	5.0	0.25
	F K edge	$9 \times 9 \times 9$	100	2	20	7.0	0.75
CeO_2	Ce $N_{4,5}$ edge	$5 \times 5 \times 5$	100	14	60	6.0	0.5
α-Ga_2O_3	optics	$11 \times 11 \times 11$	100	9	15	2.0	0.1
	O K edge	$9 \times 9 \times 9$	100	2	20	3.0	0.2
	Ga K edge	$9 \times 9 \times 9$	100	2	30	2.5	1.0
	Ga L_2	$11 \times 11 \times 11$	100	2	20	4.5	0.15
β-Ga_2O_3	optics	$11 \times 11 \times 11$	30	10	10	1.1	0.1
	O K edge	$10 \times 10 \times 10$	30	2	20	1.0	0.1
	Ga K edge edge	$10 \times 10 \times 10$	75	2	30	3.0	1.0
	Ga L_2 edge	$10 \times 10 \times 10$	100	2	20	4.5	0.15
ϵ-Ga_2O_3	O K edge	$8 \times 8 \times 8$	100	2	60	1.5	0.15

Table C.2: Converged numerical parameters of all BSE calculations.

Acknowledgments

This thesis concludes the work of nearly 8 years that I spent in Prof. Dr. Claudia Draxl's research group pursuing my Bachlor, Master, and PhD degree. Over this time, many people have supported me, influenced my work, and provided me with opportunities to advance my studies.

First and foremost, I thank CLAUDIA DRAXL for supervising my PhD thesis. This thesis would not have been possible without the opportunities that she provided for me over the years. Claudia was always available for guidance and discussion when I needed her, but also gave me the scientific freedom that I needed. Her suggestions in the final stages of the writing process have elevated this thesis.

I am grateful to FRANCESCO SOTTILE for his substantial help on the RIXS project. Our discussions on all aspects of many-body theory were invaluable for the derivation of the RIXS cross section. I especially want to thank him for his hospitality during my visits at the Ecole Polytechnique in Palaiseau.

My work on the `exciting` code would not have been possible without the help of DMITRII NABOK and ANDRIS GULANS. They patiently answered my (sometimes silly) questions on the inner workings of the code, and helped me to decipher obscure error messages. The BSE functionalities within the `exciting` code was implemented in close collaboration with BENJAMIN AURICH, and his bold visionary approach to rewriting the code has inspired me.

I thank CATERINA COCCHI for her support and guidance in the beginning of my PhD project. I have learnt a lot about envisioning projects and writing publications from her, and our discussions have shaped the way I pursued the PhD project.

I want to thank all the group members of the solid-state theory group at the Humboldt Universität zu Berlin and all scientists that I had the honor to work with in the last years. Especially, I want to thank my roommates OLGA TURKINA and CECILIA VONA for our insightful discussions and numerous coffee breaks. I thank PHILIPPE KARAN for his tremendous work during his internship in Berlin.

My friends and family have supported me during the ups and downs of my PhD project. I especially want to thank MARTY OELSCHLÄGER and CHRISTOPH VOLBERS for a decade of discussions on physics and life.

I have no words to describe how much my wife MARIELLA VORWERK has helped me not only during my PhD project, but since I met her. While her insight into many-body perturbation theory is not always the best, without her unwavering support I would not have made it through the low points of the project. I thank my daughter SELMA VORWERK for brightening our mood during the Corona spring of 2020.

Last but not least I am grateful to my parents MARKUS and MONIKA VORWERK for stimulating my curiosity and thirst for knowledge. As long as I can remember, they have always given me the freedom to lightheartedly explore my passions and talents.

Bibliography

[1]M. Riordan, L. Hoddeson, and C. Herring, "The invention of the transistor", Rev. Mod. Phys. **71**, S336–S345 (1999).

[2]J. Y. Tsao, et al., "Ultrawide-bandgap semiconductors: research opportunities and challenges", Advanced Electronic Materials **4**, 1600501 (2018).

[3]H. Amano, N. Sawaki, I. Akasaki, and Y. Toyoda, "Metalorganic vapor phase epitaxial growth of a high quality GaN film using an AlN buffer layer", Appl. Phys. Lett. **48**, 353–355 (1986).

[4]S. Nakamura, N. Iwasa, M. Senoh, and T. Mukai, "Hole compensation mechanism of p-type GaN films", Jpn. J. Appl. Phys. **31**, 1258 (1992).

[5]J. Y. Tsao, J. Han, R. H. Haitz, and P. M. Pattison, "The Blue LED Nobel Prize: Historical context, current scientific understanding, human benefit", Ann. Phys. **527**, A53–A61 (2015).

[6]M. Kim, J.-H. Seo, U. Singisetti, and Z. Ma, "Recent advances in free-standing single crystalline wide band-gap semiconductors and their applications: GaN, SiC, ZnO, β-Ga$_2$O$_3$, and diamond", Journal of Materials Chemistry C **5**, 8338–8354 (2017).

[7]Z. Galazka, "β-Ga$_2$O$_3$ for wide-bandgap electronics and optoelectronics", Semicond. Sci. Technol. **33**, 113001 (2018).

[8]S. J. Pearton, et al., "A review of Ga$_2$O$_3$ materials, processing, and devices", Appl. Phys. Rev. **5**, 011301 (2018).

[9]M. Baldini, Z. Galazka, and G. Wagner, "Recent progress in the growth of β-Ga$_2$O$_3$ for power electronics applications", Mater. Sci. Semicond. Process **78**, 132–146 (2018).

[10]N. Ueda, H. Hosono, R. Waseda, and H. Kawazoe, "Synthesis and control of conductivity of ultraviolet transmitting β-Ga$_2$O$_3$ single crystals", Appl. Phys. Lett. **70**, 3561–3563 (1997).

[11]Z. Ji, J. Du, J. Fan, and W. Wang, "Gallium oxide films for filter and solar-blind UV detector", Opt. Mater. **28**, 415–417 (2006).

[12]X. Chen, F.-F. Ren, J. Ye, and S. Gu, "Gallium oxide-based solar-blind ultraviolet photodetectors", Semicond. Sci. Technol. **35**, 023001 (2020).

[13]P. Feng, J. Y. Zhang, Q. H. Li, and T. H. Wang, "Individual β-Ga$_2$O$_3$ nanowires as solar-blind photodetectors", Appl. Phys. Lett. **88**, 153107 (2006).

[14]W.-Y. Kong, et al., "Graphene-β-Ga$_2$O$_3$ heterojunction for highly sensitive deep uv photodetector application", Adv. Mater. **28**, 10725–10731 (2016).

[15]L.-X. Qian, et al., "Ultrahigh-responsivity, rapid-recovery, solar-blind photodetector based on highly nonstoichiometric amorphous gallium oxide", ACS Photonics **4**, 2203–2211 (2017).

[16]S. Cui, Z. Mei, Y. Zhang, H. Liang, and X. Du, "Room-temperature fabricated amorphous Ga$_2$O$_3$ high-response-speed solar-blind photodetector on rigid and flexible substrates", Adv. Opt. Mater. **5**, 1700454 (2017).

[17]Y. Li, et al., "Efficient assembly of bridge β-Ga$_2$O$_3$ nanowires for solar-blind photodetection", Advanced Functional Materials **20**, 3972–3978 (2010).

[18]R. Zou, et al., "High detectivity solar-blind high-temperature deep-ultraviolet photodetector based on multi-layered (l00) facet-oriented β-Ga$_2$O$_3$ nanobelts", Small **10**, 1848–1856 (2014).

[19]X. Chen, et al., "Self-powered solar-blind photodetector with fast response based on Au/β-Ga$_2$O$_3$ nanowires array film schottky junction", ACS Appl. Mater. Interfaces **8**, 4185–4191 (2016).

[20]M. Higashiwaki, et al., "Recent progress in Ga$_2$O$_3$ power devices", Semicond. Sci. Technol. **31**, 034001 (2016).

[21]J. Zhang, J. Shi, D.-C. Qi, L. Chen, and K. H. L. Zhang, "Recent progress on the electronic structure, defect, and doping properties of Ga$_2$O$_3$", APL Mater. **8**, 020906 (2020).

[22]K. Yamaguchi, "First principles study on electronic structure of β-Ga$_2$O$_3$", Solid State Commun. **131**, 739–744 (2004).

[23]H. He, M. A. Blanco, and R. Pandey, "Electronic and thermodynamic properties of β-Ga$_2$O$_3$", Appl. Phys. Lett. **88**, 261904 (2006).

[24]H. He, et al., "First-principles study of the structural, electronic, and optical properties of Ga$_2$O$_3$ in its monoclinic and hexagonal phases", Phys. Rev. B **74**, 195123 (2006).

[25]W.-Z. Xiao, L.-L. Wang, L. Xu, Q. Wan, and A.-L. Pan, "Electronic structure and magnetic properties in Nitrogen-doped β-Ga$_2$O$_3$ from density functional calculations", Solid State Commun. **150**, 852–856 (2010).

[26]H. Peelaers, and C. G. V. de Walle, "Brillouin zone and band structure of β-Ga$_2$O$_3$", Phys. Status Solidi B **252**, 828–832 (2015).

[27]A. Navarro-Quezada, et al., "Near valence-band electronic properties of semiconducting $\beta - Ga_2O_3$ (100) single crystals", Phys. Rev. B **92**, 195306 (2015).

[28]J. Furthmüller, and F. Bechstedt, "Quasiparticle bands and spectra of Ga$_2$O$_3$ polymorphs", Phys. Rev. B **93**, 115204 (2016).

[29] J. Kim, D. Tahara, Y. Miura, and B. G. Kim, "First-principle calculations of electronic structures and polar properties of (κ,ϵ)-Ga_2O_3", Applied Physics Express **11**, 061101 (2018).

[30] J. B. Varley, A. Janotti, C. Franchini, and C. G. Van de Walle, "Role of self-trapping in luminescence and p-type conductivity of wide-band-gap oxides", Phys. Rev. B **85**, 081109 (2012).

[31] J. B. Varley, J. R. Weber, A. Janotti, and C. G. Van de Walle, "Oxygen vacancies and donor impurities in β-Ga_2O_3", Appl. Phys. Lett. **97**, 142106 (2010).

[32] T. Gake, Y. Kumagai, and F. Oba, "First-principles study of self-trapped holes and acceptor impurities in Ga_2O_3 polymorphs", Phys. Rev. Materials **3**, 044603 (2019).

[33] Y. Hinuma, T. Gake, and F. Oba, "Band alignment at surfaces and heterointerfaces of Al_2O_3, Ga_2O_3, In_2O_3, and related group-III oxide polymorphs: A first-principles study", Phys. Rev. Materials **3**, 084605 (2019).

[34] R. Schewski, et al., "Step-flow growth in homoepitaxy of β-Ga_2O_3 (100)—The influence of the miscut direction and faceting", APL Mater. **7**, 022515 (2018).

[35] J. B. Varley, and A. Schleife, "Bethe–Salpeter calculation of optical-absorption spectra of In_2O_3 and Ga_2O_3", Semicond. Sci. Technol. **30**, 024010 (2015).

[36] I. Levin, and D. Brandon, "Metastable Alumina Polymorphs: Crystal Structures and Transition Sequences", J. Am. Ceram. Soc. **81**, 1995–2012 (1998).

[37] E. O. Filatova, and A. S. Konashuk, "Interpretation of the changing the band gap of Al_2O_3 depending on its crystalline form: connection with different local symmetries", J. Phys. Chem. C **119**, 20755–20761 (2015).

[38] F. Fuchs, and F. Bechstedt, "Indium-oxide polymorphs from first principles: Quasiparticle electronic states", Phys. Rev. B **77**, 155107 (2008).

[39] P. D. C. King, et al., "Band gap, electronic structure, and surface electron accumulation of cubic and rhombohedral In_2O_3", Phys. Rev. B **79**, 205211 (2009).

[40] J. P. Allen, J. J. Carey, A. Walsh, D. O. Scanlon, and G. W. Watson, "Electronic structures of antimony oxides", J. Phys. Chem. C **117**, 14759–14769 (2013).

[41] S. Yoshioka, et al., "Structures and energetics of Ga_2O_3 polymorphs", J. Phys. Condens. Matter. **19**, 346211 (2007).

[42] F. Litimein, D. Rached, R. Khenata, and H. Baltache, "FPLAPW study of the structural, electronic, and optical properties of Ga_2O_3: Monoclinic and hexagonal phases", J. Alloys Compd. **488**, 148–156 (2009).

[43] C. Sturm, J. Furthmüller, F. Bechstedt, R. Schmidt-Grund, and M. Grundmann, "Dielectric tensor of monoclinic Ga_2O_3 single crystals in the spectral range 0.5–8.5 ev", APL Mater. **3**, 106106 (2015).

[44]C. Sturm, et al., "Dipole analysis of the dielectric function of color dispersive materials: application to monoclinic Ga_2O_3", Phys. Rev. B **94** (2016) `10.1103/PhysRevB.94.035148`.

[45]C. Cocchi, et al., "Atomic signatures of local environment from core-level spectroscopy in $\beta - Ga_2O_3$", Phys. Rev. B **94**, 075147 (2016).

[46]G. Martínez-Criado, et al., "Crossed Ga_2O_3 SnO_2 multiwire architecture: a local structure study with nanometer resolution", Nano Lett. **14**, 5479–5487 (2014).

[47]K. Nishi, et al., "Deconvolution analysis of Ga K-edge XANES for quantification of gallium coordinations in oxide environments", J. Phys. Chem. B **102**, 10190–10195 (1998).

[48]C. Revenant, M. Benwadih, and O. Proux, "Local structure around Zn and Ga in solution-processed In−Ga−Zn−O and implications for electronic properties", Phys. Status Solidi RRL **9**, 652–655 (2015).

[49]I. Tanaka, et al., "Identification of ultradilute dopants in ceramics", Nature Mat. **2**, 541–545 (2003).

[50]V. L. Pool, M. T. Klem, C. L. Chorney, E. A. Arenholz, and Y. U. Idzerda, "Enhanced magnetism of Fe_3O_4 nanoparticles with Ga doping", J. Appl. Phys. **109**, 07B529 (2011).

[51]K.-i. Shimizu, et al., "Influence of local structure on the catalytic activity of gallium oxide for the selective reduction of NO by CH_4", Chem. Commun. 1827–1828 (1996).

[52]F. Bechstedt, and J. Furthmüller, "Influence of screening dynamics on excitons in Ga_2O_3 polymorphs", Appl. Phys. Lett. **114**, 122101 (2019).

[53]T. Onuma, et al., "Electroreflectance study on optical anisotropy in $\beta - Ga_2O_3$", Appl. Phys. Lett. **115**, 231102 (2019).

[54]T. Onuma, et al., "Temperature-dependent exciton resonance energies and their correlation with ir-active optical phonon modes in β-Ga_2O_3 single crystals", Appl. Phys. Lett. **108**, 101904 (2016).

[55]L. Hedin, "New method for calculating the one-particle green's function with application to the electron-gas problem", Phys. Rev. **139**, A796–A823 (1965).

[56]M. S. Hybertsen, and S. G. Louie, "First-principles theory of quasiparticles: calculation of band gaps in semiconductor and insulators", Phys. Rev. Lett. **55**, 1418–1421 (1985).

[57]G. Strinati, "Application of the green's functions method to the study of the optical properties of semiconductors", Riv. Nuovo Cimento **11**, 1–86 (1988).

[58]G. Onida, L. Reining, R. W. Godby, R. Del Sole, and W. Andreoni, "Ab initio calculations of the quasiparticle and absorption spectra of clusters: the sodium tetramer", Phys. Rev. Lett. **75**, 818–821 (1995).

[59]S. Albrecht, G. Onida, and L. Reining, "Ab initio calculation of the quasiparticle spectrum and excitonic effects in Li_2O", Phys. Rev. B **55**, 10278–10281 (1997).

[60] L. X. Benedict, E. L. Shirley, and R. B. Bohn, "Optical absorption of insulators and the electron-hole interaction: an ab initio calculation", Phys. Rev. Lett. **80**, 4514–4517 (1998).

[61] M. Rohlfing, and S. G. Louie, "Electron-hole excitations in semiconductors and insulators", Phys. Rev. Lett. **81**, 2312–2315 (1998).

[62] F. Bechstedt, *Many-body approach to electronic excitations: concepts and applications*, Springer Series in Solid-State Sciences (Springer-Verlag, Berlin Heidelberg, 2015).

[63] R. M. Martin, L. Reining, and D. M. Ceperley, *Interacting electrons: theory and computational approaches* (Cambridge University Press, Cambridge, 2016).

[64] M. Born, and R. Oppenheimer, "Zur quantentheorie der molekeln", Ann. Phys. **389**, 457–484 (1927).

[65] J. Neugebauer, and T. Hickel, "Density functional theory in materials science", Wiley Interdisciplinary Reviews. Computational Molecular Science **3**, 438–448 (2013).

[66] N. Mardirossian, and M. Head-Gordon, "Thirty years of density functional theory in computational chemistry: an overview and extensive assessment of 200 density functionals", Molecular Physics **115**, 2315–2372 (2017).

[67] R. O. Jones, "Density functional theory: Its origins, rise to prominence, and future", Rev. Mod. Phys. **87**, 897–923 (2015).

[68] K. Burke, "Perspective on density functional theory", J. Chem. Phys. **136**, 150901 (2012).

[69] R. M. Martin, *Electronic structure: basic theory and practical methods* (Cambridge University Press, 2004).

[70] F. Giustino, *Materials modelling using density functional theory: properties and predictions* (Oxford University Press, Oxford, New York, 2014).

[71] P. Hohenberg, and W. Kohn, "Inhomogeneous electron gas", Phys. Rev. **136**, B864–B871 (1964).

[72] W. Kohn, and L. J. Sham, "Self-consistent equations including exchange and correlation effects", Phys. Rev. **140**, A1133–A1138 (1965).

[73] J. P. Perdew, and A. Zunger, "Self-interaction correction to density-functional approximations for many-electron systems", Phys. Rev. B **23**, 5048–5079 (1981).

[74] J. P. Perdew, and Y. Wang, "Accurate and simple analytic representation of the electron-gas correlation energy", Phys. Rev. B **45**, 13244–13249 (1992).

[75] U. von Barth, and L. Hedin, "A local exchange-correlation potential for the spin polarized case. i", J. Phys. C **5**, 1629–1642 (1972).

[76] J. P. Perdew, K. Burke, and M. Ernzerhof, "Generalized gradient approximation made simple", Phys. Rev. Lett. **77**, 3865–3868 (1996).

[77] J. P. Perdew, et al., "Restoring the density-gradient expansion for exchange in solids and surfaces", Phys. Rev. Lett. **100**, 136406 (2008).

[78] S. Kümmel, and L. Kronik, "Orbital-dependent density functionals: Theory and applications", Rev. Mod. Phys. **80**, 3–60 (2008).

[79] M. S. Hybertsen, and S. G. Louie, "Electron correlation in semiconductors and insulators: Band gaps and quasiparticle energies", Phys. Rev. B **34**, 5390–5413 (1986).

[80] M. van Schilfgaarde, T. Kotani, and S. Faleev, "Quasiparticle self-consistent GW theory", Phys. Rev. Lett. **96**, 226402 (2006).

[81] J. P. Perdew, R. G. Parr, M. Levy, and J. L. Balduz, "Density-Functional Theory for Fractional Particle Number: Derivative Discontinuities of the Energy", Phys. Rev. Lett. **49**, 1691–1694 (1982).

[82] J. P. Perdew, and M. Levy, "Physical content of the exact Kohn-Sham orbital energies: band gaps and derivative discontinuities", Phys. Rev. Lett. **51**, 1884–1887 (1983).

[83] L. J. Sham, and M. Schlüter, "Density-functional theory of the energy gap", Phys. Rev. Lett. **51**, 1888–1891 (1983).

[84] P. Mori-Sánchez, A. J. Cohen, and W. Yang, "Many-electron self-interaction error in approximate density functionals", J. Chem. Phys. **125**, 201102 (2006).

[85] P. Mori-Sánchez, and A. J. Cohen, "The derivative discontinuity of the exchange-correlation functional", Phys. Chem. Chem. Phys. **16**, 14378–14387 (2014).

[86] P. Mori-Sánchez, "Localization and Delocalization Errors in Density Functional Theory and Implications for Band-Gap Prediction", Phys. Rev. Lett. **100** (2008) `10.1103/PhysRevLett.100.146401`.

[87] T. Schmidt, and S. Kümmel, "One- and many-electron self-interaction error in local and global hybrid functionals", Phys. Rev. B **93**, 165120 (2016).

[88] F. Viñes, O. Lamiel-García, K. Chul Ko, J. Yong Lee, and F. Illas, "Systematic study of the effect of HSE functional internal parameters on the electronic structure and band gap of a representative set of metal oxides", J. Comput. Chem. **38**, 781–789 (2017).

[89] J. Paier, et al., "Screened hybrid density functionals applied to solids", J. Chem. Phys. **124**, 154709 (2006).

[90] M. A. L. Marques, J. Vidal, M. J. T. Oliveira, L. Reining, and S. Botti, "Density-based mixing parameter for hybrid functionals", Phys. Rev. B **83**, 035119 (2011).

[91] M. Gerosa, C. E. Bottani, C. D. Valentin, G. Onida, and G. Pacchioni, "Accuracy of dielectric-dependent hybrid functionals in the prediction of optoelectronic properties of metal oxide semiconductors: a comprehensive comparison with many-body GW and experiments", J. Phys. Condens. Matter. **30**, 044003 (2017).

[92] M. K. Y. Chan, and G. Ceder, "Efficient band gap prediction for solids", Phys. Rev. Lett. **105**, 196403 (2010).

[93] J. P. Perdew, M. Ernzerhof, and K. Burke, "Rationale for mixing exact exchange with density functional approximations", J. Chem. Phys. **105**, 9982–9985 (1996).

[94] C. Adamo, and V. Barone, "Toward reliable density functional methods without adjustable parameters: The PBE0 model", J. Chem. Phys. **110**, 6158–6170 (1999).

[95] A. Seidl, A. Görling, P. Vogl, J. A. Majewski, and M. Levy, "Generalized Kohn-Sham schemes and the band-gap problem", Phys. Rev. B **53**, 3764–3774 (1996).

[96] J. P. Perdew, et al., "Understanding band gaps of solids in generalized Kohn–Sham theory", Proc. Natl. Acad. Sci. USA **114**, 2801–2806 (2017).

[97] J. Heyd, G. E. Scuseria, and M. Ernzerhof, "Hybrid functionals based on a screened Coulomb potential", J. Chem. Phys. **118**, 8207–8215 (2003).

[98] E. Livshits, and R. Baer, "A well-tempered density functional theory of electrons in molecules", Phys. Chem. Chem. Phys. **9**, 2932–2941 (2007).

[99] M. Marques, and E. Gross, "Time-dependent density functional theory", Annual Review of Physical Chemistry **55**, 427–455 (2004).

[100] E. Runge, and E. K. U. Gross, "Density-functional theory for time-dependent systems", Phys. Rev. Lett. **52**, 997–1000 (1984).

[101] S. Sharma, J. K. Dewhurst, and E. K. U. Gross, "Optical response of extended systems using time-dependent density functional theory," *First Principles Approaches to Spectroscopic Properties of Complex Materials*, edited by C. Di Valentin, S. Botti, and M. Cococcioni, (Springer Berlin Heidelberg, Berlin, Heidelberg, 2014), 235.

[102] M. A. L. Marques, et al., *Time-Dependent Density Functional Theory*, Lecture Notes in Physics (Springer-Verlag, Berlin Heidelberg, 2006).

[103] G. Onida, L. Reining, and A. Rubio, "Electronic excitations: density-functional versus many-body Green's-function approaches", Rev. Mod. Phys. **74**, 601–659 (2002).

[104] E. K. U. Gross, and W. Kohn, "Local density-functional theory of frequency-dependent linear response", Phys. Rev. Lett. **55**, 2850–2852 (1985).

[105] E. K. U. Gross, J. F. Dobson, and M. Petersilka, "Density functional theory of time-dependent phenomena," *Density Functional Theory II: Relativistic and Time Dependent Extensions*, edited by R. F. Nalewajski, Topics in Current Chemistry (Springer, Berlin, Heidelberg, 1996), 81.

[106] S. Botti, A. Schindlmayr, R. D. Sole, and L. Reining, "Time-dependent density-functional theory for extended systems", Rep. Prog. Phys. **70**, 357–407 (2007).

[107] V. I. Gavrilenko, and F. Bechstedt, "Optical functions of semiconductors beyond density-functional theory and random-phase approximation", Phys. Rev. B **55**, 4343–4352 (1997).

[108] V. U. Nazarov, G. Vignale, and Y.-C. Chang, "Exact dynamical exchange-correlation kernel of a weakly inhomogeneous electron gas", Phys. Rev. Lett. **102**, 113001 (2009).

[109] V. U. Nazarov, and G. Vignale, "Optics of semiconductors from meta-generalized-gradient-approximation-based time-dependent density-functional theory", Phys. Rev. Lett. **107**, 216402 (2011).

[110] P. E. Trevisanutto, A. Terentjevs, L. A. Constantin, V. Olevano, and F. D. Sala, "Optical spectra of solids obtained by time-dependent density functional theory with the jellium-with-gap-model exchange-correlation kernel", Phys. Rev. B **87**, 205143 (2013).

[111] M. Hellgren, and E. K. U. Gross, "Discontinuous functional for linear-response time-dependent density-functional theory: The exact-exchange kernel and approximate forms", Phys. Rev. A **88**, 052507 (2013).

[112] J. Paier, M. Marsman, and G. Kresse, "Dielectric properties and excitons for extended systems from hybrid functionals", Phys. Rev. B **78**, 121201 (2008).

[113] P. Ghosez, X. Gonze, and R. W. Godby, "Long-wavelength behavior of the exchange-correlation kernel in the Kohn-Sham theory of periodic systems", Phys. Rev. B **56**, 12811–12817 (1997).

[114] R. Stubner, I. V. Tokatly, and O. Pankratov, "Excitonic effects in time-dependent density-functional theory: An analytically solvable model", Phys. Rev. B **70**, 245119 (2004).

[115] U. von Barth, N. E. Dahlen, R. van Leeuwen, and G. Stefanucci, "Conserving approximations in time-dependent density functional theory", Phys. Rev. B **72**, 235109 (2005).

[116] F. Bruneval, F. Sottile, V. Olevano, R. Del Sole, and L. Reining, "Many-body perturbation theory using the density-functional concept: beyond the *GW* approximation", Phys. Rev. Lett. **94**, 186402 (2005).

[117] F. Sottile, V. Olevano, and L. Reining, "Parameter-free calculation of response functions in time-dependent density-functional theory", Phys. Rev. Lett. **91**, 056402 (2003).

[118] G. Adragna, R. Del Sole, and A. Marini, "Ab initio calculation of the exchange-correlation kernel in extended systems", Phys. Rev. B **68**, 165108 (2003).

[119] A. Marini, R. Del Sole, and A. Rubio, "Bound excitons in time-dependent density-functional theory: optical and energy-loss spectra", Phys. Rev. Lett. **91**, 256402 (2003).

[120] S. Botti, et al., "Long-range contribution to the exchange-correlation kernel of time-dependent density functional theory", Phys. Rev. B **69**, 155112 (2004).

[121] S. Rigamonti, et al., "Estimating excitonic effects in the absorption spectra of solids: problems and insight from a guided iteration scheme", Phys. Rev. Lett. **114**, 146402 (2015).

[122] Z.-h. Yang, F. Sottile, and C. A. Ullrich, "Simple screened exact-exchange approach for excitonic properties in solids", Phys. Rev. B **92**, 035202 (2015).

[123] S. Refaely-Abramson, M. Jain, S. Sharifzadeh, J. B. Neaton, and L. Kronik, "Solid-state optical absorption from optimally tuned time-dependent range-separated hybrid density functional theory", Phys. Rev. B **92**, 081204 (2015).

[124]C. D. Pemmaraju, "Valence and core excitons in solids from velocity-gauge real-time TDDFT with range-separated hybrid functionals: An LCAO approach", Computational Condensed Matter **18**, e00348 (2019).

[125]A. L. Fetter, and J. D. Walecka, *Quantum theory of many-particle systems* (Dover Publications Inc., 2003).

[126]P. C. Martin, and J. Schwinger, "Theory of many-particle systems. I", Phys. Rev. **115**, 1342–1373 (1959).

[127]F. J. Dyson, "The S matrix in quantum electrodynamics", Phys. Rev. **75**, 1736–1755 (1949).

[128]E. E. Salpeter, and H. A. Bethe, "A Relativistic Equation for Bound-State Problems", Phys. Rev. **84**, 1232–1242 (1951).

[129]E. E. Salpeter, "Bethe-Salpeter equation (origins)", Scholarpedia **3**, 7483 (2008).

[130]L. Hedin, "New method for calculating the one-function with application to the electron-gas problem", Phys. Rev. **139**, A796–A823 (1965).

[131]D. Golze, M. Dvorak, and P. Rinke, "The GW compendium: a practical guide to theoretical photoemission spectroscopy", Front. Chem. **7** (2019) `10.3389/fchem.2019.00377`.

[132]D. Bohm, and D. Pines, "A collective description of electron interactions. I. magnetic interactions", Phys. Rev. **82**, 625–634 (1951).

[133]D. Pines, and D. Bohm, "A Collective Description of Electron Interactions: II. Collective vs Individual Particle Aspects of the Interactions", Phys. Rev. **85**, 338–353 (1952).

[134]D. Bohm, and D. Pines, "A collective description of electron interactions: III. Coulomb interactions in a degenerate electron gas", Phys. Rev. **92**, 609–625 (1953).

[135]L. Landau, "Theory of the superfluidity of helium II", Phys. Rev. **60**, 356–358 (1941).

[136]I. Tamm, "Relativistic interaction of elementary particles", J. Phys. (USSR) **9**, 449 (1945).

[137]S. M. Dancoff, "Non-adiabatic meson theory of nuclear forces", Phys. Rev. **78**, 382–385 (1950).

[138]M. Rohlfing, and S. G. Louie, "Electron-hole excitations and optical spectra from first principles", Phys. Rev. B **62**, 4927–4944 (2000).

[139]L. X. Benedict, and E. L. Shirley, "Ab initio calculation of $\epsilon_2(\omega)$ including the electron-hole interaction: application to GaN and CaF_2", Phys. Rev. B **59**, 5441–5451 (1999).

[140]T. Sander, E. Maggio, and G. Kresse, "Beyond the Tamm-Dancoff approximation for extended systems using exact diagonalization", Phys. Rev. B **92**, 045209 (2015).

[141]S. Albrecht, L. Reining, R. Del Sole, and G. Onida, "Ab initio calculation of excitonic effects in the optical spectra of semiconductors", Phys. Rev. Lett. **80**, 4510–4513 (1998).

[142]L. X. Benedict, E. L. Shirley, and R. B. Bohn, "Theory of optical absorption in diamond, Si, Ge, and GaAs", Phys. Rev. B **57**, R9385–R9387 (1998).

[143] T. Rangel, S. M. Hamed, F. Bruneval, and J. B. Neaton, "An assessment of low-lying excitation energies and triplet instabilities of organic molecules with an ab initio Bethe-Salpeter equation approach and the Tamm-Dancoff approximation", J. Chem. Phys. **146**, 194108 (2017).

[144] S. Hirata, and M. Head-Gordon, "Time-dependent density functional theory within the Tamm–Dancoff approximation", Chem. Phys. Lett. **314**, 291–299 (1999).

[145] M. J. G. Peach, M. J. Williamson, and D. J. Tozer, "Influence of triplet instabilities in TDDFT", J. Chem. Theory. Comput. **7**, 3578–3585 (2011).

[146] M. Shao, F. H. da Jornada, C. Yang, J. Deslippe, and S. G. Louie, "Structure preserving parallel algorithms for solving the Bethe–Salpeter eigenvalue problem", Linear Algebra Its Appl. **488**, 148–167 (2016).

[147] Y.-M. Byun, and C. A. Ullrich, "Excitons in solids from time-dependent density-functional theory: assessing the Tamm-Dancoff approximation", Computation **5**, 9 (2017).

[148] V. Olevano, and L. Reining, "Excitonic effects on the silicon plasmon resonance", Phys. Rev. Lett. **86**, 5962–5965 (2001).

[149] M. Grüning, A. Marini, and X. Gonze, "Exciton-plasmon states in nanoscale materials: breakdown of the Tamm-Dancoff approximation", Nano Lett. **9**, 2820–2824 (2009).

[150] W. A. Caliebe, J. A. Soininen, E. L. Shirley, C.-C. Kao, and K. Hämäläinen, "Dynamic structure factor of diamond and LiF measured using inelastic x-ray scattering", Phys. Rev. Lett. **84**, 3907–3910 (2000).

[151] S. M. Anderson, B. S. Mendoza, G. Fugallo, and F. Sottile, "Plasmon dispersion in graphite: a comparison of current ab initio methods", Phys. Rev. B **100**, 045205 (2019).

[152] K. K. Rao, T. J. Moravec, J. C. Rife, and R. N. Dexter, "Vacuum ultraviolet reflectivities of LiF, NaF, and KF", Phys. Rev. B **12**, 5937–5950 (1975).

[153] R. M. A. Azzam, and N. M. Bashara, *Ellipsometry and polarized light* (North-Holland, Amsterdam ; New York : New York, 1977).

[154] R. Goldhahn, "Dielectric function of nitride semiconductors: recent experimental results", Act. Phys. Pol. A **104**, 123–147 (2003).

[155] M. Feneberg, et al., "Ordinary dielectric function of corundumlike $\alpha - Ga_2O_3$ from 40 meV to 20 eV", Phys. Rev. Materials **2**, 044601 (2018).

[156] L. Tröger, et al., "Full correction of the self-absorption in soft-fluorescence extended x-ray-absorption fine structure", Phys. Rev. B **46**, 3283–3289 (1992).

[157] D. Vlachos, A. J. Craven, and D. W. McComb, "Specimen charging in x-ray absorption spectroscopy: correction of total electron yield data from stabilized zirconia in the energy range 250–915 eV", J. Synchrotron Rad. **12**, 224–233 (2005).

[158] J. Flick, M. Ruggenthaler, H. Appel, and A. Rubio, "Kohn–Sham approach to quantum electrodynamical density-functional theory: Exact time-dependent effective potentials in real space", Proc. Natl. Acad. Sci. USA **112**, 15285–15290 (2015).

[159] M. Kowalewski, and S. Mukamel, "Manipulating molecules with quantum light", Proc. Natl. Acad. Sci. USA **114**, 3278–3280 (2017).

[160] I. V. Tokatly, "Time-dependent density functional theory for many-electron systems interacting with cavity photons", Phys. Rev. Lett. **110**, 233001 (2013).

[161] H. Walther, B. T. H. Varcoe, B.-G. Englert, and T. Becker, "Cavity quantum electrodynamics", Rep. Prog. Phys. **69**, 1325–1382 (2006).

[162] M. Sindelka, "Derivation of coupled Maxwell-Schrödinger equations describing matter-laser interaction from first principles of quantum electrodynamics", Phys. Rev. A **81**, 033833 (2010).

[163] F. Stern, "Elementary theory of the optical properties of solids," *Solid State Physics*, Vol. 15, edited by F. Seitz, and D. Turnbull, (Academic Press, 1963), 299.

[164] J. C. Maxwell, "VIII. A dynamical theory of the electromagnetic field", Phil. Trans. R. Soc. **155**, 459–512 (1865).

[165] R. Del Sole, and E. Fiorino, "Macroscopic dielectric tensor at crystal surfaces", Phys. Rev. B **29**, 4631–4645 (1984).

[166] V. Ambegaokar, and W. Kohn, "Electromagnetic properties of insulators. I", Phys. Rev. **117**, 423–431 (1960).

[167] R. Kubo, "Statistical-mechanical theory of irreversible processes. I. general theory and simple applications to magnetic and conduction problems", Journal of the Physical Society of Japan **12**, 570–586 (1957).

[168] A. Schindlmayr, and R. W. Godby, "Systematic vertex corrections through iterative solution of Hedin's equations beyond the GW approximation", Phys. Rev. Lett. **80**, 1702–1705 (1998).

[169] K. Sturm, "Dynamic structure factor: an introduction", Z. Naturforsch. A **48**, 233–242 (2014).

[170] W. Schuelke, *Electron dynamics by inelastic x-ray scattering*, Oxford Series on Synchrotron Radiation (Oxford University Press, Oxford, New York, 2007).

[171] P. A. M. Dirac, and N. H. D. Bohr, "The quantum theory of the emission and absorption of radiation", Proc. R. Soc. London A **114**, 243–265 (1927).

[172] M. Blume, "Magnetic scattering of x rays (invited)", J. Appl. Phys. **57**, 3615–3618 (1985).

[173] H. A. Kramers, and W. Heisenberg, "Über die streuung von strahlung durch atome", Z. Phys. **31**, 681–708 (1925).

[174]R. Egerton, *Electron energy-loss spectroscopy in the electron microscope* (Springer US, 2011).

[175]L. J. P. Ament, M. van Veenendaal, T. P. Devereaux, J. P. Hill, and J. van den Brink, "Resonant inelastic x-ray scattering studies of elementary excitations", Rev. Mod. Phys. **83**, 705–767 (2011).

[176]F. Pfaff, et al., "Raman and fluorescence contributions to the resonant inelastic soft x-ray scattering on $LaAlO_3$/$SrTiO_3$ heterostructures", Phys. Rev. B **97**, 035110 (2018).

[177]H. Y. Huang, et al., "Raman and fluorescence characteristics of resonant inelastic x-ray scattering from doped superconducting cuprates", Sci. Rep. **6**, 1–7 (2016).

[178]J. A. Carlisle, et al., "Band-structure and core-hole effects in resonant inelastic soft-x-ray scattering: Experiment and theory", Phys. Rev. B **59**, 7433–7445 (1999).

[179]M. van Veenendaal, X. Liu, M. H. Carpenter, and S. P. Cramer, "Observation of *dd* excitations in NiO and $NiCl_2$ using *K*-edge resonant inelastic x-ray scattering", Phys. Rev. B **83**, 045101 (2011).

[180]F. Forte, L. J. P. Ament, and J. van den Brink, "Single and double orbital excitations probed by resonant inelastic x-ray scattering", Phys. Rev. Lett. **101**, 106406 (2008).

[181]L. J. Sham, and T. M. Rice, "Many-particle derivation of the effective-mass equation for the wannier exciton", Phys. Rev. **144**, 708–714 (1966).

[182]F. Bechstedt, R. Endeblein, and M. Koch, "Theory of core excitons in semiconductors", Phys. Status Solidi B **99**, 61–70 (1980).

[183]G. Strinati, "Dynamical shift and broadening of core excitons in semiconductors", Phys. Rev. Lett. **49**, 1519–1522 (1982).

[184]H. Stolz, "Dynamical theory of the optical and energy loss properties of the crystal electron system", Phys. Status Solidi B **32**, 631–644 (1969).

[185]R. Zimmermann, "Influence of the non-hermitean splitting terms on excitonic spectra", Phys. Status Solidi B **41**, 23–32 (1970).

[186]R. Zimmermann, "Possibility of the excitonic phase in insulators", Phys. Status Solidi B **39**, 95–107 (1970).

[187]W. Hanke, and L. J. Sham, "Local-field and excitonic effects in the optical spectrum of a covalent crystal", Phys. Rev. B **12**, 4501–4511 (1975).

[188]W. Hanke, and L. J. Sham, "Many-particle effects in the optical excitations of a semiconductor", Phys. Rev. Lett. **43**, 387–390 (1979).

[189]W. Hanke, and L. J. Sham, "Many-particle effects in the optical spectrum of a semiconductor", Phys. Rev. B **21**, 4656–4673 (1980).

[190]W. Schäfer, and M. Schreiber, "Ab initio calculation of many-particle effects in the optical spectra of semiconductors", Solid State Commun. **38**, 1241–1244 (1981).

[191] S. Albrecht, G. Onida, L. Reining, and R. Del Sole, "Ab initio calculation of excitonic effects in realistic materials", Comp. Mater. Sci. Computational Modelling of Issues in Materials Science **10**, 356–361 (1998).

[192] M. Rohlfing, and S. G. Louie, "Optical excitations in conjugated polymers", Phys. Rev. Lett. **82**, 1959–1962 (1999).

[193] J.-W. van der Horst, P. A. Bobbert, M. A. J. Michels, G. Brocks, and P. J. Kelly, "Ab initio calculation of the electronic and optical excitations in polythiophene: effects of intra- and interchain screening", Phys. Rev. Lett. **83**, 4413–4416 (1999).

[194] A. Ruini, et al., "Ab-initio study of Coulomb-correlated optical properties in conjugated polymers", Synthetic Metals **119**, 257–258 (2001).

[195] A. Ruini, M. J. Caldas, G. Bussi, and E. Molinari, "Solid state effects on exciton states and optical properties of PPV", Phys. Rev. Lett. **88**, 206403 (2002).

[196] G. Bussi, et al., "Interchain interaction and Davydov splitting in polythiophene crystals: An ab initio approach", Appl. Phys. Lett. **80**, 4118–4120 (2002).

[197] P. Puschnig, and Claudia Ambrosch-Draxl, "Suppression of electron-hole correlations in 3d polymer materials", Phys. Rev. Lett. **89**, 56405 (2002).

[198] K. Hummer, P. Puschnig, and C. Ambrosch-Draxl, "Lowest optical excitations in molecular crystals: bound excitons versus free electron-hole pairs in anthracene", Phys. Rev. Lett. **92**, 147402 (2004).

[199] M. L. Tiago, and J. R. Chelikowsky, "First-principles GW–BSE excitations in organic molecules", Solid State Commun. **136**, 333–337 (2005).

[200] C. Ambrosch-Draxl, D. Nabok, P. Puschnig, and C. Meisenbichler, "The role of polymorphism in organic thin films: oligoacenes investigated from first principles", New. J. Phys. **11**, 125010 (2009).

[201] K. Hummer, and C. Ambrosch-Draxl, "Oligoacene exciton binding energies: Their dependence on molecular size", Phys. Rev. B **71**, 081202 (2005).

[202] J. C. Grossman, M. Rohlfing, L. Mitas, S. G. Louie, and M. L. Cohen, "High accuracy many-body calculational approaches for excitations in molecules", Phys. Rev. Lett. **86**, 472–475 (2001).

[203] E. L. Shirley, "Ab initio inclusion of electron-hole attraction: application to x-ray absorption and resonant inelastic x-ray scattering", Phys. Rev. Lett. **80**, 794–797 (1998).

[204] J. A. Soininen, and E. L. Shirley, "Scheme to calculate core hole–electron interactions in solids", Phys. Rev. B **64**, 165112 (2001).

[205] J. J. Rehr, J. A. Soininen, and E. L. Shirley, "Final-state rule vs the Bethe-Salpeter equation for deep-core x-ray absorption spectra", Phys. Scr. **2005**, 207 (2005).

[206] E. L. Shirley, "Core and final-state excitonic effects and resonant inelastic X-ray scattering in s–p bonded solids", J. Phys. Chem. Sol. **61**, 445–447 (2000).

[207] E. L. Shirley, "Theory and simulation of resonant inelastic x-ray scattering in s–p bonded systems: graphite, hexagonal boron nitride, diamond, and cubic boron nitride", J. Electron Spectrosc. Relat. Phenom. **110-111**, 305–321 (2000).

[208] E. L. Shirley, et al., "Modeling final-state interaction effects in inelastic X-ray scattering from solids: resonant and non-resonant", J. Electron Spectrosc. Relat. Phenom. **114-116**, 939–946 (2001).

[209] John Vinson, *Bethe-Salpeter equation approach for calculations of x-ray spectra*, PhD thesis (University of Washington, 2012).

[210] J. Vinson, T. Jach, M. Müller, R. Unterumsberger, and B. Beckhoff, "Resonant x-ray emission of hexagonal boron nitride", Phys. Rev. B **96**, 205116 (2017).

[211] J. Vinson, T. Jach, M. Müller, R. Unterumsberger, and B. Beckhoff, "Resonant x-ray emission and valence-band lifetime broadening in $LiNO_3$", Phys. Rev. B **100**, 085143 (2019).

[212] S. Albrecht, *Optical absorption spectra of semiconductors and insulators: ab initio calculation of many-body effects*, PhD thesis (Ecole Polytechnique, France, 1999).

[213] G. Bussi, "Effects of the electron–hole interaction on the optical properties of materials: the Bethe–Salpeter equation", Phys. Scr. **2004**, 141 (2004).

[214] H. M. Lawler, et al., "Optical to uv spectra and birefringence of SiO_2 and TiO_2: first-principles calculations with excitonic effects", Phys. Rev. B **78**, 205108 (2008).

[215] A. Marini, C. Hogan, M. Grüning, and D. Varsano, "Yambo: an ab initio tool for excited state calculations", Comput. Phys. Commun. **180**, 1392–1403 (2009).

[216] D. Sangalli, et al., "Many-body perturbation theory calculations using the yambo code", J. Phys. Condens. Matter. **31**, 325902 (2019).

[217] P. Cudazzo, M. Gatti, A. Rubio, and F. Sottile, "Frenkel versus charge-transfer exciton dispersion in molecular crystals", Phys. Rev. B **88**, 195152 (2013).

[218] P. Cudazzo, et al., "Exciton band structure in two-dimensional materials", Phys. Rev. Lett. **116**, 066803 (2016).

[219] G. Fugallo, et al., "Exciton energy-momentum map of hexagonal boron nitride", Phys. Rev. B **92**, 165122 (2015).

[220] M. Gatti, and F. Sottile, "Exciton dispersion from first principles", Phys. Rev. B **88**, 155113 (2013).

[221] J. Koskelo, et al., "Excitons in van der Waals materials: From monolayer to bulk hexagonal boron nitride", Phys. Rev. B **95**, 035125 (2017).

[222] D. R. Hamann, M. Schlüter, and C. Chiang, "Norm-conserving pseudopotentials", Phys. Rev. Lett. **43**, 1494–1497 (1979).

[223]D. R. Hamann, "Generalized norm-conserving pseudopotentials", Phys. Rev. B **40**, 2980–2987 (1989).

[224]P. Schwerdtfeger, "The pseudopotential approximation in electronic structure theory", ChemPhysChem **12**, 3143–3155 (2011).

[225]P. Puschnig, and C. Ambrosch-Draxl, "Optical absorption spectra of semiconductors and insulators including electron-hole correlations: an ab initio study within the LAPW method", Phys. Rev. B **66**, 165105 (2002).

[226]K. Gilmore, et al., "Efficient implementation of core-excitation Bethe–Salpeter equation calculations", Comput. Phys. Commun. **197**, 109–117 (2015).

[227]J. Vinson, T. Jach, M. Müller, R. Unterumsberger, and B. Beckhoff, "Quasiparticle lifetime broadening in resonant x-ray scattering of NH_4NO_3", Phys. Rev. B **94**, 035163 (2016).

[228]J. Vinson, J. J. Rehr, J. J. Kas, and E. L. Shirley, "Bethe-salpeter equation calculations of core excitation spectra", Phys. Rev. B **83**, 115106 (2011).

[229]P. E. Blöchl, "Projector augmented-wave method", Phys. Rev. B **50**, 17953–17979 (1994).

[230]N. A. W. Holzwarth, A. R. Tackett, and G. E. Matthews, "A projector augmented wave (PAW) code for electronic structure calculations, part I: atompaw for generating atom-centered functions", Comput. Phys. Commun. **135**, 329–347 (2001).

[231]E. L. Shirley, "Ti 1s pre-edge features in rutile: a Bethe-Salpeter calculation", J. Electron Spectrosc. Relat. Phenom. **136**, 77–83 (2004).

[232]O. K. Andersen, "Linear methods in band theory", Phys. Rev. B **12**, 3060–3083 (1975).

[233]D. D. Koelling, and G. O. Arbman, "Use of energy derivative of the radial solution in an augmented plane wave method: application to copper", J. Phys. F: Met. Phys. **5**, 2041–2054 (1975).

[234]D. Singh, "Ground-state properties of lanthanum: Treatment of extended-core states", Phys. Rev. B **43**, 6388–6392 (1991).

[235]E. Sjöstedt, L. Nordström, and D. J. Singh, "An alternative way of linearizing the augmented plane-wave method", Solid State Commun. **114**, 15–20 (2000).

[236]R. Laskowski, N. E. Christensen, G. Santi, and C. Ambrosch-Draxl, "Ab initio calculations of excitons in GaN", Phys. Rev. B **72**, 035204 (2005).

[237]C. Cocchi, and C. Draxl, "Bound excitons and many-body effects in x-ray absorption spectra of azobenzene-functionalized self-assembled monolayers", Phys. Rev. B **92**, 205105 (2015).

[238]R. Laskowski, and P. Blaha, "Understanding the $L_{2,3}$ x-ray absorption spectra of early 3d transition elements", Phys. Rev. B **82**, 205104 (2010).

[239] C. Vorwerk, C. Cocchi, and C. Draxl, "Addressing electron-hole correlation in core excitations of solids: an all-electron many-body approach from first principles", Phys. Rev. B **95**, 155121 (2017).

[240] C. Draxl, and C. Cocchi, "Exciting core-level spectroscopy", arXiv preprint arXiv:1709.02288 (2017).

[241] W. Olovsson, I. Tanaka, T. Mizoguchi, P. Puschnig, and C. Ambrosch-Draxl, "All-electron Bethe-Salpeter calculations for shallow-core x-ray absorption near-edge structures", Phys. Rev. B **79**, 041102 (2009).

[242] W. Olovsson, I. Tanaka, P. Puschnig, and C. Ambrosch-Draxl, "Near-edge structures from first principles all-electron Bethe–Salpeter equation calculations", J. Phys. Condens. Matter. **21**, 104205 (2009).

[243] W. Olovsson, et al., "Al $L_{2,3}$ edge x-ray absorption spectra in III-V semiconductors: Many-body perturbation theory in comparison with experiment", Phys. Rev. B **83**, 195206 (2011).

[244] W. Olovsson, et al., "The Be K-edge in beryllium oxide and chalcogenides: soft x-ray absorption spectra from first-principles theory and experiment", J. Phys. Condens. Matter. **25**, 315501 (2013).

[245] C. Vorwerk, et al., "Exciton-dominated core-level absorption spectra of hybrid organic–inorganic lead halide perovskites", J. Phys. Chem. Lett. **9**, 1852–1858 (2018).

[246] R. Haydock, "The recursive solution of the Schrodinger equation," *Solid State Physics*, Vol. 35, edited by H. Ehrenreich, F. Seitz, and D. Turnbull, (Academic Press, 1980), 215.

[247] R. Haydock, "The recursive solution of the Schrödinger equation", Comput. Phys. Commun. **20**, 11–16 (1980).

[248] W. G. Schmidt, P. H. Hahn, and F. Bechstedt, "Excitonic and local-field effects in optical spectra from real-space time-domain calculations," High Performance Computing in Science and Engineering '02, edited by E. Krause, and W. Jäger, (2003), 133.

[249] J. Deslippe, et al., "BerkeleyGW: A massively parallel computer package for the calculation of the quasiparticle and optical properties of materials and nanostructures", Comput. Phys. Commun. **183**, 1269–1289 (2012).

[250] F. Sottile, V. Olevano, L. Reining, G. Onida, and S. Albrecht, "The exc code. solution of the bethe-salpeter equation",

[251] M. Giantomassi, et al., "Electronic properties of interfaces and defects from many-body perturbation theory: Recent developments and applications", Phys. Status Solidi B **248**, 275–289 (2011).

[252] M. Govoni, and G. Galli, "Large scale GW calculations", J. Chem. Theory. Comput. **11**, 2680–2696 (2015).

[253] S. Sagmeister, and C. Ambrosch-Draxl, "Time-dependent density functional theory versus Bethe–Salpeter equation: an all-electron study", Phys. Chem. Chem. Phys. **11**, 4451 (2009).

[254] A. Gulans, et al., "Exciting: a full-potential all-electron package implementing density-functional theory and many-body perturbation theory", J. Phys. Condens. Matter. **26**, 363202 (2014).

[255] V. Blum, et al., "Ab initio molecular simulations with numeric atom-centered orbitals", Comput. Phys. Commun. **180**, 2175–2196 (2009).

[256] C. Liu, et al., "All-electron ab initio Bethe-Salpeter equation approach to neutral excitations in molecules with numeric atom-centered orbitals", J. Chem. Phys. **152**, 044105 (2020).

[257] X. Blase, C. Attaccalite, and V. Olevano, "First-principles GW calculations for fullerenes, porphyrins, phtalocyanine, and other molecules of interest for organic photovoltaic applications", Phys. Rev. B **83**, 115103 (2011).

[258] F. Bruneval, et al., "Molgw 1: Many-body perturbation theory software for atoms, molecules, and clusters", Comput. Phys. Commun. **208**, 149–161 (2016).

[259] M. L. Tiago, and J. R. Chelikowsky, "Optical excitations in organic molecules, clusters, and defects studied by first-principles Green's function methods", Phys. Rev. B **73**, 205334 (2006).

[260] M. J. van Setten, F. Weigend, and F. Evers, "The GW-method for quantum chemistry applications: theory and implementation", J. Chem. Theory. Comput. **9**, 232–246 (2013).

[261] B. Aurich, *Bethe-salpeter equation formalism beyond the Tamm-Dancoff approximation and zero momentum transfer*, Master thesis (Humbolt-Universität Berlin, 2017).

[262] Y. Ma, et al., "Soft-x-ray resonant inelastic scattering at the C K edge of diamond", Phys. Rev. Lett. **69**, 2598–2601 (1992).

[263] P. D. Johnson, and Y. Ma, "Band structure and x-ray resonant inelastic scattering", Phys. Rev. B **49**, 5024–5027 (1994).

[264] J. J. Jia, et al., "Resonant inelastic x-ray scattering in hexagonal boron nitride observed by soft-x-ray fluorescence spectroscopy", Phys. Rev. Lett. **76**, 4054–4057 (1996).

[265] V. N. Strocov, et al., "Band structure effects in nitrogen K-edge resonant inelastic x-ray scattering from GaN", Phys. Status Solidi B **241**, R27–R29 (2004).

[266] V. N. Strocov, et al., "Momentum selectivity and anisotropy effects in the nitrogen K-edge resonant inelastic x-ray scattering from gan", Phys. Rev. B **72**, 085221 (2005).

[267] Y. Nisikawa, M. Ibuki, and M. Usuda, "Momentum-dependent resonant inelastic x-ray scattering at the Si K edge of 3C-SiC: a theoretical study on a relation between spectra and valence band dispersion", Physica B: Condensed Matter **405**, 1415–1422 (2010).

[268] J. Vinson, and J. J. Rehr, "Ab initio Bethe-Salpeter calculations of the x-ray absorption spectra of transition metals at the L-shell edges", Phys. Rev. B **86**, 195135 (2012).

[269] Y. Noguchi, M. Hiyama, H. Akiyama, Y. Harada, and N. Koga, "First-principles investigation of strong excitonic effects in oxygen 1s X-ray absorption spectra", J. Chem. Theory. Comput. **11**, 1668–1673 (2015).

[270] F. Fossard, et al., "Quantitative first-principles calculations of valence and core excitation spectra of solid C_{60}", Phys. Rev. B **95**, 115112 (2017).

[271] K. D. Nanda, and A. I. Krylov, "Visualizing the contributions of virtual states to two-photon absorption cross sections by natural transition orbitals of response transition density matrices", J. Phys. Chem. Lett. **8**, 3256–3265 (2017).

[272] K. D. Nanda, M. L. Vidal, R. Faber, S. Coriani, and A. I. Krylov, "How to stay out of trouble in RIXS calculations within equation-of-motion coupled-cluster damped response theory? Safe hitchhiking in the excitation manifold by means of core–valence separation", Phys. Chem. Chem. Phys. **22**, 2629–2641 (2020).

[273] D. R. Mortensen, et al., "Benchmark results and theoretical treatments for valence-to-core x-ray emission spectroscopy in transition metal compounds", Phys. Rev. B **96**, 125136 (2017).

[274] F. D. Vila, T. Jach, W. T. Elam, J. J. Rehr, and J. D. Denlinger, "X-ray emission spectroscopy of nitrogen-rich compounds", J. Phys. Chem. A **115**, 3243–3250 (2011).

[275] T. Kotani, and M. van Schilfgaarde, "All-electron gw approximation with the mixed basis expansion based on the full-potential lmto method", Solid State Commun. **121**, 461–465 (2002).

[276] C. Friedrich, S. Blügel, and A. Schindlmayr, "Efficient implementation of the GW approximation within the all-electron flapw method", Phys. Rev. B **81**, 125102 (2010).

[277] H. Jiang, et al., "Fhi-gap: a GW code based on the all-electron augmented plane wave method", Comput. Phys. Commun. **184**, 348–366 (2013).

[278] D. Nabok, A. Gulans, and C. Draxl, "Accurate all-electron G_0W_0 quasiparticle energies employing the full-potential augmented plane-wave method", Phys. Rev. B **94**, 035118 (2016).

[279] S. Sagmeister, *Excitonic effects in solids*, PhD thesis (2009).

[280] P. Puschnig, *Excitonic effects in organic semi-conductors*, PhD thesis (2002).

[281] C. Rödl, F. Fuchs, J. Furthmüller, and F. Bechstedt, "Ab initio theory of excitons and optical properties for spin-polarized systems: application to antiferromagnetic MnO", Phys. Rev. B **77**, 184408 (2008).

[282] H. Ehrenreich, and M. H. Cohen, "Self-consistent field approach to the many-electron problem", Phys. Rev. **115**, 786–790 (1959).

[283]F. Furche, "On the density matrix based approach to time-dependent density functional response theory", J. Chem. Phys. **114**, 5982–5992 (2001).

[284]A. Kotani, and S. Shin, "Resonant inelastic x-ray scattering spectra for electrons in solids", Rev. Mod. Phys. **73**, 203–246 (2001).

[285]S. Eisebitt, et al., "Resonant inelastic soft X-ray scattering at the si L_3 edge: experiment and theory", J. Electron Spectrosc. Relat. Phenom. **93**, 245–250 (1998).

[286] The HDF Group, "Hierarchical data format, version 5", 1997.

[287]P. Virtanen, et al., "SciPy 1.0: Fundamental algorithms for scientific computing in python", Nature Methods **17**, 261–272 (2020).

[288]T. E. Oliphant, "Python for scientific computing", Computing in Science Engineering **9**, 10–20 (2007).

[289]S. van der Walt, S. C. Colbert, and G. Varoquaux, "The NumPy array: a structure for efficient numerical computation", Computing in Science Engineering **13**, 22–30 (2011).

[290]J. D. Hunter, "Matplotlib: a 2D graphics environment", Computing in Science Engineering **9**, 90–95 (2007).

[291]L. Dagum, and R. Menon, "OpenMP: an industry standard API for shared-memory programming", IEEE Computational Science and Engineering **5**, 46–55 (1998).

[292]E. Lusk, and W. Gropp, "The MPI message-passing interface standard: overview and status," *Advances in Parallel Computing*, Vol. 10, edited by J. J. Dongarra, G. R. Joubert, L. Grandinetti, and J. Kowalik, High Performance Computing (North-Holland, 1995), 265.

[293]E. Anderson, et al., *Lapack users' guide*, , Third (Society for Industrial and Applied Mathematics, Philadelphia, PA, 1999).

[294]F. d. Groot, "Multiplet effects in x-ray spectroscopy", Coord. Chem. Rev. **249**, 31–63 (2005).

[295]A. Kotani, H. Ogasawara, K. Okada, B. T. Thole, and G. A. Sawatzky, "Theory of multiplet structure in 4d core photoabsorption spectra of CeO_2", Phys. Rev. B **40**, 65–73 (1989).

[296]M. Matsumoto, et al., "Resonant photoemission study of CeO_2", Phys. Rev. B **50**, 11340–11346 (1994).

[297]R. A. Gordon, et al., "High multipole transitions in NIXS: valence and hybridization in 4f systems", Europhys. Lett. **81**, 26004 (2007).

[298]E. Wuilloud, B. Delley, W. Schneider, and Y. Baer, "Spectroscopic evidence for localized and extended f-symmetry states in CeO_2", Phys. Rev. Lett. **53**, 202–205 (1984).

[299]V. I. Anisimov, J. Zaanen, and O. K. Andersen, "Band theory and mott insulators: Hubbard U instead of Stoner I", Phys. Rev. B **44**, 943–954 (1991).

[300]V. I. Anisimov, I. V. Solovyev, M. A. Korotin, M. T. Czyżyk, and G. A. Sawatzky, "Density-functional theory and NiO photoemission spectra", Phys. Rev. B **48**, 16929–16934 (1993).

[301] I. V. Solovyev, P. H. Dederichs, and V. I. Anisimov, "Corrected atomic limit in the local-density approximation and the electronic structure of d impurities in Rb", Phys. Rev. B **50**, 16861–16871 (1994).

[302] H. Jiang, R. I. Gomez-Abal, P. Rinke, and M. Scheffler, "Localized and itinerant states in lanthanide oxides united by $GW@LDA + U$", Phys. Rev. Lett. **102**, 126403 (2009).

[303] H. Jiang, "Revisiting the GW approach to d- and f-electron oxides", Phys. Rev. B **97**, 245132 (2018).

[304] C. Loschen, J. Carrasco, K. M. Neyman, and F. Illas, "First-principles LDA+U and GGA+U study of cerium oxides: dependence on the effective U parameter", Phys. Rev. B **75**, 035115 (2007).

[305] F. Fuchs, J. Furthmüller, F. Bechstedt, M. Shishkin, and G. Kresse, "Quasiparticle band structure based on a generalized Kohn-Sham scheme", Phys. Rev. B **76**, 115109 (2007).

[306] D. Golze, J. Wilhelm, M. J. van Setten, and P. Rinke, "Core-level binding energies from GW: an efficient full-frequency approach within a localized basis", J. Chem. Theory. Comput. **14**, 4856–4869 (2018).

[307] H. R. Phillip, and E. A. Taft, "Kramers-Kronig analysis of reflectance data for diamond", Phys. Rev. **136**, A1445–A1448 (1964).

[308] A. V. Sokolov, et al., "Band dispersion of MgB2, graphite and diamond from resonant inelastic scattering", J. Phys. Condens. Matter. **15**, 2081–2089 (2003).

[309] P. H. Hahn, K. Seino, W. G. Schmidt, J. Furthmüller, and F. Bechstedt, "Quasiparticle and excitonic effects in the optical spectra of diamond, SiC, Si, GaP, GaAs, InP, and AlN", Phys. Status Solidi B **242**, 2720–2728 (2005).

[310] W. Hanke, and L. J. Sham, "Dielectric response in the wannier representation: application to the optical spectrum of diamond", Phys. Rev. Lett. **33**, 582–585 (1974).

[311] D. Rocca, Y. Ping, R. Gebauer, and G. Galli, "Solution of the Bethe-Salpeter equation without empty electronic states: application to the absorption spectra of bulk systems", Phys. Rev. B **85**, 045116 (2012).

[312] M. Taillefumier, D. Cabaret, A.-M. Flank, and F. Mauri, "X-ray absorption near-edge structure calculations with the pseudopotentials: application to the K edge in diamond and α-quartz", Phys. Rev. B **66**, 195107 (2002).

[313] C. D. Clark, P. J. Dean, P. V. Harris, and W. C. Price, "Intrinsic edge absorption in diamond", Proc. R. Soc. London A **277**, 312–329 (1964).

[314] R. A. Roberts, and W. C. Walker, "Optical study of the electronic structure of diamond", Phys. Rev. **161**, 730–735 (1967).

[315] A. Kikas, et al., "Resonant inelastic x-ray scattering at the f 1s photoabsorption edge in LiF: interplay of excitonic and conduction states, and Stokes' doubling", Phys. Rev. B **70**, 085102 (2004).

[316] M. Magnuson, et al., "X-ray fluorescence spectra of metals excited below threshold", Phys. Rev. B **68**, 045119 (2003).

[317] R. Feifel, et al., "Role of stray light in the formation of high-resolution resonant photoelectron spectra: an experimental and theoretical study of N_2", J. Electron Spectrosc. Relat. Phenom. **134**, 49–65 (2004).

[318] R. Roy, V. G. Hill, and E. F. Osborn, "Polymorphism of Ga_2O_3 and the system Ga_2O_3-H_2O", J. Am. Chem. Soc. **74**, 719–722 (1952).

[319] M. Zinkevich, and F. Aldinger, "Thermodynamic assessment of the gallium-oxygen system", J. Am. Ceram. Soc. **87**, 683–691 (2004).

[320] S. Penner, et al., "Physico-chemical properties of unusual Ga2O3 polymorphs", Monatshefte für Chemie - Chemical Monthly **147**, 289–300 (2016).

[321] H. Y. Playford, A. C. Hannon, E. R. Barney, and R. I. Walton, "Structures of uncharacterised polymorphs of gallium oxide from total neutron diffraction", Chem. Eur. J. **19**, 2803–2813 (2013).

[322] S. Geller, "Crystal structure of B-Ga_2O_3", J. Chem. Phys. **33**, 676–684 (1960).

[323] J. Åhman, G. Svensson, and J. Albertsson, "A reinvestigation of β-gallium oxide", Acta Crystallogr. C **52**, 1336–1338 (1996).

[324] I. Cora, et al., "The real structure of ϵ-Ga_2O_3 and its relation to κ-phase", CrystEngComm **19**, 1509–1516 (2017).

[325] K. E. Lipinska-Kalita, P. E. Kalita, O. A. Hemmers, and T. Hartmann, "Equation of state of gallium oxide to 70 GPa: Comparison of quasihydrostatic and nonhydrostatic compression", Phys. Rev. B **77**, 094123 (2008).

[326] W. Setyawan, and S. Curtarolo, "High-throughput electronic band structure calculations: Challenges and tools", Comp. Mater. Sci. **49**, 299–312 (2010).

[327] K. A. Mengle, G. Shi, D. Bayerl, and E. Kioupakis, "First-principles calculations of the near-edge optical properties of β-Ga_2O_3", Appl. Phys. Lett. **109**, 212104 (2016).

[328] S. Tillack, A. Gulans, and C. Draxl, "Maximally localized Wannier functions within the (L)APW+LO method", arXiv:1908.11156 [cond-mat] (2019).

[329] A. Ratnaparkhe, and W. R. L. Lambrecht, "Quasiparticle self-consistent GW band structure of β-Ga_2O_3 and the anisotropy of the absorption onset", Appl. Phys. Lett. **110**, 132103 (2017).

[330] T. Wang, W. Li, C. Ni, and A. Janotti, "Band gap and band offset of Ga_2O_3 and $(Al_xGa_{1-x})_2O_3$ alloys", Phys. Rev. Appl. **10**, 011003 (2018).

[331] M. Mohamed, et al., "The electronic structure of β-Ga_2O_3", Appl. Phys. Lett. **97**, 211903 (2010).

[332] A. Segura, L. Artús, R. Cuscó, R. Goldhahn, and M. Feneberg, "Band gap of corundumlike $\alpha - Ga_2O_3$ determined by absorption and ellipsometry", Phys. Rev. Materials **1**, 024604 (2017).

[333] D. Shinohara, and S. Fujita, "Heteroepitaxy of corundum-structured α-Ga_2O_3 thin films on α-Al_2O_3 substrates by ultrasonic mist chemical vapor deposition", Jpn. J. Appl. Phys. **47**, 7311 (2008).

[334] M. Orita, H. Ohta, M. Hirano, and H. Hosono, "Deep-ultraviolet transparent conductive β-Ga_2O_3 thin films", Appl. Phys. Lett. **77**, 4166–4168 (2000).

[335] C. Janowitz, et al., "Experimental electronic structure of In_2O_3 and Ga_2O_3", New. J. Phys. **13**, 085014 (2011).

[336] F. Ricci, et al., "Theoretical and experimental investigation of optical absorption anisotropy in β-Ga_2O_3", J. Phys. Condens. Matter. **28**, 224005 (2016).

[337] T. Harwig, F. Kellendonk, and S. Slappendel, "The ultraviolet luminescence of β-galliumsesquioxide", J. Phys. Chem. Sol. **39**, 675–680 (1978).

[338] K. Shimamura, E. G. Víllora, T. Ujiie, and K. Aoki, "Excitation and photoluminescence of pure and Si-doped β-Ga_2O_3 single crystals", Appl. Phys. Lett. **92**, 201914 (2008).

[339] S. Yamaoka, and M. Nakayama, "Evidence for formation of self-trapped excitons in a β-Ga_2O_3 single crystal", Phys. Status Solidi C **13**, 93–96 (2016).

[340] J. K. Kübler, "The exciton binding energy of III–V semiconductor compounds", Phys. Status Solidi B **35**, 189–195 (1969).

[341] G. H. Wannier, "The structure of electronic excitation levels in insulating crystals", Phys. Rev. **52**, 191–197 (1937).

[342] N. F. Mott, "Conduction in polar crystals. II. The conduction band and ultra-violet absorption of alkali-halide crystals", Transactions of the Faraday Society **34**, 500–506 (1938).

[343] V. Saile, and E. E. Koch, "Bulk and surface excitons in solid neon", Phys. Rev. B **20**, 784–794 (1979).

[344] D. M. Roessler, and W. C. Walker, "Electronic spectrum of crystalline lithium fluoride", J. Phys. Chem. Sol. **28**, 1507–1515 (1967).

[345] A. Baldereschi, and N. O. Lipari, "Direct exciton spectrum in diamond and zinc-blende semiconductors", Phys. Rev. Lett. **25**, 373–376 (1970).

[346] J. Suntivich, et al., "Estimating hybridization of transition metal and oxygen states in perovskites from O K-edge x-ray absorption spectroscopy", J. Phys. Chem. C **118**, 1856–1863 (2014).

[347] K. Tomita, T. Miyata, W. Olovsson, and T. Mizoguchi, "Strong excitonic interactions in the oxygen K-edge of perovskite oxides", Ultramicroscopy, FEMMS 2015 **178**, 105–111 (2017).

[348]J. J. Kas, J. J. Rehr, and J. B. Curtis, "Particle-hole cumulant approach for inelastic losses in x-ray spectra", Phys. Rev. B **94**, 035156 (2016).

[349]J. J. Kas, et al., "Many-pole model of inelastic losses in x-ray absorption spectra", Phys. Rev. B **76**, 195116 (2007).

[350]J. J. Kas, J. J. Rehr, J. A. Soininen, and P. Glatzel, "Real-space Green's function approach to resonant inelastic x-ray scattering", Phys. Rev. B **83**, 235114 (2011).

[351]J. A. Bearden, and A. F. Burr, "Reevaluation of x-ray atomic energy levels", Rev. Mod. Phys. **39**, 125–142 (1967).

[352]C. Vorwerk, and C. Draxl, *NOMAD dataset of calculations for diamond*, `https://dx.doi.org/10.17172/NOMAD/2020.07.14-1` (2020).

[353]C. Vorwerk, and C. Draxl, *NOMAD dataset of calculations for LiF*, `https://dx.doi.org/10.17172/NOMAD/2020.07.14-2` (2020).

[354]C. Vorwerk, and C. Draxl, *NOMAD dataset of calculations for* CeO_2, `https://dx.doi.org/10.17172/NOMAD/2020.07.14-6` (2020).

[355]C. Vorwerk, and C. Draxl, *NOMAD dataset of calculations for* $\alpha - Ga_2O_3$, `https://dx.doi.org/10.17172/NOMAD/2020.07.14-3` (2020).

[356]C. Vorwerk, and C. Draxl, *NOMAD dataset of calculations for* $\beta - Ga_2O_3$, `https://dx.doi.org/10.17172/NOMAD/2020.07.14-4` (2020).

[357]C. Vorwerk, and C. Draxl, *NOMAD dataset of calculations for* $\epsilon - Ga_2O_3$, `https://dx.doi.org/10.17172/NOMAD/2020.07.14-5` (2020).

Publication List

[358]J. E. N. Swallow, et al., "Influence of polymorphism on the electronic structure of Ga_2O_3", arXiv:2005.13395 [cond-mat] (2020).

[359]C. Vorwerk, B. Aurich, C. Cocchi, and C. Draxl, "Bethe–salpeter equation for absorption and scattering spectroscopy: implementation in the exciting code", Electron. Struct. **1**, 037001 (2019).

[360]C. Penke, A. Marek, C. Vorwerk, C. Draxl, and P. Benner, "High performance solution of skew-symmetric eigenvalue problems with applications in solving the Bethe-Salpeter eigenvalue problem", Parallel Computing **96**, 102639 (2020).

[361]C. Vorwerk, F. Sottile, and C. Draxl, "Excitation pathways in resonant inelastic x-ray scattering of solids", arXiv:2002.12876 [cond-mat] (2020).